Design of a compact photon detection system for the PANDA Disc DIRC prototype

Entwicklung einer kompakten Photonenauslese für den PANDA Disc DIRC Prototypen

Dissertation zur Erlangung des Doktorgrades der Naturwissenschaften

vorgelegt von Julian Rieke
geb. am 07. Dezember 1986
in Göttingen

II. Physikalisches Institut
Justus-Liebig-Universität Gießen

February 1, 2017

Kurzzusammenfassung

Die Gesellschaft für Schwerionenforschung in Darmstadt wird durch eine großangelegte Erweiterung in die Forschungsanlage FAIR (Facility for Antiproton and Ion Research) integriert. Viele Forschungsgemeinschaften, die sich mit Klärungen von naturwissenschaftlichen Grundsatzfragen auseinandersetzen, werden durch FAIR neue experimentelle Zugänge erlangen. PANDA (Antiproton Annihilations at Darmstadt) stellt ein Schlüsselexperiment bei FAIR dar, bei dem mithilfe von Teilchenstrahlen aus Antiprotonen mit unerreichter Luminosität und Impulsauflösung die Eigenschaften stark wechselwirkender Quanten erforscht werden. Die ambitionierten Ziele dieses Forschungsvorhabens lassen sich nur mit moderner Detektortechnologie erreichen, die eingesetzt wird, um die Reaktionsprodukte der mikroskopischen Kollisionen genau zu studieren. Ein wichtiger Bestandteil des PANDA Detektors ist der Endcap Disc DIRC (EDD), der für die Identifizierung verschiedener Teilchenspezies von Bedeutung ist; insbesondere Pionen und Kaonen müssen selbst bei hohen Impulsen gut unterscheidbar sein. DIRC steht für *Detection of Internally Reflected Cherenkov light* und umschreibt das Funktionsprizip des Detektors, das auf der genauen örtlichen und zeitlichen Vermessung einzelner Cherenkovphotonen fußt.

Die vorliegende Arbeit stellt die Herausforderungen dar, die bei der Umsetzung der elektronischen Photonenauslese des EDD auftreten und zeigt auf, dass sich das Detektorkonzept durch geeignete Komponentenauswahl realisieren lässt. Dazu werden die Prototypen der Mikrokanalplatten Photomultiplier (MCP-PMTs) und die elektronische Auslese, die zur Detektion des Cherenkovlichts eingesetzt werden sollen, in dedizierten Versuchsaufbauten auf ihre Eignung untersucht.

Im ersten Schritt wurden dazu zunächst infrage kommende Photosensoren mithilfe eines vollautomatisierten Versuchsaufbaus studiert und ihre elektronischen Ausgangssignale bei variabler Beleuchtung der aktiven Fläche mit einer fokussierenden Lichtquelle im Einzelphotonenmodus untersucht. Dieses Konzept wurde auf einen Teststand erweitert, der den zusätzlichen Einbau von starken Permanentmagneten erlaubt. Tests unter Anwesenheit von Magnetfeldern sind notwendig, um Veränderungen der Performanceparameter der Sensoren im Detail vorhersagen zu können, wenn diese im Magnetfeld des PANDA Solenoidmagneten betrieben werden. Die Ergebnisse zeigen, dass die Magnetfelder einen starken Einfluss auf die Abbildungseigenschaften der MCP-PMTs haben, der hauptsächlich durch die Ablenkung und Kollimation der Primär- und Sekundärelektronen aufgrund der Lorentzkraft beruht. Ferner wird dargelegt, dass diese Effekte bei einer geeigneten Anodenanordnung und günstiger Ausrichtung der Sensoren zum Magnetfeld zur Verbesserung der Abbildungsgüte ausgenutzt werden können. Um auch bei stärkeren Ma-

gnetfeldern (bis 800 mT) zu messen, wie sie auch bei PANDA zu erwarten sind, wurde ein zusätzlicher Testaufbau konzipiert, um zwischen den Polschuhen eines starken Elektromagneten zu messen.

Parallel zur Untersuchung der Sensoren wurde ein Konzept zur elektronischen Auslese der Sensoren mithilfe des TOFPET-ASICs (Time Of Flight, Positron Emission Tomography, Application Specific Integrated Circuit) erarbeitet und in den Testaufbauten auf die Probe gestellt.

Zum Abschluss wurde das erfolgreich getestete System in den PANDA EDD Prototypen integriert und im Rahmen eines Teststrahlexperiments am Deutschen Elektronensychrotron (DESY) betrieben, dessen Ergebnis die Performanz des nahezu endgültigen Detektorkonzepts zusätzlich unterstreicht.

Mithilfe der vorliegenden Studien konnte gezeigt werden, dass die elektronische Auslese von Mikrokanalplatten Photomultipliertubes (MCP-PMTs) mit fein segmentierter Anodenanordnung durch den kommerziell erhältlichen TOFPET-ASIC erfolgen kann und dass sich die Kombination dieser beiden Technologien eignet, um selbst in starken Magnetfeldern einzelne Photonen mit der notwendigen Orts- und Zeitauflösung zu erfassen.

Abstract

The existing *Gesellschaft für Schwerionenforschung* (GSI) in Darmstadt will be upgraded substantially into the *Facility for Antiproton and Ion Research* (FAIR). The PANDA (Antiprotons at Darmstadt) experiment will be one corner stone of the scientific research at FAIR. An antiproton beam with unreached momentum resolution and luminosity will be used in order to probe fundamental constituents of matter. The ambitious physics goals of PANDA can only be reached with state-of-the-art detector technology which will be used to analyze the final state particles originating from the microscopic antiproton reactions. The Endcap Disc DIRC (EDD) fulfills the specific task of improving the particle identification power of the multi purpose PANDA detector. Specifically, the separation of pions and kaons with high momenta has to be achieved. DIRC stands for *Detection of Internally Reflected Cherenkov light*, a technique that identifies charged particles by means of measuring their Cherenkov angle which can be inferred from the position and time of impact of single quanta of Cherenkov light.

This thesis introduces the reader into the technical challenges which have to be overcome in order to design and build a compact and fast photon detection system for the PANDA EDD. It is also shown, that appropriate optoelectronic equipment exists, that allows to realize the detector concept of the EDD as far as the photon readout is concerned. In a first step microchannel-plate photomultiplier tubes (MCP-PMTs) are tested with a fully automated test setup. Their electronic output is studied under illumination with a well-collimated laser source operated in single-photon mode. This concept is expanded in a second setup which allows to create a magnetic field with the help of strong permanent magnets. Testing in the presence of magnetic fields is important because changes in the performance of the MCP-PMTs have to be anticipated once they are operated in the strong field of the PANDA solenoid magnet. The experiments show that magnetic fields have a strong influence on the imaging characteristics of the sensors. The main reasons for these changes are the displacement and collimation of primary and secondary electrons caused by the Lorentz force. An analysis reveals that an appropriate layout of the anode geometry and orientation of the sensor with respect to the field lines can exploit these changes and lead to an overall improvement as far as the readout of the EDD is concerned. In order to test the sensors at strong fields (up to 800 mT), a test setup was developed to operate and illuminate the sensors between the pole shoes of a strong dipole magnet.

A concept for the electronic readout of the sensors was developed in parallel to the testing of the MCP-PMTs. The commercially available TOFPET-ASICs (Time Of Flight, Positron Emission Tomography, Application Specific Integrated Circuit) was thoroughly

tested in the setups for MCP-PMTs. Ultimately, the complete photon readout has been integrated into the latest EDD prototype and was tested in a testbeam campaign at the *Deutsches Elektronensynchrotron* (DESY) in Hamburg. The performance that could be achieved with the close-to-final detector underlines the suitability of the selected components and shows that the combination of MCP-PMTs with the TOFPET ASIC is a suitable option to measure single Cherenkov photons with the necessary spatial and temporal resolution.

Contents

Erklärung

Ich erkläre: Ich habe die vorgelegte Dissertation selbstständig und ohne unerlaubte fremde Hilfe und nur mit den Hilfen angefertigt, die ich in der Dissertation angegeben habe. Alle Textstellen, die wörtlich oder sinngemäß aus veröffentlichten Schriften entnommen sind, und alle Angaben, die auf mündlichen Auskünften beruhen, sind als solche kenntlich gemacht. Ich stimme einer evtl. Überprüfung meiner Dissertation durch eine Antiplagiat-Software zu. Bei den von mir durchgeführten und in der Dissertation erwähnten Untersuchungen habe ich die Grundsätze guter wissenschaftlicher Praxis, wie sie in der „Satzung der Justus-Liebig-Universität Gießen zur Sicherung guter wissenschaftlicher Praxis" niedergelegt sind, eingehalten.

1 Introduction

The antiproton physics program at PANDA (Antiproton Annihilations at Darmstadt) will be a milestone towards fundamental understanding of QCD (Quantum Chromo Dynamics). Questions about the charmonium sector and hadrons with open charm have been formulated over the past years, but no final answers have been established to many of them. However, the success of charm physics at PANDA greatly depends on the detector's capability to correctly identify final state particles: Many interesting interactions can only be recognized in the analysis if one can be sure that a specific signature in the detector has been caused by a known particle species. This requirement imposes some technical challenges because two completely different particles can leave indistinguishable signatures in many components of the PANDA detector. One prominent example are *pions* and *kaons*, two mesons that are relatively hard to separate from each other, especially at high momenta. Pions can be created in numerous well-known reactions while many decay chains of resonances in the charmonium sector will produce kaons in the final states. These reactions are to be identified and studied which can only be done if one can be certain about the true particle identity.

The Cherenkov subdetectors at PANDA are specifically designed to improve the particle identification of the whole detector. Overall 3 Cherenkov detectors will be installed (all of which are shown and explained in chapter 2): The barrel DIRC[1], the endcap disc DIRC (EDD), and the forward RICH[2] detector represent an important part of the particle identification scheme of PANDA.

The EDD will cover the polar angles between 5° and 22° with respect to the beam axis and represents a novelty in the wide field of particle detectors. No disc shaped DIRC detector has ever been used in a real physics experiment beyond prototyping. For this reason many research and development efforts were necessary to identify suitable technologies, components, manufacturing techniques and measurement strategies to pioneer in this exciting field of detector engineering. Being inspired by the remarkable performance of

---

[1]Detection of Internally Reflected Cherenkov light
[2]Ring Imaging Cherenkov

the BarBar DIRC at SLAC, the DIRC principle was picked up by the detector designers of PANDA.

DIRC detectors exploit the fact that charged particles whose speed surpasses a given threshold will emit Cherenkov photons which will be trapped inside the radiator plate of the detector. Unlike RICH detectors, the Cherenkov photons will be guided to the perimeter of the detector where the photon detection system is located. Many creative proposals have been brought forward and discussed on how to extract key properties of the Cherenkov photons, that would allow conclusions about the primary particles. The latest design of the EDD is based on a focusing optic that translates angles of travel of Cherenkov photons into position information in a readout plane that is instrumented with position sensitive photosensors. This design has emerged as the most advantageous approach overall, but poses some stringent requirements on the photon detection system.

This thesis lays out a series of studies that show the performance of a photon detection system composed of microchannel-plate photomultiplier tubes (MCP-PMTs) with finely segmented anode geometries and the TOFPET ASIC (Time Of Flight, Positron Emission Tomography, Application Specific Integrated Circuit), a commercially available chip that was developed to be used in PET scanners. It is also shown that this system is capable of meeting the key requirements that the detector design demands of it.

The physics motivation behind PANDA and an overview of the PANDA detector as a whole is given in chapter 2 to familiarize the reader with the scientific context, the working principle and the specific tasks of the EDD.

The decision to rely on MCP-PMTs as the primary photosensors of choice over others is motivated in chapter 3. An introduction into contemporary technologies for the detection of light is also contained.

Chapter 4 introduces the electronic equipment that was used in order to build the photon detection system that was ultimately tested in the next chapters. The TOFPET ASIC and its most important technical specifications are presented. The TOFPET evaluation kit, the full scale TOFPET readout system as well as custom made printed circuit boards (PCBs) for the connection and distribution of MCP-PMT signals are shown.

The prototyping efforts and teststand setups involved in the characterization of MCP-PMT prototypes with finely segmented anode layouts are presented in chapter 5. It is shown that the sensors are capable of reconstructing the position of impact of single photons even in strong magnetic fields. The effects of magnetic fields with different strengths on the imaging characteristics of the sensors are analyzed and discussed. The experiments show that an appropriate orientation of the MCP-PMT with respect to the magnetic field

lines can improve the overall performance of the sensor.

Finally chapter 6 closes out with the presentation of the setup and the analysis of a testbeam campaign which was done with $3\,\mathrm{GeV/c}$ electrons in October 2016 at DESY, Hamburg. The novel photon detection system has been integrated into the latest EDD prototype and a series of measurements has been performed and the results were compared to a full GEANT4 simulation of the setup. It is found that the spatial resolution and the photon detection efficiency of the photon detection system agree nicely with Monte Carlo predictions and that the prototype confirms the performance of the close-to-final detector layout.

Chapter 7 summarizes the findings of this work and outlines future steps towards optimization of the photon detection system of the EDD.

2 PANDA at FAIR

2.1 Antiprotons at FAIR

The existing *Gesellschaft für Schwerionenforuschung* (GSI) at Darmstadt, Germany will be substantially upgraded to become the *Facility for Antiproton and Ion Research* (FAIR). This state-of-the art research facility will provide the infrastructure for numerous experiments that seek explanations at the borders of fundamental scientific understanding of nature. 14 initial experiments are envisaged, grouped into the *four pillars*, which form the basis of FAIRs scientific endeavors [1] [2]:

- **APPA**: Atomic and plasma physics, and applied sciences in the bio, medical, and material sciences;

- **CBM**: Physics of hadrons and quarks in compressed nuclear matter, hypernuclear matter;

- **NuSTAR**: Structure of nuclei, physics of nuclear reactions, nuclear astrophysics and radioactive ion beams (RIB);

- **PANDA**: Hadron structure and spectroscopy, strange and charm physics, hypernuclear physics with anti-proton beams.

Various new accelerators, storage rings, separators and technical auxiliaries will be needed to achieve the very ambitious goals behind the experiments at FAIR. In particular, the linear proton accelerator *p-LINAC*, the two synchrotrons *SIS 100* and *SIS 300*, and the storage/cooling rings *CR*, *RESR*, *HESR* and *NESR* will be added. Existing infrastructure like the *UNILAC* and the *SIS 18* will also be used together with the new equipment. All in all, beams of protons, antiprotons and (heavy) ions can be provided in various energy ranges. Figure 2.1 shows an overview of the already existing GSI infrastructure and the new additions that will be made during the upgrade to FAIR. As illustrated in figure 2.1,
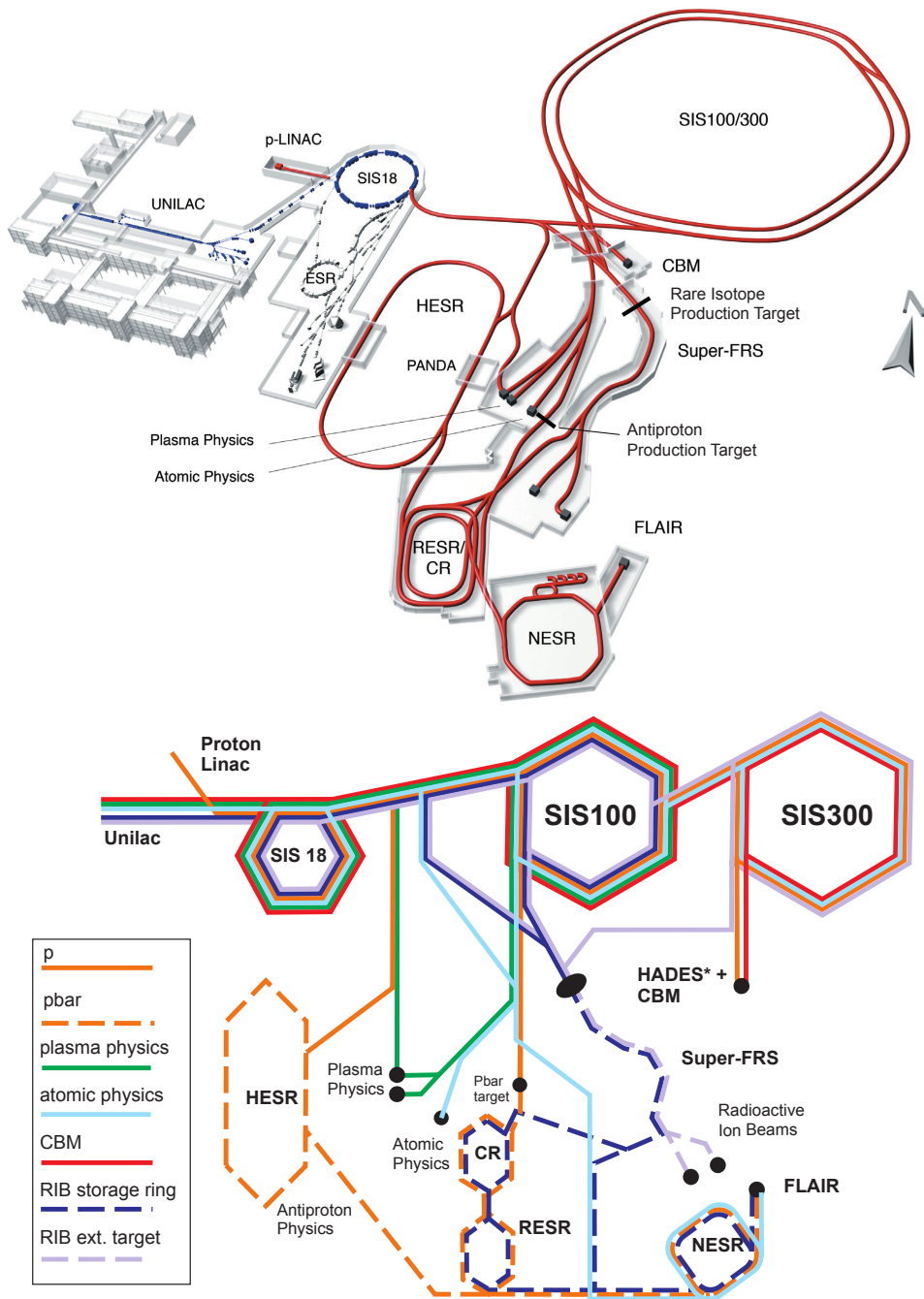
Figure 2.1: Overview of FAIR: The upper schematic shows the existing accelerators and storage rings which are already part of the GSI in blue. The additional infrastructure which comes with the upgrade to FAIR is shown in red. The lower schematic is a transit map for the different beam species which will be provided by FAIR and can be used simultaneously by the individual experiments. The PANDA experiment - which is in the center of this thesis - is located at the HESR where antiprotons can be stored and cooled. The graphics are taken from [2].

the PANDA[1] experiment utilizes a beam of antiprotons which is brought into collision with a fixed proton target. As more specifically discussed in section 2.4, the use of this particle species is very advantageous with regard to many physics goals that PANDA wishes to achieve. However, many technical challenges have to be mastered to generate an antiproton beam which fulfills all required specifications. The creation process of the antiprotons starts at the *proton linear accelerator* (p-LINAC) after which the protons will have kinetic energies of 70 MeV. The synchrotrons *SIS 18* and *SIS 100* will boost the kinetic energies to 29 GeV. These highly relativistic protons are subsequently guided onto an antiproton production target which consists of copper. A magnetic horn will separate the antiprotons from a wide variety of other particles that will also be created during the aforementioned collision process. The *Collector Ring* (CR) allows fast cooling of the caught antiprotons before they are accumulated in the *Recycled Experimental Storage Ring* (RESR). The antiprotons can be injected into the *High Energy Storage Ring* (HESR) either directly from the CR or from the RESR (figure 2.2). In the latter case, higher
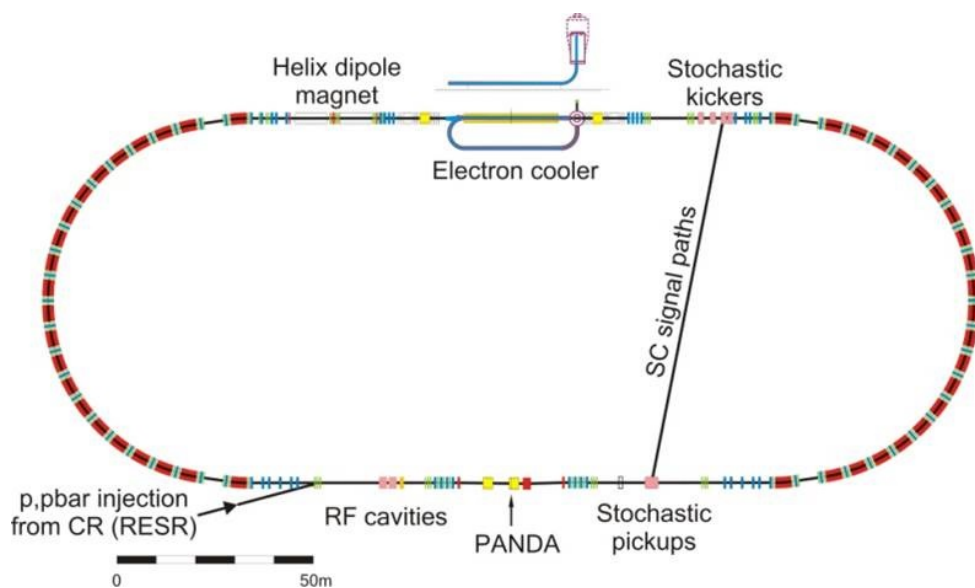
Figure 2.2: A schematic of the HESR: The antiprotons are injected at the lower left and are kept on track by a combination of dipole, quadrupole and sextupole magnets. Electron cooling as well as stochastic cooling of the antiprotons are possible. The PANDA spectrometer is located on the lower straight section. The figure was provided for use in public documents by J. Ritman.

luminosities can be achieved.

The HESR is a racetrack-shaped ring that can accommodate antiprotons with momenta between 1.5 and 15 GeV/c. It can provide electron cooling up to 9 GeV/c and stochastic cooling over the entire momentum range. It has a total circumference of 575 m and can be

---

[1]anti**P**roton **AN**ihilations at **DA**rmstadt

operated in two different modes: The *high resolution mode* is ideal for scanning resonances, because the antiprotons have a well-defined momentum distribution with a momentum uncertainty of $\Delta p/p = 4 \times 10^{-5}$ (see also section 2.4). In this mode, the HESR stores about 10^{10} antiprotons and provides a luminosity of $2 \times 10^{31} \, \text{cm}^{-2}\text{s}^{-1}$. Alternatively the ring can be operated in the *high luminosity mode*. This mode requires the RESR and provides an increase in the number of stored antiprotons and in luminosity by a factor of 10 compared to the high resolution mode. However, the momentum uncertainty will be increased to $\Delta p/p = 10^{-4}$.

These performance parameters are an important requirement for the successful operation of PANDA and the achievement of the physics goals presented in section 2.4 depends very much on them.

2.2 The PANDA spectrometer

To maximize the overall scientific usefulness of the antiproton research branch at FAIR, a state-of-the art particle detector for the analysis of single collision events is as important as the excellent beam quality provided at the HESR. The design of the target spectrometer (TS) and the forward spectrometer (FS) (see figure 2.3) at PANDA incorporates detector concepts that allow an integral analysis of interesting physics events even at the highest interaction rates. Both spectrometers can be divided into multiple subdetector systems, each of them serving a very specialized purpose. This section will briefly outline the most important components of the TS, while putting an emphasis on those systems that are also the most important ones with respect to the Endcap Disc DIRC. Figure 2.3 shows a CAD model of the whole PANDA detector. The TS consists of all components before the gap to the dipole magnet. The instrumentation downstream of this gap is considered part of the FS.

2.2.1 Target system

Starting at the interaction point, the innermost subsystem is the target system [4] itself, which provides the reaction partner for the antiproton beam. Ideally, the target density variations between consecutive collision events are small in order to provide a constant luminosity and controllable event rates. In order to achieve that, two different designs of the target system have been established. One option is to create small droplets of frozen
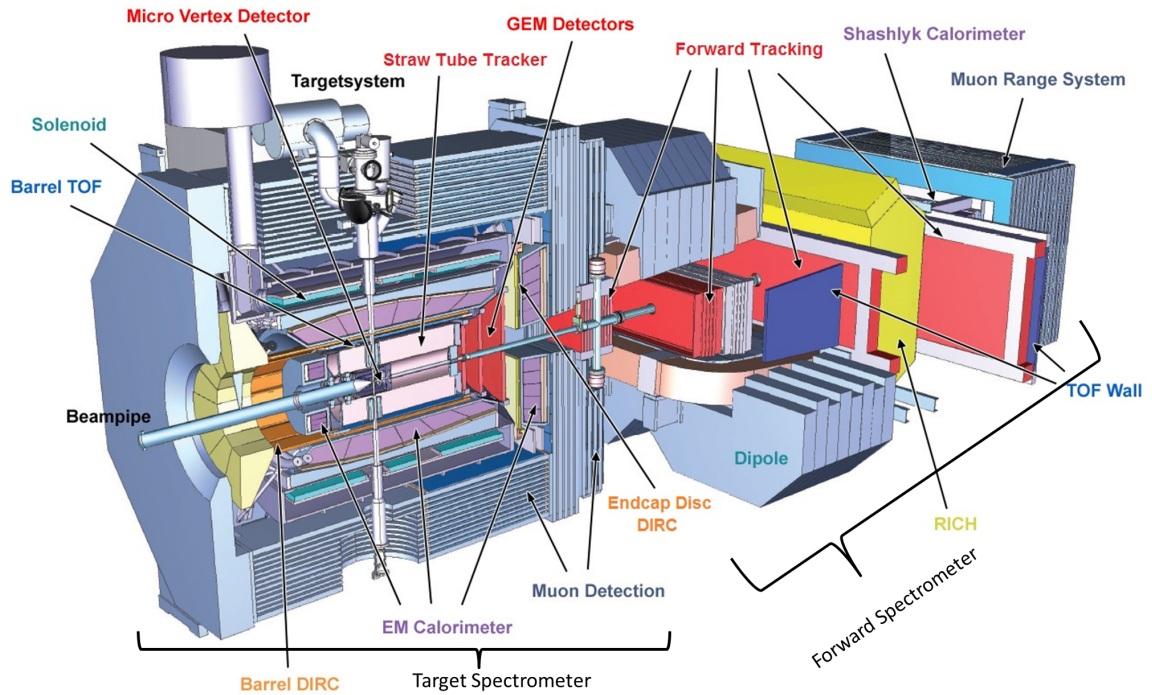
Figure 2.3: The PANDA spectrometer (figure slightly modified from [3]): The antiproton beam enters from the left. The target spectrometer (TS) encloses the interaction point. Small polar angles are covered by the forward spectrometer (FS).

hydrogen in a triple point chamber which is located on top of the solenoid magnet. These pellets have diameters between 10 and 30 μm and can be vertically injected into the target tube which leads the hydrogen into the vacuum of the beam pipe. The collisions take place directly in the HESR. The main strength of the pellet approach is the reachability of very high target densities which can be exploited to achieve high luminosities. Furthermore, the search for the primary interaction vertex can always be confined to the volume of the pellet that served as the interaction partner in the collision with the antiproton. This fact can be exploited if the location of the pellet is known at the time of the collision. One disadvantage of the pellet system comes from the fact that the effective target density is not very homogeneous as a function of time, because of the discrete appearance of the pellets in the interaction region.

Alternatively, a cluster jet target has been developed to complement the strengths and weaknesses of the pellet approach. A variety of pre-cooled and compressed gases can be prepared and adiabatically expanded into the vacuum of the HESR beam pipe through a gas nozzle with a diameter of some micrometers. If the conditions are prepared appropriately, a so-called cluster jet - moving at supersonic speed - will be created during a condensation phase. Many parameters of these cluster jets, like the cluster size, speed,

19

density and also the yield of the cluster creation can be varied through the parameters of operation, like the type of gas, its temperature and pressure and also by the diameter of the nozzle. The advantages are a more homogeneous luminosity profile and the adaptability of the system. However, one does not reach the overall target densities of the pellet targets.

2.2.2 Tracking systems and magnets

The subdetector system which is closest to the interaction point is called *Micro Vertex Detector* (MVD) [5]. Together with the *Straw Tube Tracker* (STT) [6] and the *Gas Electron Multiplier* (GEM) stages, these components form the tracking system of the target spectrometer of PANDA. Tracking is one essential input for event reconstruction as it allows to measure the flight trajectory of charged secondary particles. Due to the curvature of the flight path of charged particles in the magnetic field of the PANDA solenoid and the forward dipole, it is also possible to derive the momentum vectors of these tracks. An accurate reconstruction of the trajectory of charged particles is also one key requirement for the operation of the Endcap Disc DIRC, because any given error on the track angle reconstruction will directly translate into an error in the measurement of the Cherenkov angle of this track, which will subsequently diminish the PID performance. An illustration of the tracking systems of the TS can be seen in figure 2.4.

The MVD consists of 4 barrel parts and 6 discs which are placed closely around the interaction point. The inner layers (red in figure 2.4) will be equipped with $100 \times 100\,\mu$m sized *hybrid pixel detectors* while the outer layers (green) will be instrumented with *silicon strip detectors*. One main task of the MVD is to accurately reconstruct vertex displacements with an accuracy of about $100\,\mu$m. A $D^{\pm}$ meson for example has a $c\tau$ of $311.8\,\mu$m which can be resolved with the help of this subsystem. For both parts - the pixel and the strip part - a dedicated, radiation hard and free running readout scheme has been developed. *PASTA*[2], the custom made 64 channel ASIC for the strip part, has been a development based on the TOFPET ASIC which is also the most promising readout candidate for the Endcap Disc DIRC. The toughest challenges for the MVD are the design of the low mass support, the cooling requirements that have to be implemented into the very small volume, and the radiation tolerance of the electronic equipment.

The STT is made up of 4636 cylindrical gaseous proportional counters. Each of them

---

[2]PAnda STrip Asic
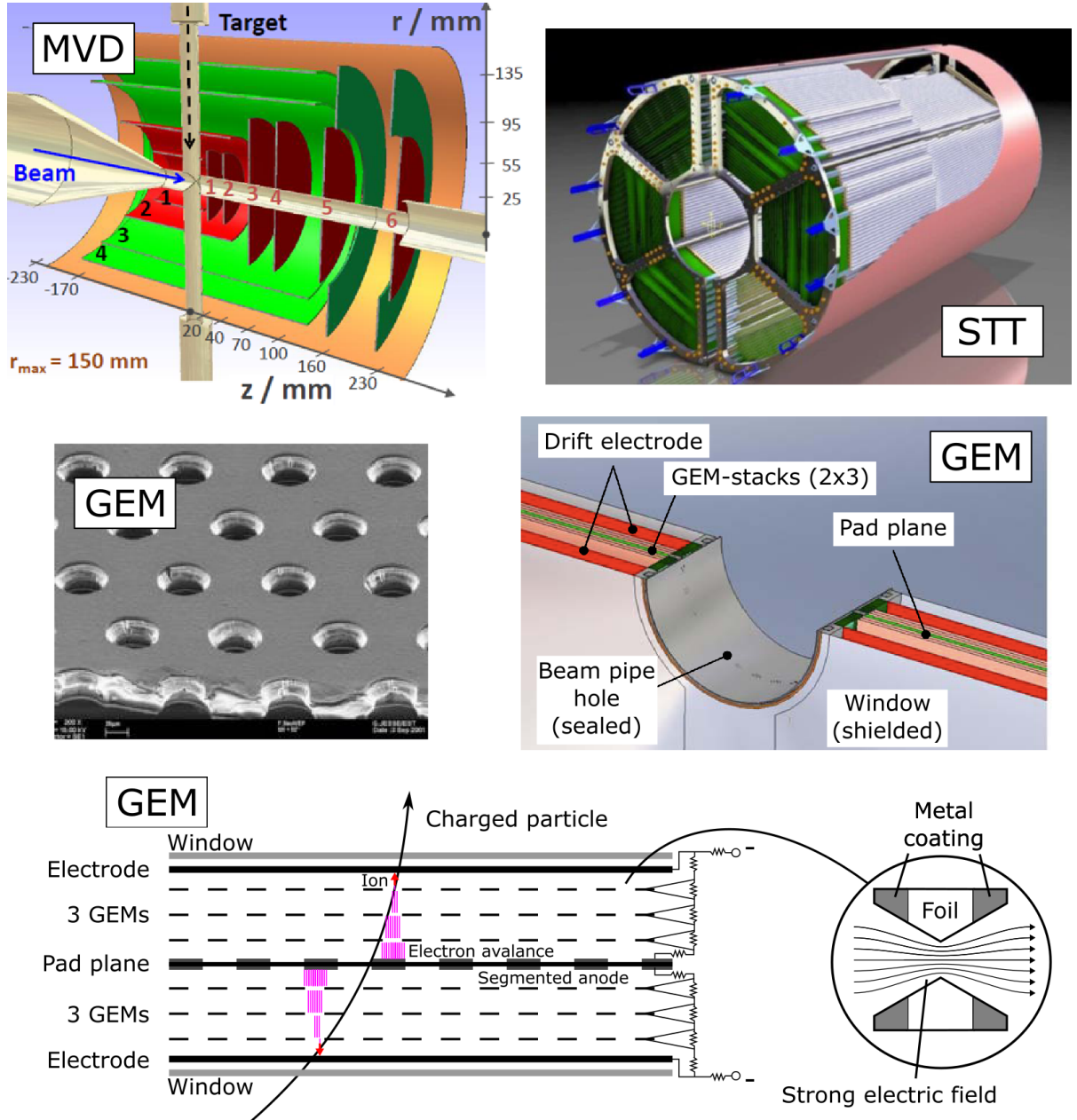
Figure 2.4: Overview of the tracking detectors at PANDA. The trajectories and momenta of charged particles in the target spectrometer will be reconstructed with the MVD, STT and GEM trackers . More details are given in the text. The upper 4 figures are taken (and partially modified for better readability) from [5], [6] and [7].

has a diameter of 10 mm and a length of 1.5 m. These so-called *straws* are combined in layers - almost parallel to the beam axis - to efficiently instrument the volume between the MVD and the EMC which corresponds to a hollow cylinder with inner and outer radii of 150 mm and 420 mm, respectively. Each straw is filled with a counting gas (Ar/CO_2) up to a pressure of 2 bars while a thin gold-plated tungsten wire is drawn along its central axis. The gas is contained in each straw by a 27 μm thin aluminized foil which is strong enough to withstand the overpressure.

As illustrated in figure 2.4 the straws are combined into several layers, partly tilted (at 3°) against each other what improves the overall precision of the tracking. If a charged particle travels through the STT it can traverse more than 20 of these straws, leading to ionization of counting gas atoms/molecules in each one of them. Because of an applied voltage between the metallized inner surface and the counting wire, an electron avalanche is triggered, leading to a measurable electrical signal at both ends of the counting wire. With the help of a fast electronic readout, the fastest electrons of the avalanche can be detected and the position of the initial ionization can be reconstructed. A big advantage of this subdetector is its very low material budget and its excellent position resolution of about 150 μm in radial and 3 mm in longitudinal direction. Additionally, dE/dx information can be derived from the magnitude of the charge avalanche what helps with the identification of the primary particle.

The forward region between 5° to 22° will be covered with 3 GEM discs. A CAD model of one of these discs and an illustration of the working principle are shown in the lower part of figure 2.4 (see also [8] for a deeper introduction). The GEM discs consist of a gas volume which is sealed by windows on both sides. Drift electrodes and the central pad plane are attached to a high voltage source while 3 GEM foils are placed between the two on either side. The purpose of these GEM foils is to work as a *secondary electron multiplier* (a subject which will be revisited in chapter 3). They are made from about 50 μm thick Kapton foils which are copper-coated on both sides and perforated by many tiny holes (about 70 μm diameter). Both copper faces of the foils are supplied with appropriate voltages what leads to a sharp increase of the electric field strength inside the holes.

Similarly to the STT, incoming ionizing radiation will separate an electron from a counting gas molecule or atom. The electrons will be accelerated by the high voltage between the drift electrode and the pad plane. The field strength inside the GEM foil pores will be high enough to trigger an electron avalanche. By placing 3 foils in series, a sufficient gain of the primary electron can be achieved so that a measurable electrical signal can be picked up. By segmentation of the pad plane (into approximately 35,000 channels in

total), the readout can be made position sensitive what allows tracking in the forward region.

Strong magnetic fields are essential for precise measurements of the momentum of charged particles [9]. The superconducting solenoid magnet at PANDA creates a magnetic field of up to 2 T with an error of only 2 %. It surrounds a cylindrical volume of about 2.8 m length and an inner radius of 105 cm. Free spaces for an entry and exit of the target system could be left due to the segmentation of the coil of the solenoid. The cooling equipment (solenoid supply box) which is necessary to maintain the superconductivity of the magnets is placed on top of the target spectrometer.

PANDA is a fixed target experiment. Hence, many secondary particles will be observed in the forward region where the normal conducting dipole magnet will provide a bending power of 2 Tm. This magnet serves multiple purposes. Firstly, it allows - in conjunction with the forward tracking systems - a precise momentum reconstruction of charged secondary particles. Secondly, it works as a bending magnet for antiprotons which have not undergone a collision reaction. Thirdly, the iron return yokes - of both the solenoid and the dipole - are instrumented with a muon range system [10]. It consists of alternating layers of iron yoke and Mini Drift Tubes (MDTs).

2.2.3 Calorimeters

The tracking system in the magnetic fields of both PANDA magnets allows to determine the momentum of charged particles. In addition, a set of *Electromagnetic Calorimeters* (EMCs) will be installed in the forward and the target spectrometers [11] [12]. They will allow a precise measurement of the total energy of γ and $e^{\pm}$ particles that deposit their energy in electromagnetic showers within the calorimeter volume. They also play an important role in the PID concepts of PANDA, as will be shown in section 2.3.

The calorimeters in the target spectrometer are separated into 3 units. Two of them - the barrel and endcap part - are shown in figure 2.5. The additional backward endcap EMC can be seen in the overview in figure 2.3. The biggest part is the barrel calorimeter with 11,360 lead tungstate crystals. This material, also known as $PbWO_4$ or simply PWO, has come forward as an excellent choice to be used as an inorganic scintillation material in the PANDA EMC. Its advantages are a very short radiation length X_0 of 8.9 mm and a small Molière radius of 20 mm what helps to more efficiently capture as much energy of incoming particles as possible: With a total length of 20 cm, the crystals will provide $22 X_0$ already. Furthermore, a good decay time of less than 10 ns and sufficient radiation
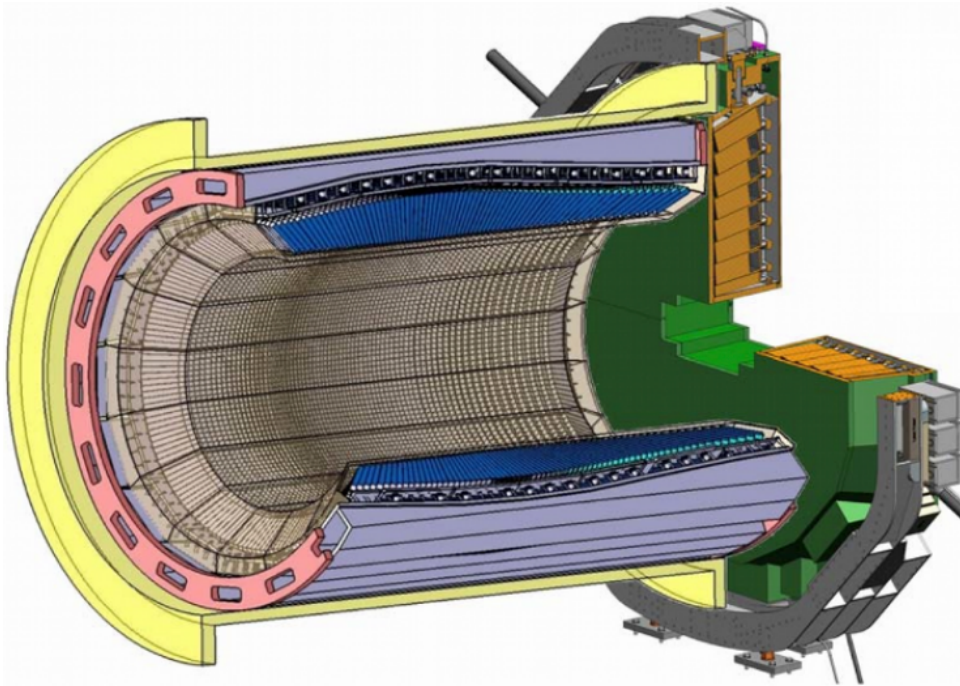
Figure 2.5: The PANDA barrel and endcap EMCs. Picture taken from [12].

hardness support this material choice. The tapered crystals will be wrapped in reflective foils and read out by *Large Area Photo Diodes* (LAPDs) in the barrel part.

The forward endcap part will hold 3600 PWO crystals. The backward endcap EMC will hermetically seal the interaction volume with another 592 crystals which allows an almost complete 4π coverage. Both endcaps are read out with vacuum based phototriodes. All in all, the EMCs will provide energy resolutions below $\frac{\sigma_E}{E} = 1\% \oplus \frac{2\%}{\sqrt{E[\text{GeV}]}}$.

2.3 PID and Cherenkov detectors at PANDA

The previous sections outlined how the momentum and energy of certain particles can be measured. This section will introduce the third pillar of event reconstruction in high energy physics and hadron physics experiments: The identification of secondary particles (i.e. particles that are created during the primary collision and then detected), or simply PID[3]. Figure 2.6 shows a classical PID scheme that can be found in many experiments. Apart from the *Hadronic Calorimeter* (HCAL), all components from figure 2.6 are present at PANDA. It is illustrated that PID can only be achieved by cooperation of all detector components. However, there are also some detectors at PANDA that are *solely* devoted

---

[3]PID: Particle IDentification

to improving the overall capability of differentiating certain particle species. PID is important for numerous physics aspects. *Hadron spectroscopy*, which will be explained more in section 2.4, is one exemplary case where a successful realization is highly dependent on PID to reliably detect certain meson species in the final state.
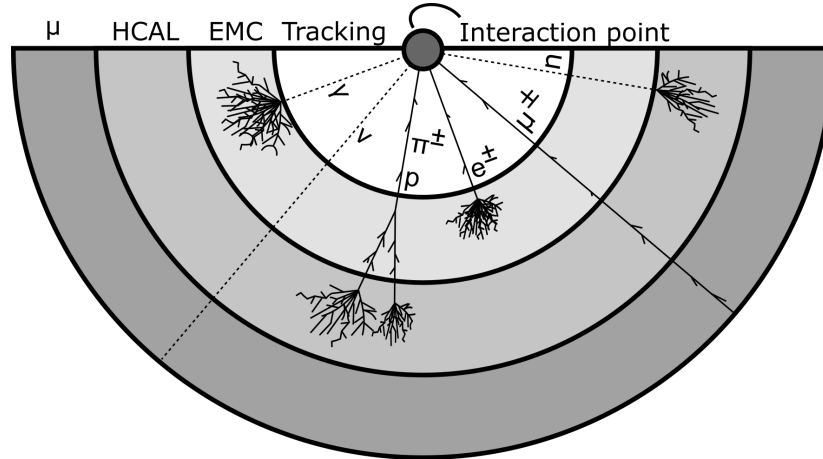
Figure 2.6: A classical PID scheme is based on the specific signatures that certain particle species leave in different detector components: A dashed line indicates no measurable reaction of the species in the corresponding detector component. PANDA does not have a dedicated hadronic calorimeter (HCAL) but the separation of certain meson species (e.g. pions and kaons) is necessary for many physics cases. Hence, some additional PID detectors are needed as explained in the text.

2.3.1 Time of flight

If two different particles have the same momentum (and the same electrical charge) they cannot be told apart by tracking in magnetic fields. One possibility to circumvent this problem is to measure the time that the particles need to travel a certain - ideally long and well-defined - distance. Let's say a particle has the (possibly relativistic) momentum $p = |\vec{p}|$ and a mass of m. The time t it needs to overcome the distance l in its direction of travel can be calculated to be:

$$t = \frac{\sqrt{p^2 + (m\,c)^2}}{p}\frac{l}{c}. \tag{2.3.1}$$

Where c is the speed of light in vacuum. It can be seen, that the time of flight (TOF) depends on the mass m which can be used to identify the particle. The *difference* in TOF

Δt between two particles with masses m_1 and m_2 thus becomes:

$$\Delta t = \frac{l}{c\,p}\left(\sqrt{p^2 + (m_1\,c)^2} - \sqrt{p^2 + (m_2\,c)^2}\right). \tag{2.3.2}$$

For highly relativistic particles we can assume that $p \gg m\,c \Rightarrow \frac{m\,c}{p} \ll 1$ which allows a TAYLOR expansion of the square root:

$$p\sqrt{1 + \left(\frac{m\,c}{p}\right)^2} = p\left[1 + \frac{(m\,c)^2}{2p^2} + \mathcal{O}\left(\frac{m\,c}{p}\right)^4\right]. \tag{2.3.3}$$

With this we can write:

$$\Delta t = \frac{l\,c}{2\,p^2}\left(m_1^2 - m_2^2\right). \tag{2.3.4}$$

This equation already reveals the limitations of this PID technique. The resolution of the time measurement has to be good enough to differentiate the flight times of different particles properly. Ultimately, for a given length l and given masses, $\Delta t \to 0$ for $p \to \infty$ which shows that the separation works only up to certain momenta when Δt becomes smaller than the timing resolution.

In the target spectrometer of PANDA the *Scintillating Tile Hodoscope* (SciTil) [13] will provide TOF for charged particles. The forward spectrometer has dedicated *TOF walls* built in. In both cases multiple scintillating volumes are read out with fast photosensors to measure an individual time of arrival. The differences between these times can be used as a TOF in the subsequent event analysis.
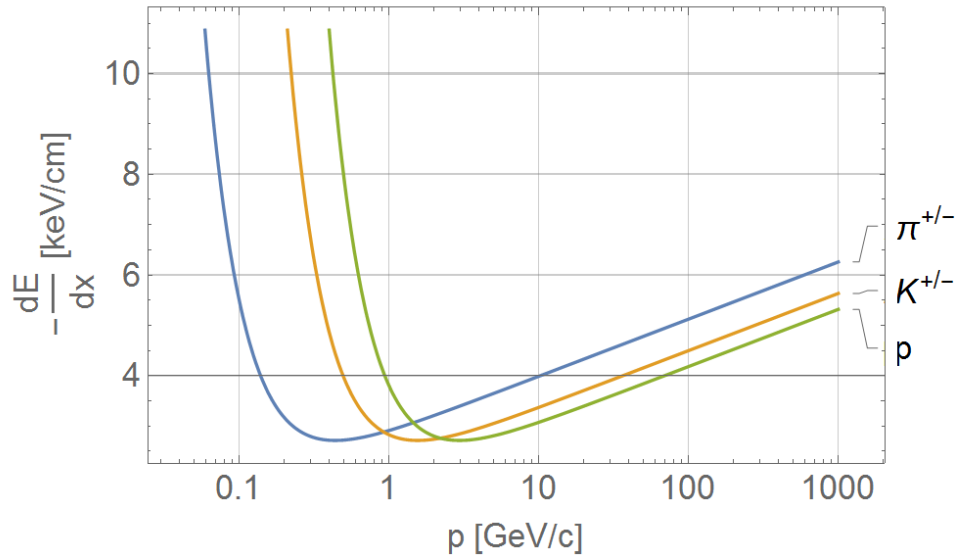
2.3.2 Energy loss

The well-known BETHE-BLOCH equation describes the energy loss of heavy (compared to electrons), charged incident particles (i.P.) due to ionization of surrounding matter:

$$-\frac{dE}{dx} = \frac{4\,\pi}{m\,c^2}(\alpha\,\hbar\,c)^2\frac{z^2}{\beta^2}\left(\frac{\mathcal{Z}\,\rho}{A\,u}\right) \times \left[\ln\left(\frac{2m\,c^2\,\beta^2\,\gamma^2}{I}\right) - \beta^2\right] \tag{2.3.5}$$

m: mass of the electron	c: speed of light in vacuum
α: fine structure constant	z: charge number of i.P.
$\beta \cdot c$: speed of i.P.	γ: LORENTZ factor of i.P.
$\mathcal{Z}$: charge number of absorber	ρ: density of absorber
A: mass number of absorber	I: mean excitation potential of absorber

The amount of deposited energy per unit of path length (due to ionization) can be measured with an appropriate detector. With this measurement, different charged particles - with the same charge and momentum - can be distinguished from each other within a certain momentum range. Figure 2.7 gives some examples for pions, kaons and protons in Argon.

Figure 2.7: Energy loss of different particle species in Argon as calculated with equation 2.3.5: If a detector system can measure the amount of deposited energy during the passage of a charged particle and the length of the interaction is also known, the particle can be identified by the specific ionization rate. However, this technique works only in a confined region of the momentum spectrum that depends on the particles that are to be separated and the envisaged separation power of the setup.

In PANDA the *Straw Tube Tracker* (STT) is just one example for a subdetector that will provide dE/dx information. As the straws are also filled with Argon, the amount of ionization of the counting gas in the straws is related to the pulse height of the resulting electrical signal.

2.3.3 The Cherenkov effect

If the speed of a charged particle surpasses the phase velocity c/n of a given optical medium, so-called *Cherenkov radiation* will be emitted. c and n are the speed of light in vacuum and the refractive index of the optical medium, respectively. This phenomenon is often compared to the emission of sound by a source which moves faster than the speed of sound, e.g. a jet plane. Cherenkov radiation is electromagnetic radiation, and its direction of travel encloses the *Cherenkov angle* θ_c with the direction of travel of the charged particle that caused the radiation (see figure 2.8). Consequently, the momentum vectors of all Cherenkov photons that can be emitted at a certain point in space and time will span the surface of a cone - the so-called *Cherenkov cone*. The Cherenkov angle only depends on the refractive index n of the optical medium and the speed of the charged particle in units of the speed of light in vacuum β. The relation reads:
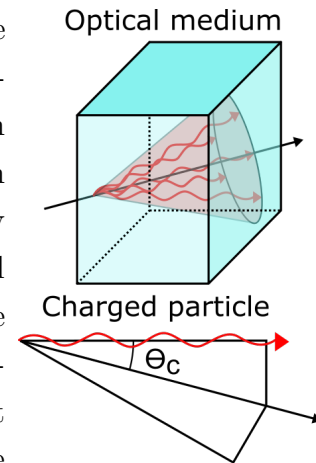

Figure 2.8:
The Cherenkov effect

$$\cos \theta_c = \frac{1}{n(\lambda)\,\beta} \Rightarrow \theta_c = \arccos \frac{1}{n(\lambda)\,\beta} = \arccos \frac{\sqrt{m^2 + p^2}}{n(\lambda)\,p} \tag{2.3.6}$$

The refractive index of optical materials depends on the wavelength of light. Hence, n has been written as a function of the wavelength of the emitted photon. Since the mass m of the particle appears in the equation, the Cherenkov effect can be used for particle identification, too.

If the charged particle (with the charge ze) travels the distance $\mathrm{d}x$ (above the threshold speed), the amount of Cherenkov photons N that are created in a small wavelength region $[\lambda, \lambda + \mathrm{d}\lambda]$ can be calculated by using the well-known FRANK-TAMM equation [14]

$$\frac{\mathrm{d}^2 N}{\mathrm{d}x\,\mathrm{d}\lambda} = \frac{2\pi\alpha z^2}{\lambda^2}\,\sin^2 \theta_c \tag{2.3.7}$$

where α is the fine structure constant. The total number of photons created along a trajectory of length l can be obtained by integrating this expression over the wavelength
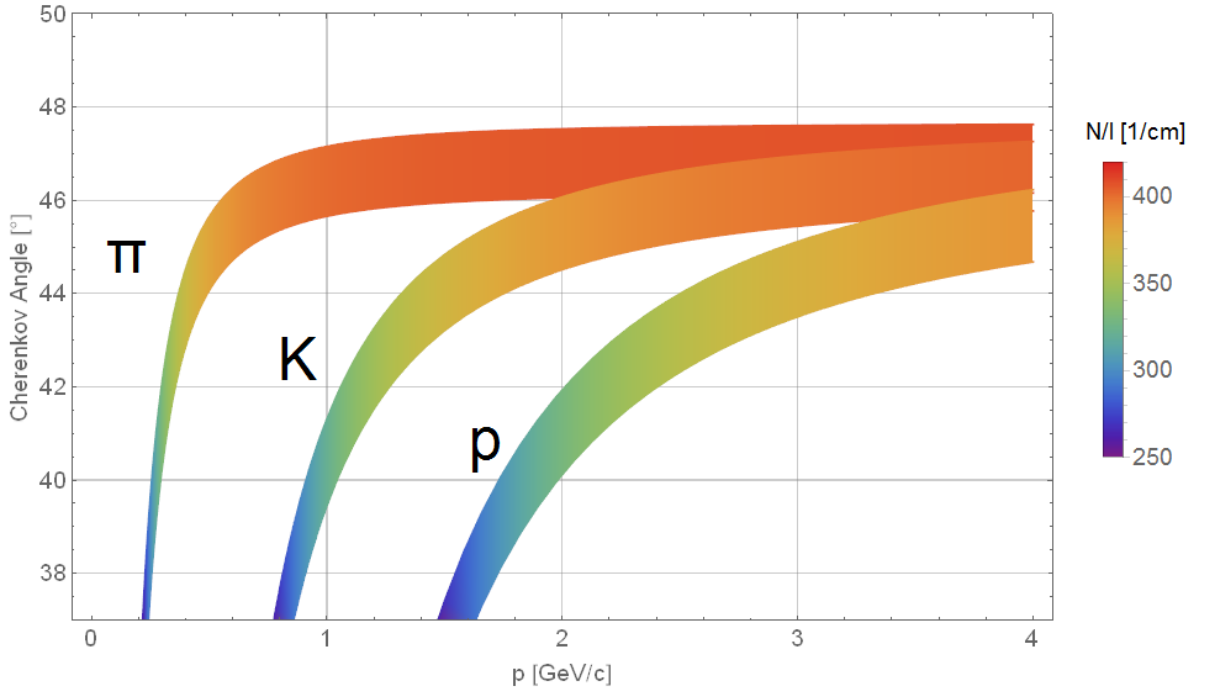
band and the trajectory of the particle:

$$N_{\text{Phot}}(l, \lambda_1, \lambda_2) = 2\pi\alpha z^2 \int\limits_0^l \int\limits_{\lambda_1}^{\lambda_2} \mathrm{d}x\mathrm{d}\lambda \frac{\sin^2\theta_c}{\lambda^2}. \tag{2.3.8}$$

The Cherenkov angle and photon yield for some typical particles are shown in figure 2.9.

Figure 2.9: Cherenkov angles and photon yield for different particles: The Cherenkov angles of pions, kaons and protons with momenta up to 4 GeV/c in fused silica are shown. The (wavelength-dependent) refractive index of the optical medium has been approximated with the SELLMEIER equation (see also eq. 5.1.17 in chapter 5) to account for dispersion. The bands show how the Cherenkov angle varies at different momenta due to dispersion. A wavelength band from 300 to 600 nm has been chosen. The color of the bands gives the amount of Cherenkov photons that are created during the passage of 1 cm of fused silica in this wavelength band (according to equation 2.3.8).

Cherenkov radiation can be exploited in several detector designs. The easiest possibility is the *Threshold Cherenkov Counter* (TCC). It works by the mere detection of Cherenkov light and is comparably straightforward to build. However, it can only tell apart two particles, if only one of them emits Cherenkov radiation and the other one doesn't.

More sophisticated designs aim to measure the Cherenkov angle and not only the presence of Cherenkov light (see figure 2.10). *Ring Imaging Cherenkov* (RICH) [15] detectors use a Cherenkov radiator to cover a certain angular region. The Cherenkov light leaves the
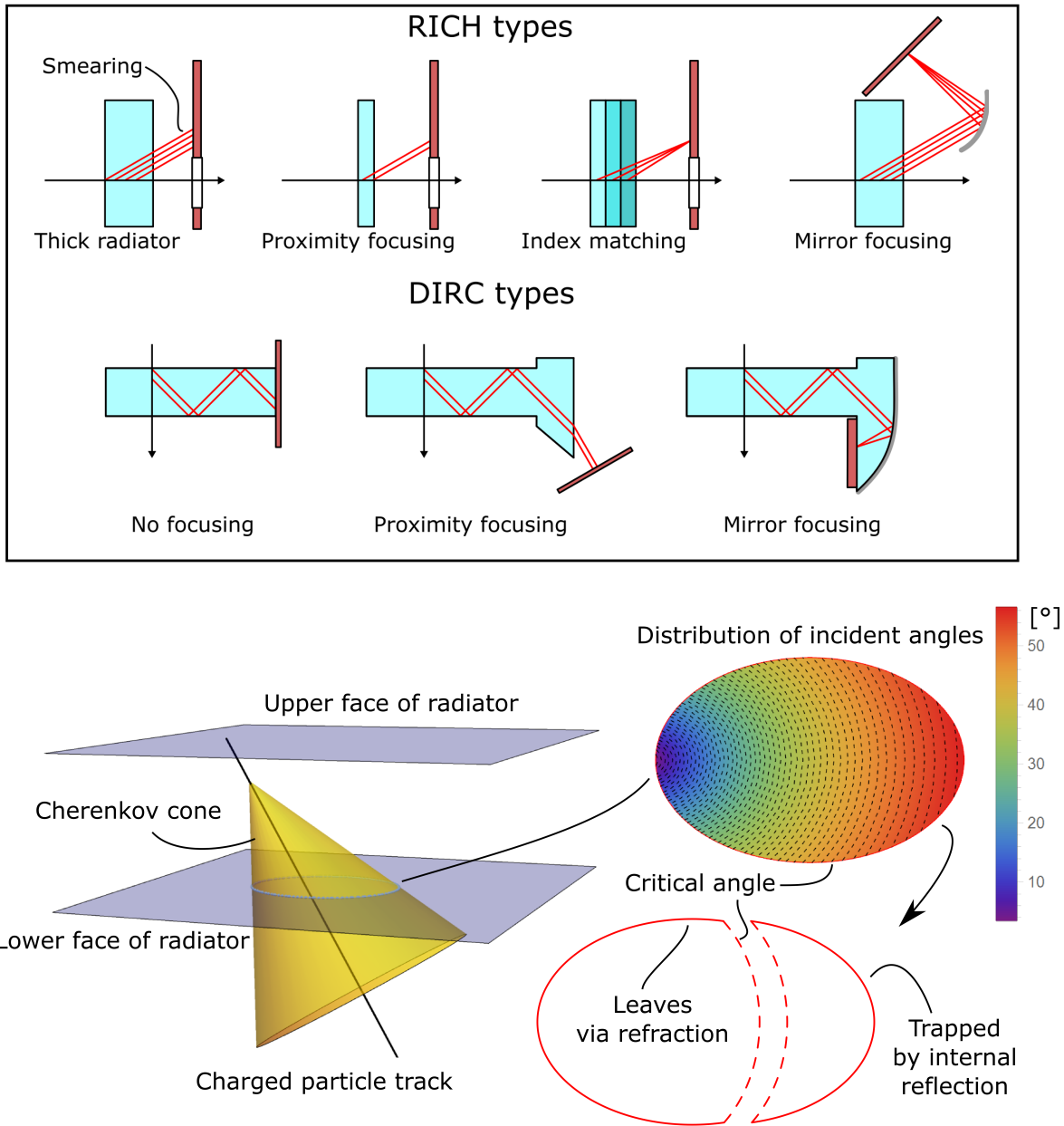
Figure 2.10: The upper part of the figure illustrates different RICH and DIRC detector concepts as explained in the text. The lower part shows the part of the Cherenkov cone that is trapped by total internal reflection in a DIRC detector. In this example, the charged particle has an angle of 30° with respect to the radiator surface and the Cherenkov angle is also 30°. The colors inside the ellipse represent the angle of incidence of all lines originating from the tip of the Cherenkov cone. All photons (which can only impinge along the perimeter of the ellipse) with an angle of incidence greater than the critical angle will be caught inside the radiator. The rest will leave via refraction. The so-called *trapping fraction* is defined by the fraction of photons that are subject to total internal reflection. RICH detectors have a comparably low refractive index what leads to smaller trapping fractions compared to DIRC type detectors.

radiator and is subsequently imaged onto a position sensitive readout plane. The image of the Cherenkov cone on the readout plane is an (elliptic) ring whose diameter (or semiaxes) are determined by the speed of the original particle, and by the imaging technique. A better resolution can be achieved by optimization of the imaging. *Proximity Focusing* describes the technique of using a very thin radiator what means that Cherenkov photons are only created on a closely confined section of the particles trajectory. This reduces the smearing of the image due to reduction of photons which originate from different locations in the radiator along the particle track. However, it also reduces the overall light yield. One attempt to overcome this limitation is by gradually increasing the refractive index of the radiator in the direction of particle travel. The rate of change can be optimized to realign Cherenkov photons from different origins back onto the same position in the readout plane. Another common approach is the so-called *Mirror Focusing* approach. Curved mirrors are used to focus all photons with a given angle of travel onto the same point in the readout plane, regardless of their point of origin along the particle track. The forward spectrometer of PANDA will host a mirror focusing RICH to complement the two Cherenkov detectors in the target spectrometer.
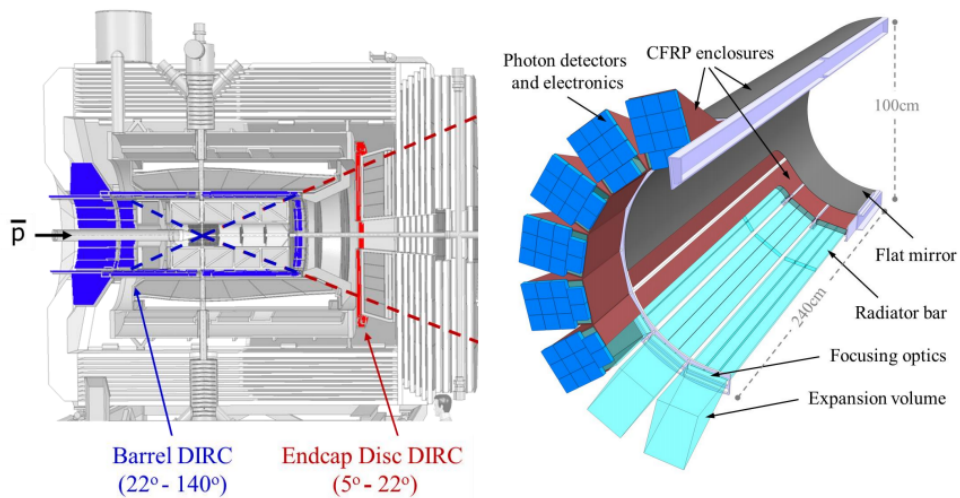
Figure 2.11: The PANDA Barrel DIRC will cover polar angles between 22° and 140° and 2π in azimuthal direction. Figures taken from [17].

The *Barrel DIRC* [16] and the *Endcap Disc DIRC* employ the *Detection of Internally Reflected Cherenkov light*. The main difference - compared to a RICH type detector - is the fact that the Cherenkov photons of interest do not leave the radiator but are trapped inside of it by total internal reflection. A photon is trapped inside the radiator if its angle of incidence on the radiator face is greater than the critical angle of the corresponding

optical transition (i.e. fused silica to air). The critical angle ξ_c can be calculated like

$$\xi_c = \arcsin\left(\frac{n_1}{n_2}\right) \tag{2.3.9}$$

where n_1 and n_2 are refractive indexes of the radiator and its environment (e.g. air). For the transition from fused silica to air ($n_1 = 1.46$ and $n_2 = 1$) one gets $\xi_c \approx 43.2°$. As illustrated in figure 2.10, the angles of incidence vary across the Cherenkov cone if the track enters the radiator non-perpendicularly. Therefore, some part of the Cherenkov light will be caught inside by total internal reflection while another part of the cone will leave the radiator via refraction.

The PANDA barrel DIRC will cover the angular region between 22° and 140° as shown in figure 2.11. It consists of bars and wedges made of fused silica. In order to improve the imaging performance, a lens has been developed to be placed between the bars and wedges. The photon readout will be realized by a combination of MCP-PMTs with segmented anode structures and the FPGA-based TRB3 readout [18].

2.3.4 The PANDA Endcap Disc DIRC

The design of the PANDA Endcap Disc DIRC (EDD) has been subject to optimization since the beginning of its development in Giessen in 2006. First approaches foresaw a *Time of Propagation* (TOP) [19] design with dichroic mirrors and a fast photon readout instead of imaging optics. It was found that the necessary time resolution for this design is not achievable and the first focusing design came into the center of the research efforts. A *3D Disc DIRC* [20] concept was brought forward, aimed to combine time-of-arrival information with a 2-dimensional position-of-impact information measured with a combination of focusing optics and fast, position sensitive photon detectors. However, a big step towards the final design was achieved by identifying the choice of the photosensor as the central design criterion. His first concept was built around *digital Silicon Photomultipliers* dSiPMs (see section 3.2.2). These sensors showed some very advantageous properties but were ultimately subordinated to MCP-PMTs only due to their sensitivity towards radiation inflicted damage. A general discussion of modern photosensors and their suitability for the EDD can be found in chapter 3 where pros and cons of different technologies are compared. Ultimately, a design with MCP-PMTs was developed that stands to benefit from learned lessons during the development of the detector system. It can be seen in figure 2.12.

The EDD design now consists of four independent quadrants. Each of them has a $2\,\mathrm{cm}$ thick radiator plate made out of fused silica. This material has been chosen because it combines a very high transparency, sufficient radiation hardness and a high refractive index of about 1.46. A circle around the center of the detector would require a radius of roughly one meter to circumscribe the four radiators. The quadrants will be combined to form a regular dodecagon where all 12 sides are equipped with 9 *Readout Modules* (ROMs) each. Each of the ROMs has one MCP-PMT and 3 *Focusing elements* (FELs). The FELs image all photons with a given angle of travel φ' on a well-defined position z along the MCP-PMT. The position z is also influenced by the quantity α_{FEL} which is the angle between the normal vector of the ROM and the projection of the direction of travel of the photon into the plane of the radiator, as demonstrated in figure 2.12. Like the radiator, the prisms and FELs consist of fused silica and are coupled to each other via high quality optical bonds. The optics of the EDD have to fulfill very stringent quality requirements as far as their surface quality, coplanarity, and material purity are concerned. The anode layer of the MCP-PMTs (as explained in more detail in the following chapters) is segmented into 3×100 anode strips that are read out separately. This technique provides information about the position-of-impact along the z-axis as shown in the figure. More
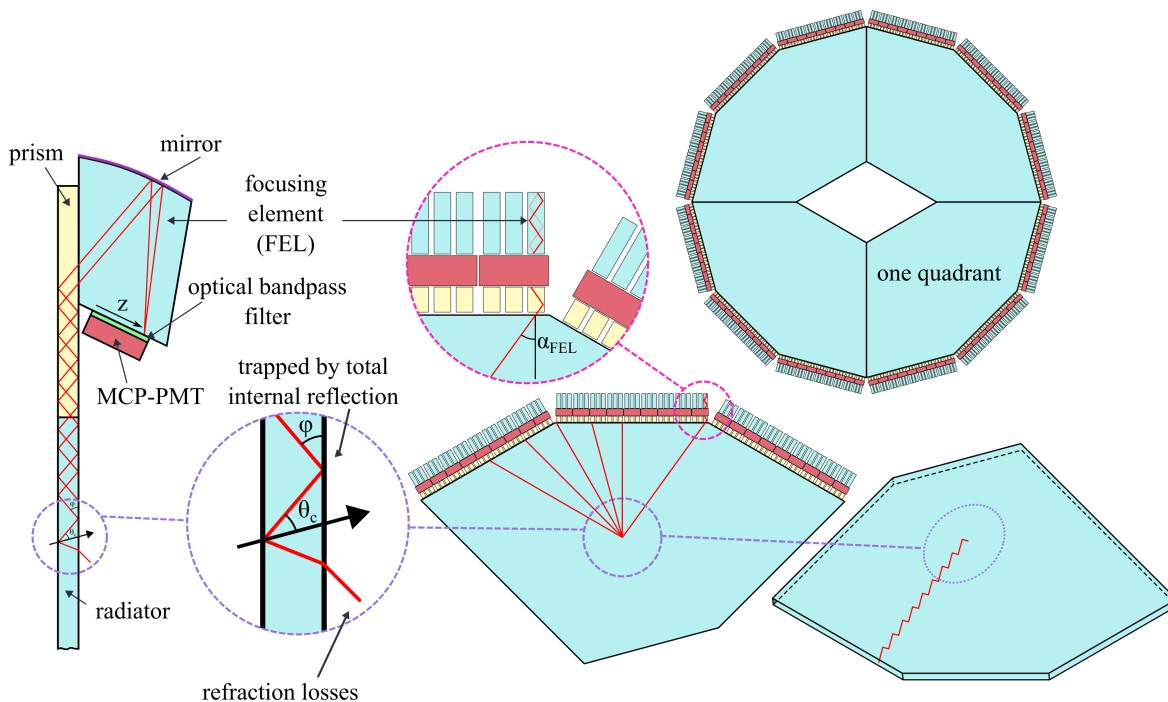
Figure 2.12: The current design of the PANDA EDD. Detailed explanations can be found in the text and in [21].

detailed information on the design can be found in [21].

The reconstruction of the Cherenkov angle relies on an analytically derived relationship between the position-of-impact of the Cherenkov photon z, the imaging function of the FEL $z(\varphi')$ and the momentum of the charged particle that emitted the Cherenkov photon. The relation between φ and φ' reads

$$\tan\left(\varphi'\right) = \tan\left(\varphi\right) / \cos(\alpha_{\mathrm{FEL}}). \tag{2.3.10}$$

It is assumed that the angle of travel φ is conserved throughout the passage of the photon through the radiator and that the photon enters the corresponding FEL through the center of the prism. The derivation and a step-by-step reconstruction algorithm of the Cherenkov angle can be found in [23]. Monte Carlo simulations have shown that the design fulfills the PANDA requirements of 4σ separation power for pions and kaons up to $4\,\mathrm{GeV/c}$ [21]. These studies are based on readout performance parameters as given for the TOFPET ASIC [24]. More about the requirements for the photon readout can be found in the following chapters. One central goal of this dissertation is to show the compatibility of appropriate MCP-PMTs with a TOFPET-ASIC readout.

2.4 Physics cases at PANDA

The PANDA experiment has been devoted to the exploration of the non-pertubative regime of *Quantum Chromo Dynamics* (QCD) [22]. This theory describes the fundamental properties of hadrons, their constituents and their interactions. The theoretical description of the underlying processes has proven to be much more complicated than other *gauge theories* like the well-understood QED. The main difference between both theories is that QED allows computations in the form a perturbation series because the coupling constant $\alpha_{\mathrm{QED}} \approx 1/137$ is small enough to allow very precise predictions. In the so-called *soft* regime of QCD, which corresponds to low energy phenomena, the coupling constant α_{s} is too big to allow this computational technique. Approximations are possible in the framework of *lattice-QCD* which aims at solving the theory on a discrete grid of spacetime points, and other problem specific model theories. However, first level theoretical explanations - built up only from the axioms of QCD itself - for the formation of hadrons and the phenomenon of *quark confinement* are still obstructed by the mathematical complications of the theory.

PANDA will provide valuable experimental input for this exciting branch of physics by researching four pillars of the antiproton program at FAIR:

1. **Hadron structure:** A fundamental description of nucleons has been developed in the framework of *Generalized Parton Distribution functions* (GPDs). Measurements at PANDA (e.g. via the DRELL-YAN Process) will deepen the insight and allow to compare predictions derived via these models with real data. The *nucleon form factors* describe the distribution of electric charges inside the building blocks of nuclear matter, namely the protons and neutrons. They are therefore thoroughly connected to the structure of nucleons which makes them an interesting access point for the study of fundamental properties of QCD. PANDA will give an additional handle on understanding these distributions and expand the knowledge about the nature of hadrons.

2. **Nuclear physics and hadrons in nuclear media:** While there is little doubt that QCD plays an important role in the description of nuclear forces, the challenge of describing strong interactions between color-neutral composites falls into the realm of nuclear physics. With a dedicated nuclear setup, PANDA will also allow to perform experiments that shine light onto these riddles of nature. In addition, a hypernuclear research program is foreseen to study the properties of nuclei that hold strange or heavy quarks in their constituents.

3. **Hadron spectroscopy:** Unlike e^+e^- machines, PANDA can directly deliver many exotic and non-exotic quantum numbers through $p\,\overline{p}$ reactions. Not only *production* reactions are possible, where the state of interest is a byproduct among other final state particles; it will be also possible to do direct *formation* processes of hadronic resonances. The latter can be precisely studied by beam energy scans, exploiting the excellent momentum resolution of the HESR. The luminosity that can be achieved at PANDA will allow these investigations to be done on short timescales due to fast collection of the necessary statistics. The advantage over high-energy hadron production - like the $p\,p$ collisions at several TeV at CERN - is the absence of the huge combinatorial background that would have to be deconvoluted from the physics events of interest - a complication that would add many challenges to the discovery of new states. Additionally, the measurements of the widths of newly found, or already known states is not limited by the PANDA detector resolution in formation processes, but only limited by the (excellent) momentum resolution of the accelerator. A summary of resonances that will be investigated by PANDA can
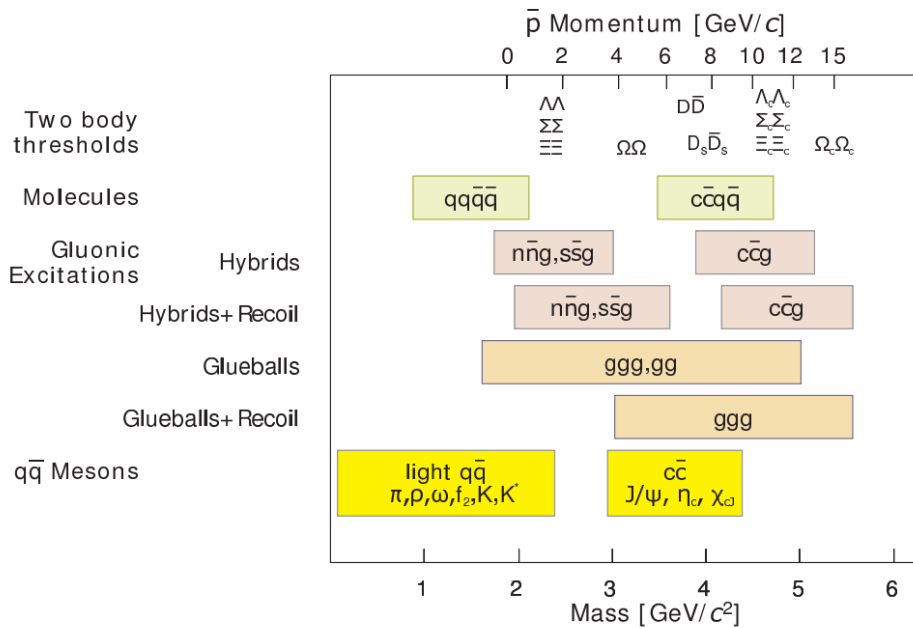
Figure 2.13: [9] Hadron spectroscopy at PANDA: The figure shows some interesting areas of study that will be accessed by the PANDA physics program. Classical hadrons like mesons and baryons can be studied and a search for exotic states can be conducted. Exotic states have gluons that contribute to the quantum numbers of the state or consist of quark combinations that have not been observed so far.

be seen in figure 2.13. In addition to exotic states, glueballs and hybrids, the *charmonium* sector and the *open charm* sector are of special interest for understanding

the role of the Cherenkov detectors at PANDA. Many of these resonances can be identified by their decay products which prominently include kaons. Identification of the kaons, i.e. separating them from pions, will allow to systematically search for interesting physics channels with strangeness in the final state.

2.4.1 Simulated kaon distributions

The aforementioned importance of Cherenkov detectors in the spectroscopy of charmonium or charmed mesons will be substantiated by the results of a Monte-Carlo study that has been conducted to examine the phase space of kaons produced by reactions which are expected at PANDA. The study was also done to cross-check previously published results in [21] and [25]. The PANDA-Root framework and the EvtGen [26] package were used for the simulations.

Some important benchmark channels have been listed in [25] that are summarized in table 2.1. These channels will be searched for kaons with high momenta that have to be identified by the Cherenkov detectors of the target spectrometer.

| $D^0 \overline{D}^0$	$D^0 \to K^- \pi^+$	$\overline{D}^0 \to K^+ \pi^-$
$D^0 \overline{D}^0 \gamma$		
$D^+ D^-$	$D^+ \to K^- \pi^+ \pi^+$	$D^- \to K^+ \pi^- \pi^-$
$D^+ D^- \gamma$		
$D_s^+ D_s^-$	$D_s^+ \to \Phi \pi^+ (50\%)$	$D_s^- \to \Phi \pi^- (50\%)$
$D_s^+ D_s^- \gamma$	$D_s^+ \to \overline{K}^{*0} K^+ (50\%)$	$D_s^- \to K^{*0} K^- (50\%)$
$D^{*0} \overline{D}^{*0}$	$D^{*0} \to D^0 \pi^0$	$\overline{D}^{*0} \to \overline{D}^0 \pi^0$
$D^{*0} \overline{D}^{*0} \gamma$		
$D^{*+} \overline{D}^{*-} \gamma$	$D^{*+} \to D^0 \pi^+ (67\%)$	$D^{*-} \to \overline{D}^0 \pi^- (67\%)$
	$D^{*+} \to D^+ \pi^0 (33\%)$	$D^{*-} \to D^- \pi^0 (33\%)$
$\Phi \Phi$	$\Phi \to K^+ K^-$	

Table 2.1: [25] Decay modes for the kaon phase space study.

2.4.1.1 Kaons from $D\overline{D}$ reactions

The kaon phase space distribution was simulated at an antiproton momentum of $6.57\,\mathrm{GeV/c}$ for the reaction

$$p\,\overline{p} \to D^{\pm}\,D^{\mp} \text{ and } D^{\pm} \to K^{\mp} + 2\pi^{\pm}. \qquad (2.4.11)$$

All other production and decay channels have been suppressed (similar to [25]). In a second step, all possible decay channels of the EvtGen package that were provided with the contained decay library have been allowed for the decay of the $D^{\pm}\,D^{\mp}$ system (similar to [21]). However, the initial production reaction was still fixed to $p\,\overline{p} \to D^{\pm}\,D^{\mp}$ only. 10,000 $p\,\overline{p}$ pairs have been generated for both scenarios. The results for this study can be seen in figure 2.14. The figure also illustrates the regions of acceptance of both the barrel DIRC and the EDD. Furthermore, the minimal momentum of $1\,\mathrm{GeV/c}$ for kaons has been highlighted in the histogram because pions and kaons above this momentum can only be securely separated by the Cherenkov detectors at PANDA. Visual agreement with both previous studies was achieved. Figure 2.14 shows how important both Cherenkov
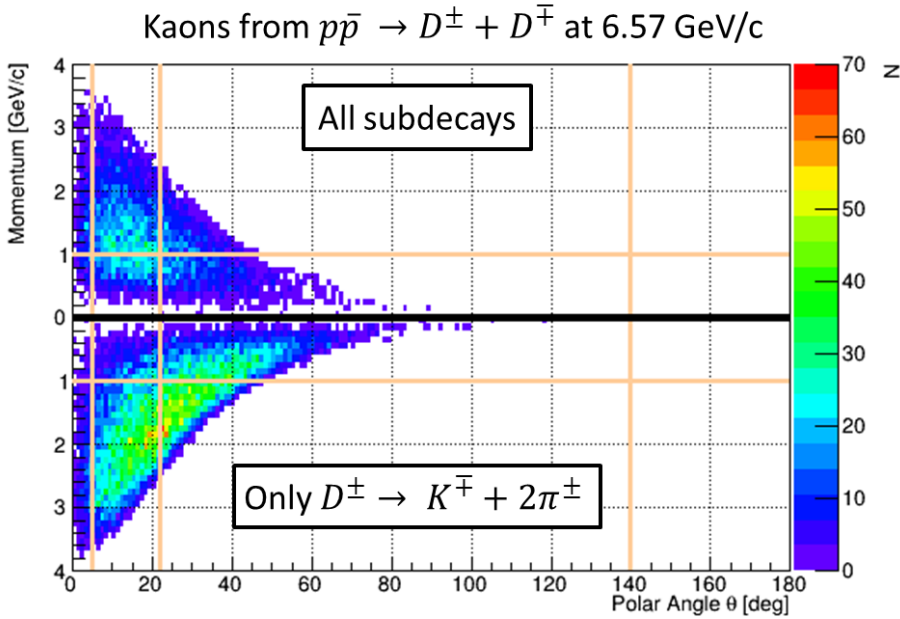
Figure 2.14: Phase space of kaons from $D\overline{D}$ reactions: The upper portion of the figure shows the kaon phase space distribution for all decay channels of the $D\overline{D}$ system. The lower portion shows the contribution of the $K + 2\pi$ system. The orange lines highlight the angular acceptance of the barrel DIRC and the EDD and the minimum momentum of $1\,\mathrm{GeV/c}$.

detectors are for the identification of charm physics. Many kaons with polar angles above $22°$ will be created that have momenta well above $1\,\mathrm{GeV/c}$ that can only be reliably

identified by the barrel DIRC. Due to the fact that PANDA is a fixed target experiment, many kaons will be boosted in forward direction and fall into the detection region of the EDD.

2.4.1.2 Kaon production at high beam momentum

In a next step an antiproton momentum of $15\,\mathrm{GeV/c}$ was set (the maximum that the HESR will be able to deliver) and the reactions from table 2.1 were enforced in each event (similar to [25]). An equal weight of all primary reactions was chosen, i.e. all $p\,\bar{p}$ reactions of the first column of table 2.1 occur with the same probability. Alternatively, only the first column of table 2.1 was enforced, but all subdecays from the EvtGen package were allowed for the subsequent decays. (similar to [21]). The results for both cases are shown in figure 2.15. Figure 2.15 shows that the strong LORENTZ boost of the CMS system at
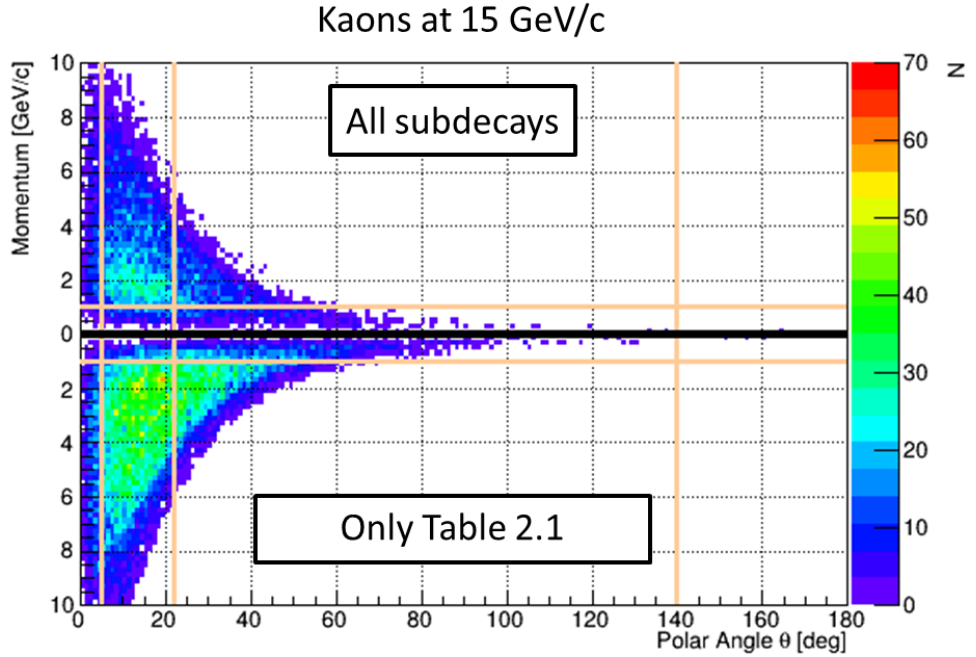
Figure 2.15: Kaon phase space at high beam momentum: The upper portion shows kaons that originate from the set of primary reactions that is shown in column 1 of the table 2.1 if all subdecays are allowed subsequently. The lower plot is generated with the same primary reactions which are then restricted to the subdecays shown in the remaining two columns of table 2.1.

high beam momenta does not stop many kaons from traveling at high polar angles, which is why both barrel and endcap part of the Cherenkov detectors are essential to achieve a full coverage and allow integral event analysis.

2.4.1.3 Kaons at different beam momenta

In a third scenario the decay of the $p\,\overline{p}$ system was restricted to the first column of table 2.1 again, but all subsequent decays from the EVTGEN package were allowed. The beam momentum was then scanned from $6.57\,\text{GeV/c}$ up to $15\,\text{GeV/c}$ and the amount of charged kaons in both acceptance regions (barrel and disc) were counted. The results can be seen in figure 2.16.
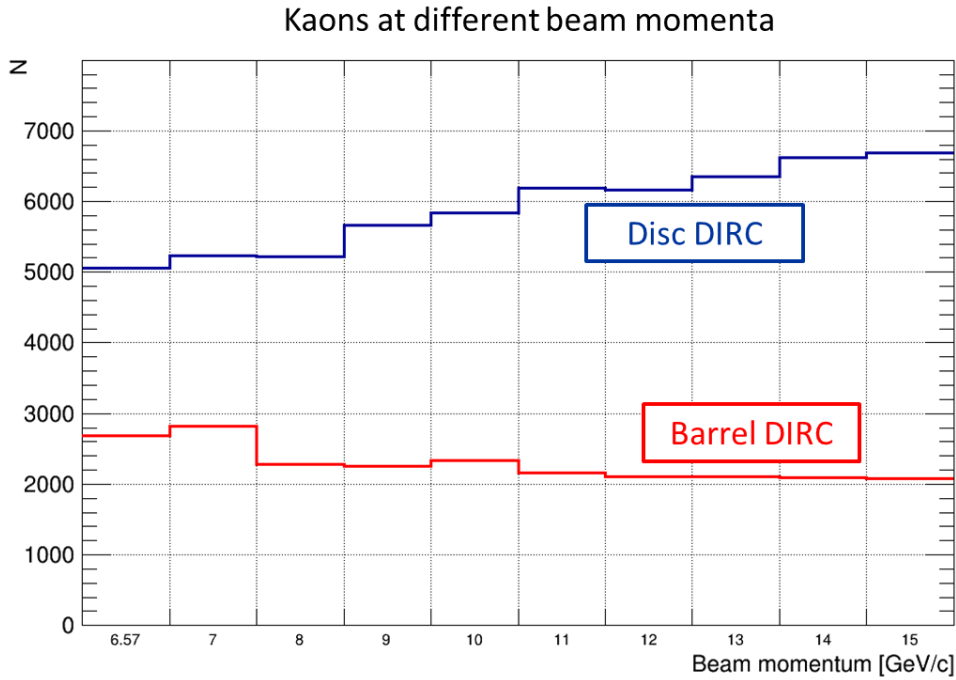
Figure 2.16: Kaon count in both Cherenkov detectors at different beam momenta: The figure shows how many kaons will fall into the acceptance regions of the barrel and the disc DIRC at different beam momenta. All primary reactions (equal weight) from table 2.1 and all subdecays from the EVTGEN decay library were allowed.

Figure 2.16 shows that the number of kaons that have to be identified by both Cherenkov detectors does not strongly depend on the beam momentum. The reason is that the threshold energies of the charm sector require relatively high beam momenta already. This means that a strong LORENTZ boost of the CMS system in forward direction is already present from the start.

3 Photosensors

3.1 Introduction

In the infancy of high energy physics experiments, photon detection was accomplished by naked eye. One of the most important physicists of all times and Nobel prize winner, Ernest Rutherford, conducted his famous experiment by observing little flashes of light through an optical microscope. This allowed him to study α particles scattering off a gold foil and ultimately refute the contemporary atomic model. In modern detector concepts like the PANDA EDD all information has to be handled electronically. This statement seems trivial at first sight, but it is the starting point for an abstract model of a photosensor, because it raises the question how properties of the light that we want to study can be translated into electronically contained information. The classification of possibly suitable sensors is guided by exactly this question. In the aforementioned abstract picture, a photosensor can be broken down into several functional units. In combination these units allow to form devices suitable for different tasks involving the detection of light. The most significant units as far as categorization is concerned are

1. conversion of photons
2. amplification mechanism
3. output signal provision.

Usually photosensors are categorized by their technique of photon conversion first. Subsequently, the remaining tasks guide the classification process. Of course this does not imply that the sensors of the same class perform comparably or are engineered in the same way. Following this logic, the probably most commonly used photon detectors can be grouped into the class of so-called *solid state detectors*. They employ modern semiconductor technology to detect a photocurrent which is generated by incident electromagnetic radiation in the depletion zone of two differently doped regions. Hence, their detection mechanism exploits the *inner photoeffect*. This class of sensors holds some interesting options for

the EDD which will be presented, together with a little introduction and overview, in section 3.2. The class of so-called *vacuum based photosensors* will be presented in section 3.3. These sensors use the *outer photoeffect* to convert photons into photoelectrons which are subsequently registered. Before a discussion of details of these most promising candidates, it is also instructive to coarsely filter out some of the remaining options. A complete overview of modern technologies for the detection of electromagnetic radiation is of course well beyond the humble scope of this work. However, it is equally unnecessary because many of the widely used detectors are unable to fulfill the requirements of the EDD. These requirements are coupled to the current detector design which has been explained in section 2.3.4. Naturally, different designs also impose different characteristic challenges. The key requirements for the EDD design, as far as the photosensors are concerned, are shown below.

R.1 Single photon sensitivity for photons between 300 and 600 nm.

R.2 Immunity to magnetic fields of the order of 1 Tesla, even with varying angles of incidence.

R.3 Time of arrival measurement with at least 1 ns precision.

R.4 Position of impact measurement with at least 150 μm RMS.

R.5 Very compact form factor.

R.6 Rate capabilities of up to the order 1 MHz per cm^2.

R.7 Radiation hardness of circa 100 Gy integrated lifetime dose.

R.8 Lowest possible material budget to minimize the influence on consecutive measurements (e.g. EMC) at PANDA.

R.9 Sufficient lifetime of several years of PANDA run time, corresponding to about 5-7 C/cm^2.

Apart from the two predominant classes of solid state and vacuum based sensors, there are some other types which can be ruled out of the competition with comparably little thought.

Gaseous detectors are widely used to detect ionizing radiation like γ rays originating from radioactive nuclei. However, their conversion process relies on the ionization of gas molecules caused by the incoming radiation. Unfortunately the ionization cross section for commonly used counting gasses is very small in the spectral range in which the EDD has to operate.

The expression *gaseous detector* could be extended to devices that employ gas volumes for amplification by triggering a discharge avalanche independent of the conversion process. As an example, so-called gaseous photomultiplier tubes (GPMTs) have been developed

which use micropattern gas detectors (MPGD) for the amplification of single photoelectrons [27]. These devices show both advantages and disadvantages compared to vacuum based PMTs. They are more immune to magnetic fields. GPMTs can be used in magnetic fields above 1 T [28]. Additionally they are less sensitive to the alignment of the magnetic field and the axis of the sensor which is caused by the permanent scattering of the photoelectron. Moreover, large area coverage can be achieved more easily. On the downside, the detection efficiencies of GPMTs are significantly reduced due to photoelectron backscattering in the gas phase. These scattering processes also worsen the timing resolution due to the stochastic nature of the electron path trough the drift stage. Due to the natural fact that more positively charged ions are present inside the tube, additional bombardment of the photocathode with ions leads to accelerated aging effects and degradation of the quantum efficiency. A reduction of this bombardment can be achieved by implementing additional protective mechanisms. However, in many cases, the only way to avoid the fast aging is to operate the tube at lower gains, which would be problematic in the case of the EDD, as typical GPMT gains are usually below 10^6 anyway. Chemical compatibility of photocathodes and materials for the production of the MPGDs is also an issue as, for example, the outgassing of many commonly used GEM foils tends to poison the photocathode. Due to these complications and the relatively young technology, there is no GPMT at hand that could compete with state of the art vacuum based PMTs as described in section 3.3.

Cryogenic photon detectors convert photons through physical processes that only take place at very low temperatures. One interesting example is the so-called superconducting nanowire single-photon detector (SNSPD) [29] (figure 3.1). This device consists of nanowires which are connected to an external quenching circuit. The detector is operated well below the critical temperature at which the nanowire becomes superconducting. Furthermore, a constant offset current is driven through the wire (figure 3.1 a). The resulting current density is slightly below the critical current density of the nanowire. Upon the impact of a single photon, a very small region of the nanowire becomes normal conducting and forms a resistive hot spot. This hot spot is still much smaller than the width of the nanowire but forms an effective barrier for the electric current. Consequently, the current has to flow around the hotspot through the remaining cross section of the wire which is still superconducting (figure 3.1 b). However, the bias current was chosen to generate current densities just below the critical density with the entire cross section being superconducting. As a result, the critical current density is exceeded in these regions. This mechanism, in combination with Joule heating from the resistive region, disturbs the superconducting

state in the remaining volume of the wire. The resulting finite resistance of the entire nanowire leads to a voltage drop which can be picked up electronically (figure 3.1 c). The quenching of the offset current allows the wire to re-establish its superconducting state, making the device ready for the next detection cycle (figure 3.1 d).
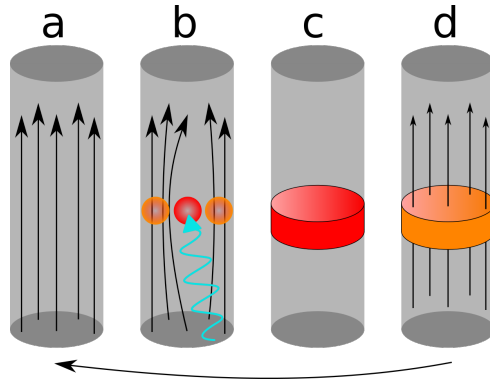
Figure 3.1: Sketch of the mode of operation of a superconducting nanowire single-photon detector (SNSPD). The steps are explained in the text. Graphic inspired by [29].

SNSPDs can have very good time resolutions below 100 ps. Their detection efficiency can outperform most of the other photodetectors, especially in the infrared region [30]. However, the obvious disadvantage of required cooling (down to some Kelvin) is a definitive show stopper for the EDD, as there is no space for bulky cooling equipment in the foreseen installation space. *Chemical sensors*, like photo plates, exploit the light sensitivity of certain chemical compounds. Incident electromagnetic radiation triggers a chemical reaction. The creation of a sufficient amount of products of this reaction can be used as proof for the presence of light. However, none of these sensors are suitable for the detection of single photons, nor do they provide electronic output or sufficient rate capabilities. They can be dismissed for these and numerous other reasons. Table 3.1 summarizes the categorization that has been presented in the introduction of this chapter.

3.2 Solid state detectors

Solid state detectors use semiconductors for the conversion and amplification of light. They fall into two branches, namely passive and active devices. Passive devices, also known as *photoresistors*, are simply layers of semiconducting (possibly doped[1]) material.

---

[1]Doping is the process of introducing impurities into the crystalline lattice of a semiconductor. Depending on the choice of the doping agent, the material can be transformed into an n-type or p-type. N-types feature donor atoms with additional valence electrons compared to the replaced lattice atom.

Category	Conversion technique	Amplification technique	Comments
Solid state detectors	Intrinsic photoeffect	Intrinsic carrier multiplication	See section 3.2
Vacuum based detectors	Extrinsic photoeffect	Secondary electron emission	See section 3.3
Gaseous detectors	Photoionization	Townsend avalanche	Not suitable for EDD
Cryogenic detectors	Disruption of Cooper pairs (and others)	Disturbance of superconductivity (and others)	Not suitable for EDD
Chemical detectors	Initiation of chemical reaction	None	Not suitable for EDD

Table 3.1: Overview of sensor classes and properties.

Active detectors, also named *photodiodes* feature p-n junctions.

Photoresistors exploit the fact that charge carriers in semiconductors need energetic excitation in order to be able to contribute to the conductivity of the material. This effect can be explained by the *electronic band structure model* of semiconductors (fig. 3.2).

According to this model electronic states in solids are confined to quasi-continuous energetic bands. Energies between the bands cannot be populated and are called forbidden regions. The bands are populated with electrons according to the Fermi-Dirac distribution. At zero temperature all states below a certain energy called *Fermi level* (E_F) are populated. However, no state above the Fermi level is populated. In isolators and semiconductors the Fermi level lies between two special bands called *valence band* and *conduction band.* Here, the valence band is the energetically highest band which is still fully populated at absolute zero temperature, while the conduction band is the energetically lowest band which is not populated (figure 3.2). Consequently, electrons in such a system cannot be continuously accelerated by arbitrarily little energies. The only way to accelerate the electrons (e.g. by an externally applied voltage) is to provide enough energy to lift them into the conduction band first. Once lifted, electrons in the conduction band

---

They increase the electron carrier concentration. P-types have acceptor atoms with less valence electrons than the replaced atom. They provide additional hole carrier concentration.

45
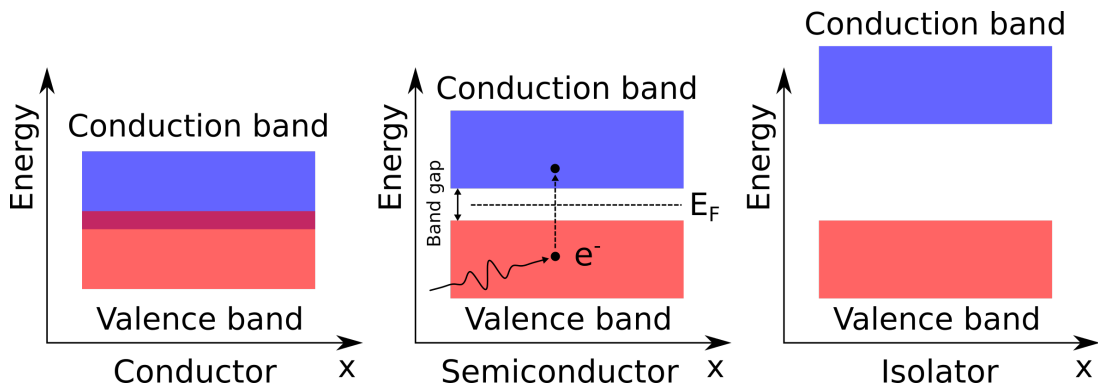
Figure 3.2: Band structure of a conductor, a semiconductor and an isolator. In the case of the conductor electrons from the valence band can be excited by arbitrarily small energies because the valence band and the conduction band overlap. For the semiconductor, energies above the width of the band gap are necessary. These excitation energies can be provided thermally or by absorption of incident radiation. Isolators have very big excitation energies which can normally not be provided by visible photons.

(and the corresponding holes in the valence band) can contribute to the conductivity of the solid. The minimal amount of energy which is necessary for the excitation of electrons is just the width of the *band gap*, the forbidden region between valence band and conduction band. The semiconductor can also be doped to increase the spectral sensitivity. Doping will create additional energy levels between the two bands and effectively lower the transition barrier.

At any temperature above zero, some charge carriers will always be thermally excited. If a voltage is applied, small currents will result. If electromagnetic radiation with sufficient quantum energy impinges on the solid, its energy can be converted into excitation upon absorption of the photon. Higher intensities lead to higher excitation rates and higher conductivity of the semiconductor (equivalent to lower resistance). In this sense, photoresistors are semiconductors with band gaps which are appropriately chosen to be overcome by the energy of the photons that have to be detected. Their response to an increase in intensity will be a decrease in resistance. Unfortunately for the EDD, photoresistors do not provide any intrinsic amplification process and are not suitable for the detection of single photons. However, the next section will present a way of fixing this problem.

3.2.1 (Avalanche) Photodiode

In contrast to the aforementioned photoresistors, *active* solid state photodetectors include a so-called pn-junction. A photodiode is the simplest example of such a device. It consists of two doped semiconductors (one being n-type the other being p-type) which are con-

tacted electronically and connected to each other. Additionally a *reverse bias* is applied across the entire diode. This means that an external voltage source is connected like in figure 3.3. In order to understand the fundamental mode of operation of these devices, one can make some simplifying assumptions, also known as the *depletion approximation*. In this simplified picture, a diffusion current of majority carriers (electrons in n-type and holes in p-type) will create a so-called depletion region between the two differently doped solids, resulting in a charge distribution described by a step function (figure 3.3). This depletion region is further extended by the reverse bias. Using Poisson's equation

$$\rho(x) = \epsilon \frac{\mathrm{d}E(x)}{\mathrm{d}x} \tag{3.2.1}$$

it is straightforward to derive the electric field $E(x)$. Then the potential U can be obtained by evaluating

$$U(x) = -\int\limits_{x_0}^{x} E(y)\mathrm{d}y. \tag{3.2.2}$$

A deeper mathematical treatment can be found for example in [33]. One finds the Shockley equation for the current density:

$$j = \underbrace{\left(\frac{eD_e}{L_e}n_0 + \frac{eD_h}{L_h}p_0\right)}_{j_r} \times (\exp(eU/k_bT) - 1) \tag{3.2.3}$$

with $j \equiv$ current density, $e \equiv$ elementary charge, $D_e, D_h \equiv$ diffusion coefficients for electrons/holes, $n_0, p_0 \equiv$ concentration of electrons/holes on the p/n side, $L_e, L_h \equiv$ diffusion length of electrons/holes, $U \equiv$ applied voltage, $k_b \equiv$ Boltzmann constant , $T \equiv$ absolute temperature.

Equation 3.2.3 shows that the reverse current j_r is present even if the external voltage is large (and negative) because the exponential function goes to zero. In case of a photodiode j_r is related to the dark current at constant voltage and temperature. It only depends on material parameters. This point will be important again later. The reverse current is only caused by *minority carriers* (i.e. electrons in the p-type and holes in the n-type). This is the reason why it is small and often times negligible compared to currents that result from a forward bias (reversed polarity of the external voltage).

The described setup can be used as a photodetector, because incident radiation can create electron hole pairs inside the depletion region of the reversely biased junction. These charges will immediately be swept away by the electric field, resulting in a net current as

sketched in figure (3.3). After a calibration of the device, a measurement of the resulting *photocurrent* allows a measurement of the intensity of the incoming light. Photodiodes
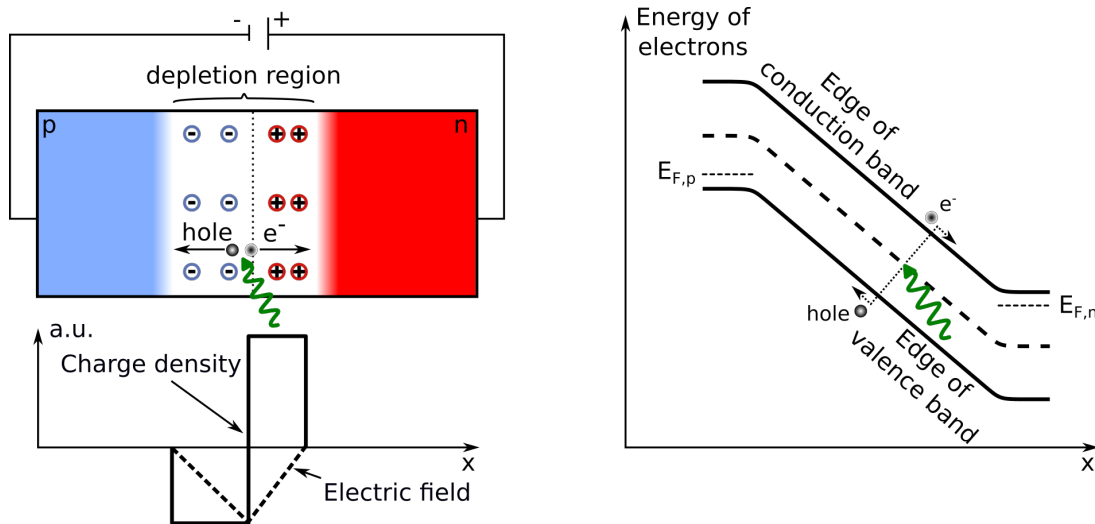
Figure 3.3: Left: Schematic of a pn-junction at reverse bias. The depletion zone between the p-doped region on the left and the n-doped region on the right is extended by the external voltage. The ionized donors and acceptors create space charges which in turn generate an electric field. Photons of sufficient energy can create electron hole pairs. Both drift in different directions, but their charges are also opposite. Consequently, there is a finite net current that results from the charge separation. **Right:** The band diagram of the pn-junction at reverse bias. Figure adapted from [32].

with a simple pn-junction have a drawback. They only have a small space charge region. Electron hole pairs that are generated outside of it are not immediately separated as no electric field is present outside the depletion region. These charge carriers can still diffuse to the junction but the reaction time is much longer and the probability of recombination is enhanced which worsens the detection efficiency of the device. To solve this problem, an additional layer of undoped (or only slightly doped) semiconductor is placed between the n-type and the p-type terminals of the pn-junction. In this case, the depletion region can broaden through this new central layer of the buildup. A much bigger fraction of electron hole pairs is now generated in this region where a fast and efficient separation is possible. These photodiodes are called *pin*[2] or *psn*[3] photodiodes. They are probably among the most common devices used for the detection of light today, but they are not yet sensitive to single photons. However, the latter can be achieved by introducing an additional junction into the buildup. This new junction is designed to provide very high electric field strength and accelerate injected charge carriers even more. Once the accelerated carriers exceed the band gap energy, new electron hole pairs can be created by collisions

---

[2]the letter 'i' stands for *intrinsic*
[3]the letter 's' stands for *soft* for the case of a slightly doped additional layer

with the bulk atoms. Because this process iterates several times an *avalanche* of charge carriers will result. These so-called *Avalanche Photodiodes* (APDs) are the simplest solid state sensors with an internal multiplication stage for the converted charge carriers. The increase in sensitivity comes at the price of additional noise because thermally separated charges are multiplied as well. In order to detect a single photon the *gain*[4] of the device has to reach a level of about 10^6. Typical APDs cannot reach these realms unless the bias voltage is driven beyond the *breakdown voltage*. The corresponding devices are called *Geiger APDs* or *Single Photon Avalanche Diode* (SPAD). Normally APDs work in *proportional mode*: The resulting charge output is proportional to the amount of electron hole pairs that was initially created. In G-APDs one single electron hole pair (created by a single photon for example) can be sufficient to initiate a self-sustaining avalanche that saturates the entire device. Special measures have to be taken to protect the device by interrupting the avalanche before the high currents destroy the device. These so-called *quenching* techniques range from simple quenching resistors to active quenching circuits with more sophisticated electronic components. The latter have the advantage of reducing the *dead time* or *recovery time* of the diode. This is the amount of time needed to quench the avalanche and restore the diode's state when it is ready to detect the next photon. G-APDs are binary devices. The output is no longer proportional to the amount of incident light. In a photon counting application it is important to not undersample by allowing multiple photons to hit the same cell within the dead time or the hit information will be lost. A common practice is to decrease the size of the cells and tile them to fill out the active area in a given application. If the cells are small enough the probability of more photons impinging on the same cell decreases with the size. With an appropriate density of cells (which can be very application specific) in a tiled geometry, the entire ensemble can give a proportional feedback by counting the number of activated pixels per time.

3.2.2 (Digital) SiPMs

Arrays of G-APD which provide the user with the analog current signals of the interconnected individual cells are called *Silicon Photomultipliers* (SiPMs). In the simplest designs, the passively-quenched diodes are simply connected in parallel what leads to an analog summing of the individual outputs (figure 3.4). Unfortunately this practice has several drawbacks. Firstly, no position information can be achieved by analyzing the output due to the summing process. Secondly, the excellent intrinsic timing properties

---

[4]multiplication factor of one charge
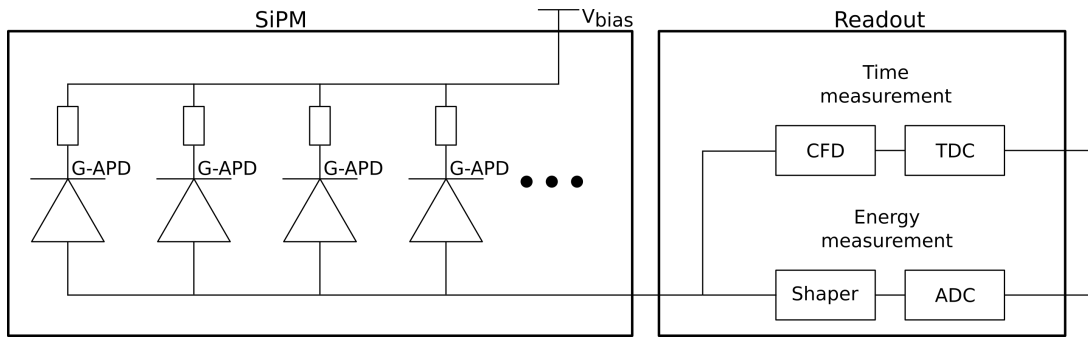
Figure 3.4: Schematic of a complete SiPM photon readout: The SiPM consists of multiple G-APDs connected in parallel. All cells are reversely biased with an external voltage source. Each detected photon generates an avalanche in one cell. The readout electronic sees the analog sum of all connected cells. As SiPMs only provide an analog output pulse, the external readout can consist of application specific devices. The most common practice is to measure the time of arrival and the pulse area. The latter gives information about the amount of photons that were detected by the entire ensemble.

are deteriorated. However, these setups are mainly intended to be used in scintillation applications (Calorimetry, PET, ...) where no spatial resolution is required in many applications. For the EDD the position resolution is very important which is why another level of sophistication is necessary.

Digital Silicon Photomultipliers (dSiPMs) have a fully integrated readout and active quenching circuit for each individual cell. The advantage is that the user doesn't have to detect and examine the analog output with external readout equipment. This is especially convenient in the case of many tens of thousands of pixels. Furthermore the aforementioned drawbacks of timing deterioation and loss of cell information can be overcome. Together with the fine segmentation of the tiled geometry an excellent position resolution can be achieved. dSiPMs are a very interesting choice for the EDD and have been extensively studied in the past. Their capability to detect single Cherenkov photons with a timing resolution of $140\,\text{ps}$ (σ) has been shown in [34]. However, some modification in the logic of the global readout scheme and the availability of individual timestamps for each single cell would have to be implemented in the existing devices in order to improve their suitability for single photon detection; again these devices were originally developed for scintillation applications. [21] shows a performance study of an EDD design which is based on dSiPMs. The design exploits the dSiPMs compactness and the generic immunity against magnetic fields.

Unfortunately, dSiPMs have also some disadvantages which are possibly inherent drawbacks of the solid state technology. The primary problems are connected to high dark

count rates (or *noisy pixels*)[5] (DCR) which get even worse after exposure to fluxes of hadrons or high energetic leptons like the ones expected in PANDA [35]. This effect arises from the creation of impurities and recombination/generation centers by displacement of bulk atoms of the G-APDs. Equation 3.2.3 showed that the reverse current is influenced by the charge carrier concentrations. If the energy levels of the newly introduced centers are in the forbidden region, the reverse current and the DCR can be enhanced because additional charge carriers can be excited from these states. Introducing shielding layers into the detector to prevent the harsh radiation from damaging the sensors would also negatively influence the measurements of the consecutive detectors and is therefore not possible.

In addition to the donor-like defects, the radiation damage can also create meta-stable states in the band structure. During an active avalanche, these states can be populated and decay after some short time. They trigger another avalanche which is again not caused by incident light. This effect is called *afterpulsing*.

Optical crosstalk happens when electron hole pairs recombine inside a G-APD. This process is very similar to fluorescence from an LED. This unwanted effect can also increase the DCR by introducing an artificial light source for the neighboring cells. However, many setups feature mechanical countermeasures to keep the optical crosstalk at bay.

It has been mentioned that a fine segmentation of the readout plane is necessary to prevent undersampling. The introduction of many cell boundaries is an unavoidable downside of this strategy. A reduction of the effective active area of the tiled geometry is the consequence.

These disadvantages, especially the problem of radiation hardness, have steered the EDD-R&D efforts away from semiconductor based photodetectors towards Microchannel-Plate Photomultiplier Tubes (MCP-PMTs). These sensors share many of the advantages but are immune to the radiation levels at PANDA. A systematic overview on MCP-PMTs will be given in the next section.

3.3 Vacuum based Photosensors

Cathode ray tubes and even vacuum based phototubes existed long before the first active semiconductor devices were invented. The first of these predecessors of the modern solid

---

[5]Dark counts are detector responses which are indistinguishable from the ones generated by incident photons, but happened in the absolute absence of light. The main source of dark counts is the generation of electron hole pairs by thermal excitation.

state detectors were *phototubes* which were invented in 1892/1893 by J. Elster and H. Geitel [36]. By that time, the physics behind the conversion process was still unknown and the wavelength dependency of the photoelectric effect could not be explained. A satisfactory explanation was found by Einstein in 1905. In the 1930s the first *photomultipliers* were built. In the late 1950s the first *microchannel plate* based devices were invented. The following sections will explain the working principles, properties, advantages and disadvantages of these devices, while always keeping the suitability for operation in PANDA as a criterion.

3.3.1 Phototubes and Photomultipliertubes
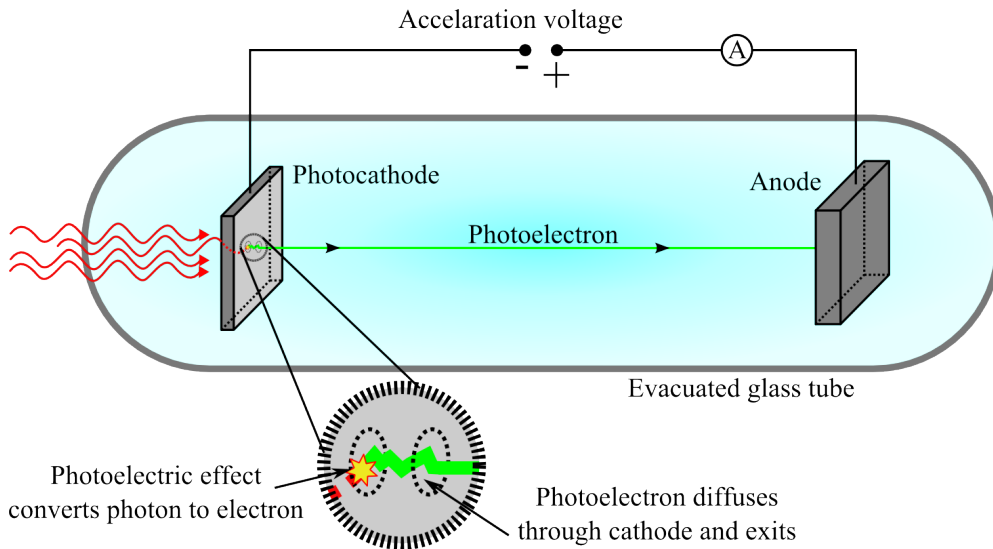
Figure 3.5: Working principle of a phototube: Photons impinge on the photocathode inside the evacuated glass tube. They are converted to photoelectrons via the photoelectric effect. The photoelectrons diffuse through the cathode and can leave the cathode on the other side. The electric field in the tube accelerates the electrons towards the anode. The resulting photocurrent can be measured and the light intensity can be derived. More on photocathodes will be said in section 3.4.6.

A phototube is the vacuum based counterpart of the simple pn-photodiode. Its basic mode of operation in sketched in figure 3.5. It consists of an evacuated glass tube with a photocathode and an anode which are connected to the outside via electrical feedthroughs. Photons can enter the glass tube and strike the photocathode. If the quantum energy of the light is sufficient (i.e. the wavelength is short enough) single electrons can absorb the energy of the photon and subsequently leave the cathode and enter the vacuum of the tube. These electrons are called *photoelectrons* because they were excited by a photon. Photocathodes can be categorized into two classes: There are *reflective type* and *trans-*

mission type cathodes. The latter is shown in figure 3.5. As the name suggests, the photoelectron leaves the cathode on the opposite site from where the photon impinged. Reflective types eject the photoelectron on the same side. Both have specific advantages, but the first devices were built with reflective types which can be realized by a simple sheet of metal. Modern approaches to the construction of durable and efficient photo-cathodes are much more sophisticated and their *lifetime* and *quantum efficiency* play an important role in the evaluation of the suitability of the corresponding devices. Hence, section 3.4.6 will give a deeper introduction to the topic.

For now let us consider the photoelectron which was just released into the vacuum of the glass tube. It will experience an electromagnetic force which is a result of the externally applied voltage between the cathode and the anode. At some point the electron will be caught by the anode and will contribute to the photocurrent which can be measured in series. The more photons strike the cathode, the more photoelectrons will be generated per unit time, resulting in a stronger photocurrent. This basic mechanism is the basis for all sensors presented in the following sections. The only difference between them is the technique for the *multiplication* of photoelectrons which corresponds to the amplification of the signal as far as our abstract model is concerned. Again this step is absolutely necessary to achieve single photon sensitivity.
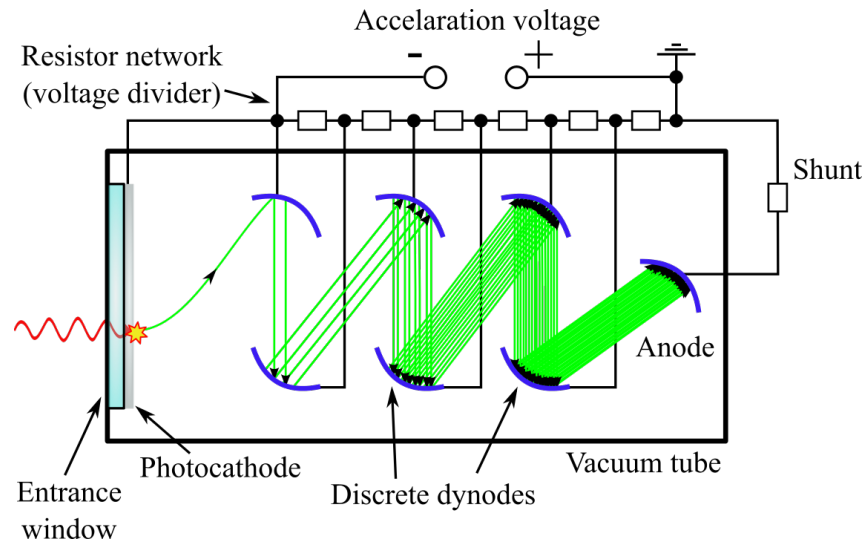
Figure 3.6: The PMT works like a photocell but has a discrete set of dynodes built in. Together they work as an electron multiplier. The primary photoelectron is multiplied in an avalanche-like process. After the amplification a measurable signal can be extracted from the anode even if only a single photon was present initially.

The *photomultiplier tube* (PMT), as shown in figure 3.6, has a discrete set of electrodes called *dynodes*. They can either consist of materials with a high *secondary electron yield*

(SEY) or they are made from a substrate which is covered with thin layers of such materials. The latter technique is often called *Atomic Layer Deposition* (ALD). Many materials, ZnO, BeO or PbO being prominent ones, can be used for this purpose and the optimization of these structures is highly challenging. [37] and the references therein present how strongly some of the candidate materials like MgO, Al_2O_3 or multilayered MgO/TiO_2 depend on numerous parameters like the chemical purity, the thickness of the outermost layer, the kinetic energy and the angle of incidence of the primary electron and many more. Table 3.2 presents a collection of materials published in [38]. The process of sec-

Material	η_{max}	W_{max} [eV]	Material	η_{max}	W_{max} [eV]
Ag	1,5	800	LiF	8,5	700
Al	1,0	30	Ag	1,5	800
Diamond	2,8	750	NaI	19	1300
Na	0,8	300	MgO-Crystal	20-25	1500
W	1,4	650	MgO-Layer	5-15	500-1500
KBr	14	1800	GaP + Cs	120	2500

Table 3.2: [38] Some common dynode materials and their maximum *secondary electron emission coefficient* η_{max} at the primary electron energy W_{max} at which the highest coefficient is reached.

ondary electron emission is very closely related to the (outer) photoelectric effect. The processes differ only by the primary particle species (photon and electron). Hence it is very unsurprising that certain materials, like the ones mentioned earlier, perform well in both cases. Different theoretical and numerical models have been developed to systematically describe and optimize performance parameters. However, the small variations in the manufacturing process which significantly alter the final result also impose many engineering challenges.

The timing resolutions of PMTs are mainly influenced by the electron multiplication phase and the photocathode. The stochastic nature of the amplification process leads to fluctuations in the total charge generated (pulse height distribution) and the transit time of the avalanche. Figure 3.7 shows some parameters of the output signal that directly influence the timing performance. The variations can be kept small if the geometric lengths of the electron paths are short. More sophisticated methods of electrostatic guidance of the electrons can also improve the timing. Typical time resolutions of modern PMTs can be in the order of a few hundreds of picoseconds. However, they can vary significantly with the design of the tube and the dynode geometry.
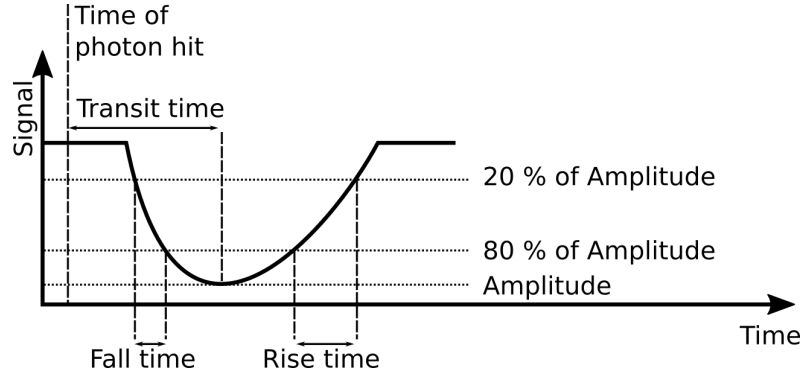
Figure 3.7: Time definitions of the output pulse. A short fall time improves the timing resolution of the device. The amplitude and the transit time vary from pulse to pulse due to the stochastic properties of the electron multiplication.

PMTs can be made position sensitive by implementing multiple, segmented multiplication stages and readout anodes behind one photocathode. These devices are called *Multianode PMTs* (MaPMTs). The EDD prototype of 2013 was equipped with 16 channel MaPMTs with 1 mm pitch. However, these sensors are very sensitive to external magnetic fields. The problem is that the electron trajectories inside the tube have to be optimized to provide the best performance during the electron multiplication, but like any charged particle in an electromagnetic field, the electrons will experience the LORENTZ force

$$\vec{F} = q \left(\vec{E} + \vec{v} \times \vec{B} \right). \tag{3.3.4}$$

q and m are the electric charge and the mass of the particle, $\vec{E}$ and $\vec{B}$ are the electric and magnetic fields. Solving the equation of motion for complicated fields $\vec{E}$ and $\vec{B}$ can only be done numerically and with state-of-the-art simulation software. However, a qualitative argument can be obtained from considering the case of *time-independent* and *homogeneous* fields. [39] gives a very comprehensible treatment of this scenario and shows that it can be solved analytically. One elegant solution is done via transforming into a frame where only a magnetic field is present while the electric field vanishes. After solving the equation of motion in this frame, the solution can be transformed back into the original frame. In conclusion, the motion of the charged particle can be broken down into three contributions:

1. A constant acceleration $q\vec{E}_{\parallel}/m$ with $\vec{E}_{\parallel}$ being the component of $\vec{E}$ which is parallel to $\vec{B}$.

2. A circular rotation in the plane which is perpendicular to $\vec{B}$. The frequency of this rotation is the cyclotron frequency $\omega_c = |q|B/m$ while the radius $r_c = v_\perp/\omega_c$

depends on initial conditions.

3. A drift velocity $\vec{v_D} = \left(\vec{E} \times \vec{B}\right)/B^2$, perpendicular to both $\vec{E}$ and $\vec{B}$. Note that it does neither depend on the charge nor on the initial conditions.

The actual motion of the particle is a superposition of all three components. If the z axis of the coordinate system is aligned with the magnetic field, the solution for the particle trajectory can be written as follows:

$$x(t) = -\frac{\vec{v_\perp}}{\omega_c} \cos\left(\omega_c t + \theta_0\right) + \frac{E_y}{B}t + X_0 \tag{3.3.5}$$

$$y(t) = \frac{\vec{v_\perp}}{\omega_c} \sin\left(\omega_c t + \theta_0\right) - \frac{E_x}{B}t + Y_0 \tag{3.3.6}$$

$$z(t) = \frac{qE_z}{2m}t^2 + \dot{z}(0)t + z_0 \tag{3.3.7}$$

$x(t)$ and $y(t)$ are written for a positively charged particle but can simply be made applicable for negative ones by substituting $\omega_c \to -\omega_c$. Figure 3.8 shows an example of such a trajectory. The effect of the additional magnetic field on the electron multiplication inside the PMT can be very drastic if high field strengths are present. Most electron multipliers with discrete dynodes simply fail because the trajectory of the photoelectron will no longer lead to the first dynode and no avalanche will be triggered. It can also happen that secondary electrons are misguided, leading to an interruption of the avalanche. One way of meeting this complication is a replacement of the discrete dynode structure with a so-called *fine mesh*. It consists of layers of tightly packed thin wires with high SEY. Like the classical dynodes, the various layers are held at different potential which generates accelerating electric fields between them. The advantage is that the electrons can now be deviated from their normal trajectory, but will simply impact another multiplication wire elsewhere. Even though there is no telling *where* exactly they will be multiplied, one can rely on the fact *that* they will be multiplied and measure the position of the charge cloud to calibrate for an image shift caused by the external B-field. Surely this technology has also its limits and strong B-fields which are not aligned with the tube axis will eventually lead to failure as well. However, fine mesh PMTs qualify as a suitable option for the EDD but two disadvantages still remain in comparison to MCP-PMTs. Firstly, fine mesh PMTs are only available in cylindrical shape. Hence, the packing density cannot be as good as with rectangular devices. Secondly, current designs feature a rather long tube axis compared to MCP-PMTs. This mechanical constraint complicates the implementation in the very tight installation region foreseen at PANDA.
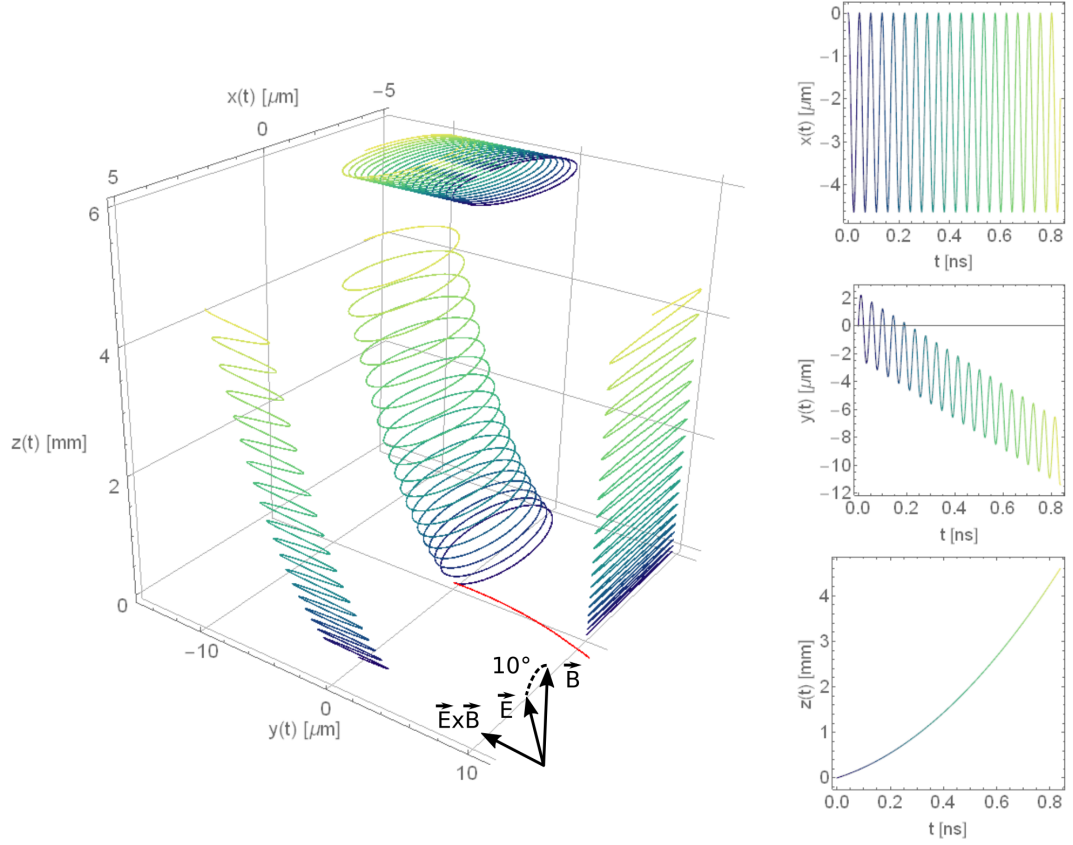
Figure 3.8: The left side shows the trajectory of a positron in a static and uniform electromagnetic field with projections in the coordinate planes. The magnetic field is aligned with the z axis and has a magnitude of $0.8\,\text{T}$. The electric field lies in the x-z plane and has an angle of $10°$ with respect to the magnetic field. The field strength is $50\,\text{V/mm}$. The particle starts in the origin and has a initial kinetic energy of $10\,\text{eV}$. Its initial momentum vector lies in the y-z plane and is aligned at $10°$ against $\vec{B}$ as well. For these parameters, the cyclotron frequency is $\omega_c \approx 140\,\text{GHz}$ and the cyclotron radius is $r_c \approx 2.3\,\mu\text{m}$. One can see how the motion can be understood as a superposition of a constant acceleration along the axis of the magnetic field (z direction), a constant drift velocity along $\vec{E} \times \vec{B}$ (negative y direction) and a rotation in a plane parallel to $\vec{B}$ (x-y plane), as described in the text. The right side shows how the individual components of the trajectory depend on time. The colors of the curves represent the time coordinate. Dark blue marks the starting time and light yellow the last time that has been evaluated.

In the absence of a magnetic field (while holding all other parameters constant), the particle would follow a parabolic trajectory which is shown in red. After the same time of flight it would be displaced by more than half a millimeter in x and more than a quarter of a millimeter in y. Due to the strong gyration of the electron around the vertical magnetic field lines, the motion in x and y is practically suppressed. In other words: Switching on a strong magnetic field will force the electrons to gyrate around the field lines. By doing so, they will give up their continuous motion in any direction perpendicular to the magnetic field (apart from the small drift velocity). This *collimating effect* has the biggest influence on the trajectory.

3.4 Microchannel Plate PMTs

PHILO. T. FARNSWORTH patented the first microchannel plate (MCP) as an electron multiplier in 1930 [40]. Since then photosensors with MCPs have become popular in different areas where detection of small quantities of light plays an important role. Night vision devices among other military applications as well as scientific research and industrial applications are examples. The mode of operation of an MCP based photodetector is shown in figure 3.9.
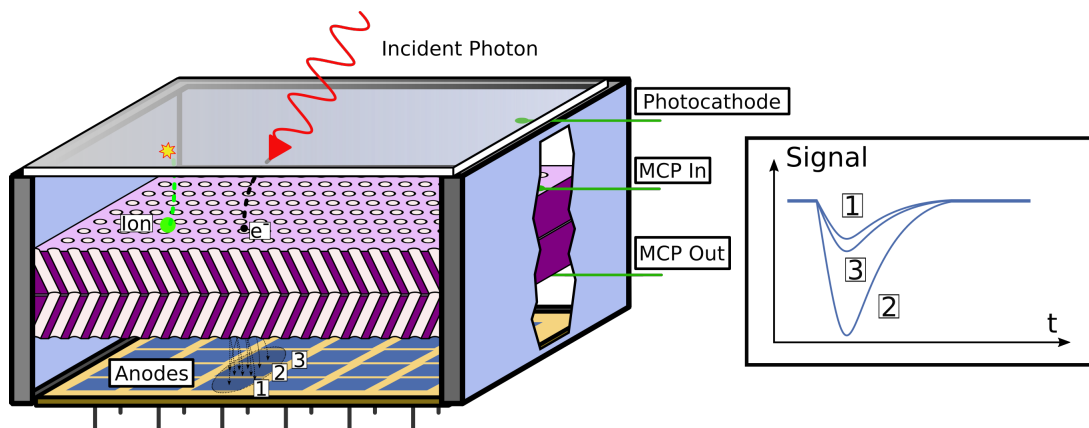
Figure 3.9: Mode of operation of an MCP-PMT.

Single quanta of electromagnetic radiation with a suitable wavelength are converted to photoelectrons when they strike the photocathode like in the case of PMTs. The photoelectrons are then multiplied by a set of microchannel plates (MCPs) which are included in the vacuum tube. The resulting electron avalanche can be read out with different techniques. The very common method of anodes with vacuum feedthroughs is shown in the picture. This solution is the first choice for the EDD. Like in the case of Ma-PMTs the anode can also be segmented to provide additional position resolution. Depending on the size of the anode segments and the geometry of the tube multiple anodes can be hit by the avalanche caused by one single photon as shown in the picture. In this case the amount of charge on each pad can be used to find the center of mass of the electron cloud which further improves the position resolution. Because the MCP is already a *continuous* electron multiplier it does not have to be modified to work with segmented anode geometries. Unfortunately the photocathode of MCP-PMTs can be very sensitive to the bombardment of ions which are produced by ionization of residual gas atoms or atoms originating from outgassing of components inside the vacuum tube. This effect is believed to limit the lifetime of the sensors as the quantum efficiency of the photocathode

degrades gradually. More on the lifetime aspect will be given in section 3.4.6.
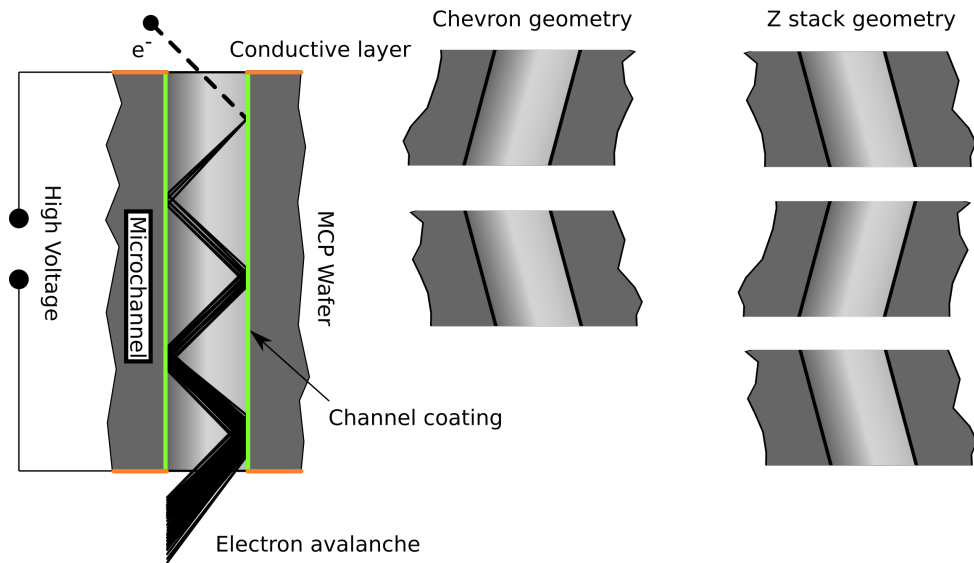
Figure 3.10: Electron amplification in the microchannels of an MCP-PMT. More explanations are given in the text.

MCPs can be built with the help of fiber drawing and etching techniques. A deeper introduction into production and fundamental properties of MCPs can be found for example in [41]. Basically, they are wafers with microscopic channels which are coated with high SEY materials on the inside (figure 3.10). The figure shows the amplification of a single primary electron when captured by an MCP pore. Each single channel can be seen as a continuous dynode structure. Most MCP-PMTs contain two MCPs which are connected in series. The Chevron geometry (3.10 in the middle) achieves higher gains than a single MCP. The channels of the two MCPs are tilted against each other to hinder ion backflow to the photocathode. Typical tilting angles vary around 10°. Some applications also feature three MCPs in a so-called Z stack geometry. These setups can reach multiplication factors of 10^7 and more (3.10 on the right). Typical channel diameters vary around 10 to 30 μm but can be considerably smaller nowadays. Electrons that enter into one of the pores will eventually collide with a channel wall and trigger an avalanche. Different readout options and improvements have been invented to increase the performance of MCP-PMTs. The following section will introduce and explain the most relevant ones for the scope of this work.

1. **Reduced input and output gaps** reduce lateral drift offsets of the photoelectron or the electron cloud after the amplification process. They also reduce the size of the charge footprint in the readout plane. Both can lead to increased spatial resolutions

and timing resolutions.

2. **Funnels** artificially increase the open-area-ratio (*OAR*, see section 3.4.1) and thereby increase the collection efficiency of the sensor.

3. **Fiber plate entrance windows** guide incoming light towards the photocathode by means of total internal reflection. This option is useful when the position of impact on the entrance window has to be measured irrespective of the photon angle.

4. **Channel tilting** hinders the backflow of ions to the photocathode and improves the lifetime of the sensor. This technique has become a standard and MCP-PMTs with straight channels are rare today.

5. **Protective foils** made e.g. from Al_2O_3 with a few nm thickness can be placed anywhere in the vacuum gaps or between the MCPs to catch ions and prevent them from striking the photocathode. Unfortunately the foils can also catch photoelectrons and disturb the amplification process.
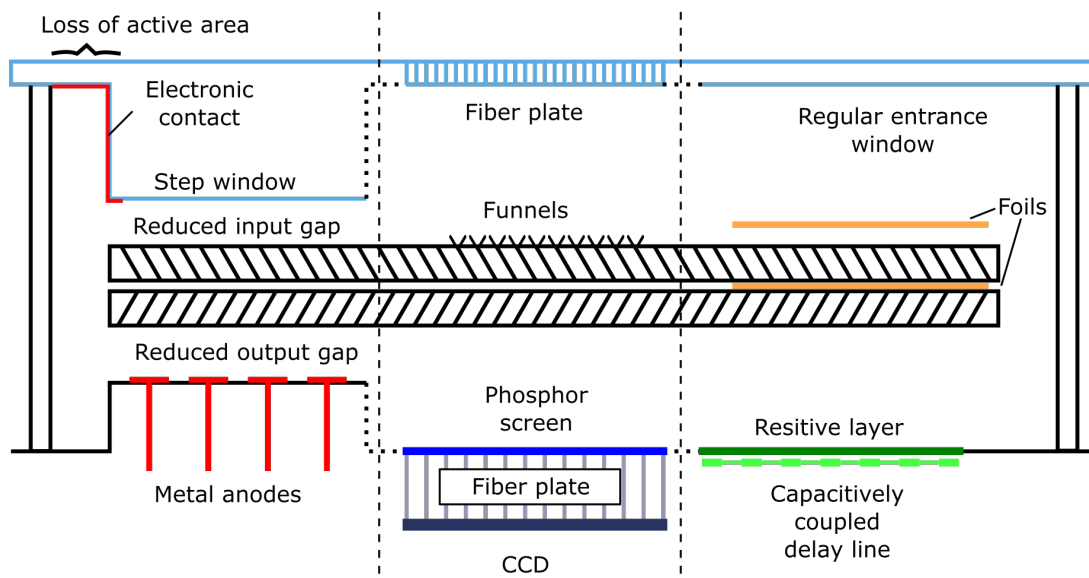
Figure 3.11: Different readout options and modifications of an MCP-PMT.

Figure 3.11 illustrates various modifications of MCP-PMTs as explained above. The figure shows how the input and output gaps of an MCP-PMT can be reduced by introducing a step window or bringing the readout plane in close proximity to the output of the last MCP. A drawback of the step window is a loss of active area because the perimeter of the photocathode on the inside of the entrance window has to be contacted electronically. The area where the contact is established is not sensitive to light [42]. An alternative to the metal anode readout technique uses a phosphor screen which produces visible light when struck by the electron avalanche. The light is created via luminescence and can

subsequently be registered with a CCD chip or similar technologies. A third possibility features a capacitive readout. This technique is explained in figure 3.12.
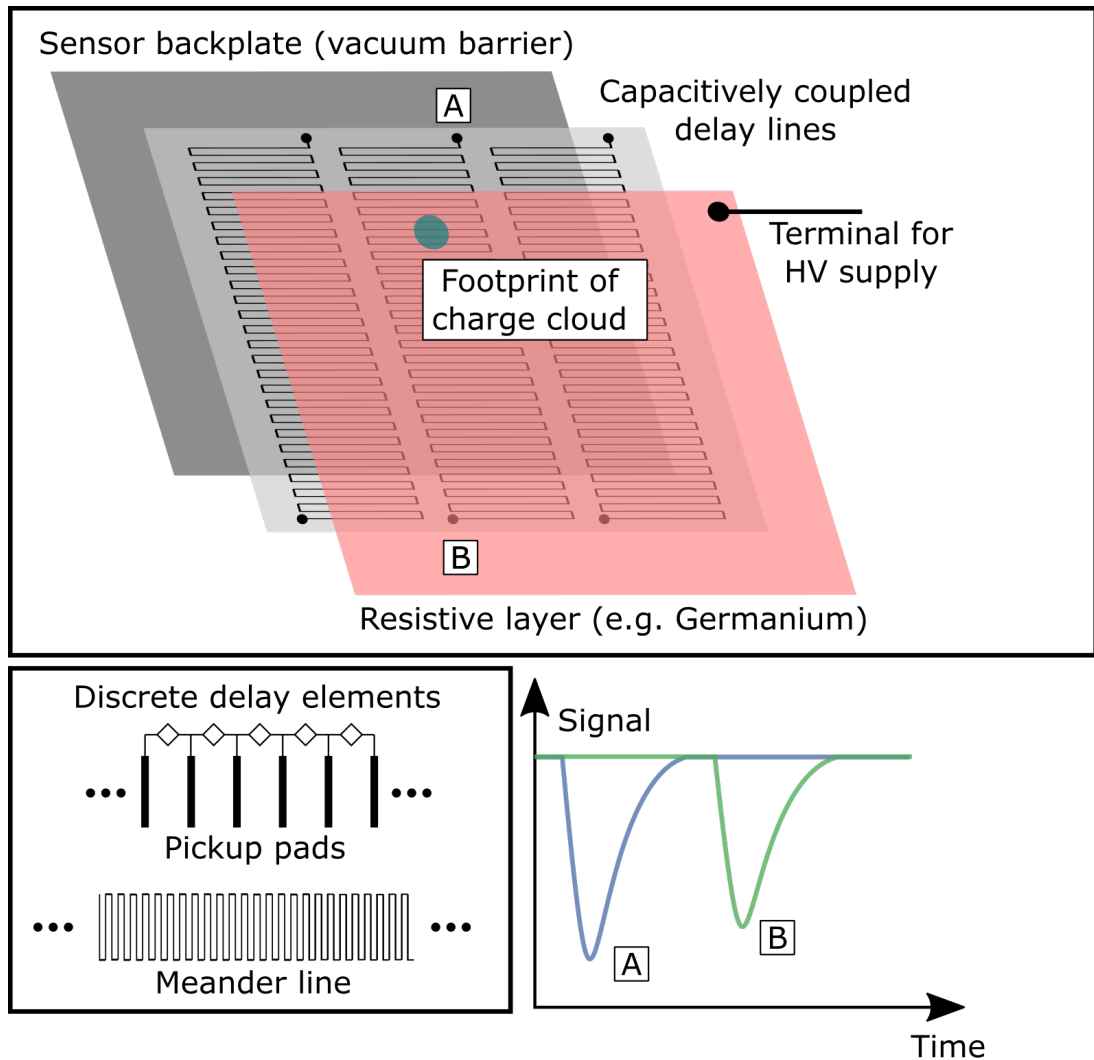
Figure 3.12: One possible buildup of a capacitively coupled delay line readout. More information is given in the text.

The first layer seen from the direction of the incoming electron avalanche is a resistive layer which is connected to the (lowest voltage terminal of the) voltage divider. The electrons induce a signal in the readout anode which is just underneath the resistive layer. It is also possible to place the readout anode behind the back plate outside of the vacuum what simplifies testing of different geometries. Once the signal is coupled into the anode, it splits up and travels into opposite directions along the delay line. When it arrives at both

61

ends of the delay line, the difference in the time of arrival can be used to infer the position of impact along the delay line. The MCP output can be measured simultaneously and gives an additional timestamp. This can help to resolve ambiguities when the photon rates are high. The delay line can also be composed of discrete delay elements which are connected to pickup pads. The pads are responsible for the capacitive coupling to the Germanium resistive layer. The position resolution of this technique depends on the temporal resolution of the readout and the total delay of each line. The longer the delay the better the position resolution. Unfortunately longer delays are also more vulnerable to pile-up what limits the rate capability.

3.4.1 Detection efficiency

The *detection efficiency* (*DE*) of an MCP-PMT is defined by the number of registered photons (N_R) divided by the number of photons that the sensor was illuminated with (N_I).

$$DE = \frac{N_R}{N_I} \qquad (3.4.8)$$

It can also be interpreted as the probability to detect an incident photon. Two processes are important to quantify *DE*: The conversion of the photon into a photoelectron and the amplification of the photoelectron. The conversion efficiency is usually called *quantum efficiency* (*QE*) and is mainly determined by the photocathode. The *QE* also depends on the

Figure 3.13: The unit cell of hexagonal packaging of MCP pores.

wavelength of the incoming photon. The probability that a given photoelectron is amplified and results in a measurable electron avalanche is usually called *collection efficiency* (*CE*). These quantities are connected via

$$DE = QE \times CE. \qquad (3.4.9)$$

The collection efficiency is mainly determined by the geometry of the MCPs, more specifically by the so-called *open area ratio* (*OAR*). The *OAR* is given by the ratio of the area of all pores to the total area of the MCP. The unit cell of the hexagonal closest package can be seen in figure 3.13. The *OAR* only depends on the pitch and the radius of the microchannels. The unit cell (regular hexagon) has an area of $\frac{\sqrt{27}}{2} p^2$ and contains

$1 + 6/3 = 3$ pores, each with an area of πr^2. This means that

$$OAR = 3\pi\, r^2 / \left(\frac{\sqrt{27}}{2}\, p^2 \right) = \frac{2\pi}{\sqrt{3}} \frac{r^2}{p^2} = \frac{\pi}{2\sqrt{3}} \frac{d^2}{p^2} \tag{3.4.10}$$

where $d = 2r$ is the diameter of the pores. Ideally, the pitch would be as close as possible to the diameter of the holes because this would result in the maximum *OAR* of $\frac{\pi}{2\sqrt{3}} \approx 90.1\%$. However, the mechanical stability of the MCP has to be sufficiently accounted for. A real example can be seen in figure 3.14 where a d^2/p^2-ratio of about 70% was achieved (resulting in an *OAR* of about 63%).

Electrons which do not immediately enter a pore have a very little probability of being amplified because the first multiplication step is the most important in the whole avalanche. However, these electrons can scatter off the MCP surface and enter another pore somewhere else. This effect contributes to the *cross talk*: a response of the sensor in a region where no signal is expected.

It is worth mentioning that this approximation is only valid in the absence of magnetic fields. The *CE* can be both increased and decreased depending on the strength and especially the orientation of the field lines with respect to the axis of the multiplication channels (not necessarily the tube axis as the channels are tilted in the Chevron geometry). More about this will be said in section 3.4.5.

3.4.2 Timing

MCP-PMTs have excellent timing properties. The electron trajectories are very short what results in fast transit times and low transit time spreads (TTS). Time resolutions of $27\,\mathrm{ps}$ (σ) are achievable [43]. Timing information can be derived from the MCP output signal and from the anode signal. In the first case a signal can be measured when the MCP provides secondary electrons for the avalanche during the multiplication process. This procedure is preferable if no position resolution but instead a very good timing information is needed. The MCP signal is usually coupled out via a capacitor to avoid high voltages on the signal line. One example is the MCP-TOF counter that has been used in the DIRC testbeam 2015 at CERN [54]. Two MCP-PMTs have been inserted into the hadron beam with $29\,\mathrm{m}$ meters flight distance between them. The time of flight information of the beam particles was sufficient to separate pions from protons up to $10\,\mathrm{GeV/c}$ beam momentum using the timing information of both MCPs which yielded timing resolutions below $80\,\mathrm{ps}$ (σ) [44]. Consequently MCP-PMTs have the potential to
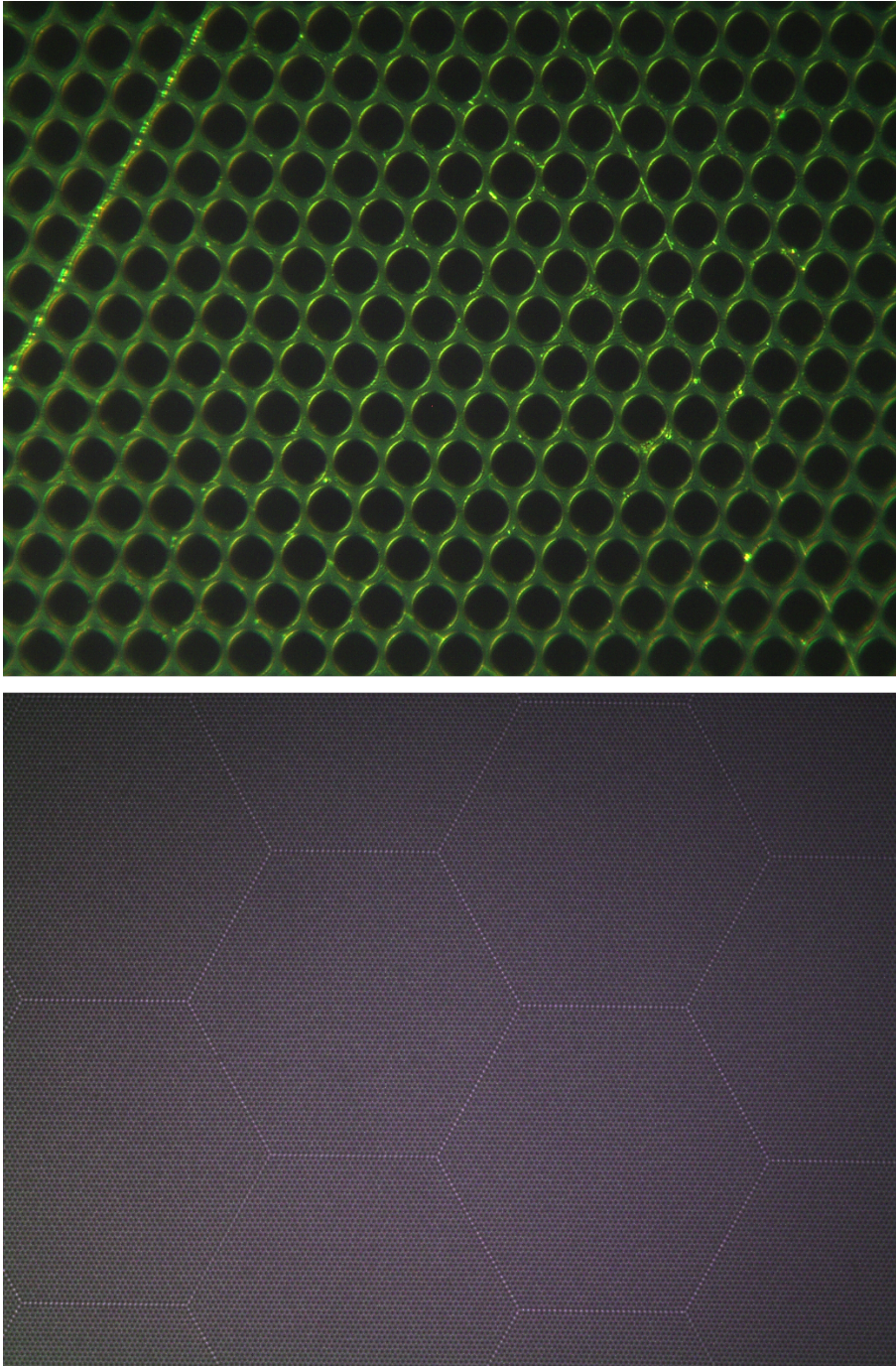
Figure 3.14: Microscope images of an MCP. The top picture shows a close up of individual pores with a diameter of $10\,\mu$m and a hole-to-hole distance of $12\,\mu$m. The *OAR* for this geometry is about $63\,\%$. The bottom picture shows a larger scale of the plate. One can see that the macroscopic MCP consists of multiple hexagonal portions. Both pictures are a courtesy of PHOTONIS.

completely fulfill the requirements for the EDD as far as time resolution is concerned. Alternatively the timing can be obtained from the readout of the electron avalanche. In this case the time resolution depends on the readout technique.

The readout with a phosphor screen coupled to a CCD readout (see figure 3.11) has some drawbacks in this category. The limitations arise from the frame rate of the CCD and ultimately from the decay time of the phosphor screen. The decay time is a measure of how fast the luminescence of the screen will stop after the flux of incoming electrons has been stopped. Typical decay times are in the order of milliseconds. Faster screens, like the ones offered by PROXIVISION[6] are even rated at some hundreds of nanoseconds. Still these timing resolutions are orders of magnitude worse compared to metal anode and delay line readouts.

Delay line readouts, like the ones offered by ROENTDEK[7] or SURFACE CONCEPT[8] can achieve timing resolutions of 100 ps RMS and better and are theoretically suitable options for the EDD. However, all these systems need some more R&D efforts before they are usable for the Disc DIRC. To the authors knowledge, there is no system with a sufficiently large (i.e. $50 \times 50 \, \text{mm}^2$) active area, a rectangular geometry, and a compact vacuum housing readily available. In principle, there should not be any technical limitations for such a system, but it remains to be shown that it can be built and fulfills all the specifications. The metal anode readout can achieve the best timing resolutions of the three options presented here. Time resolutions below 50 ps (σ) are possible.

3.4.3 Rate capability

As stated in the introduction of this chapter, the photosensors of the EDD have to be able to cope with notable hit rates due to the high interaction rates which are envisaged during the high luminosity runs at PANDA. Realistic expectations for the lifetime of the sensors and for fluxes of charged particles into the geometrical acceptance of the EDD already imply a limit on the maximum hit rate that the photosensors have to withstand. An analysis presented in [21] gives peak interaction rates between 15.9 MHz and 23.7 MHz per sensor for 2" squared MCP-PMTs with an active area of $25 \, \text{cm}^2$. It is also shown that the envisaged PID performance of the EDD can be reached with these limitations. Following this approach, the selection of a suitable sensor is restricted to models which can handle a hit rate of about $1 \, \text{MHz/cm}^2$ or more. An important criterion is a stable

---

[6] www.proxivision.de

[7] www.roentdek.com

[8] www.surface-concept.com

operation at these rates without significant drop of the pulse gain.
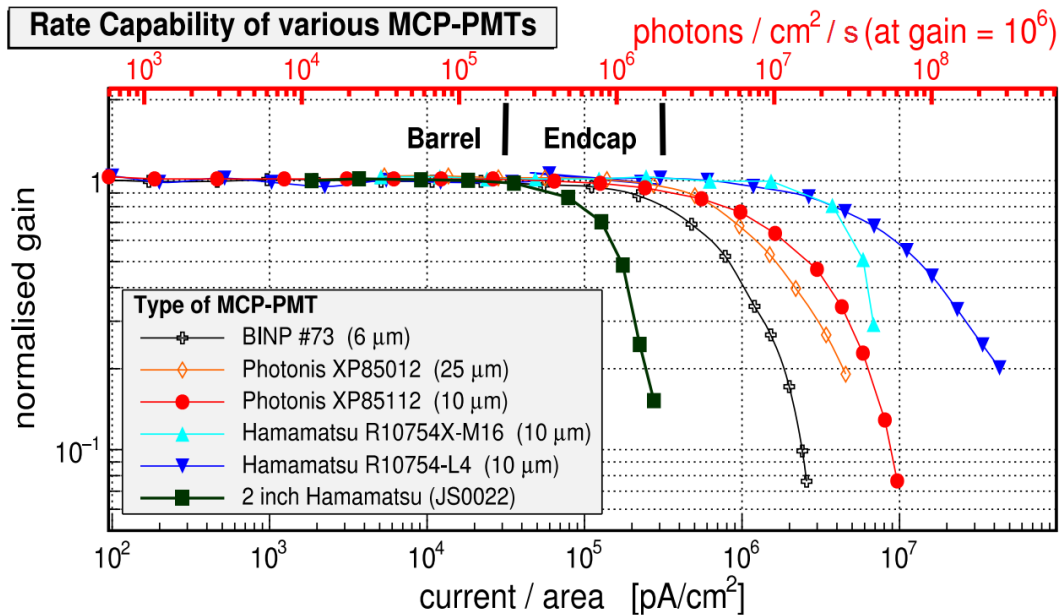
Figure 3.15: Slightly modified from [45]. Rate capabilities of various MCP-PMTs: The curves show how the average pulse gain of the sensors drop with increased photon fluxes. After the detection of a photon the sensor needs a certain *recovery time* until it is capable of detecting the next. During this phase a recharge current flows through the MCP until it is ready to provide enough charge for the next electron avalanche. The recovery time mainly depends on the capacitance and the resistance of the MCP and therefore also on its size. Larger MCPs tend to need longer recovery times. Another rate restriction can arise from concentrated illumination of a small area of the photocathode. A certain photon rate could be handled by a given MCP-PMT if it was homogeneously distributed over the entire active area while it could not be handled if it was focused onto a small spot. In the EDD a rather homogeneous spread of the photon flux is to be expected. It can be seen that both Photonis MCPs (XP85012 & XP85112) are stable up to a rate of about $2\,\text{MHz/cm}^2$ (see also [47]) which would suffice for the highest expected rates according to the requirements presented above. The 2" Hamamatsu tube drops significantly earlier and faster what could lead to loss of photons at very high rates.

The authors of [45] show the rate capabilities of several modern MCP-PMTs (figure 3.15). One can see that the Photonis Planacon XP85112 2" tube can fulfill even this extreme rate requirement. However, the photon rate is not only a concern for the multiplication stage but also for the readout. Especially in the case of the delay line readout, high hit rates can lead to ambiguities. This can result in incorrect pairing of incoming pulses leading to falsely reconstructed impact positions of the initial photons.

The company SURFACE CONCEPT offers a delay line readout with diameters between 30 and 45 mm. These readouts can cope with a maximum permanent random count rate of 5 MHz while only using two delay lines, one for each coordinate (4 analog channels in total). The 2D spatial resolution is in the order of 100 μm. For the 40 mm option the total propagation time through one delay line is about 20 ns and a typical time peak width

(FWHM) in series production varies around 180 ps. The timing resolution could still be improved by measuring the MCP output signal together with the signals from the delay lines. Another interesting alternative to increase the rate capability is the use of multiple delay lines which increases the rate capability linearly with the total number of delay lines used. With this technique basically *any* rate limitation of the delay line readout can be overcome by consecutively segmenting the delay lines more and more. A drawback is the increase in the total number of analog channels (i.e. the ends of the delay lines) that have to be read out and a decreasing spatial resolution due to shorter signal propagation times. It should be noted that typical hit rates at PANDA are notably lower than the expected peak interaction rate that has been the basis for these estimations. Additionally, one should keep in mind that the actual luminosity of PANDA will be reduced by a factor of 10 until the RESR (see chapter 2) is operational. Consequently, the hit rate would also be reduced by the same factor without the RESR. In addition, the use of optical bandpass filters in front of the photocathode, or photocathodes with taylored spectral sensitivities are also a viable option to reduce the hit rates. Even though this would lead to an effective loss of photons, these options would also reduce chromatic errors and therefore not deteriorate the PID performance too much.

3.4.4 Spatial resolution

The focusing light guides of the EDD convert the angle of travel of the Cherenkov photons into a position of impact on the photocathode of the MCP-PMTs as explained in section 2.3.4. This is why the spatial resolution of the photosensor is one of the most important prerequisites for achieving the envisaged PID performance of the EDD. Two major readout options for MCP-PMTs have been identified in the preceding sections: A multi anode readout and a capacitive readout with a delay line. In the case of a segmented anode readout, the spatial resolution is mainly determined by the size of the individual anode pads. In the case that the charge cloud of the electron avalanche is bigger than the anode pads, more than one pad will be hit. The amount of charge captured by the individual anodes can be used to reconstruct the point of impact more precisely by finding the center of mass of the charge collected by all anodes (see also figure 3.9). If the footprint of the charge cloud is considerably smaller than the anode pads it is very likely that only one anode will collect a measurable charge and the centroiding technique can no longer be used. However, the loss in additional spatial resolution is compensated by a reduced average hit rate on the anodes. A common value given for the spatial resolution of

MCP-PMTs with big (compared to the size of the charge footprint) segmented anodes is the size of these anodes divided by $\sqrt{12}$. The additional factor $1/\sqrt{12}$ corresponds to the standard deviation of a uniform probability density function on the interval $[0, 1]$ which is the correct measure for the average error if each hit is assigned to the center of the anode. With a given anode pitch of $0.5\,\text{mm}$, a spatial resolution of $\sigma \approx 500\mu\text{m}/\sqrt{12} \approx 145\mu\text{m}$ can be expected.

The spatial resolution of the delay line readout mainly depends on the total propagation length and the time resolution of the analog readout (see figure 3.12). ROENTDEK claims to achieve spatial resolutions of $45\,\mu\text{m}$ (RMS) ($17\,\mu\text{m}$ (RMS) being the best result) in combination with a timing resolution of $100\,\text{ps}$ (RMS) ($21\,\text{ps}$ (RMS) being the best result). This readout is available for circular shapes with diameters up to $150\,\text{mm}$ and can withstand rates in the order of some MHz.

3.4.5 MCP-PMTs in magnetic fields

Figure 3.8 already illustrated the effect of magnetic fields on electron trajectories inside vacuum based photosensors. Of course the same behavior is also expected for MCP-PMTs. However, unlike in the case of discrete dynodes, the continuous structure of the MCP allows different flight paths of the photoelectron. Like in the case of the Fine Mesh PMT, the electron will simply be amplified elsewhere and any offset of the image can, in principle, be calibrated out. However, there are some additional effects that have to be considered. Firstly, it is true that even deviated electrons will still impinge on the

Figure 3.16: Geometry of photoelectron impact with different angles of the magnetic field $\vec{B}$.

MCP, but the geometry of the impact can be changed decisively.

One phenomenon that has been observed is a substantial loss in gain if the channel axis is aligned with the magnetic field and the Larmor radius of the electron is comparable to the diameter of the microchannels (sometimes called *Chevron Effect*). The reason for this drop in gain can be understood from figure 3.16. The electron will penetrate substantially into the channel without colliding with the wall. A magnetic field with the same magnitude (i.e. the same Larmor radius of the photoelectrons) but a different field line angle with respect to the channels would not disturb the first multiplication process (which is the most important one) as much, leading to no significant loss in gain.

In general it is also important to estimate how the average angle of incidence and the

kinetic energy of the electron is influenced by the magnetic field because the SEY depends on these parameters. This is why the MCP gain can also be increased by an external magnetic field (figure 3.17). In addition to the influence on the amplification of
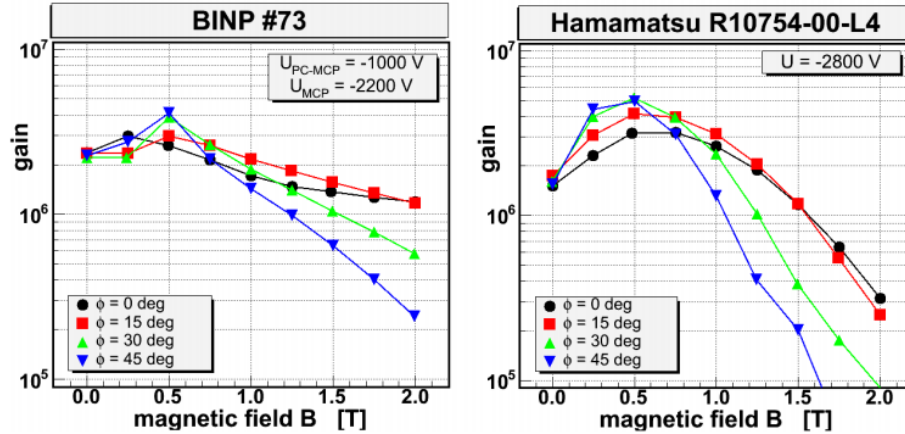
Figure 3.17: [43] The dependence of the MCP gain as a function of the strength of the magnetic field and its angle with respect to the sensor axis. One can observe that the gain is increased for smaller fields, but drops again for stronger ones.

the MCP-PMT and the image shifts, the magnetic field will also shrink the lateral size of the electron cloud. This can be important depending on the readout technique that the sensor employs. Let us consider that the tube has a finely segmented anode geometry with vacuum feedthroughs for each individual anode pad. In the absence of magnetic fields, the charge cloud will cover multiple anode pads and centroiding can be done to improve the position resolution. If the footprint of the charge cloud is considerably smaller, the behavior of the tube will change. The average number of active pixels per amplified photoelectron will be reduced by a strong field (figure 3.18). There is even the risk of undersampling the electron cloud because the gaps between the anode pads could suddenly be as big as the footprint of the compressed avalanche. Any charges that do not impact the anodes directly can slowly drift towards the pads, but may not be registered in the pulse. This problem has to be addressed and must not lead to significant loss in pulse gain. The readout technologies that use capacitive signal coupling should not experience any performance reduction due to smaller charge footprints because the resistive layer is continuous. However, to the author's knowledge, no tests with strong magnetic fields have been performed that would definitely prove the suitability of this technology for the EDD.
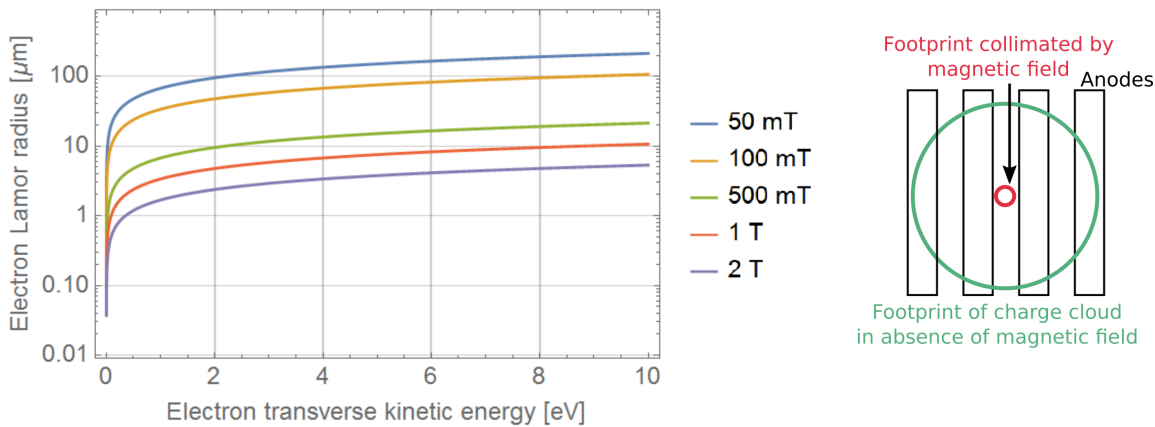
Figure 3.18: Left: The larmor radius of electrons for different transverse (i.e. perpendicular to the magnetic field) kinetic energies and magnetic fields. One can see that the field strengths that are expected at PANDA could collimate the charge cloud to a size of only several micrometers.
Right: The reduced size of the charge footprint could lead to a significant part of the charge being deposited between the anode pads (undersampling). Consequently, the pulse gain of the sensor might be reduced significantly leading to a loss of single photon sensitivity.

3.4.6 Lifetime and radiation hardness

Until only a few years ago, the lifetime of MCP-PMTs was a real concern. The problem of continuing degradation of the quantum efficiency was putting a hard limit on the durability of the sensors. Even today, all the causes for the loss of the QE are not entirely understood. However, it is a prevalent approach to normalize the loss in QE to the total amount of anode charge that was produced during the lifespan of a sensor. One good reason for this is the fact that ions, which are created in the vacuum of the tube, are believed to be the primary cause for the degradation of the photocathode. These ions are produced during the multiplication phase when secondary electrons collide with neutral atoms. They are accelerated by the electric fields inside the tube that is normally intended to guide the electrons, and can eventually strike the photocathode (see also figure 3.9). The photocathodes (which are almost entirely transmissive types in imaging applications such as the EDD) are very sensitive to this chemical poisoning. This is because they are highly fragile and thin layers that have been optimized to provide the best photoelectron yield for incoming light. The optimization results in a trade-off between a thick layer that captures all incoming photons but also presents an obstacle for the photoelectrons during their passage, and a very thin photocathode which is easily traversed by the photoelectrons but also by some of the incoming photons which cannot be converted. In most cases a well defined amount of material, or multiple layers of functionalized substances, are deposited on the back side of the entrance window of the sensor. GaAs, InGaAs or

the solar blind materials Cs-Te and Cs-I are commonly used but many photocathodes in MCP-PMTs that are designed to detect visible light are made from either *bialkali* (e.g., Sb-K-Cs) or *multialkali* (e.g., Na-K-Sb-Cs). However, the photoelectron yield of most of these photocathodes depends very strongly on the chemical purity, the crystallinity (which influences the scattering length of photoelectrons inside the cathode) and other very delicate parameters which can be significantly altered by ion bombardment. Neutral atoms can also undergo chemical reactions with the photocathode and change its work function. For this reason, the QE of the otherwise suitable MCP-PMTs began to degrade significantly at less than $100 \, \mathrm{mC/cm^2}$ [45]. Under the assumptions that each charged particle in the EDD creates about 25 photons that will be detected (which is a reasonable number to achieve reliable PID information according to simulations) and each p$\bar{\mathrm{p}}$ interaction averages about 3 tracks in the acceptance of the EDD one can calculate the required lifetime of the sensors [21]. Given an average p$\bar{\mathrm{p}}$ interaction rate of $10 \, \mathrm{MHz}$ for 5 years of operation (including maintenance periods in the total 10 years of lifetime of PANDA) at the HESR one can derive

$$Q = \frac{5 \, \mathrm{years} \times 10^7 \, \frac{\mathrm{events}}{\mathrm{s}} \times 3 \, \frac{\mathrm{tracks}}{\mathrm{event}} \times 25 \, \frac{\mathrm{photons}}{\mathrm{track}} \times 10^6 \, \frac{\mathrm{electrons}}{\mathrm{photon}} \times e}{25 \, \frac{\mathrm{cm^2}}{\mathrm{sensor}} \times 108 \, \mathrm{sensors}} \approx 7 \, \frac{\mathrm{C}}{\mathrm{cm^2}} \qquad (3.4.11)$$

with e being the elementary charge. One can see that this requirement is more than an order of magnitude higher than the typical $100 \, \mathrm{mC/cm^2}$ that were available a few years ago. However, this estimation relies again on a fully equipped FAIR facility including the RESR from day one. Reduced luminosities due to a delayed integration of the RESR would significantly reduce the required lifetime.

Another disturbance caused by the electron amplification is the desorption of atoms of the MCP surface. This has two negative effects. Firstly, it emits more neutral atoms into the vacuum which can be subsequently ionized and damage the photocathode. Secondly, the desorption can lead to local changes of the MCP gain.

Some measures to counter the aging have already been shown in figure 3.11. The following list outlines some additional approaches.

1. Recent developments steer towards more robust photocathodes that are less vulnerable to chemical poisoning [50]. One example is the exposure of the photocathode to vapors of cesium and antimony. Often times an increase in robustness goes along with an unwanted increase in the dark count rate of the hardened photocathode.

2. Cleaning of all vacuum surfaces by means of *electron scrubbing* helps to remove all

those particles on the surfaces that are easily desorbed by an electron avalanche.

3. General improvements on the vacuum applied to the tube.

4. Usage of different MCP substrates which opens the possibility to use higher temperatures during outbaking leading to improvements in the vacuum quality.

5. Hermetical sealing of the first vacuum gap from other parts of the vacuum region can reduce the flow of harmful particles towards the photocathode. Of course this technique is limited by the constraint that the photoelectrons still have to find a way towards the MCP without being disturbed by the sealing.

6. Another active ion barrier can be made from an electrostatic grid instead of thin Al_2O_3 films. They are also placed between the photocathode and the first MCP [51]. Unfortunately they also reduce the CE by about 40%.

ALD (Atomic Layer Deposition) coatings are another very promising technique to enhance the lifetime of MCP-PMTs: Thin layers of high SEY materials are applied to the microchannel plates and prevent outgassing from the MCP-stack. It is safe to say that this technique has led to a real breakthrough in lifetime enhancement. In some cases the lifetime was improved by a factor of 50. The only real downside of ALD coatings are the increased manufacturing costs and the reduced availability of such tubes. Figure 3.19 shows the liftetime of some ALD treated sensors and allows a comparison with regular ones.

One can see that the required lifetime can be reached with modern ALD tubes. The final results of the lifetime measurements and their reproducibility can be very important for the EDD because an increase in lifetime can potentially be exploited by collecting more photons in each event. If the lifetime of MCP-PMTs can be reliably enhanced beyond 5-7 C/cm^2 it might even be advisable to reconsider the wavelength band of the Cherenkov radiation which could potentially increase the PID performance of the EDD altogether.

Unlike the aforementioned vulnerability to chemical poisoning of the photocathode from the inside of the vacuum tube, MCP-PMTs are very insensitive to incoming neutron radiation or fluxes of charged hadrons. This is a key advantage compared to SiPMs. The slow ions from the inside of the tube deposit much more energy in comparison. The only concern regarding external radiation is the effect on the entrance window of the sensor. Like all other optics of the EDD, the entrance windows of the MCP-PMTs have to be chosen to be radiation hard enough. A decrease in the transmission of the entrance window would be just as troublesome as a corresponding degradation of the QE of the photocathode.
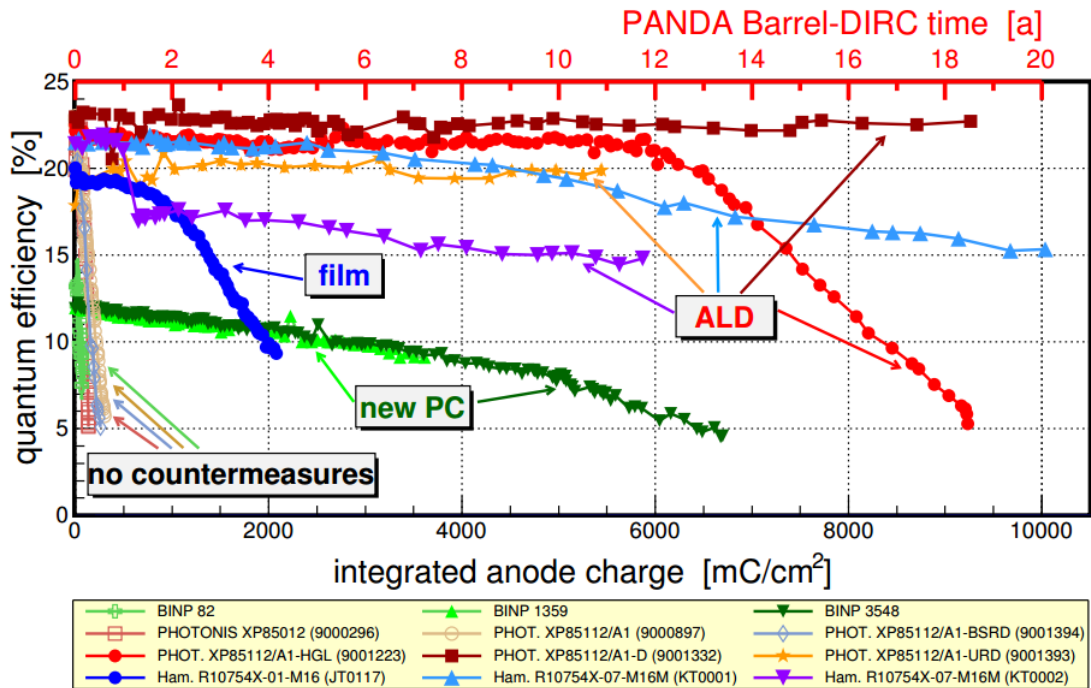
Figure 3.19: [52] The quantum efficiency of some MCP-PMTs as a function of the integrated anode charge. Sensors with no countermeasures show a very limited lifetime. Classical protection techniques like protective films increase the lifetime significantly. The class of ALD coated sensors truly excels in the lifetime comparison. The PHOT. XP85112/A1-D (9001332) for example has surpassed $9\,\mathrm{C/cm^2}$ of total anode charge without any recognizable degradation of its QE. The kink in the Hamamatsu KT0002 (violet line) measurement is not aging related but is caused by a short circuit in a HV divider.

The radiation hardness of the optics of the EDD has been studied and suitable hardware has been identified. The corresponding studies and results are mainly presented in [54]. A dedicated study concerning the radiation hardness of readily available entrance windows is shown in chapter 5.

4 Prototype Electronic Readout

4.1 Introduction

The photon detection system of the EDD has to be integrated into the reserved volume inside the target spectrometer. Due to the costs of big magnets, space is a very precious resource inside the PANDA solenoid. Figure 4.1 shows a CAD image of the current design of the EDD being implemented in the PANDA environment. The volume where the FELs and the photon readout have to be accommodated is simply too small for a bulky readout scheme. In addition, it would not be easy to find room for cabling that would allow to connect all MCP-PMT channels to a (possibly bigger) readout system outside of the tight environment. The small single photon signals would also be deteriorated or possibly dampened when transmitted through long cables with small cross sections. Hence, it was decided to install a digitizing unit directly to the back of the MCP-PMT. This allows to concentrate the data traffic to the outside through a single high speed transceiver which can communicate digitally, preferably through optical fibers. A priori there are multiple options available that could be considered. However, like in the case of the photosensors, many

Figure 4.1: Installation space for the EDD readout.

(otherwise promising) readout systems fail to fulfill some prerequisites and are therefore not suitable for an application in the EDD. In particular, the required compactness of the readout solution reduces the options to those based on FPGAs[1] or ASICs[2]. Additionally, high power consumption and the associated heat production have to be avoided since

---

[1] Field Programmable Gate Array
[2] Application Specific Integrated Circuit

effective cooling is hard to achieve within the spatial limitations. The comparably weak single photon signals of the MCP-PMTs have to be picked up with sufficient efficiency to guarantee flawless detection of Cherenkov photons. Hence, an option that includes a built-in preamplifier or any other technical measure that allows a reliable recognition of single photon pulses is preferable. The system does also have to be compatible with the very high channel densities that are an inherent feature of the EDD design. Last but by no means least it has to fulfill the tight performance constraints as far as time resolution and rate capability are concerned.

To the best knowledge of the EDD designers, including the author of this work, very few readily available options can meet the stringent demands of the EDD readout scheme. In principle, one option is the TRB3 [18] readout system that is based on FPGAs and is also used by the PANDA barrel DIRC. However, a lot of design work would have to be invested to manage an integration and especially a viable cooling scheme for this system, as its projected heat generation is reason for concern. The TOFPET ASIC, a commercially available product distributed by PETSYS Electronics, has been identified as the most promising candidate [21]. It was developed for the use with SiPMs (see section 3.2.2) and was not originally intended to be used with vacuum based sensors like MCP-PMTs. The suitability of the ASIC for reading out single photon signals of an MCP-PMT with a sufficiently high anode segmentation is one major subject of research of this work. The technical specifications of the ASIC - as provided by the manufacturer - fulfill all requirements and an implementation into the

Figure 4.2: [53] The TOFPET ASIC

PANDA DAQ system should be doable with moderate design efforts. It has an intrinsic time resolution of 25 ps (RMS) and allows a charge measurement via time-over-threshold. Each ASIC features 64 input channels with built-in amplifiers providing a dynamic range of 300 pC for the total input charge. Despite being designed for such high input charges (corresponding to thousands of photoelectrons at a gain of 10^6) it is also well-suited for photon counting. It can be operated at clock frequencies between 80 and 160 MHz and uses LVDS[3] for digital IO. Each channel has a derandomizer so that up to 4 hits can occur in the same channel before it enters its dead time. This leads to a maximum channel hit

---

[3]Low Voltage Digital Signaling

rate of 160 kHz. Its maximum output data rate is 640 Mb/s if operated in double-data-rate (DDR) mode.

In order to proof the compatibility with MCP-PMTs, hands-on measurements were necessary with a close-to-final photosensor. Such measurements have been successfully conducted under laboratory conditions as well as in a real testbeam situation. The tests and their results are presented in the following chapters. The purpose of the following pages is to familiarize the reader with the electronic equipment that was bought or constructed in order to do these tests.

4.2 The TOFPET Evaluation Kit
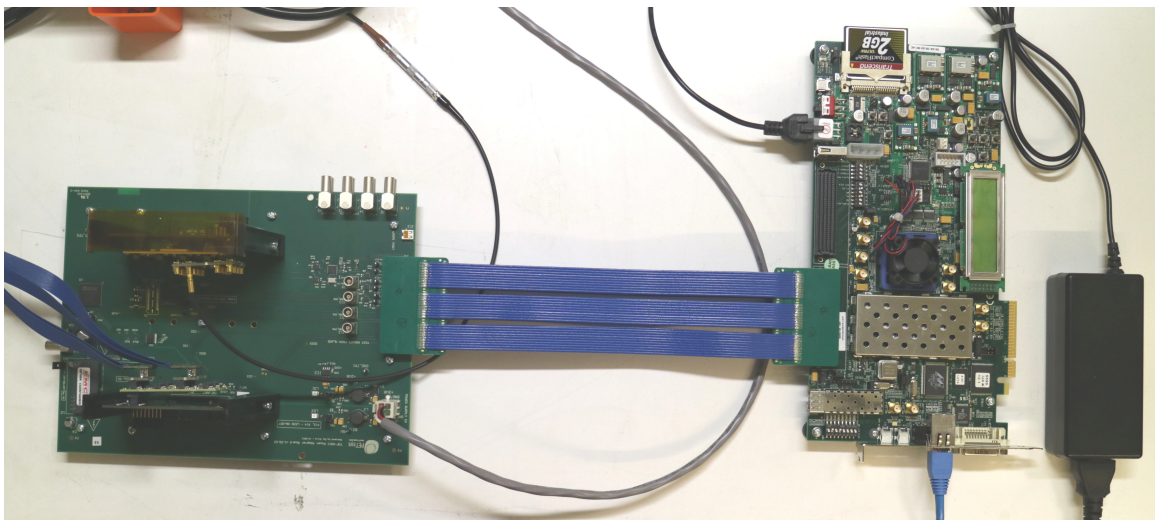
Figure 4.3: The TOFPET Evaluation kit consists of the ML605 FPGA board (on the right side), the PAB and two FEB-As, providing 4 ASICs with 256 channels (left side). The FEB-As are mounted facing each other so that coincidence measurements with scintillation detectors can be easily done with a radioactive source in the middle. In this application a set of custom PCBs was developed to be able to connect to the ASIC input nodes.

The first step towards system testing was taken with the *TOFPET Evaluation Kit*. This is a system composed of 3 main parts that can be seen in figure 4.3. The right side of the photograph shows the ML605 board. This FPGA board was used to establish communication between the high level applications run on the DAQ PC and the digital logic of the ASIC. The ML605 was connected to the *Power Adapter Board* (PAB) via a custom cable assembly provided by PETSYS. The PAB serves as a basic platform that can be equipped with two *Front End Boards A* (FEB-As). Each FEB-A carries two abutted ASICs with a total of 128 channels. Hence, the evaluation kit can provide up to 256

channels. The PAB also holds a voltage generator that can be used to supply SiPMs with bias voltages. Since the MCP-PMTs need much greater voltages than SiPMs (few kV as compared to some tens of volts) the on-board voltage generator was not used. The FEB-As are designed to directly mate with Hamamatsu MPPCs (Multi Pixel Photon Counters) and feature distinct high pitch SMD connectors that are directly compatible with these sensors. In order to connect arbitrary signals to input nodes of the ASICs, a dedicated adapter PCB was designed that follows the signal routing scheme of the FEB-As. This adapter board can be seen in figure 4.4. Like all other custom PCBs it was designed with the Software package ALTIUM DESIGNER. The other side of the adapter
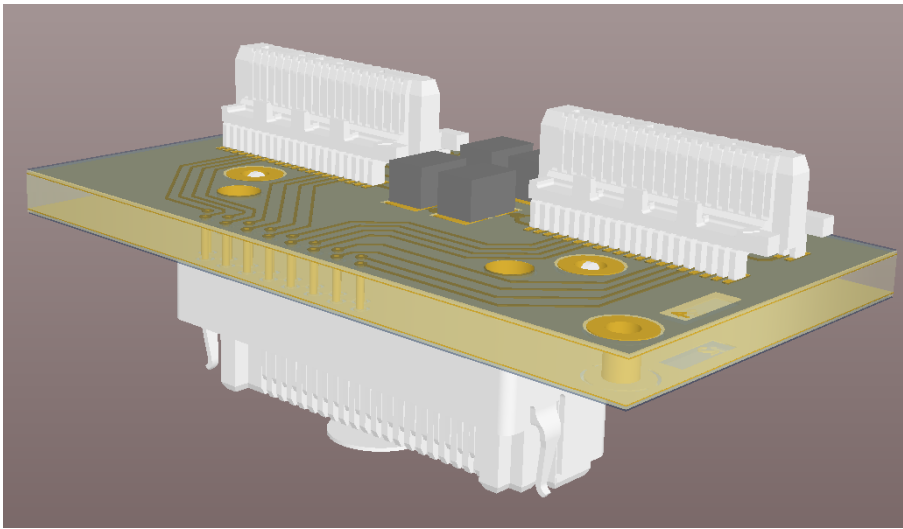
Figure 4.4: Adapter PCB for the evaluation kit. The upper side can be inserted into the FEB-A while the lower side connects to a coaxial cable assembly that transmits the MCP-PMT pulses.

PCB was equipped with another high pitch SMD connector that is compatible with a high density coaxial cable assembly provided by SAMTEC. These cable assemblies are ideally suited to connect the hundreds of channels through a well-shielded and impedance-controlled transmission line. Depending on the MCP-PMT that had to be connected (i.e. Hamamatsu or Photonis prototypes) to the readout, one of two additional PCBs were included in the signal path. Both variations can be seen in figures 4.5 and 4.6.

All custom PCBs were manufactured with two internal ground layers and signal routings on both outer layers. The layer stackup of the boards was designed to generate an impedance of $50\,\Omega$ which also corresponds to the impedance of the SAMTEC coaxial cable assembly. The ASICs input resistance was also trimmed to $50\,\Omega$ to optimize the signal injection from the transmission line. This could be done via an appropriate parameter setting during the configuration of the ASIC. The PCBs shown below were used for all
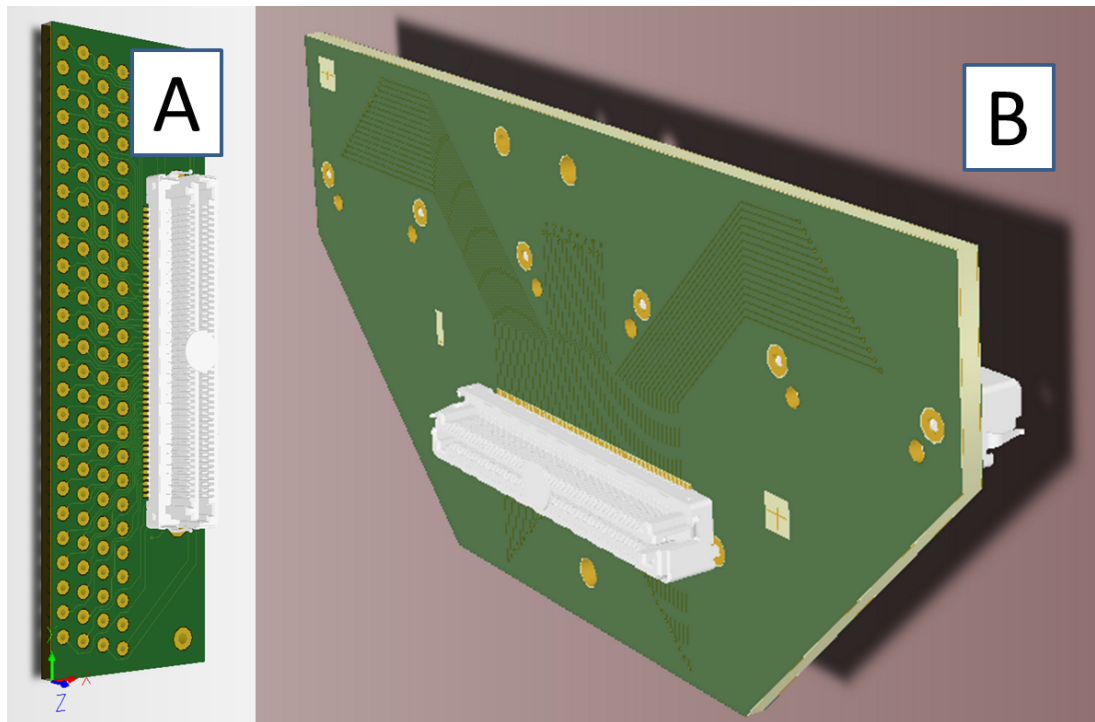
Figure 4.5: CAD images of the test boards for the Photonis MCP-PMT: **A** shows the PCB that can be connected to the back side of the custom made Photonis MCP-PMT prototype presented in the next chapter. It transmits signals from 96 channels to the feedthrough and distribution PCB shown in **B**. This card splits the 96 signals into 3×32 paths that can be connected to the TOFPET readout individually.
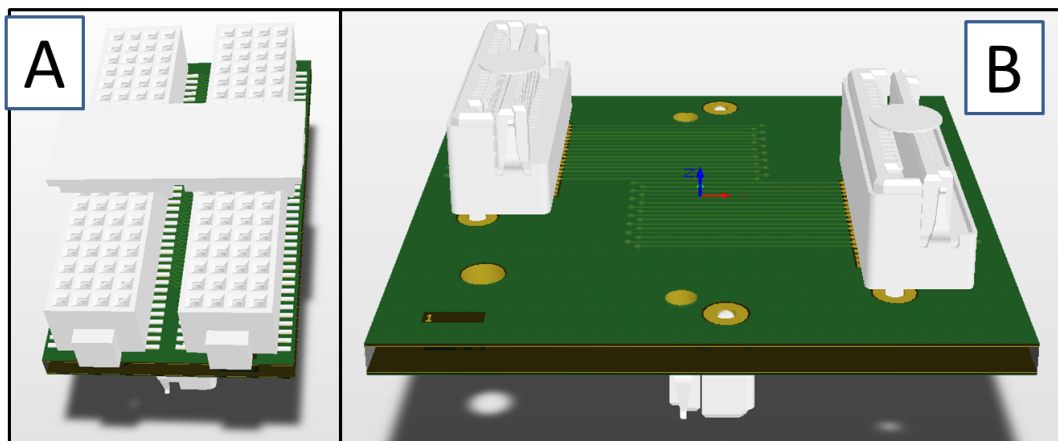
Figure 4.6: CAD models of the test boards for the Hamamatsu MCP-PMT: **A** shows the PCB that can directly connect to the back side of the sensor. For our application, the segmentation of the Hamamatsu MCP-PMT is too high in one direction (see figure 5.2 in the next chapter). This is why two neighboring anode strips are shortened by the PCB in **A**. **B** shows the PCB for feedthrough and redistribution. 64 channels can be connected to the TOFPET readout with one set of the two boards.

tests in the laboratory and in the testbeam campaign at DESY and will be shown in use in the next chapters.

4.3 Full Scale TOFPET Readout

After the tests with the evaluation kit were conducted successfully (see chapter 5), a readout system with more than 256 channels was necessary in order to fully equip an EDD prototype with up to 5 MCP-PMTs. PETSYS Electronics also provides a scalable readout solution which is very modular and can be extended to read out many thousands of channels through one acquisition. In this system, the PAB is replaced by a *DAQ card* and a *Frond End Board D* (FEB-D). The DAQ card (figure 4.7) is directly connected to the DAQ PC via a PCI-e connection. In our case two FEB-Ds were bought. Each
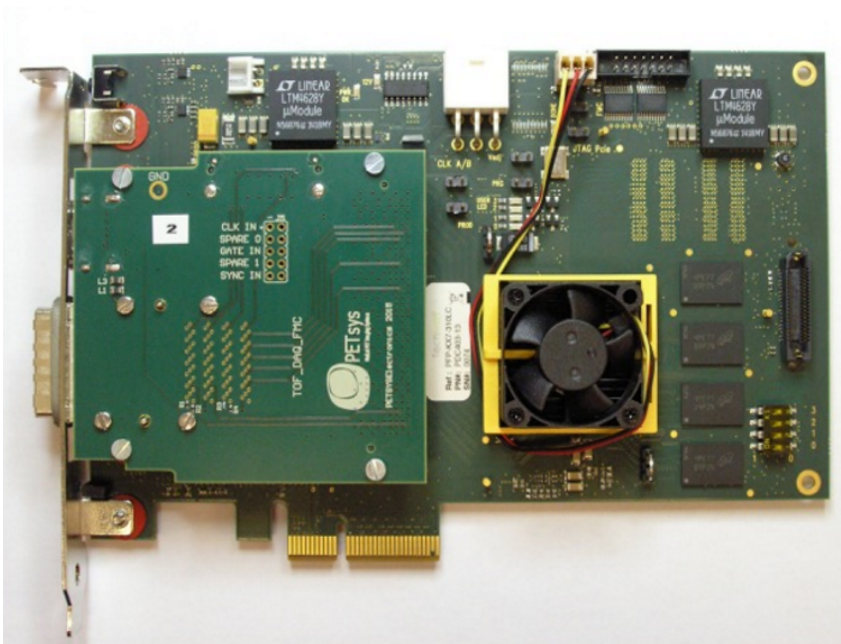
Figure 4.7: The DAQ card communicates with the DAQ PC via a PCI-e connector and unifies the data streams of multiple FEB-D boards.

FEB-D can be equipped with up to 8 FEB-As which are in principle the same boards as in the evaluation kit. However, by the time of purchase a new version of the FEB-A was released and a new adapter board had to be designed (see figure 4.8). This was done in a way to keep full compatibility with the existing hardware for sensor connectivity, feedthrough and redistribution. With our fully equipped system, consisting of 12 FEB-As, 1536 MCP-PMT channels can be connected.
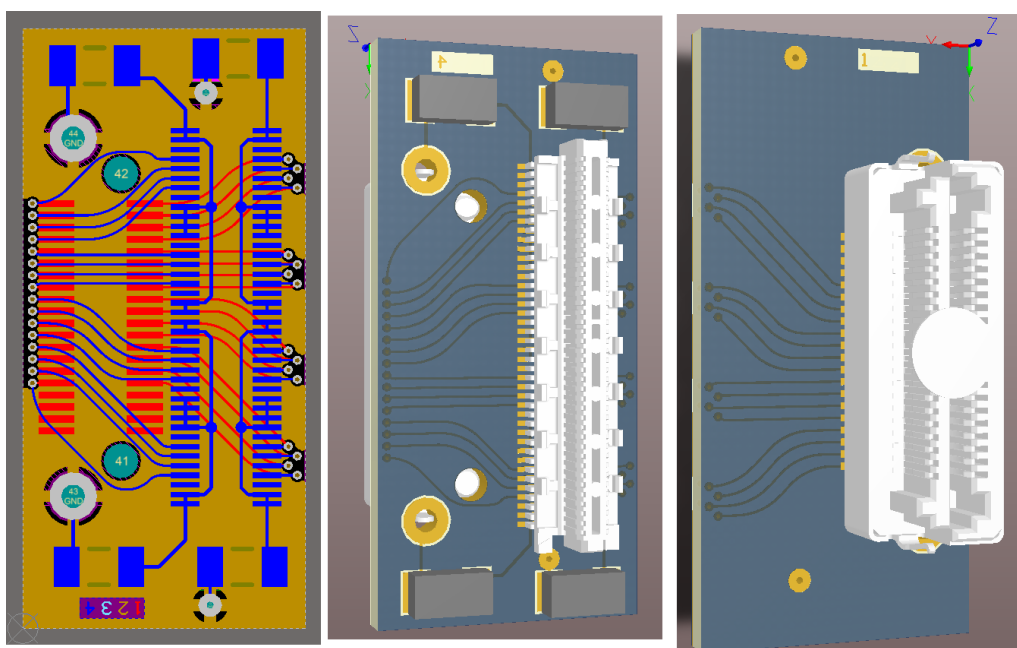
Figure 4.8: Adapter PCB for the latest TOFPET FEB-A. It can be used to route MCP-PMT signals into the input nodes of the TOFPET ASIC.
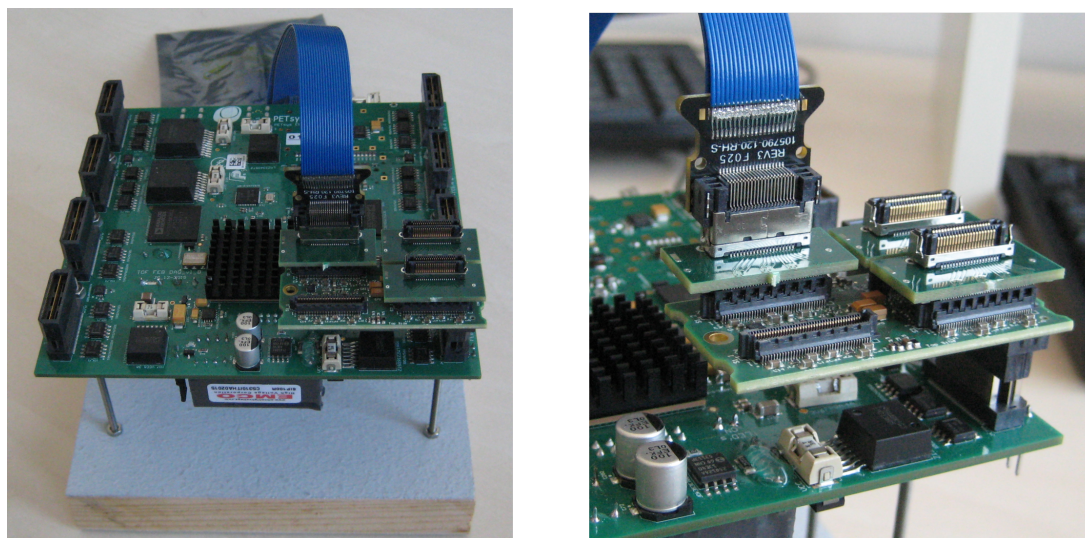
Figure 4.9: Close-up of the full scale readout connectivity: The FEB-D holds one of 8 possible FEB-As. Three adapter PCBs as shown in figure 4.8 are inserted into the high-pitch SMD connectors of the FEB-A. One SAMTEC cable assembly (blue) allows to insert 32 analog signals into the ASIC. The mechanical holding structure that was used in the testbeam was removed to improve the visibility of the components.

5 Prototyping

The way to the current design of the PANDA EDD went through numerous R&D efforts including many prototypes that have been analyzed in testbeam campaigns with the help of multiple generations of students. During the testing and design work, many new technologies became available and significant progress in some key technologies took place. Radiation hardness studies on SiPMs raised serious concerns about their suitability in the radiation harsh environment of PANDA. At the same time, enormous advances on the lifetime enhancement and rate capabilities of MCP-PMTs were achieved. The lineup of suitable electronic readout options was enriched by some promising candidates like the TOFPET ASIC or advanced delay line readouts for MCP-PMTs. In the meantime, many different detector designs and strategies to measure the Cherenkov angle of incoming charged particles as accurately as possible under the given circumstances have been discussed in the research community and were partly tested in the field. All ideas, studies, discussions and experiences finally allowed the proposition of the current detector concept which has been carefully justified in [21]. After the convergence of the technical designs, it remained to be shown that the expected performance parameters of the different detector components can be reached individually and that their combination results in a detector which satisfies all given requirements.

The major challenge of this work is to proof that the required position resolution of the photon detection system can be achieved with a compact setup, using an MCP-PMT with a customized anode geometry, a readout system based on the TOFPET ASIC in magnetic fields with magnitudes up to $1\,\mathrm{T}$ and a position resolution below $150\,\mu\mathrm{m}$. The following section will demonstrate the prototyping and the experiments that have been carried out during the course of this work in order to lend credence to the design proposal.

5.1 Testing of MCP-PMTs

5.1.1 Specifications of the prototypes

Table 5.1: Key specifications of the main two MCP-PMT options for the EDD.

Vendor	Photonis	Hamamatsu
Specification	XP85132-S-MD3	R13266-07-M768
Photocathode	Bialkali	Multialkali
Active area	53×53 mm^2	53×53 mm^2
Anode configuration	3×100	6×128
Anode dimensions	16.8×0.35 mm^2	8.48×0.3 mm^2
Column pitch	0.51 mm	0.4 mm
Overall high voltage	2400 - 2800 V	3200 - 3600 V
MCP type	Chevron	Chevron
MCP channel diameter	10 μm	10 μm
Comments	Custom anode layout	Protective film on 1$^{\text{st}}$ MCP

Two different MCP-PMT types have been identified as promising candidates for the EDD. The most important specifications are summarized in table 5.1. The Photonis device is very similar to the standard PLANACON MCP-PMT. This sensor is widely used and can be customized in many different ways. It is also the only sensor which satisfies both the rate and lifetime requirements if it is equipped with an ALD-coated set of MCPs [45] (see figure 3.15). If the compatibility with the TOFPET ASIC and immunity against magnetic fields can be shown, this sensor can be considered suitable in every regard.

The other choice is the Hamamatsu 128x6 MCP-PMT which still needs to improve its rate capability. It has also the drawback of a reduced collection efficiency due to the protective foil on the first MCP which will be removed in the next iteration of the sensor. In return it has slightly smaller anodes which should translate into better position resolution but also cause higher data rates due to more active anodes for each incoming charge cloud. Both sensors are shown in figure 5.1. A scaled sketch of their anode geometries can be seen in figure 5.2.
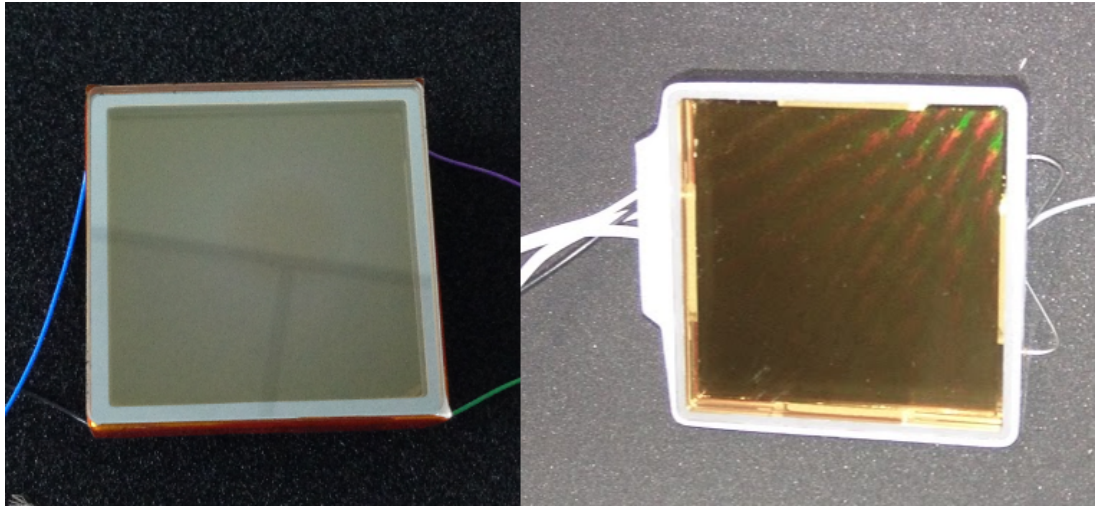
Figure 5.1: Photographs of the two main sensor candidates for the EDD: The left picture shows the Hamamatsu R13266-07-M768. The Photonis XP85132-S-MD3 can be seen on the right.
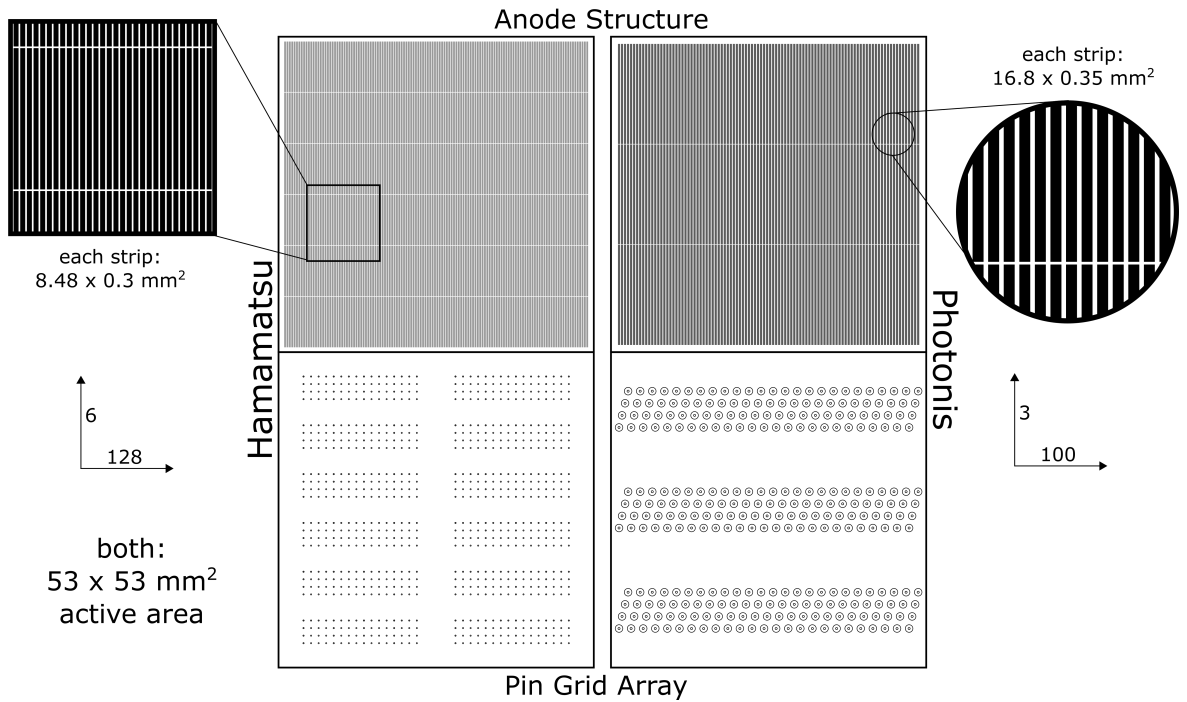
Figure 5.2: Scaled sketch of the anode geometry of both sensors. The upper left side shows the 6×128 anodes of the Hamamatsu sensor inside the quadratic active area. The 3×100 anodes of the Photonis device are shown on the upper right side. Below, one can see a scaled sketch of the pin grid array (PGA) on the backsides of both sensors. Each pin is connected to on anode via a vacuum feedthrough. The dimensions are given in table 5.1.

5.1.2 The automated test setup
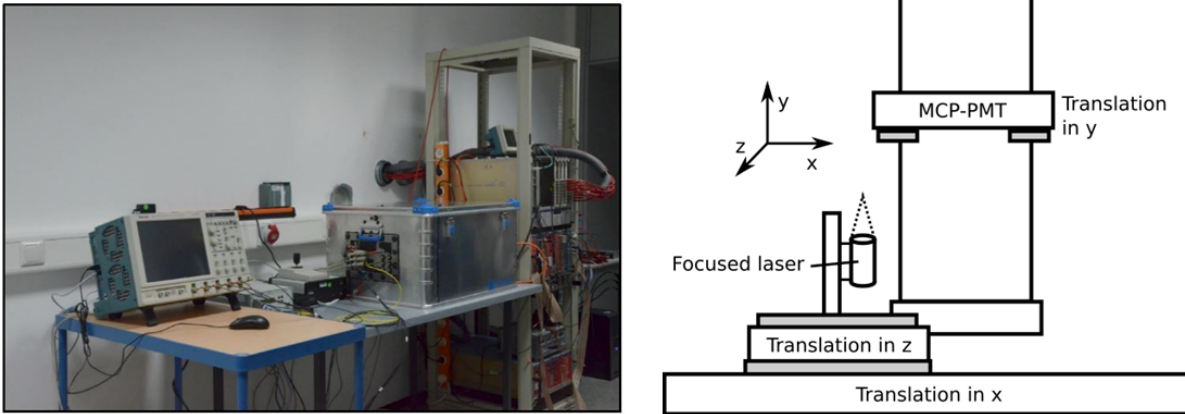
Figure 5.3: The automated test setup (also described in [55]): The left picture shows the setup in the lab. The right figure illustrates the working principle of the motor stages inside the box.

In order to verify the performance of the MCP-PMTs, several test setups have been built. The following section gives an overview of important properties of the sensors and how they were experimentally quantified. The first test stand which was used for MCP-PMT testing was built inside an aluminum dark box (see figure 5.3). The lid and the folds of the aluminum box have been coated with dark paint, silicone or rubber strips. This seals the inside off from external light. Furthermore, numerous feedthroughs for the anode signals, the high voltage supply and the laser light have been installed. The setup also features three translation stages inside the box which allow 3-dimensional scans. As schematically shown in figure 5.3, two translation stages allow a surface scan of the photocathode of a given sensor. The third translation stage can be used to optimize the distance between the light source (i.e. a focusing laser optic) and the MCP-PMT. This is an important option as the optimal distance between the light source and the device under test can differ from sensor to sensor. The thicknesses of different entrance windows can vary by several millimeters. The effective size of the light spot depends significantly on the working distance. Adjusting the distance with the help of the motor helps to precisely illuminate the photocathode on the backside of the entrance window. The effect of the working distance on the focusing quality is illustrated in figure 5.4. Between consecutive measurements, the laser was brought closer to the screen in steps of $100\,\mu$m. The intensity distribution for each measurement was fitted with a 2-dimensional Gaussian function. The standard deviations in both dimensions (x and y direction) are shown as a function of the working distance with an unknown offset in the lower part of the figure. According to the
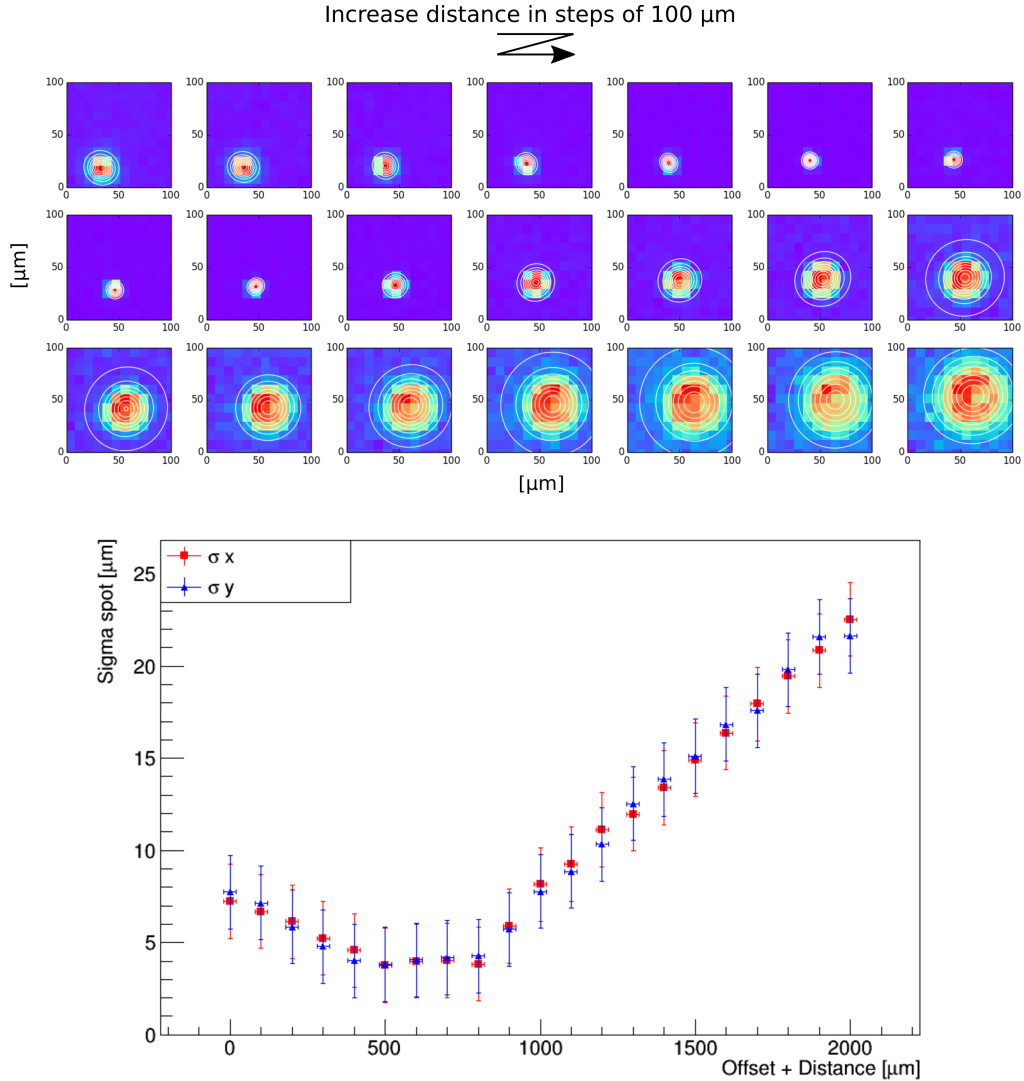
Figure 5.4: The upper part of the figure shows the size of the laser spot of the PiLas [56] laser after it has been focused by the test optics. The spot was measured with a CCD chip. The spot size depends strongly on the working distance i.e. the distance between the focusing optic and the screen.

vendor, the minimum spot width is $9\,\mu$m (σ) at the optimal working distance of $38\,$mm. To resolve this, an additional magnification optic would be needed in this measurement because the pixel size of the CCD chip is $9\,\mu$m itself. However, it can also be seen that small misalignment in the order of a millimeter still leads to a very small spot in the order of $20\,\mu$m. Apart from the very good position resolution, the laser is operated in a pulsed mode which allows a timing resolution in the order of $50\,$ps. The pulse repetition rate as well as the intensity of the laser can be continuously adjusted with the help of an external

87

attenuator and an external frequency generator that triggers the laser.

The translation stages can be moved manually with a joystick or via a LabVIEW acquisition program that automatically handles the entire measurement. For most of the testing, an oscilloscope was used but the setup could also be used with different readout hardware. One disadvantage of the stepper motors is their tendency to emit electromagnetic noise inside the metal box even during stand-by. This noise can be strong enough to influence the signal shape and thus disturb the measurement. A remotely controllable (i.e. by the LabVIEW acquisition software) socket outlet, programmed to power down the motors before each data taking, was used as a countermeasure to guarantee a smooth acquisition.

As with all measurements with MCP-PMTs it is ideal if all anodes which are not connected to a readout can be grounded via a resistor that has the same resistance as the input of the readout. However, for many testing purposes it also suffices to ground neighboring anodes. This measure prevents worsening of the imaging characteristics caused by charge buildup.

It is also important to operate the laser in single photon mode. Unfortunately, due to the quantized nature of light, it is not possible to generate light pulses that always expose a sensor under test to the exact same number of photons on each repetition. The number of photons that impinge on the sensor (and are subsequently registered with a certain probability) follow a Poissonian distribution. An optical attenuator, which can be used to reduce the amount of incident light, can only influence the mean number of incident photons. In other words: The shot noise of the light source can lead to laser pulses containing 0, 2, 3 or even more photons even if the average number of photons λ is exactly 1. The corresponding probability is given by a Poissonian with mean λ.

For completeness, it should be explained why an attenuator, the finite detection efficiency of the MCP-PMT or any other device that has a certain probability of absorbing single photons does not disturb the Poissonian nature of the amount of *detected* photons. Why are we still left with a Poissonian distribution after attenuating the light and losing a certain fraction during the detection process? This can be worked out rather quickly: Let's assume that the pulsed light source emits λ photons on average and that the number of photons in each pulse n follows a Poissonian distribution:

$$P_{\text{laser}}(n) = \frac{\exp(-\lambda)\,\lambda^n}{n!}. \tag{5.1.1}$$

If we now consider one photon, let's assume that its probability of getting through the

attenuator, entering the front glass of the sensor, being converted into a photoelectron and being amplified and measured afterwards is given by p. This means that - if n photons are sent towards the MCP-PMT - the probability of k photons being detected is given by a Bernoulli distribution

$$P_{\text{detect}}(n,k) = p^k \, (1-p)^{n-k} \, \frac{n!}{k! \, (n-k)!}.$$ (5.1.2)

To get the total probability of detecting k photons, we must consider all $n \geq k$, specifically:

$$P_{\text{det}}(k) = \sum_{n=k}^{\infty} \frac{\exp(-\lambda)\lambda^n}{n!} p^k \, (1-p)^{n-k} \, \frac{n!}{k! \, (n-k)!}$$ (5.1.3)

$$= \sum_{n=k}^{\infty} \frac{\exp(-\lambda) \, p^k \, \lambda^n \, (1-p)^{n-k}}{k! \, (n-k)!}$$ (5.1.4)

$$= \frac{\exp(-\lambda) \, p^k}{k!} \sum_{n=k}^{\infty} \frac{\lambda^n (1-p)^{n-k}}{(n-k)!}$$ (5.1.5)

$$= \frac{\exp(-\lambda) \, p^k}{k!} \exp[\lambda \, (1-p)] \, \lambda^k$$ (5.1.6)

$$= \frac{\exp(-\lambda \, p)(\lambda \, p)^k}{k!} = \frac{\exp(-\hat{\lambda})(\hat{\lambda})^k}{k!}.$$ (5.1.7)

We found that the resulting distribution is indeed Poissonian again. $\hat{\lambda}$ is now the average number of *detected* photons. For this reason, it is also impossible to measure the detection efficiency without a calibrated light source. However, as far as this work is concerned, the term *single photon intensity* is defined by an intensity that will only lead to a measurable output in less than 1 out of 10 repetitions. In the mathematical framework it could be stated like

$$P_{\text{det}}(k=0) \geq 90\% \Leftrightarrow \hat{\lambda} \leq \ln(10/9).$$ (5.1.8)

The advantage of this tight requirement is that the data will have a negligible contamination of events where more than one photoelectron has been amplified. The downside is that 90% of the pulses will not create meaningful data. The upper limit on *multi photon events* can be derived to be

$$P_{\text{det}}(k>1) = 1 - P_{\text{det}}(k=0) - P_{\text{det}}(k=1) \leq 1 - 0.9 - 0.9 \times \ln(10/9) \approx 0.5\%.$$ (5.1.9)

If we assume realistic values for the QE and CE of an MCP-PMT, e.g. QE $= 0.2$ and

$CE = 0.65$, it follows for the average number of photons in one laser pulse (λ):

$$\lambda = \frac{\hat{\lambda}}{QE \times CE} \leq 0.81. \tag{5.1.10}$$

This entire procedure is certainly based on the assumption that all sensors are actually capable of detecting single photons (i.e. $QE \times CE \sim 0.1$). For the intensity tuning, it is also very important to know where exactly the laser hits the sensor. Ideally the spot hits exactly above a set of anodes that are read out. In this case the entire charge of the multiplication can be caught and no amplified photoelectron is missed.

First results which have been measured with this setup have been published in [55]. The setup is well suited for quick testing (e.g. of newly acquired models) of MCP-PMTs without applying any magnetic fields. The latter is not possible in this setup because the translation stages use magnetic switches to detect their end position. If the stages are placed in a comparably weak magnetic field, the switches are already permanently activated. Apart from this, the manufacturer could not guarantee flawless functioning of the electric motors in magnetic fields. For these reasons special test stands with the possibility of applying external magnetic fields have been designed and are presented later in this chapter.

One example of a measurement with the automated setup can be seen in figure 5.5. It shows the count rate of two neighboring anodes of the Photonis device.

5.1.3 Test stand with permanent magnets

As explained in section 3.3, an external magnetic field is expected to shrink the footprint of the charge cloud on the readout plane of the MCP-PMT. To the author's knowledge, no elaborate theoretical or numerical treatment of such a scenario is available that claims to predict the focusing effect quantitatively with sufficient accuracy. However, the effects of magnetic fields (also on the position resolution) have been studied for different sensors in the past [43] [46] [57] [58]. The first step towards applying a magnetic field to the sensor during a measurement was taken by using permanent neodymium magnets with dimensions of $65^2 \times 30 \, mm^3$. A CAD schematic of the box that was used for holding the test setup for permanent magnets can be seen in figure 5.6. All major components of the test stand are mounted to the bottom plate of the box with multiple screws to prevent any movement. A special assembly piston was designed, built and attached to the setup. It can guide the magnets into their position in the machined aluminum frame.
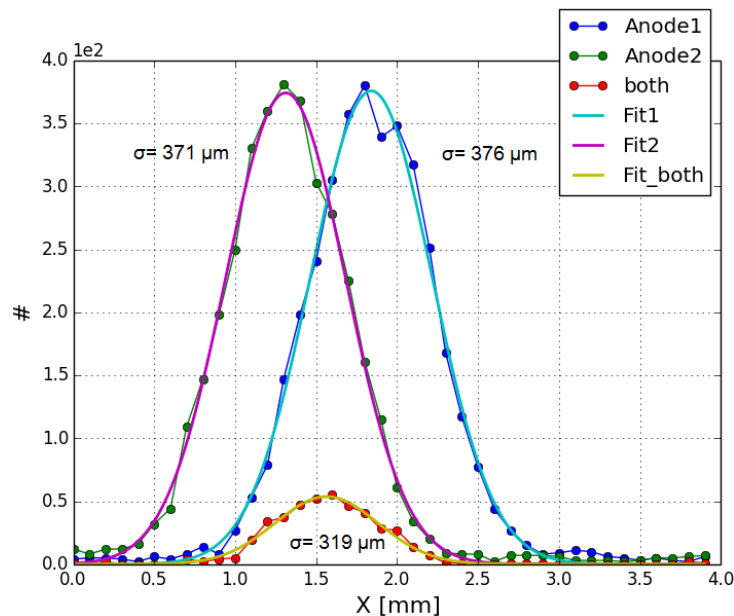
Figure 5.5: The figure shows the amount of hits above threshold for a scan of the Photonis device in the automated test setup supplied with 2450 V. It also shows the count rate for both anodes exceeding the threshold in one event. All three distributions are fitted with Gaussian functions and the widths are displayed. By looking at the intersection of the curves at about 1.6 mm, it can be seen that the probability of both anodes firing simultaneously is not given by the combined probability of both anodes firing individually. These results will be confirmed later with the test setup with permanent magnets.

The repelling force between the magnets during the assembly would otherwise be too strong to allow joining the components by hand. In addition, the danger of two magnets turning and suddenly attracting each other is avoided. Clashing magnets of this strength (over one ton of force equivalent once they touch) can send small metal fragments flying upon collision or squeeze fingers or hands. Once assembled, the two magnet walls can be fixed in 6 (2×3) different positions, each of which giving a different magnetic field strength at the place of the sensor mount between both walls. In the absence of any sensor, the magnetic field at the location of the MCP-PMT mount was measured with a Hall probe for each of the 6 different settings of the magnet walls. 24, 33, 34, 43, 55 and 65 mT can be set. The homogeneity of the magnetic field is not as good as the one of a large electromagnet because there are still gaps between the four permanent magnets which are occupied by the aluminum holding structure. However, the magnitude of the field varies only by some mT over the surface of a $50 \times 50 \, \text{mm}^2$ tube. The rectangular front and back faces of the aluminum box feature feedthroughs for high voltage cables and an optical fiber. The longer side plates can be equipped with machined plastic or metal adapter plates. They hold PCBs for routing electronic signals from the MCP-PMT to a dedicated readout system outside the box. Alternatively, 4 LEMO connectors can
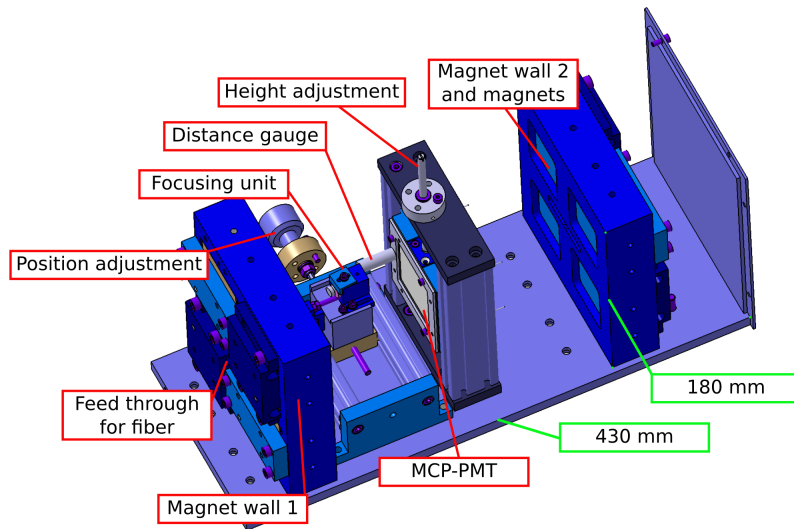
Figure 5.6: Setup of the test stand for permanent magnets. Two walls hold a total of 8 permanent magnets with surface fields above 500 mT. More details of this setup are given in the text. The figure was also published in [31].

be used to quickly examine pulses on an oscilloscope. In order to illuminate the sensor with the PiLas, a mount for the optical focusing unit has been accommodated between the magnet walls. Both walls have a hole in the center which can be used to guide the fiber through from both directions. Unlike the automated setup (figure 5.3), the working distance of the optical system cannot be adjusted (and then optimized) during an active measurement. For this reason, distance gauges have been individually machined for each sensor that was tested in the setup. They can be placed between the mount of the optical system and the frame that holds the MCP-PMT. The laser head can then be moved until both faces touch the gauge. After fixing the laser in this particular distance, the user can be sure to operate at the correct working distance.

After all the aforementioned preparations are done and the light intensity is correctly adjusted, the box can be closed to make the setup light tight. The MCP-PMT can be supplied with high voltage and the signals can be analyzed. In order to perform a scan, two screws can be used to either drive the optical stage (horizontal scan) or the MCP-PMT holding frame (vertical scan). Measurements with different magnetic fields and with both sensors have been performed. Firstly, the results obtained with the oscilloscope will be presented. These results have also been published in [31]. Secondly, the performance of the Photonis device when read out with the TOFPET evaluation kit is shown. Unfortunately, the Hamamatsu prototype became unusable after an internal component loosened during transportation. As a result, no TOFPET data has been taken with the Hamamatsu

R13266-07-M768.

5.1.3.1 Hamamatsu prototype with permanent magnets

In this experiment two neighboring anodes of the Hamamatsu device have been read out with an oscilloscope that was connected via a custom cable assembly. Standard LEMO cables were soldered to mating sleeves that could be attached to the pins on the backside because the PCBs (as shown in chapter 4) were not yet available. The neighboring anodes were grounded via resistors. All scans were done with a high voltage of 3.4 kV. Figure 5.7 shows the results of the measurements. A total of 5 different field strengths have been chosen. The first scan was done without any magnets installed into the setup. Afterwards, the field strength was gradually increased from 24 mT up to the maximum of 65 mT. The field could not be increased further, because the space between both magnet walls was completely used by the sensor and the required cabling. The only way to increase the magnetic field strength beyond 65 mT is to use stronger permanent magnets or to use an electromagnet. The latter was done to produce B-fields up to 800 mT in the next iteration of the testing. However, the expected effects, like image shifts, changes in detection efficiency, and a decreasing size of the charge cloud footprint, that have been discussed in section 3.3 can already be observed in this setup.

Figure 5.8 shows how the pulse amplitudes of both anodes vary when the laser spot is scanned across both anodes for a magnetic field of 65 mT. As the output pulses are really fast (< 1 ns) and the high voltage is at its maximum of 3.4 kV, the pulse amplitude is much bigger compared to the Photonis device. From studying figures 5.7 and 5.8 we can already infer that the Hamamatsu device can deliver very good position resolution (well below the pixel width) with the given parameter settings. The reason is that the charge is spread over multiple anodes but it also carries enough electrical charge to create measurable pulses on them. This means that the relative amount of charge collected by the individual anodes can be calibrated against the position of impact of the photon. Once this is done, event-based reconstruction of single photon hits can be done.
The simplest algorithm to reconstruct the impact position of single photons for each light pulse is linear weighting of the amount of charge collected by all anodes, like:

$$x_{\mathrm{rec}} = \left(\sum_{i=1}^{N} x_i \, C_i \right) / \left(\sum_{j=1}^{N} C_j \right) \qquad (5.1.11)$$
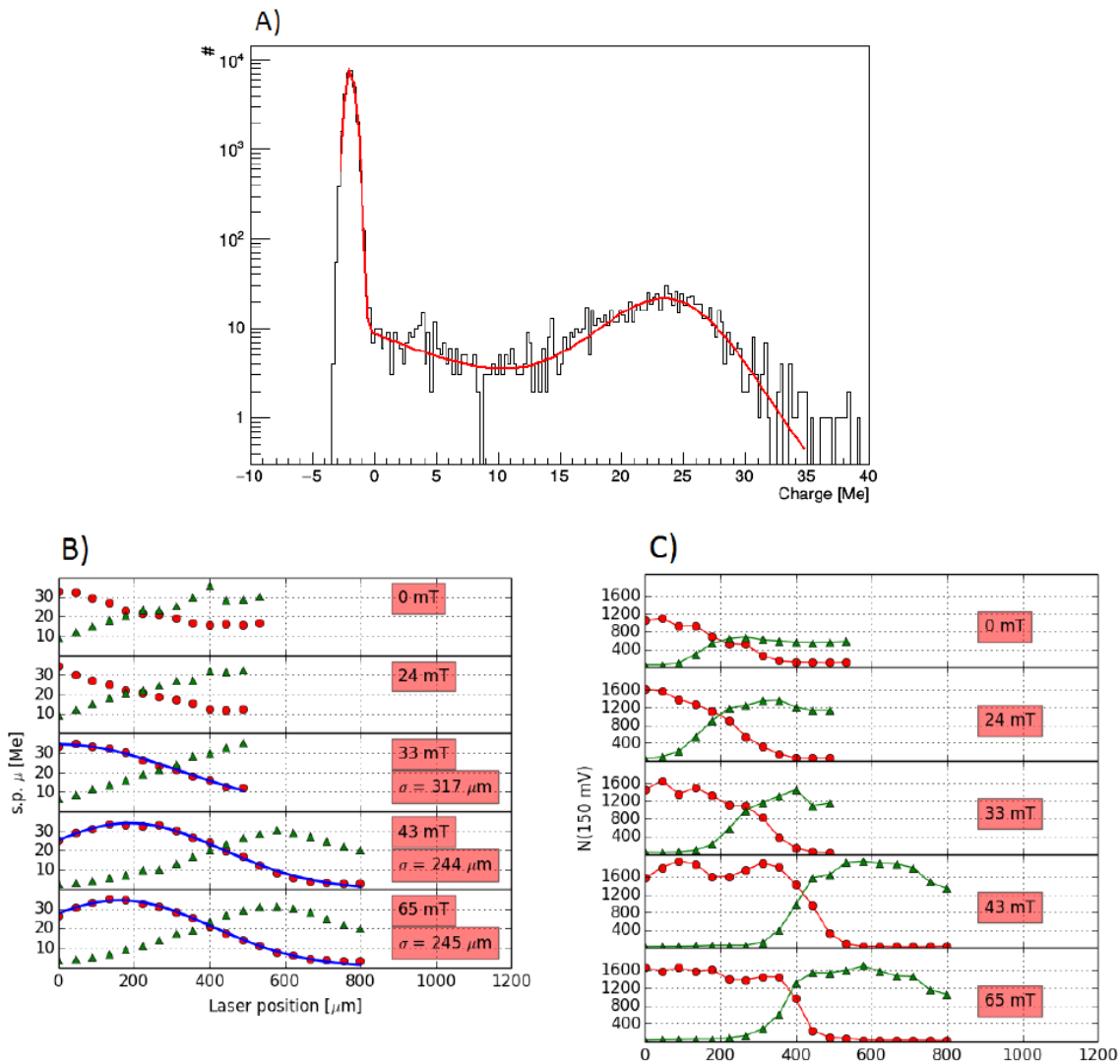
Figure 5.7: A shows a typical charge spectrum of one anode, recorded at one given position and a given magnetic field. 30,000 pulses have been recorded at each individual setting. This spectrum is fitted with the sum of two Gaussian functions and an exponential function. The two Gaussian functions model the pedestal peak and the single photon peak. The exponential function describes the transition between both peaks and improves the goodness of fit. Each spectrum at a given laser position and a given magnetic field is fitted. The difference between the mean of the pedestal peak and the mean of the single photon peak is extracted. This difference is shown against the position of the laser spot in **B**. The green and red curves in **B** and **C** describe one of the two anodes, respectively. Additionally, the last 3 curves in **B** have been fitted with a Gaussian function again and the width is displayed. Graphic **C** shows the total number of waveforms exceeding a threshold of 150 mV at each setting. It can be seen that increasing magnetic field strengths improve the detection efficiency in this measurement. However, no increase in the overall gain can be inferred because the maxima of the curves in **B** are always around 30 Me. Image shifts due to non-perpendicular magnetic field lines can also be seen by tracing the point of intersection of both curves in **B** and **C**. This figure is also published in [31].
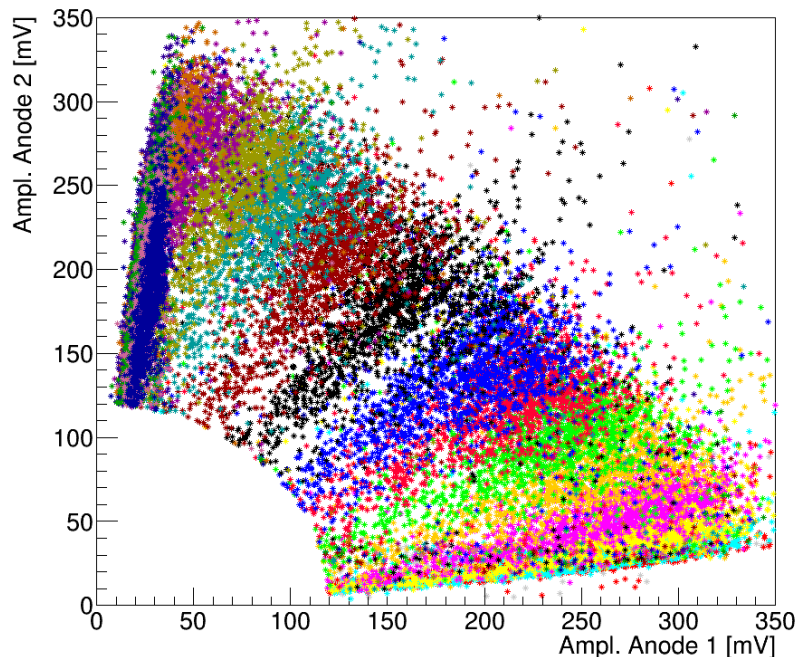
Figure 5.8: Amplitude distributions of a position scan of two neighboring anodes for the Hamamatsu MCP-PMT: Each color corresponds to one particular position of the laser spot. If $\sqrt{A_1^2 + A_2^2} > 120\,\mathrm{mV}$ in a given event (A_1 and A_2 being the amplitudes of the signal of anode 1 and anode 2 respectively), a marker is set in the graphic. The slope of the lines corresponds to the amount of charge sharing. This measurement was done at a field strength of $65\,\mathrm{mT}$ with permanent magnets. The lines corresponding to the measurements in the middle of both anodes (blue, black and brown) are separated more clearly because the charge sharing between the two active anodes is maximized. However, this effect can only be used if both anodes receive sufficient charge to output a measurable pulse.

x_rec is the reconstructed position of impact of the photon. N is the number of active anodes that are involved in the reconstruction process. The C_i are the charges collected by the ith anode and the x_i are the positions of those anodes. More elaborate reconstruction methods could make use of likelihood estimation techniques or lookup tables for the dependence of the charge distribution on the impact position of the photon. Likelihood calculations are computationally relatively expensive. Just like the lookup table approach, they also need calibration beforehand, which is a smaller problem for the operation at PANDA. However, the question of the reconstruction technique only becomes important if more than one anode is usually involved in the reconstruction. This is really only the case for the Hamamatsu device. The Photonis device that was tested in the same setup has a significantly smaller number of active anodes. Once a significant magnetic field is applied, only one anode outputs a measurable pulse in the majority of events (see figures 5.5 and 5.12).
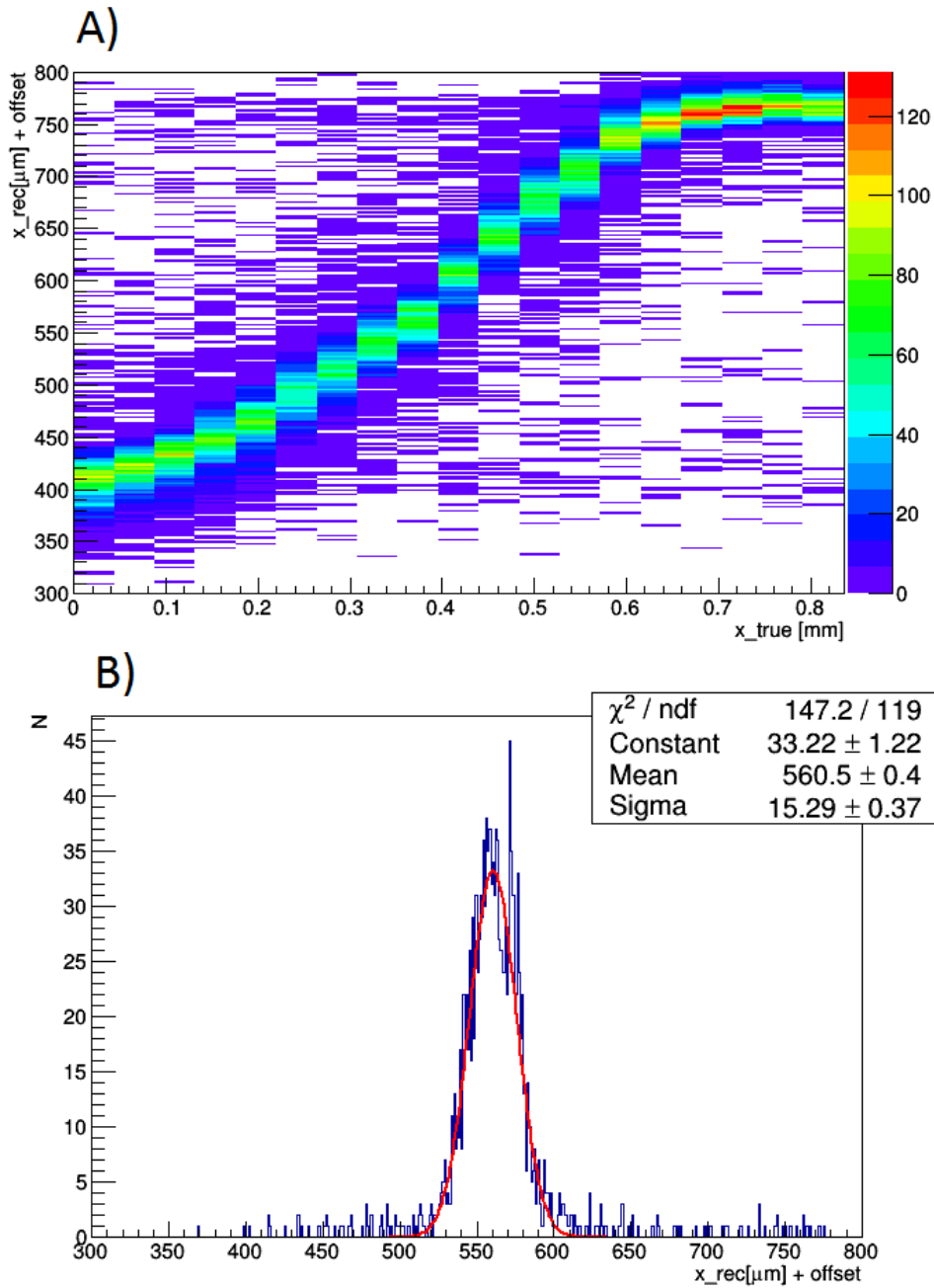
Figure 5.9: Reconstruction of the laser data taken with the Hamamatsu MCP-PMT at 65 mT: **A** shows the reconstructed positions of photon impact calculated with equation (5.1.11) for the scan at 65 mT. A reconstruction was only done if at least one of the anodes exceeded the threshold of 150 mV in this particular event. This behavior and the shape of **A** are consistent with results published in [59]. **B** shows one central column of **A** which has been fitted with a Gaussian function. A very narrow width below 16 μm has been obtained. The figure is taken from [31].

The result of the reconstruction of the 65 mT data can be seen in figure 5.9. At first sight, a position resolution of below 20 μm looks really promising. However, we have to remind ourselves that an increased number of active pixels translates into more data traffic. Additionally, the rate capability of the MCP-PMT will even become worse with an increased gain (as more charge has to be provided for each individual amplification) as explained in section 3.3. It is important to find a point of operation where all requirements are fulfilled simultaneously. Nonetheless, the results show how accurate the position could be reconstructed with these devices if some of the other requirements could be relaxed.

5.1.3.2 Photonis prototype with permanent magnets

In the next step, the Photonis MCP-PMT was tested in the setup. This time four anodes were read out and more laser positions were included in the scans. A cable assembly with LEMO coaxial cables and appropriate mating sleeves was used and the neighboring anodes were grounded via resistors. Like before, the laser intensity and the distance between the sensor and the focusing optics were adjusted and the signals were read out with a fast oscilloscope. 15,000 laser pulses were recorded at each combination of laser position and magnetic field. An overview of the count rate as a function of these two parameters is given in figure 5.10. In this measurement one can clearly see the collimating effect of the magnetic field on the charge cloud footprint and also on the improvement of the position resolution. This property is further illustrated in figure 5.11. It can be seen that the width of the count rate curve narrows down by about a factor of 2 at 30 mT already. Like in the case of the Hamamatsu device, single events were reconstructed according to equation 5.1.11 if at least one anode exceeded a given threshold, 15 mV in this case. An example for 65 mT is given in figure 5.12 which is similar to figure 5.9. From comparing both figures it becomes clear that less charge sharing can be observed with the Photonis tube. It is also interesting to compare the results of the reconstruction for different strengths of the magnetic field. In order to do so, the mean and the standard deviation of the distribution of reconstructed positions (i.e. the columns of figure 5.12) can be computed and compared for different magnet settings. The upper plot in figure 5.13 shows these numbers without any magnetic field applied to the sensor. The lower plot shows the same when the magnets are as close to the sensor as possible, which results in a magnetic field of 65 mT. In the region between about 1 and 3 mm the four anodes can reliably catch the entire charge cloud of the multiplied photoelectrons and the reconstruction is meaningful. Outside this region, a significant fraction of the charge will be collected by grounded anodes. One can
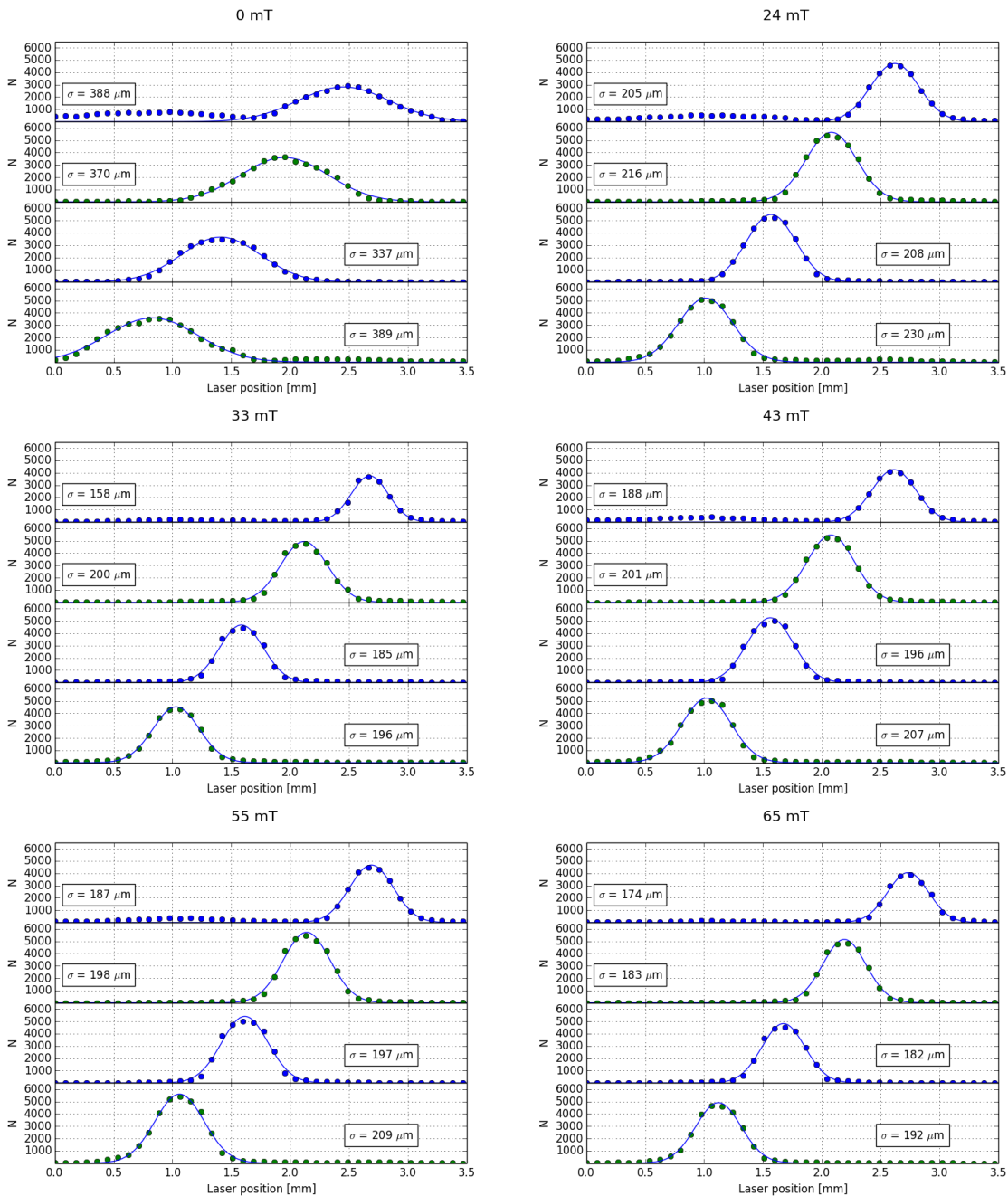
Figure 5.10: Count rate as a function of magnetic field and laser position for the Photonis MCP-PMT in the setup with permanent magnets: The magnetic field was increased gradually from 0 to 65 mT by means of moving the magnet walls closer to the sensor. 15.000 events were recorded at each position and each magnetic field setting. The number of waveforms exceeding the threshold of 20 mV has been plotted against the position of the laser spot for all four anodes. This threshold was chosen in order to isolate single photon events after an inspection of the amplitude distributions. The resulting curves have then been fitted with a Gaussian function and the width of the best fit is displayed. One can already see by eye that the distributions narrow down significantly when a small field of 24 mT is introduced. The dependence of the width on the strength of the magnetic field is shown in figure 5.11.

see that the RMS of the reconstructed position improves by about a factor of 3 if the laser is centered over one anode. If the laser shines between two anodes the RMS is worse because in many cases one of the single anodes will fire separately which results in a wide distribution as can be nicely seen again in figure 5.12. This feature becomes also clear in the step-like shape of the curve of means for 65 mT compared to a much smoother curve for 0 mT. The comparison reveals that stronger magnetic fields really tend to improve the
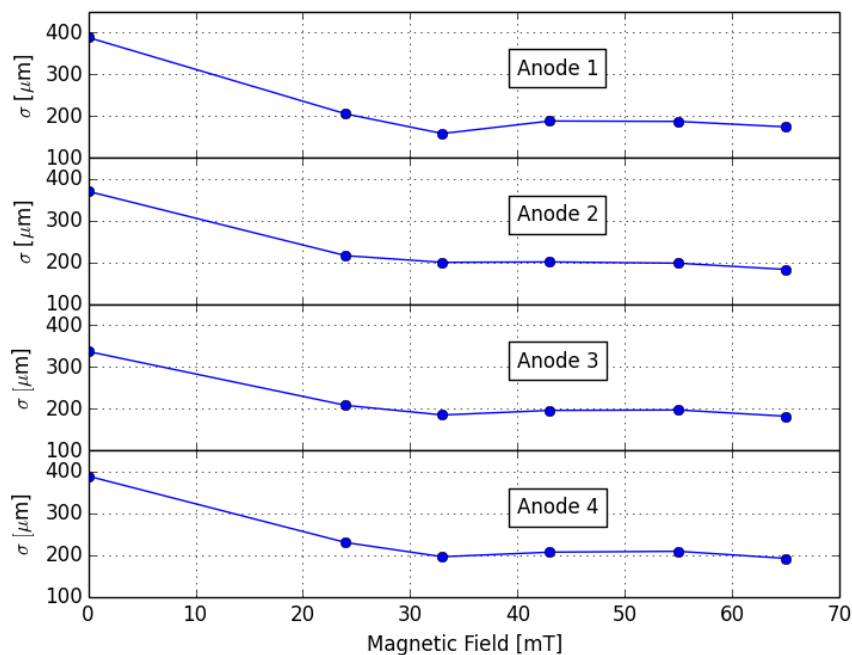
Figure 5.11: The width of the count rate curve as a function of the magnetic field for four neighboring anodes of the Photonis MCP-PMT: The widths of the curves from figure 5.11 are shown as a function of the magnetic field created by the permanent magnets. It can be seen that all four anodes reach a plateau at about 30 mT and no more significant compression of the charge cloud footprint could be observed in this measurement.

position resolution because the collimation of the charge cloud overpowers the benefits of charge sharing in this particular setup. This behavior has been anticipated in the design of the EDD as stated in [21], which is why the custom anode layout of the Photonis device has been chosen to have this exact geometry.
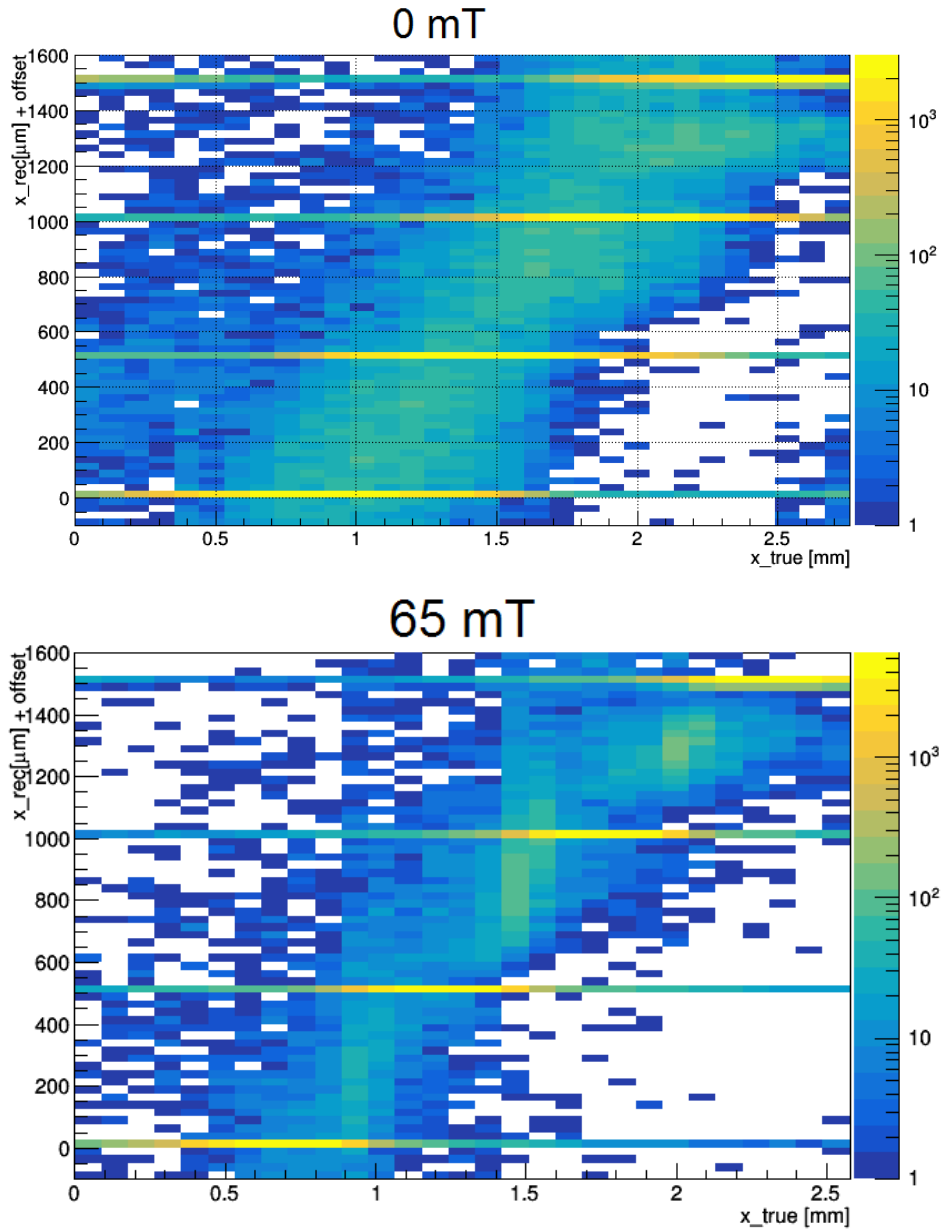
Figure 5.12: Reconstructed impact positions at different field strength for the Photonis MCP-PMT: The upper plot shows the reconstructed position versus the true point of impact of the photon (e.g. the laser position) without any magnetic fields applied. The lower plot shows the same at 65 mT. The horizontal lines in both plots represent events where only one single anode was triggered by the photon. Comparing both images shows how the entire distribution is compressed by an external magnetic field.
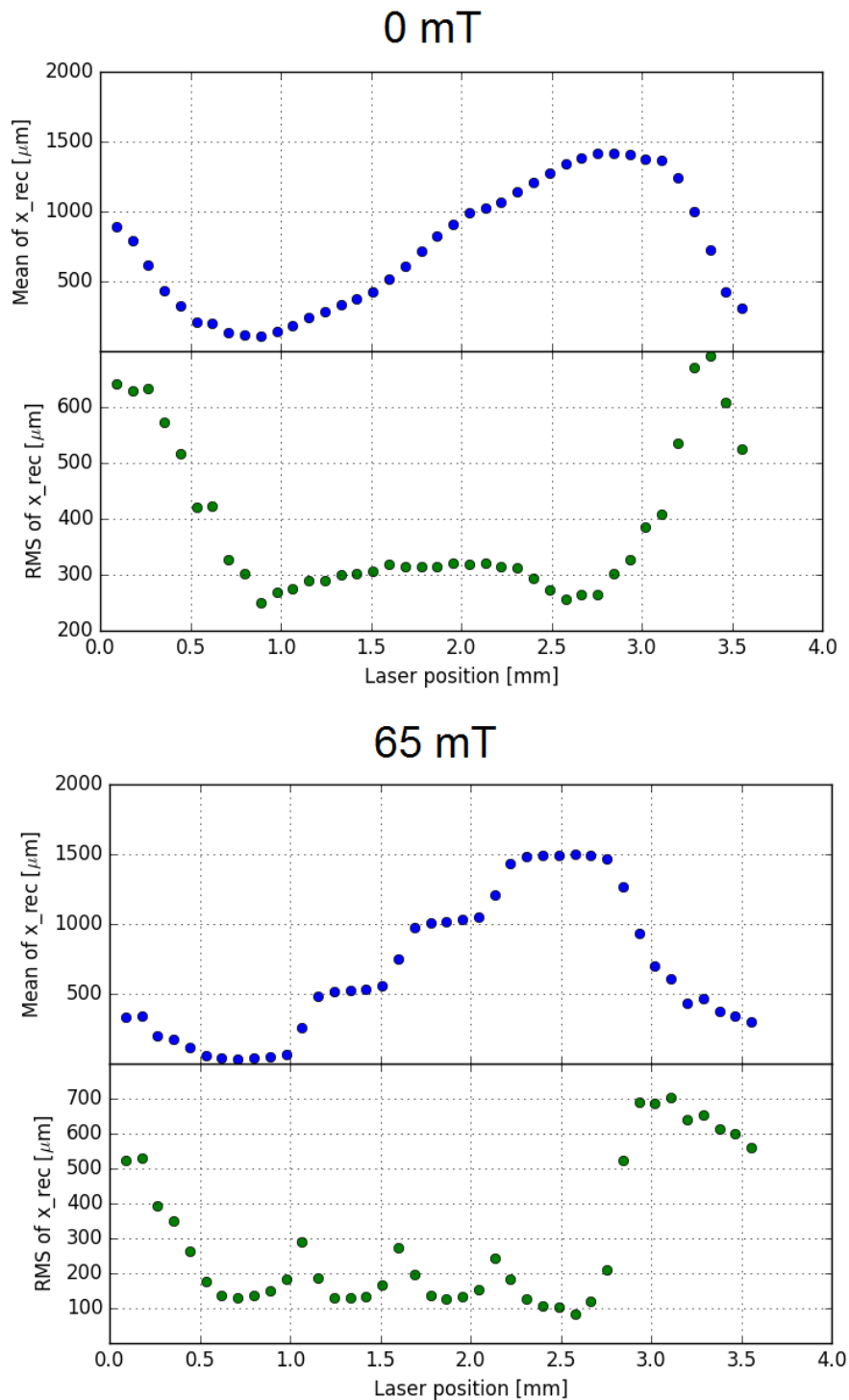
Figure 5.13: Comparison of reconstructed events at 0 and 65 mT for the Photonis MCP-PMT. The blue data points (in the upper part) show the mean of a given distribution of reconstructed impact positions at a given magnetic field. The green points (in the lower part) show the corresponding RMS. Due to reduced charge sharing in stronger magnetic fields, the impact positions are more often reconstructed by only one active anode, leading to a more step-like appearance and less variations in the reconstruction (lower RMS). The reconstructed points outside the range from 1 to 3 mm are not meaningful because a notable amount of the charge cloud is caught by neighboring anodes which are not included in the reconstruction.
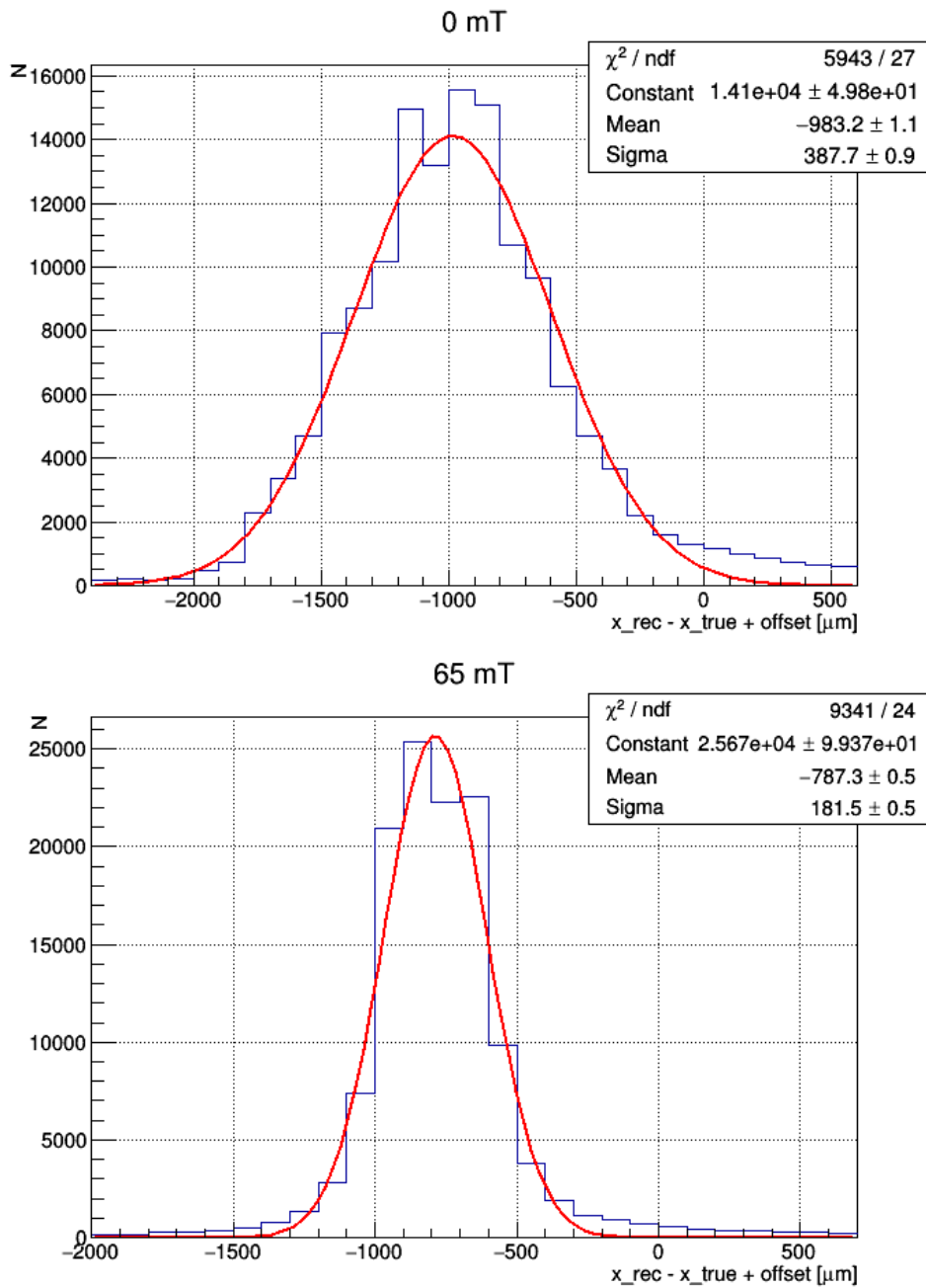
Figure 5.14: The difference between reconstructed and true photon impact position at different magnetic fields for the Photonis MCP-PMT: An alternative measure for the position resolution can be obtained by evaluating $x_{\text{rec}} - x_{\text{true}}$ for the entire scan at a given magnetic field. The width of this distribution can be thought of as the mean deviation of single events from the diagonal of figure 5.12. Both figures show this distribution for the scans at 0 and 65 mT and a reduction from about 388 to 182 μm (σ) can be seen.

Another approach to quantify the position resolution is to reconstruct the difference between the reconstructed impact position and the laser position. The result of this technique can be seen in figure 5.14. The width of the corresponding distribution narrows from 388 to 182 μm after switching from 0 to 65 mT. From these results, it follows that the ideal setup is one where the magnetic field influences the imaging of the tube in such a way, that almost all photons only trigger one anode. The only case where this is not realistic, is if the photons strike the transition region between two anodes. However the size of this region also depends on the size of the charge cloud and becomes smaller with increasing field strengths. Consequently, the logical continuation is to reproduce these measurements with stronger magnetic fields and close to final readout electronics. This step was carried out and will be presented in section 5.2.

5.1.4 Testing of the quantum efficiency

Before advancing to the combined testing of the MCP-PMTs and the TOFPET ASIC readout, the following section will present some more characterizations of the sensors alone. Firstly, the quantum efficiencies (QE) of both MCP-PMTs have been measured with a dedicated setup in Erlangen [48]. The opportunity to use the existing setup was kindly provided by the group of Dr. Albert Lehmann. The test stand is also used for the MCP-PMT lifetime measurements that have briefly been discussed in section 3.3. The basic functioning of the setup is illustrated in figure 5.15. It allows to measure the spatial dependence of the quantum efficiency by a direct measurement of the photo current between the photocathode and the input terminal of the MCP inside the MCP-PMT. To calibrate the luminous flux and correct for the fluctuations of the laser output, a photodiode is included in the setup. During an active measurement the laser head scans the surface of the photocathode. At each position of the laser, a current measurement is performed. From time to time the laser head is positioned in front of the reference diode to monitor the light intensity. In addition, dark current measurements are done for both the MCP-PMT and the diode. At each measurement the dark current is subtracted from the current which is measured under illumination. Once the luminous flux is known, the QE can be calculated from the photo current of the photocathode and the MCP input. It should be noted that all measurements are done at the same wavelength of 372 nm. The entire measurement takes several hours and has been done overnight for each sensor. The results for the Hamamatsu device shown in figure 5.16 reveal an interesting circular shaped feature in the QE of the photocathode. This structure can also be seen by eye
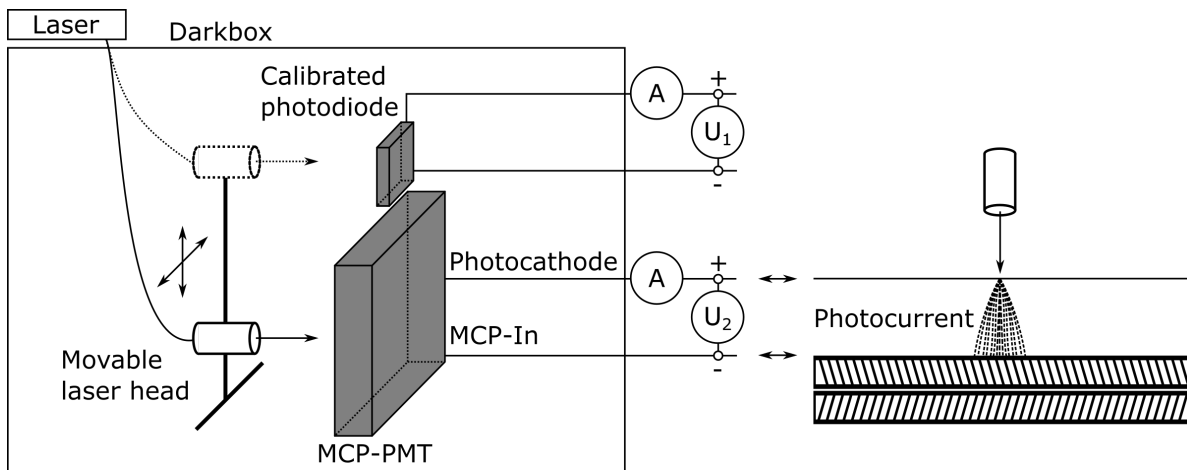
Figure 5.15: Schematic of the test stand to measure the spatially resolved quantum efficiency of MCP-PMTs: Inside a dark box the MCP-PMT and a calibrated photodiode are illuminated with a light source which is mounted on translation stages. Two picoamperemeters measure the photo current of the photodiode and MCP-PMT. There are also two voltage sources. One applies a bias voltage for the operation of the diode and the other one supplies a voltage between the photocathode and the MCP-input terminal.

(even in the photograph in figure 5.1). The origin of this circle, which has also been observed at other sensors of this series, is unknown.

The measurement of the Photonis MCP-PMT also shows an interesting structure, which can be seen in the upper left corner of figure 5.17. The QE is degraded around the HV connectors. This inefficiency could be caused by the welding of the HV cables that was done to replace the nickel ribbons which are the standard HV connection for Planacon MCP-PMTs. This seems plausible as the corner where the degradation is observed coincides with the location where the customization of the HV connections was done. Apart from that, no abnormalities in the distribution are observed. In addition to the spatial dependence of the QE it is also interesting to measure the spectral dependence, i.e. the QE as a function of the wavelength of the incoming light. This measurement has also been done in a second test setup in Erlangen. Figure 5.18 illustrates how the measurements are performed. In principle, the spectral QE measurement is very similar to the one of the spatial dependence of the QE at a fixed wavelength. The only difference is, that this time the wavelength is altered but the light impact position on the photocathode is fixed. The various wavelengths are selected with a monochromator which consists of a rotatable diffraction grating and an aperture. A gas lamp is used to create light with a wide range of wavelengths. The wavelengths of interest are filtered out by a monochromator with a spectral resolution of about 1 nm. Before the start of a measurement, the lamp is warmed up for about an hour. After that, the emission spectrum is constant and can be
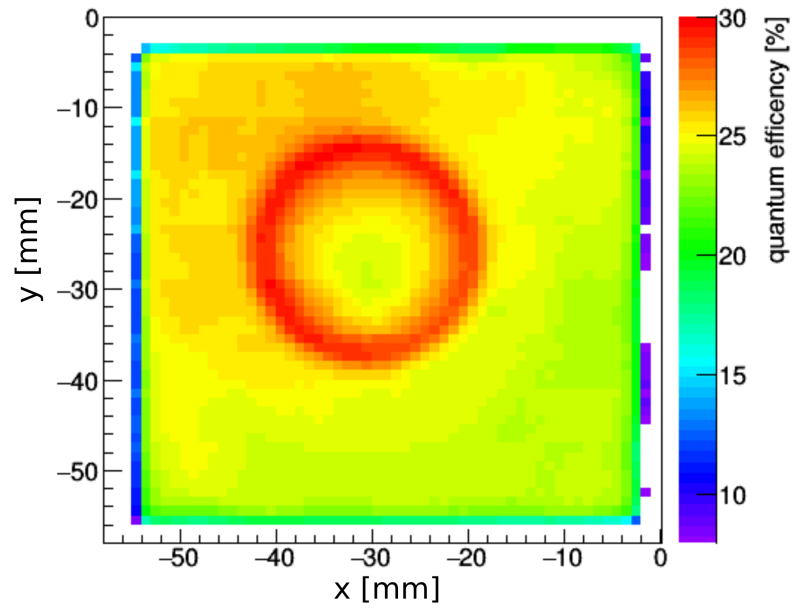
Figure 5.16: Spatial dependence of the quantum efficiency of the Hamamatsu MCP-PMT prototype: Most of the active area of the sensor has a QE between 20 to 25 %. However, the measurements revealed that a circular region on the photocathode shows an increased QE which goes up to about 30 %. The origin of this shape could not be clarified. Upon close examination of the sensor, this circular region can be seen through the front glass, even on the photograph in figure 5.1.
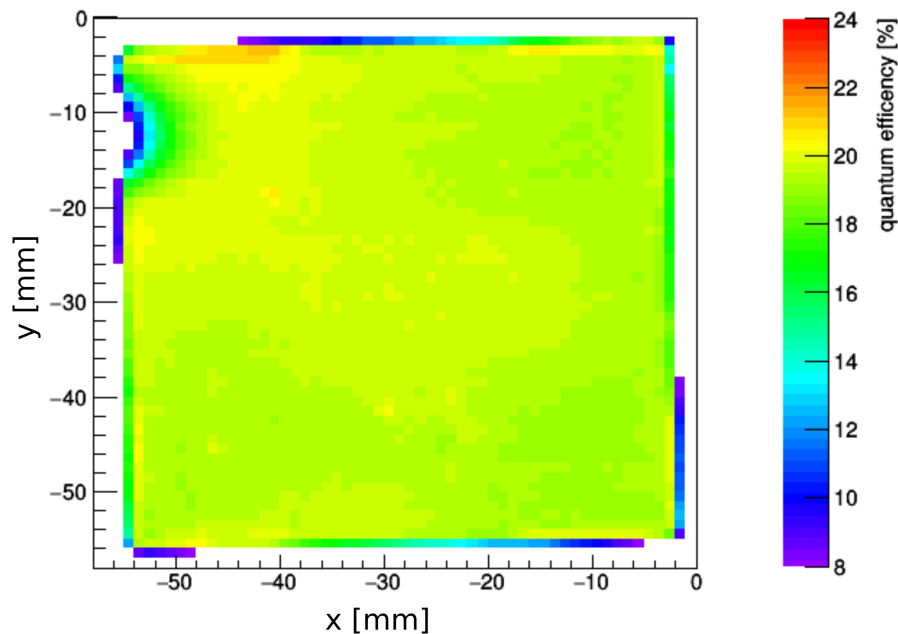
Figure 5.17: Spatial dependence of the quantum efficiency of the Photonis MCP-PMT prototype: This sensor shows a QE that varies only very slightly around 20 % over the full active area. Interestingly, the QE is decreased around the region where the HV supply cables have been welded.
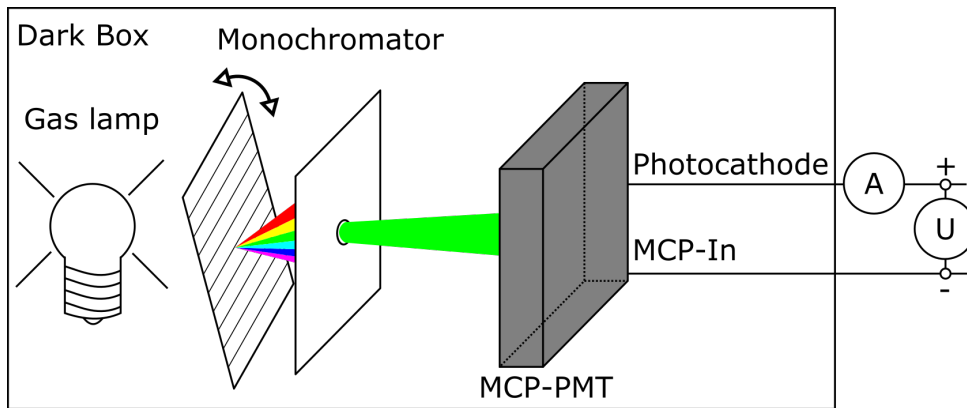
Figure 5.18: Simplified illustration of the measurement of the spectral response of the photocathodes of the MCP-PMTs.

measured with the reference diode. Once this calibration is done, the reference diode is replaced with an MCP-PMT and the photo current is measured. All wavelengths impinge the photocathode on the same area. By knowing the luminous flux for each wavelength from the reference measurement with the diode, the spectral QE can be calculated from the measurement of the photo current. The spectral sensitivity of both prototypes, as measured with the setup explained above, are shown in figure 5.19.

5.1.5 Radiation hardness of entrance windows

All (optical) components of the EDD have to withstand the radiation environment in PANDA. Glasses for the construction of the larger optical components of the detector - such as radiator, prisms and FLGs - have been tested for their radiation tolerance rather rigorously [54]. However, the front glasses of the MCP-PMTs have to be radiation hard as well, even if the photon readout is not as exposed as the central part of the radiators due to shading of the EMC. In order to introduce an additional quality check, a setup for radiation induced loss of transparency has been built and tested with glass samples provided by Photonis.

In this test setup, the glasses are fixed in an optical mount that can be placed inside a photospectrometer (see figure 5.20). The setup needs at least an hour of warm-up time, just like the setup for the measurement of the spectral QE from the last section. Once it is ready to use, the first step involves a measurement of the geometric acceptance of the holding mount of the glass samples. It can be performed by simply placing the blank (i.e. no glass inserted) holding mount in the apparatus and running a measurement. All later measurements will be referenced to this one in order to correct for light being
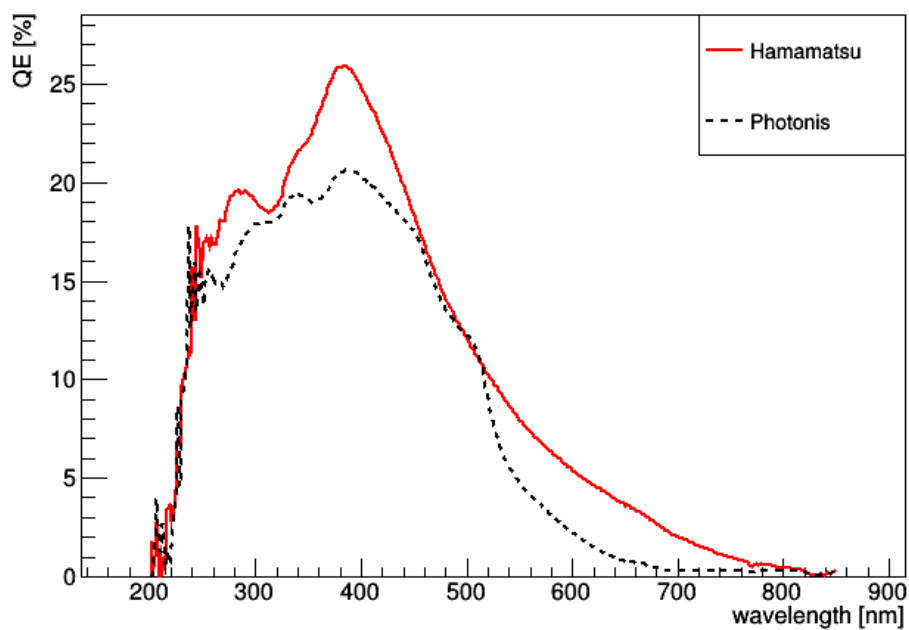
Figure 5.19: Spectral sensitivity of both MCP-PMT prototypes. A more detailed description of the test setup can be found in [49].

Figure 5.20: Holding structure and four packaged entrance window samples (fused silica and sapphire) for the test of radiation induced loss of transparency.

absorbed by the mechanical structure. This measurement has to be repeated each time the setup is switched off and on again in order to correct for long term variations.

In the next step all glass samples have been measured individually for their spectral transmission and those measurements were referenced to the one with just the holding structure in the beam. The wavelength range that was used for the testing spans from 195 nm to 605 nm. The step width is again 1 nm. In order to correct for losses due to the reflection of the light on the glass surfaces - when entering and leaving the glass sample - it is necessary to apply a correction (figure 5.21). These corrections can be calculated with the well known FRESNEL and the SELLMEIER formulas: For the special case of perpendicular incidence, the reflection coefficient R just depends on the refractive indices of the two media which the light has to pass through. R can be understood as the fraction of the light intensity that is reflected during the passage of the light through one optical interface. We can calculate R as follows:
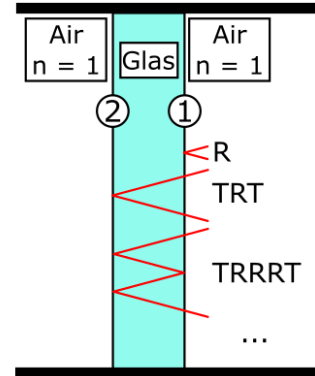
Figure 5.21: Sketch of the photospectrometer setup with two optical interfaces that reflect incoming light.

$$R = \left| \frac{n_1 - n_2}{n_1 + n_2} \right|^2 \qquad (5.1.12)$$

where n_1 and n_2 are the refractive indices of the two media. Notice that for perpendicular incidence, the two indices can be exchanged with each other. That means that the interface from the air to the glass sample reflects the same fraction of the incoming light as the interface from the glass back to the air. However, as sketched in figure 5.21, there is an infinite number of possible reflection paths that can occur. Surely, it would be sufficient to just take the first leading orders into account but the final result is actually simpler when all paths are accounted for. Apparently the total reflectance ($\mathfrak{R}$) of the glass sample is

$$\mathfrak{R} = R + (1 - R)^2 \underbrace{\sum_{n=0}^{\infty} R^{2n+1}}_{R \div (1 - R^2)}. \qquad (5.1.13)$$

This can be further simplified

$$\mathfrak{R} = \frac{2R}{1 + R}. \qquad (5.1.14)$$

Assuming an initial intensity I_0 impinging on the glass sample, the photospectrometer

would measure the intensity

$$I_{\mathrm{M}} = (1 - \mathfrak{R}) \, I_0 \tag{5.1.15}$$

if the sample had no bulk absorption at all. Consequently, the reflection losses of the measured intensity I_{M} can be corrected like

$$I_0 = \frac{I_{\mathrm{M}}}{1 - \mathfrak{R}} = \frac{I_{\mathrm{M}}}{1 - \frac{2R}{1+R}} = I_{\mathrm{M}} \frac{1+R}{1-R}. \tag{5.1.16}$$

Any additional losses are then associated with the (radiation induced) bulk absorption of the sample, which is the interesting part for the purpose of this study. In order to compute the correction factor $\frac{1+R}{1-R}$ we have to know the refractive index of the sample which is also a function of the wavelength of the light. In order to account for the chromatic dependence of the refractive index, the SELLMEIER equation is used

$$n^2(\lambda) = 1 + \frac{B_1 \, \lambda^2}{\lambda^2 - C_1} + \frac{B_2 \, \lambda^2}{\lambda^2 - C_2} + \frac{B_3 \, \lambda^2}{\lambda^2 - C_3} \tag{5.1.17}$$

where the B_i and C_i are material constants. Figure 5.22 shows the correction factor $\frac{1+R}{1-R}$ for the wavelengths of interest with the appropriate Sellmeier coefficients inserted. All
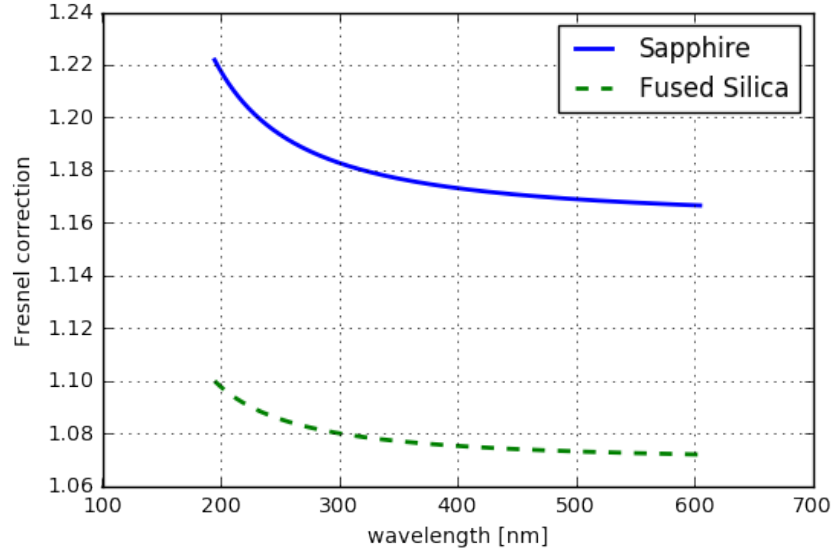
Figure 5.22: Corrections for Fresnel losses for the Sapphire and Fused Silica Samples. The derivation is explained in the text.

sample windows were thoroughly cleaned and their transmission was measured with the spectrometer (Run 1). The windows were rotated by 180° to check the reproducibility of the measurements and to get an estimate for the systematic error (Run 2). Afterwards the

windows were irradiated with γ radiation which was provided by a ^{60}Co source. A total dose of $100\,$Gy was deposited on all windows simultaneously and the transmission was measured again in the same setup as before. For each glass window and each wavelength, the (Fresnel corrected) transmission before (T_1) and after the irradiation (T_2) was derived. The (radiation induced) transmission loss $\mathfrak{T}$ was then checked by evaluating

$$\mathfrak{T}(\lambda) = \frac{T_1 - T_2}{T_1}(\lambda) \qquad (5.1.18)$$

for each wavelength. Figure 5.23 shows the results obtained with the fused silica glass
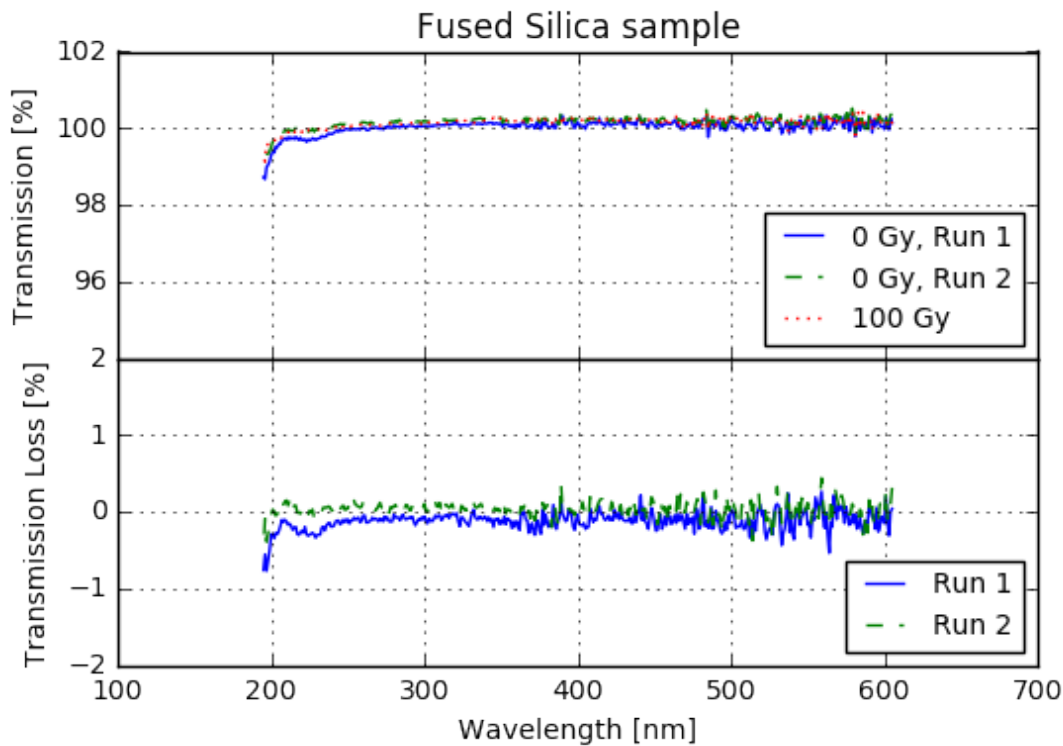
Figure 5.23: Transmission and radiation induced transmission loss of the fused silica front glass sample.

sample. The window showed no loss in transparency that could be resolved with the setup. This result was to be expected as fused silica has been shown to be radiation hard well beyond $100\,$Gy [54]. For this reason the large scale optics of the EDD will be made out of fused silica. The reproducibility of the measurement was also very good. The curves for Run 1 and Run 2 in figure 5.23 are almost identical except for a small dip in the blue curve for Run 1 around $220\,$nm. This structure is also present in the measurements with the sapphire glass and is likely to be caused by the instrument.

The results presented in figure 5.24 show that the sapphire windows are not as transparent

between 200 and 250 nm as the fused silica sample. The salvaged sample is a glass that has been removed from a defect MCP-PMT (salvaged) while the other sample is a new one. Both transmission curves show a slight dip in the region around 220 nm which was also observed before. Interestingly, the transmission rises to about 101% above 250 nm for both samples which is caused by a slight overcompensation of the Fresnel losses. Additionally, the reproducibility of the measurements is not as good as in the measurement before. The rotation of the glass sample shifts the transmission curves by about 1% in the lower wavelength region. The reason could be remaining impurities on the surface of the windows that have not been removed by the cleaning procedure.

The transmission loss of the first sample is compatible with 0 for most wavelengths. Only between 220 and 300 nm around 1% of transmission loss was measured. Because of the dubious structure of the curves around 220 nm, this result can't be interpreted as a confirmed loss in transparency because the magnitude of the effect is not significant compared to the uncertainties. For the salvaged sample the transmission loss varies around 0.5% for most wavelengths. However, as the systematic uncertainty is at least about 1%, this is again no proof for radiation induced loss of transparency.
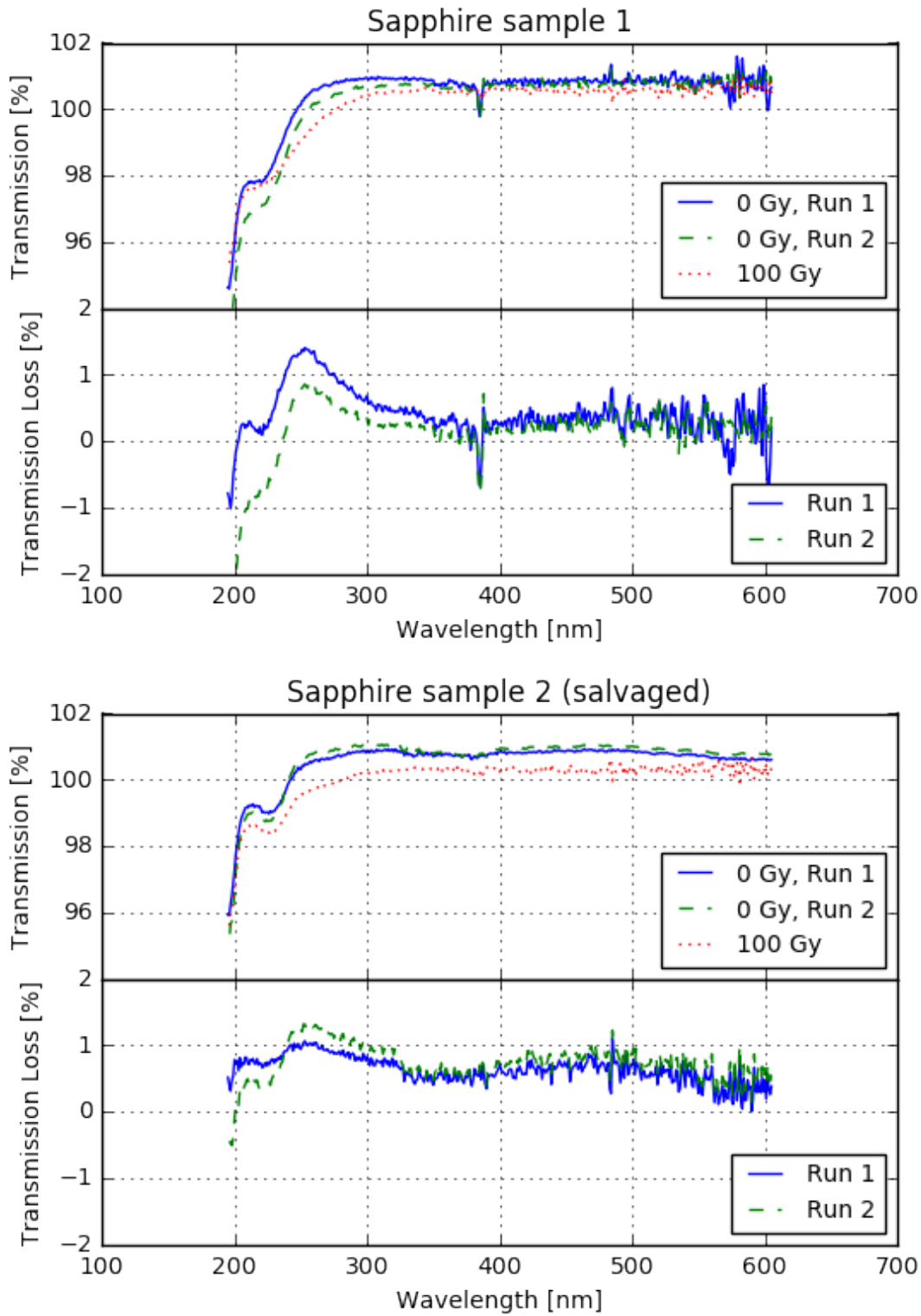
Figure 5.24: Transmission and radiation induced transmission loss of the two sapphire front glass samples.

5.2 Testing of TOFPET-ASIC readout

This section will present the research that has been done to evaluate the performance of the combination of the Photonis MCP-PMT prototype and the TOFPET ASIC evaluation kit. These steps can be reproduced with a Hamamatsu MCP-PMT once a suitable specimen can be obtained. The necessary hardware to connect both sensors to the readout system is available and will be shown first.

In order to establish a reliable electrical connection for all pins on the backside of the Photonis sensor, custom printed circuit boards (PCBs) have been designed (as shown in chapter 4), produced and assembled. Because of the high channel density, fine pitch SMD[1] components had to be used and assembled using vapor-phase soldering techniques. The MCP-PMT signals can be transmitted through two high pitch coaxial cable assemblies and two custom PCBs as shown in figure 5.25. Figure 5.26 shows how both MCP-PMTs can be connected. The upper assembly in figure 5.25 can be used to read out 128 channels
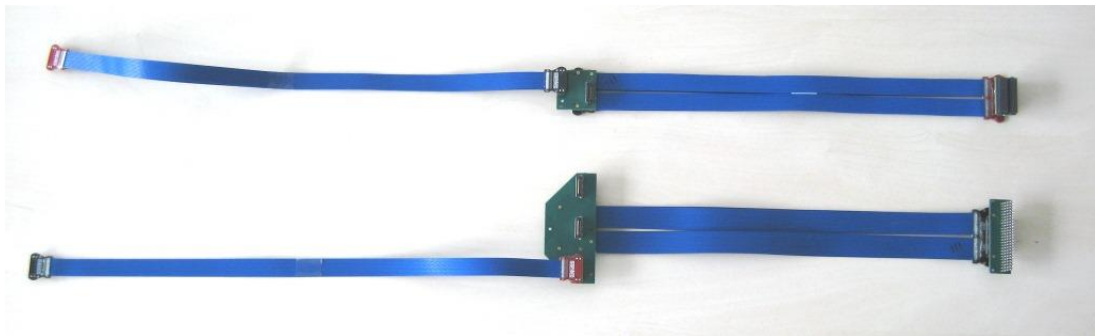
Figure 5.25: High channel count signal transmission assemblies for Photonis (bottom) and Hamamatsu (top) MCP-PMTs. The sensors connect to the right side.

of the Hamamatsu MCP-PMT, with pairs of neighboring columns being shorted. Six pieces suffice to read out the entire sensor, resulting in 3×128 channels. The lower assembly in figure 5.25 accommodates 96 transmission lines for one column of the Photonis prototype. Only 4 anodes per column at the perimeter are not connected. Both assemblies consist of one PCB that holds a high channel density connector to connect to the sensor (right side in the picture), a high density coaxial cable assembly, a seconds PCB for redistribution of the signal lines to the pin assignment of the ASIC input (middle) and a second coaxial cable assembly that leads to the readout. The second PCB also serves as a feedthrough platform, as all tests have to be performed in light tight environments. All vias of this PCBs are covered with solder resist in order to not allow light to fall through

---

[1]**S**urface-**M**ounted **D**evice

the inner channels with diameters of $100\,\mu$m. All components (coaxial cables and PCBs) are designed with a transmission line impedance of $50\,\Omega$ to reduce signal reflections on the electrical interfaces. At the end of the transmission assemblies (left side in the picture) an additional PCB connects the assembly to the readout system (oscilloscope, TOFPET evaluation kit or full scale TOFPET readout).
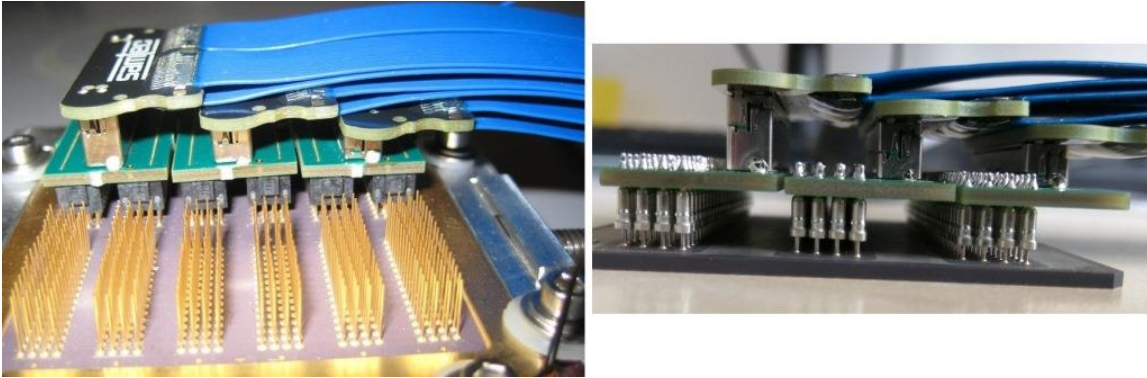
Figure 5.26: Left: 3 of 6 transmission assemblies have been connected to the Hamamatsu MCP-PMT prototype. Right: One fully equipped pin grid array of a Photonis MCP-PMT.

The signal quality and the signal-to-noise ratio of these assemblies are superior to the first iteration which used custom flex print cables for the signal transmission and was used in the CERN testbeam in 2015 [54]. The main improvement comes from the use of the shielded coaxial cables with a well controlled line impedance. Testing of the signal quality was done by using dedicated adapter PCBs at both ends of the assembly and injecting well known pulses into one end and reading out the other end with a fast oscilloscope. The signals could then be compared to a regular coaxial cable. Even very small pulses with amplitudes between 1 and 2 mV could be nicely sent

Figure 5.28: Close up of the connections to the TOFPET evaluation kit

through the assembly without distortions of the pulse shape. The noise level of the assembly was measured below 2 mV.

These readout connectors have been used to examine the performance of the Photonis MCP-PMT and the TOFPET ASIC in the setup with permanent magnets. The maximum field strength of 65 mT was chosen for the following tests. Figures 5.28 and 5.27 show some details of the setup. Apart from the different readout system, the main difference to

Figure 5.27: Test setup with permanent magnets and TOFPET evaluation kit: The aluminum box in the middle of the picture holds the MCP-PMT and the 8 permanent magnets. The laser module and the NIM crate with the high voltage module are on the left side of the picture. The Hall probe can be used to double check the magnetic field strength. The TOFPET evaluation kit with the ML 605 FPGA board and the black voltage divider box are on the right side of the aluminum box. A dedicated fast pulse generator (not seen in the picture), which is triggered directly by the laser module is additionally connected to one input node of one TOFPET ASIC to serve as a reference pulse.

the previous setup is that a dedicated pulse generator is now necessary to provide a trigger pulse which is fed into one ASIC through a capacitor. The external pulser is triggered by the laser module in such a way, that each laser pulse is accompanied by one trigger pulse. Having a trigger pulse is absolutely necessary for the subsequent analysis of the acquired data because it helps to filter out dark counts by applying a time cut relative to the time of arrival of the trigger. The efficiency of the readout can also be analyzed by normalizing the registered amount of photons to the total number of recorded triggers. In order to measure the trigger pulse detection efficiency, a separate study has been done beforehand. The trigger pulser was configured to release pulses at a frequency of about 1 kHz. These pulses were recorded for 600 seconds with the ASIC and subsequently analyzed. The results can be seen in figure 5.29. The main result from this test is, that at least 99.44 % of the incoming pulses have been successfully registered. It should be stressed that an efficient detection of the trigger pulses is not very important for the evaluation of the detection efficiency of single photon signals. A missed pulse will just lead to discarding the associated event and will not influence the efficiency measurement of the MCP-PMT pulses. The injection of the trigger pulses into the ASIC could probably be improved by a more careful design of the corresponding hardware, but for these tests, as well as for

the testbeam campaign at DESY (see section 6) this solution is sufficient.

The next step of the study is to test if the pulses from the Photonis MCP-PMT are registered efficiently when operated in single photon mode. In order to test this, the laser spot was placed between two anodes and the surrounding 4 anodes and the trigger pulse from the laser unit were read out with an oscilloscope. For each event (i.e. trigger pulse) the waveform amplitudes of all 4 anodes were recorded. It was then counted how often the pulses exceeded the very low threshold of 5 mV. The result can be seen in figure 5.30. The figure reveals that anodes 2 and 3 output pulses with an amplitude of 5 mV or more in about 1/4 of the events. This means that the intensity of the laser is close to the single photon level (resulting in multi-photon-events in only about 3.4% of the events). In the next step the 4 anodes were connected to the TOFPET ASIC evaluation kit in a pack of 64 neighboring anodes of the central column. Nothing else was changed and no equipment was power cycled. Thanks to the custom made adapter PCB, this step could be done by simply unplugging one card and inserting another one. A measurement with the evaluation kit was initiated and subsequently analyzed. Figure 5.31 shows the amount of registered hits of all connected anodes normalized to the amount of triggers (channel 100).

Upon first thought this result might be interpreted as disappointing because there is no structure caused by the small laser spot. However, due to the repetition rate of the laser of only about 1 kHz this figure is dominated by dark counts. The picture looks very similar even if the laser is turned off completely. Increasing the repetition rate to overcompensate the dark counts is not desirable, because the size of the laser spot is very small and a lot of intensity falls on a very small area which might lead to growing saturation effects. This is why it is important to have the timing information of the trigger pulse which has been injected into the evaluation kit through one input channel of one of the 8 TOFPET ASICs. We can reference the time of arrival of all hits to their corresponding timestamp of the trigger channel that has been written into the hit log. If we do so, we arrive at figure 5.32.

Now we can see that there is a small peak at about 150 ns late of the trigger and a spike at 0 which corresponds to all triggers being referenced to themselves. It means that real photon hits (not dark counts) are registered about 150 ns after the corresponding trigger pulse. This knowledge empowers us to discard almost all dark counts by only allowing hits to appear in the figures that have a correct time of arrival relative to the last trigger. If we redraw figure 5.31 with this selection criterion, we arrive at figure 5.33. This figure reveals a nice agreement with the oscilloscope measurements for the two central anodes
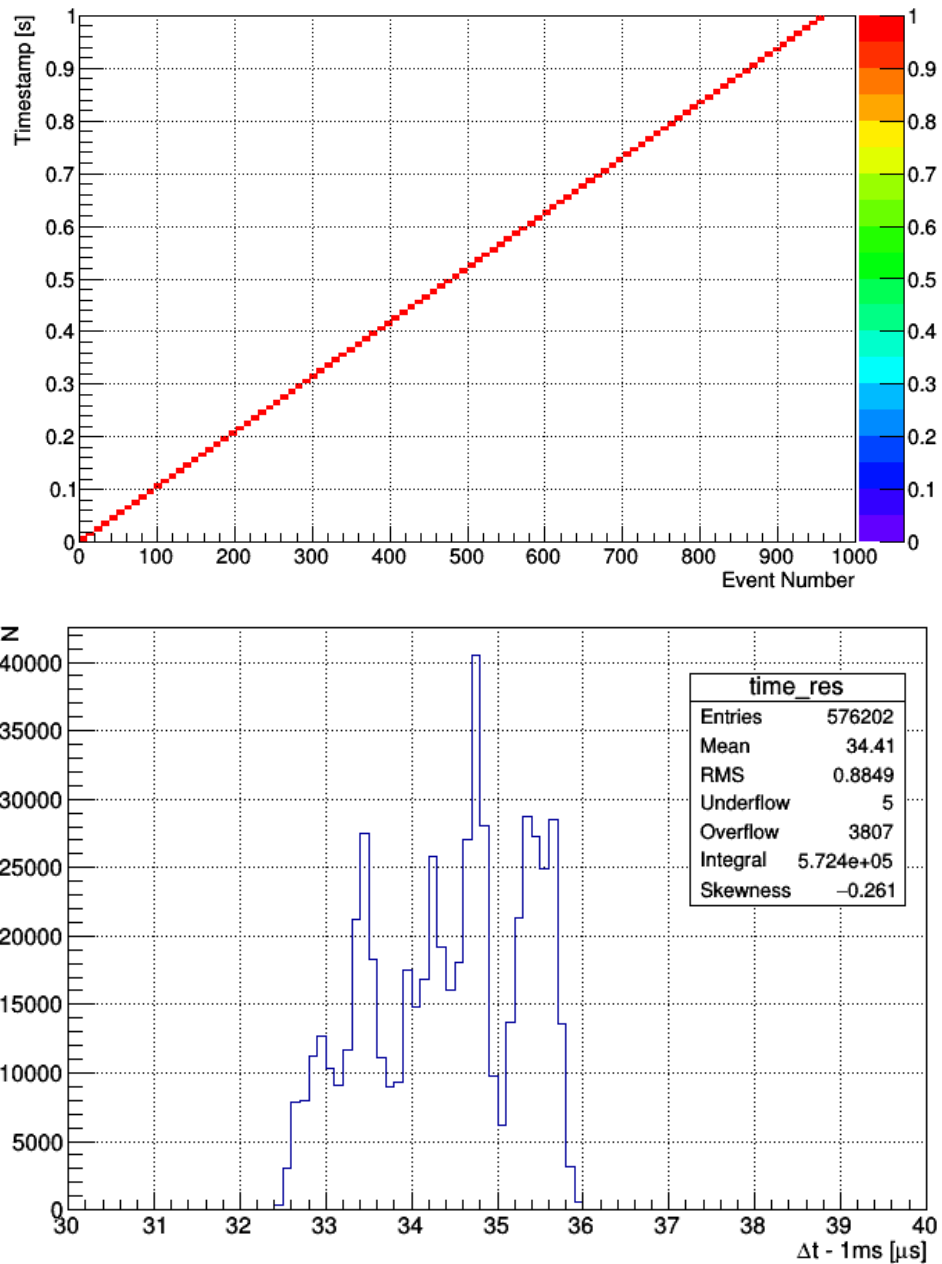
Figure 5.29: Evaluation of the trigger pulse detection efficiency of the TOFPET ASIC evaluation kit: The upper plot shows the progression of the timestamps of the detected trigger pulses versus the event number for the first second of the test measurement. The x axis has 1000 bins, one for each event. The lower plot shows the time difference between consecutive trigger pulses. Because the rate of the pulser is set to $1\,\mathrm{kHz}$, there would be a sharp peak around $1\,\mathrm{ms}$ in an ideal world. In reality, there is an offset of about $35\,\mu\mathrm{s}$ and a variation of a few $\mu\mathrm{s}$. However, only 3812 events out of 576202 ($\approx 0.66\%$) are outside of the 10μ window which shows a good detection efficiency of the trigger pulses.
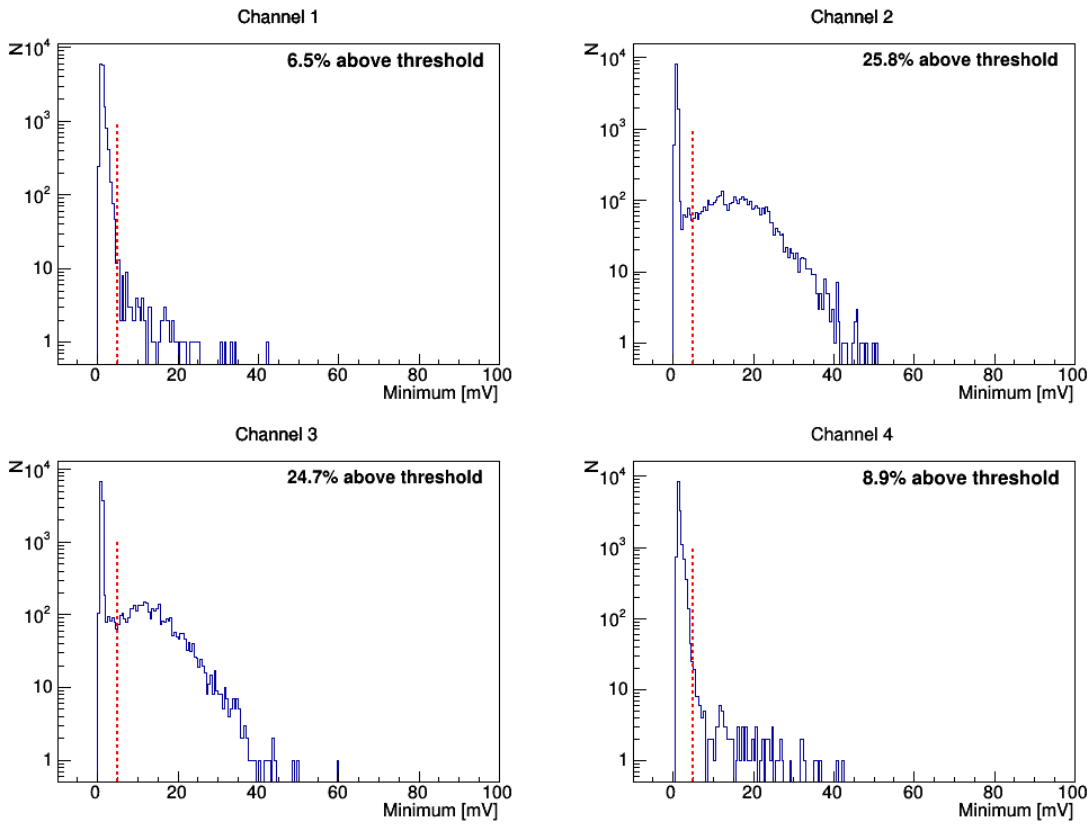
Figure 5.30: Amplitude distributions of the Photonis prototype under single photon illumination: The focused light spot is placed between channel 2 and 3 to test the case with maximum charge sharing.
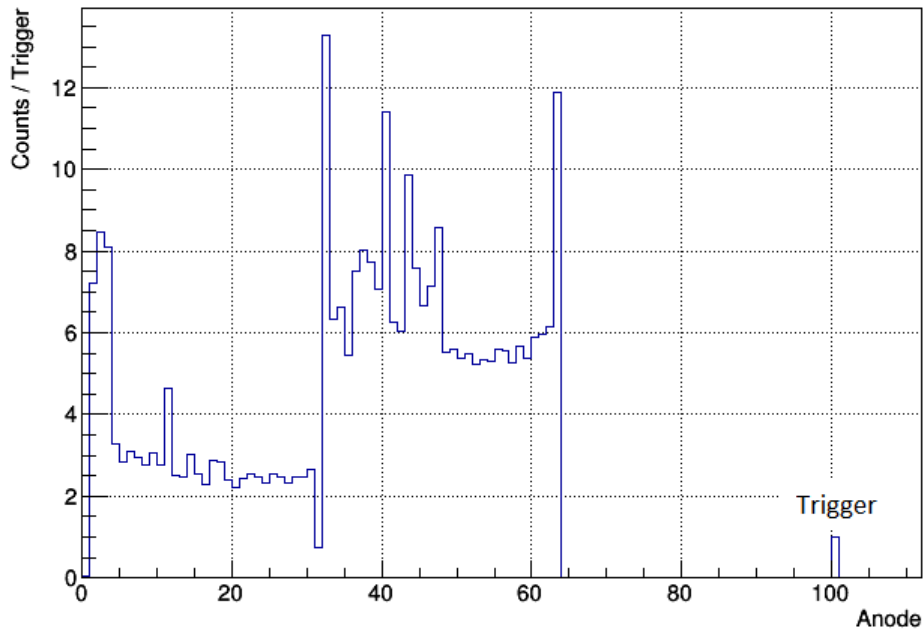
Figure 5.31: The distribution of registered hits per trigger before any time cuts are applied to the data. All channels are dominated by dark counts and no photon peak can be observed.
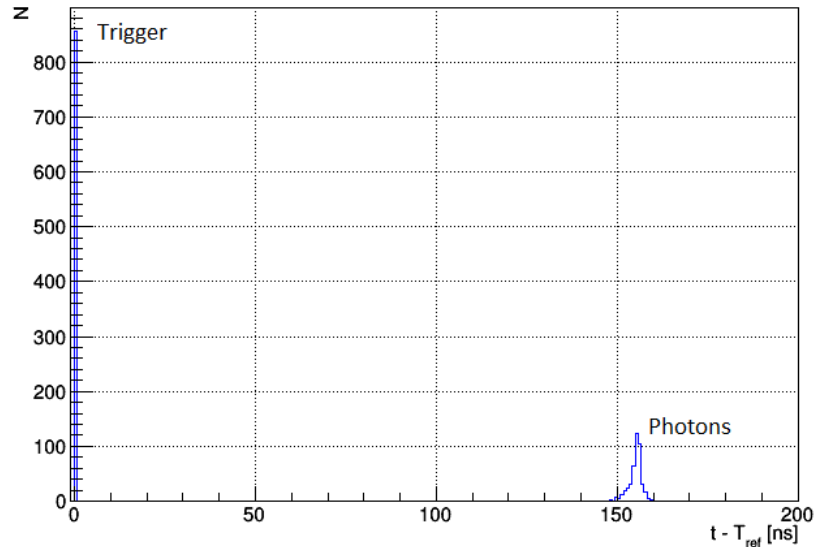
Figure 5.32: The figure shows the time distribution of all hits when referenced to the time of arrival of the corresponding trigger pulse. The spike at 0 corresponds to the trigger pulses being referenced to themselves. The peak at about 150 ns corresponds to the actual photon hits (all 64 channels included) which are detected at a constant offset with respect to the trigger pulse. The time information can be used to discard dark counts.

which detect pulses at about 1/4 of the events.

This promising result had to be confirmed by some cross check experiments. The first measure involved changing the intensity of the laser light. This was achieved with the help of an attenuation device that was mounted to the laser head of the PiLas. The intensity was increased and the sensor response was checked with the oscilloscope again. Figure 5.34 shows that the agreement remains after the change. Both systems (oscilloscope and evaluation kit) register hits above 5 mV in about 78 % of the events. It should be noted that this measurement contains a considerable amount of multi-photon events. Theoretically, already about 48 % of the events should be multi-photon events. Evidence for this can also be observed when comparing the figures 5.30 and 5.34. In the latter, the maximum amplitudes in the spectrum reach as far as about 70 mV whereas the single photon tail in figure 5.30 already ends at about 40 mV. However, this test was only intended to double check the detection efficiency while varying some of the parameters. The next cross check is done by actually moving the laser spot across the central anode column and record data at each individual position. Timecuts are applied again in order to select the actual photon hits. It should be pointed out that the entire scan was done with the exact same settings at all individual laser positions. No tuning of the thresholds or the high voltage of the sensor was necessary along the way. This scan was done at a
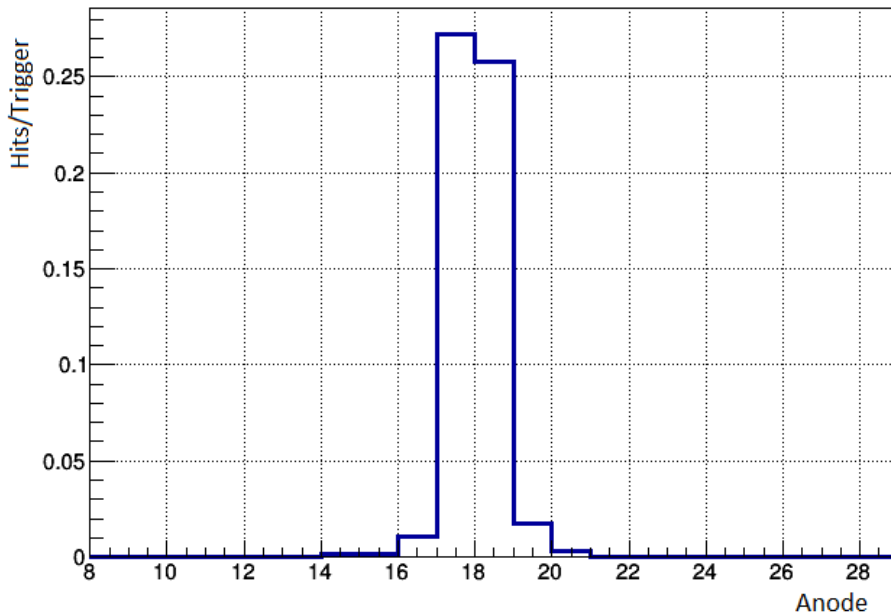
Figure 5.33: The figure shows the spatial distribution of the actual photon hits, normalized to the total number of triggers. The photon hits were separated from the dark counts by applying appropriate time cuts. Compared to figure 5.31 a clear photon peak is visible and the hit rates of about 25% for the central anodes agree with the expectations from the oscilloscope measurement (see figure 5.30).

single photon level again and the result can be seen in figure 5.35.

This series of measurements proves that the TOFPET ASIC is in fact well suited for efficiently detecting single photon pulses from the MCP-PMT prototype at field strength of about 65 mT. The interesting question that remains now is how the system will behave if the external magnetic field is even stronger, because at PANDA, field strengths up to 1 T are to be expected. These fields can however not be created by any setup that uses permanent magnets. Therefore a strong electromagnet had to be used to conduct the next experiments. The first idea was to use a strong solenoid magnet like the PCMAG at DESY [60]. The advantage of the PCMAG is that it provides a lot of space for the installation of the test setup. The aluminum box could entirely be placed inside this magnet. There would even be space to rotate the box to simulate non-perpendicular angles of incidence of the magnetic field with respect to the sensor axis. However, there are some more significant drawbacks. Firstly, a solenoid magnet has strong, inhomogeneous stray fields around its endcaps. This translates into additional challenges when designing the measurement setup, because metal parts could be moved by these stray fields. Secondly, the PCMAG is at Hamburg and is used very frequently by many international researchers. A very systematic planning is necessary to ideally exploit any given time slot. Unexpected problems would have to be solved on the fly. Last but not least, the security precautions
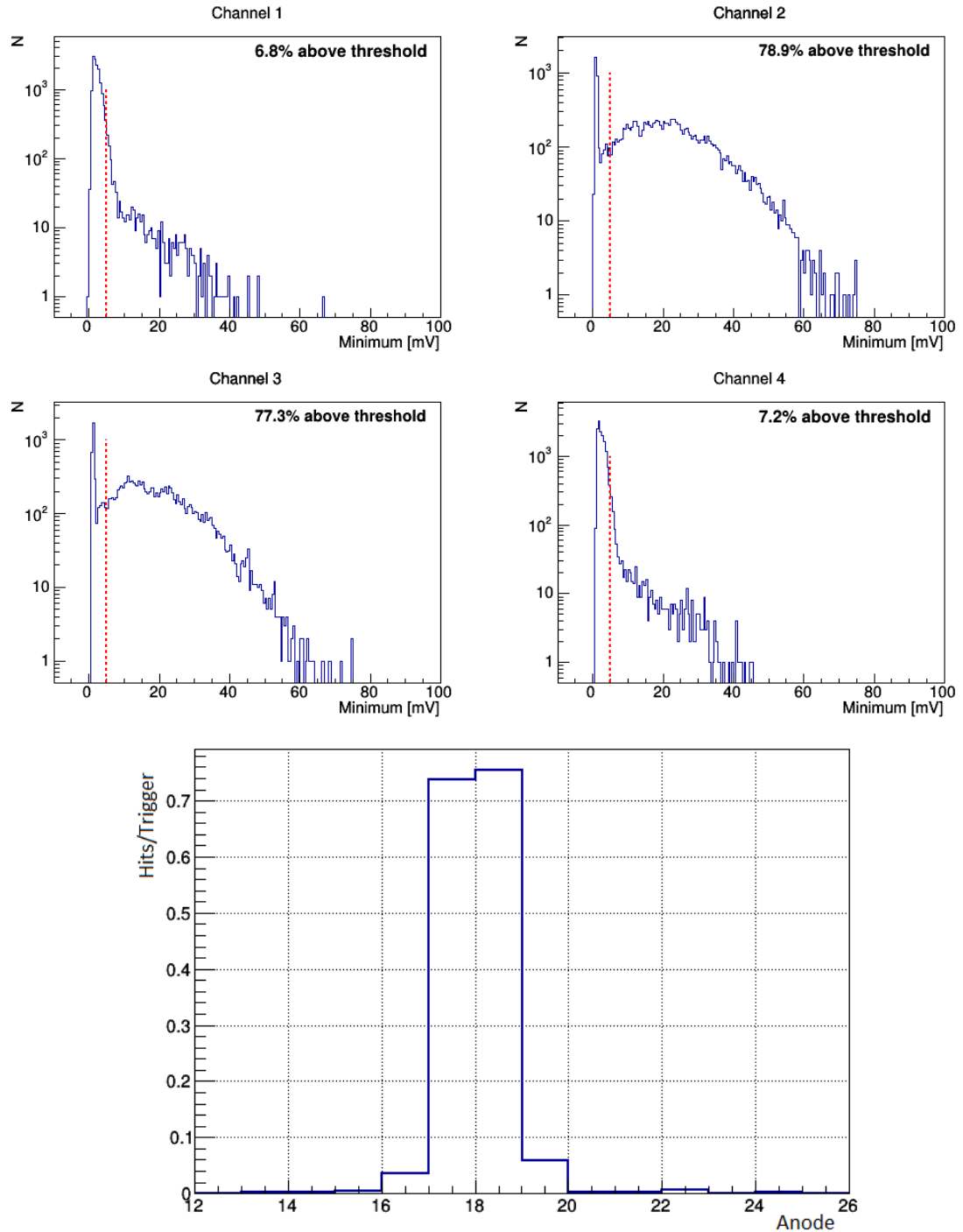
Figure 5.34: First cross check of the ASIC pulse detection efficiency: The upper part of the figure shows the measurements with the oscilloscope while the lower part shows the measurements obtained with the ASIC. After increasing the light intensity of the laser (beyond single photon level), the method of comparing hit rates between oscilloscope and ASIC readout has been repeated. It can be seen that the agreement persists as both methods show a hit rate around 78%.
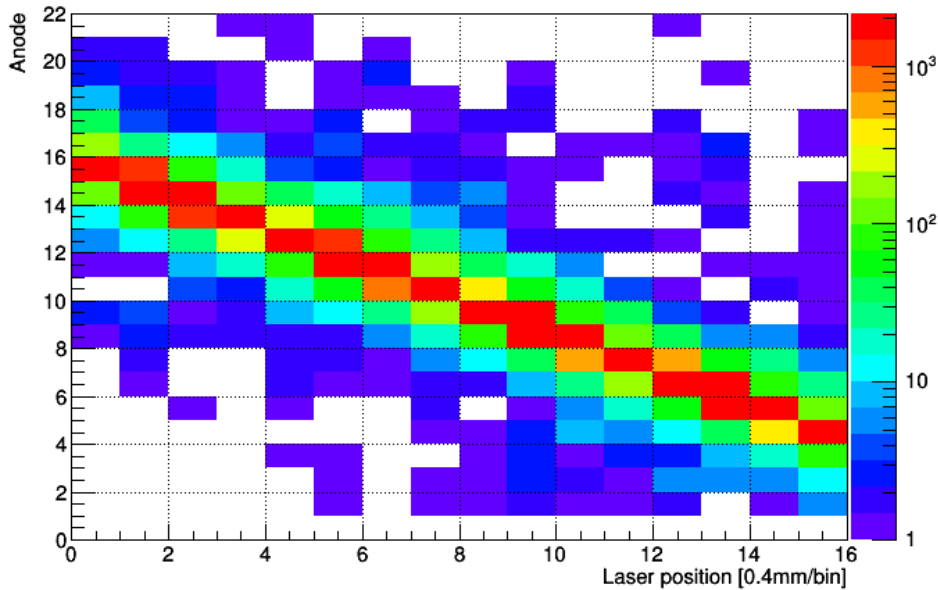
Figure 5.35: Second cross check: The laser head has now been moved across the central anode column of the MCP-PMT. At each position a measurement has been performed and appropriate time cuts have been applied. If no transition region between two anodes is illuminated, the count rate from the most active anode to its neighbors already drops by an order of magnitude, showing a good charge cloud collimation by the magnetic field of only 65 mT strength.

with the PCMAG are very rigorous and entering the beam cave is usually only possible after long ramping phases.

An interesting alternative to a solenoid magnet is a big dipole magnet. The problem here is that the sensor has to be illuminated from the front while it needs to face one pole shoe. This is the only way to align the sensor axis with the magnetic field lines. This means that the pole shoe distance of the dipole magnet has to be big enough to accommodate whatever equipment is needed to illuminate the sensor accurately enough to perform meaningful testing. However, an increase in poleshoe distance translates into a reduction of the strength of the magnetic field - all other parameters left unchanged. The poleshoe gaps of the available dipole magnets were not big enough to leave enough room for a setup similar to the ones presented so far. In a discussion with Dr. Albert Lehmann from Erlangen, he brought up the idea to introduce a high quality mirror in the setup. This mirror would allow to shrink the size of a setup considerably in the critical dimension. Figure 5.36 shows the design that follows this idea. The setup is designed to fit into a dipole magnet located at the ground floor of the Giessen physics building. This magnet could be used for this research by courtesy of Dr. Detlev Hofmann and his group. Magnetic field strengths of up to 1 T can be generated, while the stray field of the magnet
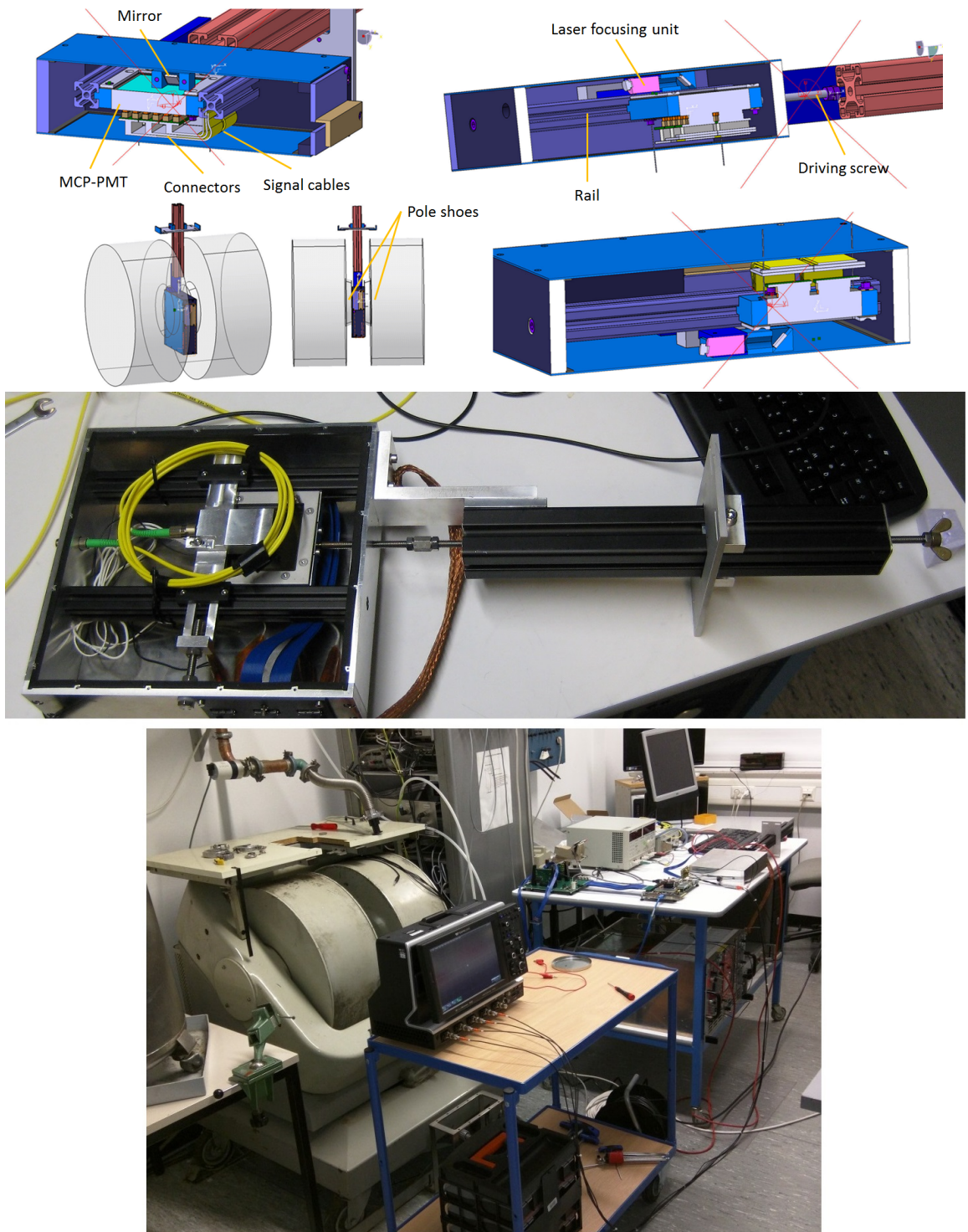
Figure 5.36: Technical drawings and photographs of the setup inside the Giessen dipole magnet. The laser light is reflected off a high quality mirror onto the surface of the MCP-PMT. Both the sensor and the illumination unit can be moved to scan the entire surface of the sensor with the laser spot. The length of the light path is adjusted to the working distance of the microfocus unit. The box has enough room to accomodate a fully equipped MCP-PMT and can still be placed between the pole shoes of the dipole magnet.

was not measurable beyond a distance of more than about 10 cm to the pole shoe gap. This allowed to approach the magnet safely with all (ferromagnetic) pieces of equipment. The upper part in figure 5.36 shows CAD drawings of an aluminum dark box that can be placed between the pole shoes of the Giessen dipole magnet. The unit can be mounted to the magnet and fixed with several screws. In order to move the sensor inside the box, a long threaded bar can be turned via a wing nut which is still accessible when the system is mounted inside the magnet. The aluminum box has an adapter plate for cable connections and a feedthrough for the optical fiber. The manufactured aluminum box can be seen below the CAD schematics in figure 5.36. The picture was taken just before the box was closed and installed into the magnet. The lower photograph in figure 5.36 shows the Giessen dipole magnet and its current source on the ground floor of the physics building and the entire DAQ setup around it.

After a careful setup of all components, the laser spot was again placed between two anodes and a scan of the magnetic field strength was performed. The field ranged from 0 to 800 mT. At each position a measurement was done for 10 seconds while the laser was repeating at about 1 kHz. Figure 5.37 shows the analysis of this scan. Very similarly to the results with the permanent magnets, the biggest jump in charge cloud compression is achieved in the first step from 0 to 100 mT. After this step, an increase in magnetic field strength doesn't lead to significant increase in charge cloud collimation anymore. Interestingly, a comparably huge background around the point of impact is observed at 0 mT. It contributes a lot to the total RMS of this column. The reason for this is the so-called *cross-talk*. It originates from photoelectrons which don't directly enter an MCP pore but scatter off the surface of the first MCP. They follow a ballistic trajectory and can sometimes enter another MCP pore several millimeters away from their original location. Because these back-scattered photoelectrons carry very little kinetic energy, a comparably small magnetic field can already heavily influence their trajectories. This is why the cross talk is significantly reduced already at 100 mT. This observation is very important with regard to the analysis of the testbeam data which has also been taken at 0 mT. A big improvement of the position resolution of the MCP-PMTs can be expected in the real PANDA experiment when a magnetic field is present, compared to the testing at CERN and DESY.

A second interesting detail of figure 5.37 is that the total count rate decreases again for very strong fields. This observation can be explained with a drop of the gain due to the magnetic field as explained in chapter 3.3. In the next step the evolution of the hitpattern is studied when the MCP-PMT is moved with respect to the laser spot. This can be re-
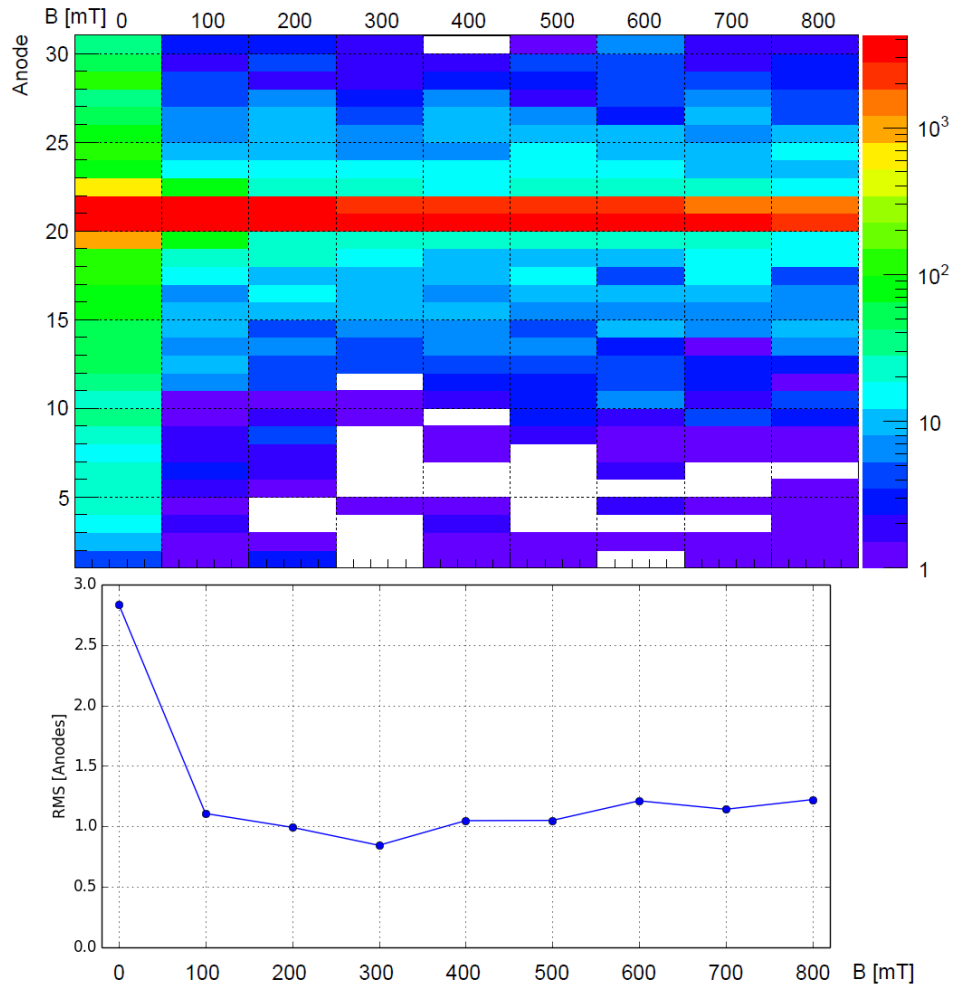
Figure 5.37: Scan of the magnetic field in the Giessen dipole magnet. The upper plot shows the accumulated photon hit patterns for all 9 measurements which were performed at different magnetic field strengths: The first column shows the measurement at 0 mT, the second at 100 mT and so on. The laser spot was placed between two anodes to maximize the effect of charge sharing and search for the effect of undersampling (as explained in section 3.4.5). The lower plot shows the RMS of these distributions. It can be seen that an increase in field strength above 100 mT doesn't lead to significant increases in charge cloud collimation anymore. Consequently, the RMS of the hit patterns reaches a plateau at 100 mT. However it can also be seen, that the total amount of registered hits drops with an increasing field. The strong background at 0 mT is mainly caused by cross-talk, which is reduced significantly by the magnetic field.

alized with this setup and the corresponding analysis can be seen in figure 5.38. It shows that the strong magnetic field collimates the charge cloud so much that only one anode will be struck in the majority of the events. Only in the transition area from one anode to the next there is some significant charge sharing, just like we observed earlier in the setup with permanent magnets (e.g. figure 5.13). It can also be seen that no significant undersampling is present even at 800 mT.

This series of experiments proves that the combination of the Photonis MCP-PMT prototype and the TOFPET ASIC is a very powerful one that satisfies some key requirements for operation at PANDA. However, some aspects are still open. Firstly, the time resolution of this combination is still to be determined. A corresponding study of this quantity will be presented in chapter 6. The circumstances at the testbeam allow a more meaningful derivation of the single photon timing resolution, as will be discussed there. The main reason is the time smearing due to multiple additional pieces of hardware that were necessary to conduct the measurements in the lab (laser module, laser head, external pulser etc.). One could measure the timing resolution between two pixels in the lab, which would cancel some of these contributions, but this would require some more elaborate setup. Two anodes - ideally far apart to exclude crosstalk or charge sharing - whould have to be in the focus of the single photon light source simultaneously. This could be done with a beam splitter and two focusing units. The alternative of simply illuminating the whole sensor with a homogeneous intensity distribution (i.e. no focusing unit at all) would have several drawbacks: The probability of both anodes being struck in one event simultaneously is very low in single photon mode if both anodes are far apart from each other. Increasing the light intensity however, would mean to not measure the single photon timing resolution. Also, one can never be sure if a hit in one anode is really caused by a photon impinging above the anode in question, or if the hit is in fact caused by charge sharing or cross talk. Luckily the testbeam provides a possibility for a very controlled measurement of this quantity.
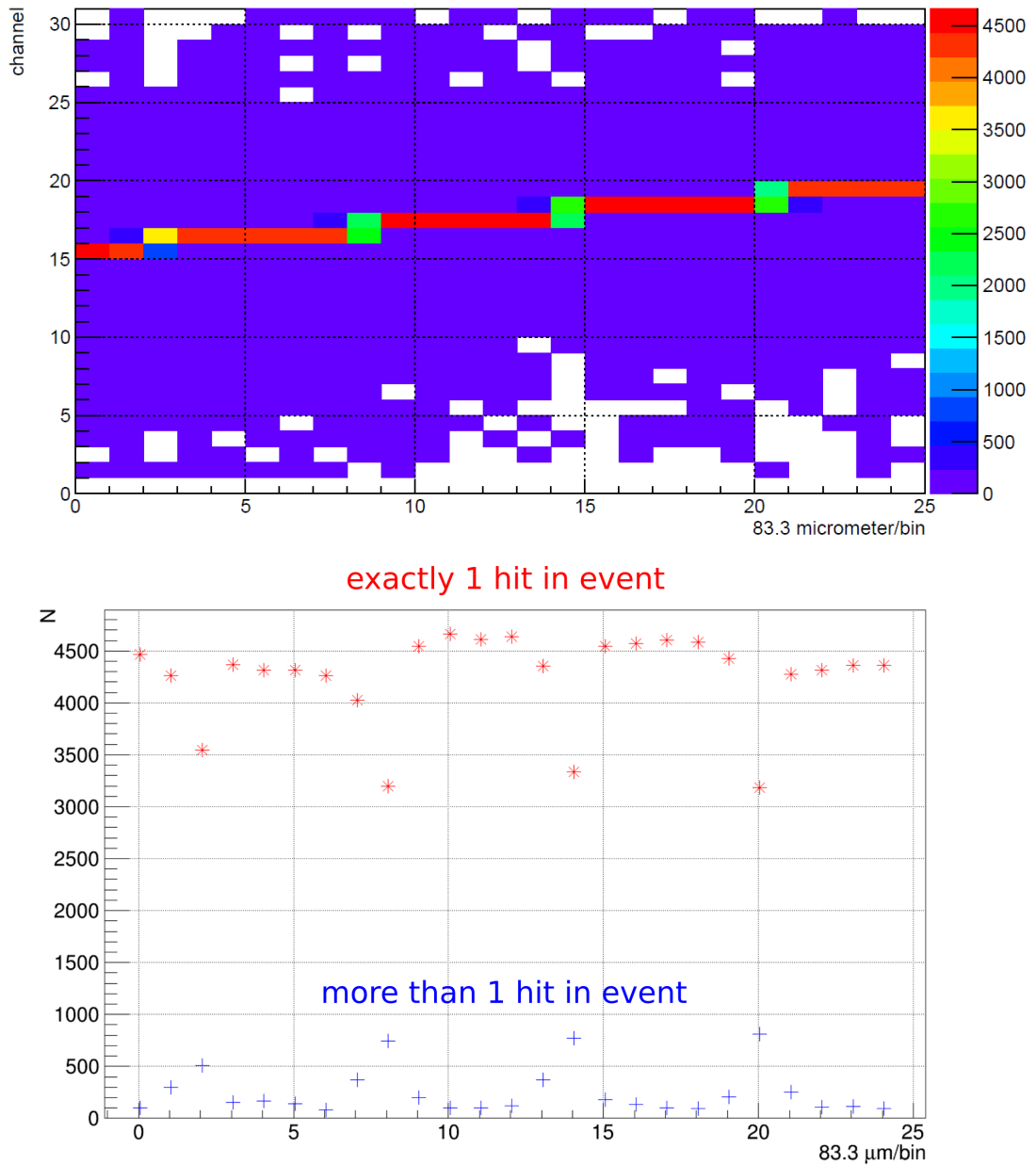
Figure 5.38: Position scan at 800 mT: At the maximum field strength of 800 mT a position sensitive measurement was performed. It illustrates again the strong collimation of the charge cloud and allows a quantification of possible undersampling. The MCP-PMT was moved several times by fractions of a millimeter to scan over some anodes and the corresponding transition regions between them. The upper plot shows again the hit patterns at each position while the lower plot shows the number of events where one or more than one hits were registered in a given event. It can be seen that the number of one-hit-events drops significantly between two anodes while the number of multi-hit-events increases by roughly the same amount. This shows that even at these strong fields the detection efficiency in the transition region is only slightly decreased due to undersampling effects.

6 DESY Testbeam

6.1 The testbeam facility

With the full scale TOFPET readout system presented in chapter 4 and the 2016 proto-type (figure 6.2), a testbeam campaign at DESY[1] has been undertaken during October of 2016. Due to delivery delays it was only possible to measure with a total of 3 FELs and it was decided to assemble one full ROM and read it out with the Photonis MCP-PMT that was tested in the preceding chapter. An overview of the testbeam facilities
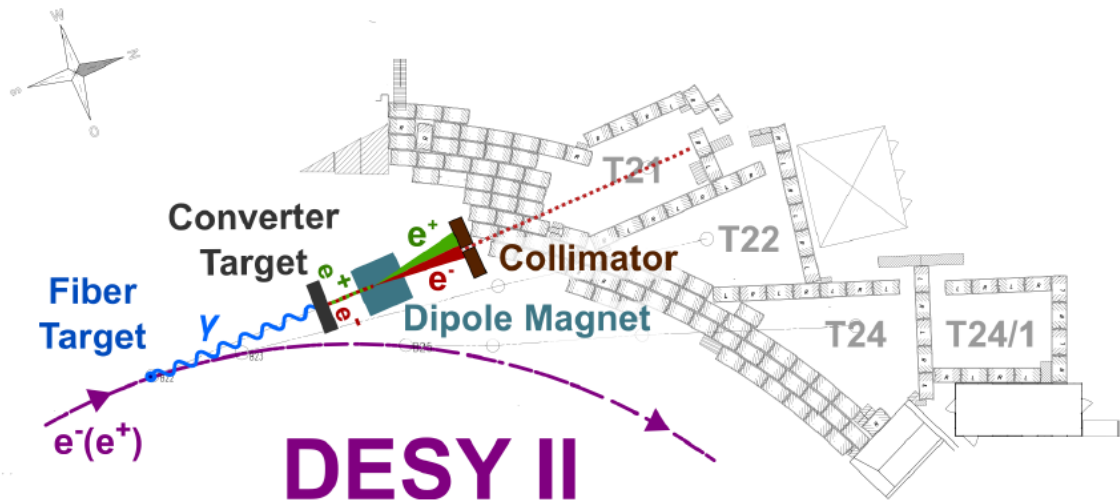
Figure 6.1: Overview of the DESY testbeam facility. The figure has been provided by DESY.

provided at DESY can be seen in figure 6.1. The electron synchrotron *DESY II* provides a beam of high energy electrons. A fiber target is placed in the beam halo of DESY II where bremsstrahlung is generated. The bremsstrahlung is subsequently converted into electron-positron-pairs on a dedicated conversion target. A dipole magnet, whose magnetic field strength can be controlled by the user, selects the momentum of the generated

---

[1]Deutsches Elektronen SYnchrotron

Table 6.1: Key parameters of the DESY testbeam.

Spatial uncertainty of e^- on radiator	$\approx 5\,\text{mm}$
Angular uncertainty of e^-	$\approx 1\,\text{mrad}$
Beam momentum	$3\,\text{GeV/c}$
Size of primary collimator	$5\times 5\,\text{mm}^2$
Size of secondary collimator	$15\times 15\,\text{mm}^2$

electrons with the help of a two-stage collimator system. Three beam areas (T21, T22 and T24) are available and can be provided with electron beams simultaneously. The testbeam with the EDD prototype was done in T24. Depending on the performance and the requirements of other user groups, the electron beam could deliver average particle rates of several kHz allowing a fast acquisition of the necessary statistics. All in all, several TB of photon data were taken during the testbeam campaign.

6.2 The 2016 EDD prototype

A CAD image of the 2016 EDD prototype is shown in figure 6.2. It consists of a light-tight housing which is accessible from both sides via sliding doors. The radiator is a $50 \times 50\,\text{cm}^2$ fused silica plate with a thickness of $2\,\text{cm}$. Up to five ROMs can be mounted to one side of the plate. A dedicated feedthrough area has been reserved for cabling purposes.

In addition, a connector for optical fibers has been placed in the holding frame for the radiator plate, allowing the illumination of the opposing ROMs with the PiLas. The entire prototype was attached to a rotation table and mounted on a 2-dimensional translation stage. The ROM housing is a 3-d-printed plastic allowing to gently hold the sensitive optics and electronics in place without the risk of scratches on any optical surfaces. A CAD drawing of a ROM is shown in figure 6.3.

Prior to the testbeam the prisms and FELs were coupled together permanently so that no on-site assembly was necessary. Depending on the choice of sensor, the ROM can be assembled with a Hamamatsu or Photonis prototype which are attached to the main body of the ROM via additional 3-d-printed constructions. The MCP-PMT can be electronically connected and then optically coupled to the readout plane of the FEL via an index-matching liquid, minimizing FRESNEL losses that would occur in an air gap. The main body of the ROM was connected to a precision rail that was screwed onto a solid
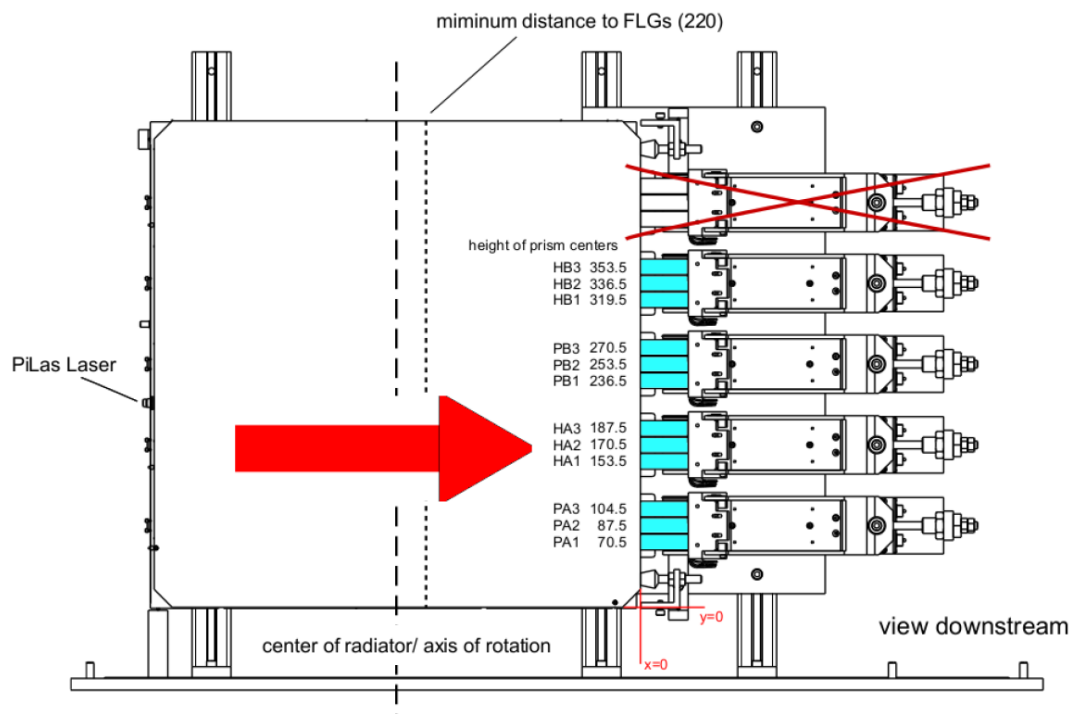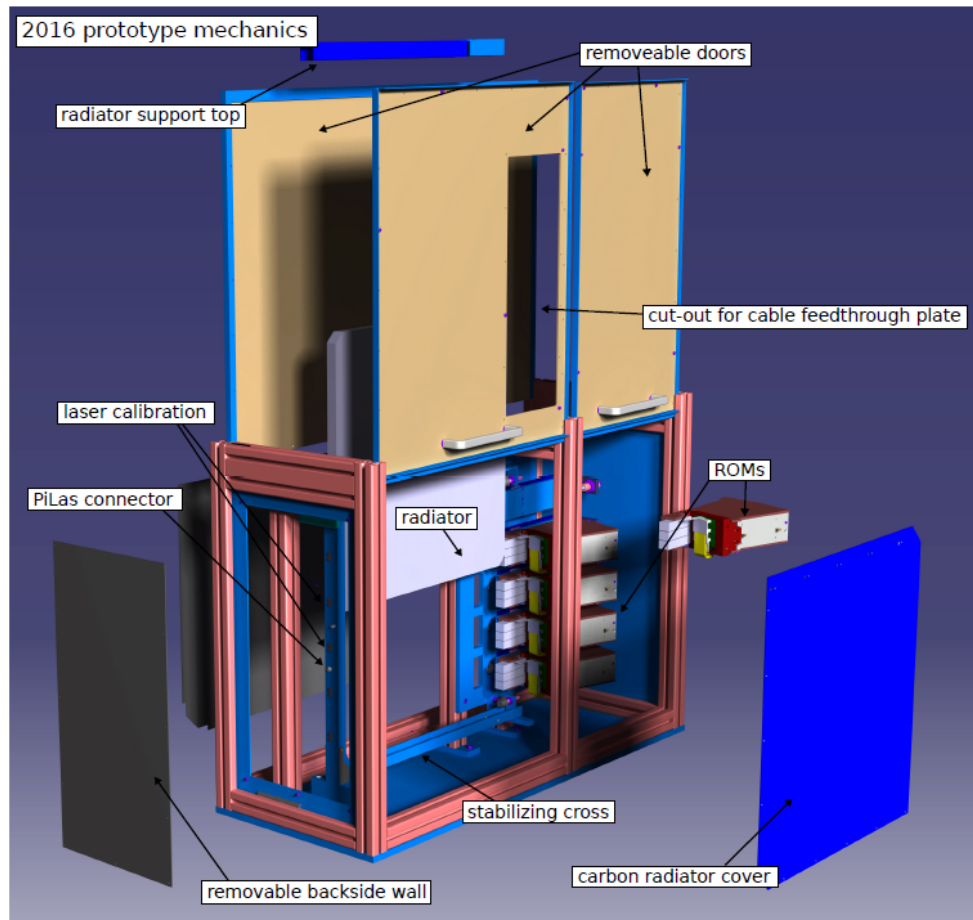
Figure 6.2: The 2016 EDD prototype. More information is given in the text. The upper figure is taken from [54]. The coordinate system is located on the lower right in the lower figure.
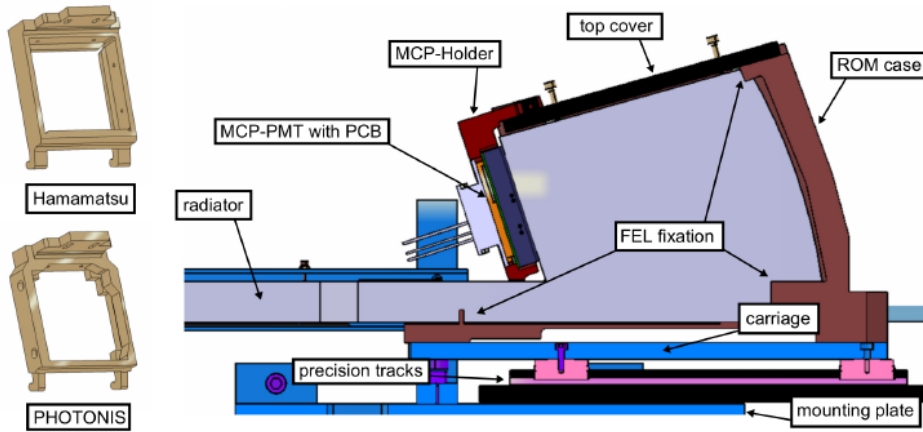
Figure 6.3: CAD schematic of the 2016 EDD prototype ROM. The holding brackets for the sensors are on the left. More information is given in the text. The figure is taken from [54].

holding plate which was directly fixed to the housing frame. With the help of laser reflections from the surfaces of the radiator and the prisms, the ROM was properly aligned with the radiator and both were ultimately coupled to each other via index-matching liquid. In the next step all electronic connections were established. This included the connection of the voltage divider circuit to a high voltage source and the connection of all signal lines. The full scale TOFPET readout system was placed outside the dark box and was attached to the signal lines via the feedthrough PCBs on the outside of the box. All FEB-Ds were then connected to the DAQ PC. Photographs taken during the assembly can be seen in figure 6.4. Due to possibly different environmental conditions, the baselines for the TOFPET readout were determined again and were saved in a configuration file. After the assembly and preparation of the prototype, the setup of the trigger system was the final step. Two scintillating counters that were provided by DESY were connected to standard NIM-based *Constant Fraction Discriminators* (CFDs). An electromagnetic calorimeter block was placed in the beam line behind a wall of lead bricks. This shielding wall had the purpose of stopping scattered electrons from entering the calorimeter while a little hole in the center of the wall allowed undisturbed electrons to enter the EMC. The event was only valid if the calorimeter output exceeded a given threshold which corresponds to events were sufficient energy was deposited in the EMC. This allowed to discard events where the electron was deflected before or during the process of creating Cherenkov radiation which would worsen the quality of the accumulated data. The EMC was also connected to a CFD. The logical output of all CFDs (representing the scintillating counters and the EMC) were connected to a logical AND-module. The beam was turned on to set the thresholds of all CFDs appropriately to be able to detect beam electrons via a coincidence
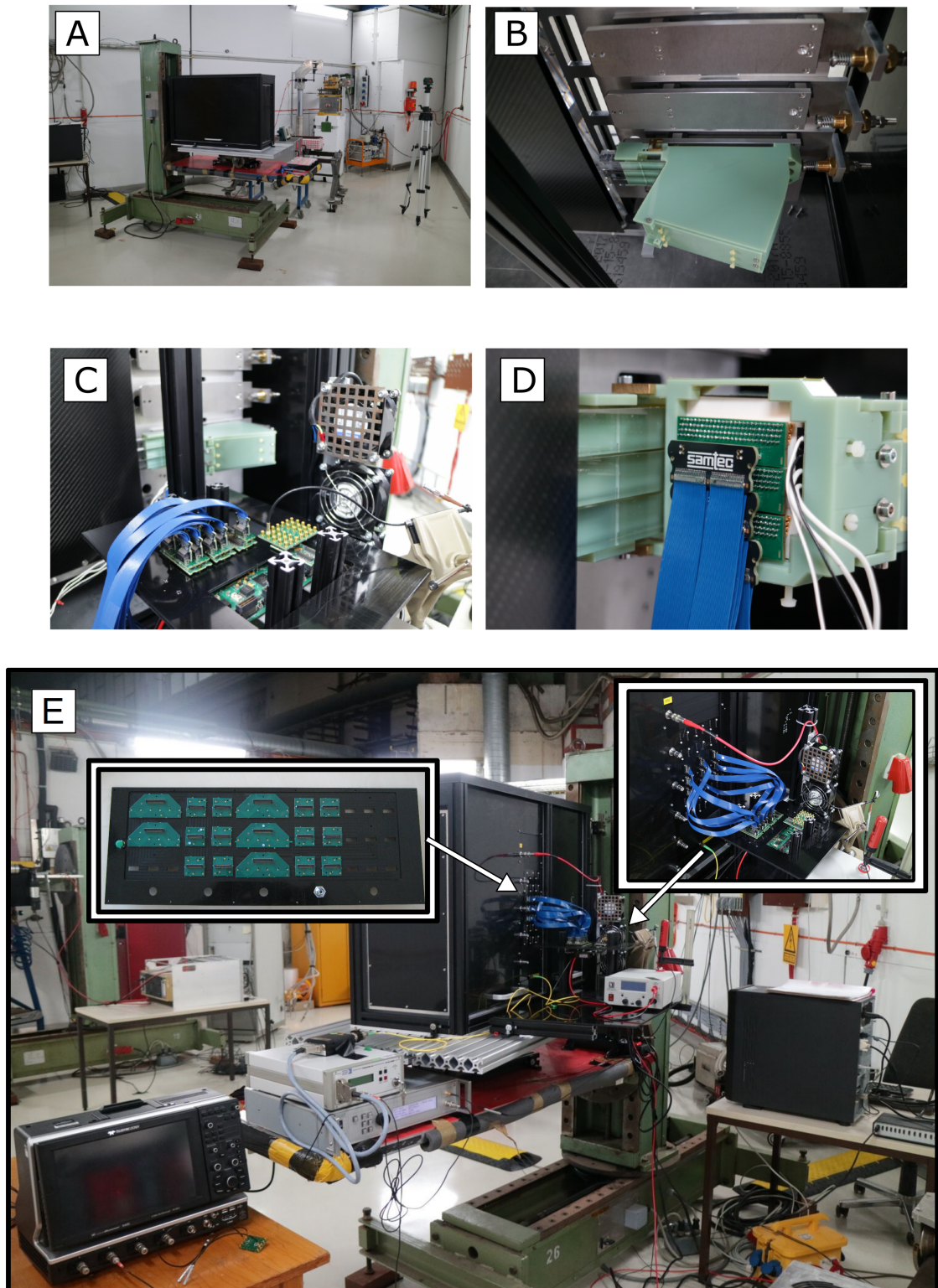
Figure 6.4: Photographs taken during the assembly of the 2016 EDD prototype at DESY. At first the mechanics were mounted on the table as shown in **A**. The radiator and ROM were installed and coupled as shown in **B**. **D** and **C** show the connections of the Photonis MCP-PMT and the TOFPET readout outside the dark box, respectively. **E** shows the prototype just before data taking.

condition.

Alternatively, the trigger pulse could be generated via the laser module of the PiLas. This allows to take data either with the beam switched on or with artificial illumination via the laser. An important difference is that the relative timing between the trigger pulse and the arrival of the light at the MCP-PMT is reversed between both modes. If the laser is used, the trigger pulse will arrive some hundreds of nanoseconds before the laser light. However, if the electron beam is used, the light will be detected some hundreds of nanoseconds before the trigger logic is able to provide a trigger pulse. This plays an important role in the data analysis, as all photon hits in the hit log of a laser run have to be referenced to the *last preceding* trigger, while the hits taken during a beam measurement have to referenced to the *next proceeding* trigger in the hit log. A schematic of the setup in the beam area can be found in figure 6.5.
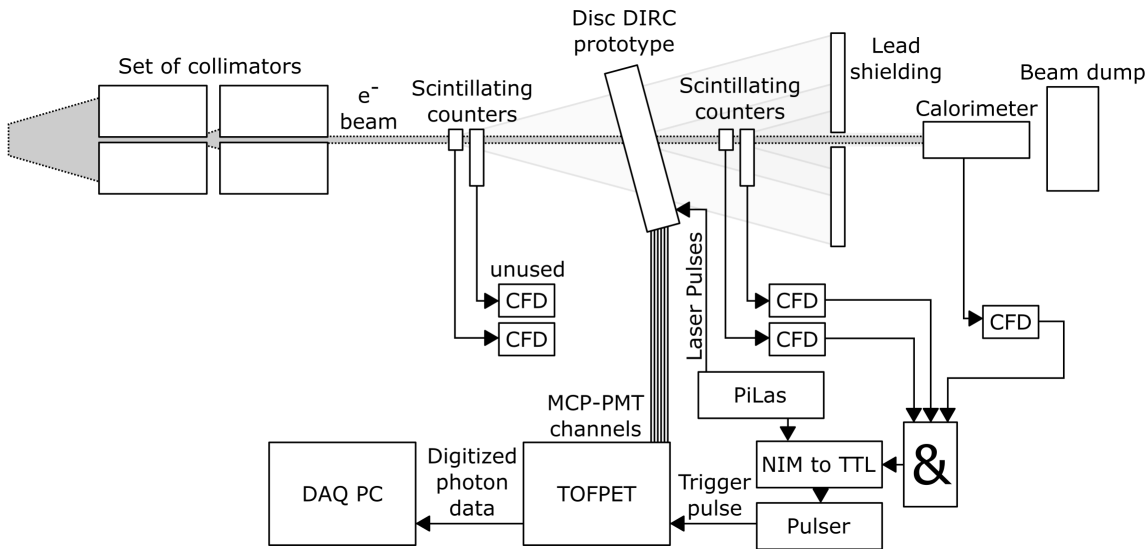
Figure 6.5: Schematic representation of the testbeam setup.

Before actual beam data were taken, a system check was performed with the help of the PiLas system. Unlike the measurements that were done with this laser in the lab, the intensity of the laser light was several orders of magnitude higher and the beam was not focused but simply injected into the radiator plate via a diffusor. From there, the light chaotically traveled through the disc under all possible angles, leading to the illumination of all channels of the MCP-PMT. Figure 6.6 shows the relationship between the pixel ID of the MCP-PMT and the time of arrival of the hit after subtracting the timestamp of the corresponding trigger pulse. That means that the first (upper) column occupies the channels 0 to 95, the central column occupies the channels 96 to 191 and the last (bottom)

column counts from 192 until 287. The time of arrival of the photons is smeared out by
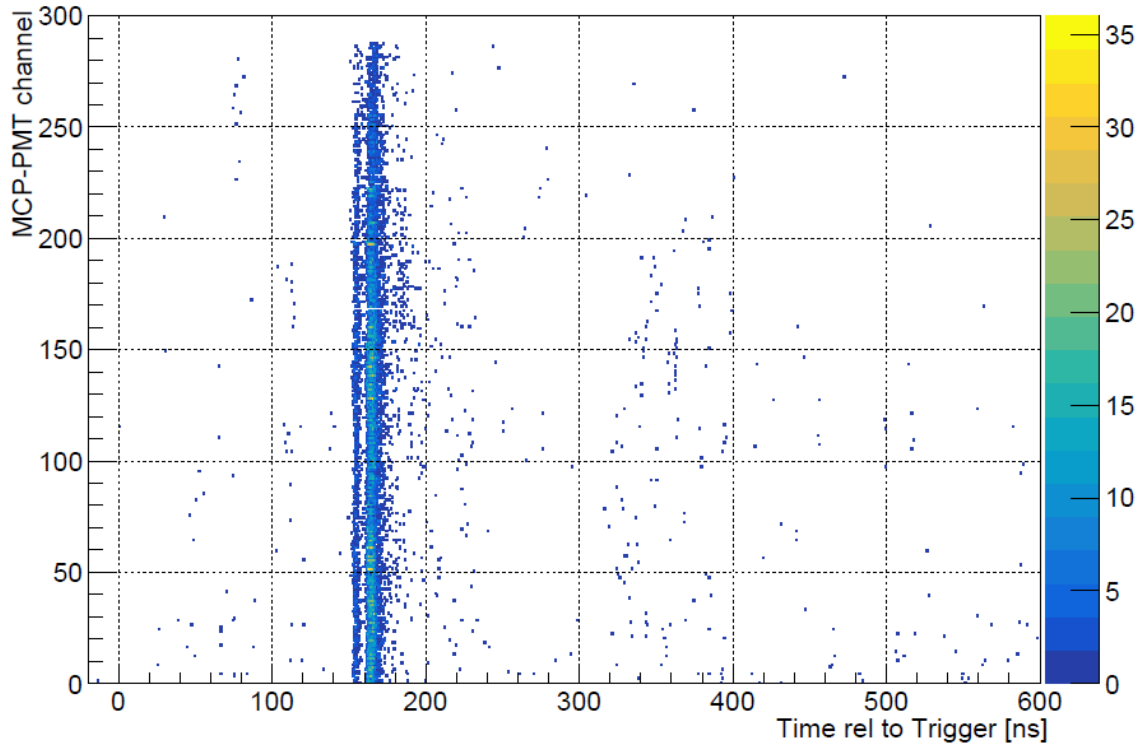
Figure 6.6: System check with the PiLas system: The time of arrival relative to the trigger pulse for all connected anodes of the MCP-PMT.

a couple of nanoseconds. This effect originates from different photon paths through the radiator. It should also be noted that this mode of operation has little to do with the single photon mode. During each laser pulse, each anode is probably struck by several photons and the pulse output of the sensor will deviate substantially from what is to be expected in a beam measurement. The thin line about 10 ns before the main one in figure 6.6 is an indication of this. It is only present in laser measurements and is likely to be caused by a capacitive coupling of the MCP stack to the anode as the MCP draws the strong currents it needs to supply the simultaneous avalanches all across the sensitive area of the photosensor. A cross check with the oscilloscope showed this signature at the exact same position, hence a false reading by the readout can be excluded. This effect has also been observed in the lab before the setup was brought to DESY. However, the laser test system is only supposed to show the functionality of the photon readout. A setup where all pixels are separately illuminated at the single photon level is desirable but practically much harder to build. After the successful test with the laser system, the trigger scheme was reset to the coincidence condition (see fig. 6.5) and actual beam data was taken. A

picture of the prepared prototype just before the area was left and the electron beam was switched on can be seen in figure 6.4,**E**.

6.3 Analysis of the data

The measurement program involved various position scans and angle scans which were done by rotating the prototype or moving it with the x-y-table. The interesting visualizations of the effects of rotating or moving the prototype and a comparison to predictions from a dedicated Monte Carlo simulation will be presented after an introduction into the analysis of the raw data. The first step of the analysis began directly after the data was taken at a given position and a given angle. A preliminary analysis was done with the help of online tools, specifically developed for quality assurance of the recorded data. This allowed to redo measurements in case some error or unpredictability occurred. The reliability of the analog trigger detection through the ASIC was also checked in a separate step. This was done by recording 10,000 digital trigger pulses created by the AND logic (see figure 6.5) without the use of the analog pulser that was connected to the ASIC. The difference in time between one trigger and the next one was derived and visualized in a histogram. In the next step the trigger pulses that the ASIC recorded from the analog output of the pulser were cross checked in the same way. A comparison can be seen in figure 6.7. It can be seen that the trigger setup with the analog pulser is indeed reliable. Thus the timestamps from the trigger channel could be used to identify Cherenkov photon hits in the time spectrum. This can be done by subtracting the timestamp of the corresponding trigger pulse from the timestamps of all other channels that recorded hits. This technique is very similar to what was done in the laboratory measurements presented in chapter 5. Again, the only difference is that the trigger pulse *after* the hits has to be associated with them.

The photon data taken at the position x = 453.9 mm and y = 170.5 mm (according to the coordinate system in figure 6.2) with a tilt angle of 14° will now be shown as an example of a typical run that was recorded. Practically speaking, the beam hit the radiator at the height of the central FEL of the ROM and was about 5 cm away from the opposing edge. The data taking for this run took 600 seconds and more than 1,000,000 triggers (electrons) were recorded. A very instructive plot can be generated by drawing the time of arrival of the hits (referenced to the trigger pulse) versus the pixel ID of the hit, just like we did for the laser measurement in figure 6.6. Figure 6.8 shows this plot for beam data where all 3 columns of the MCP-PMT have been drawn above each other again.
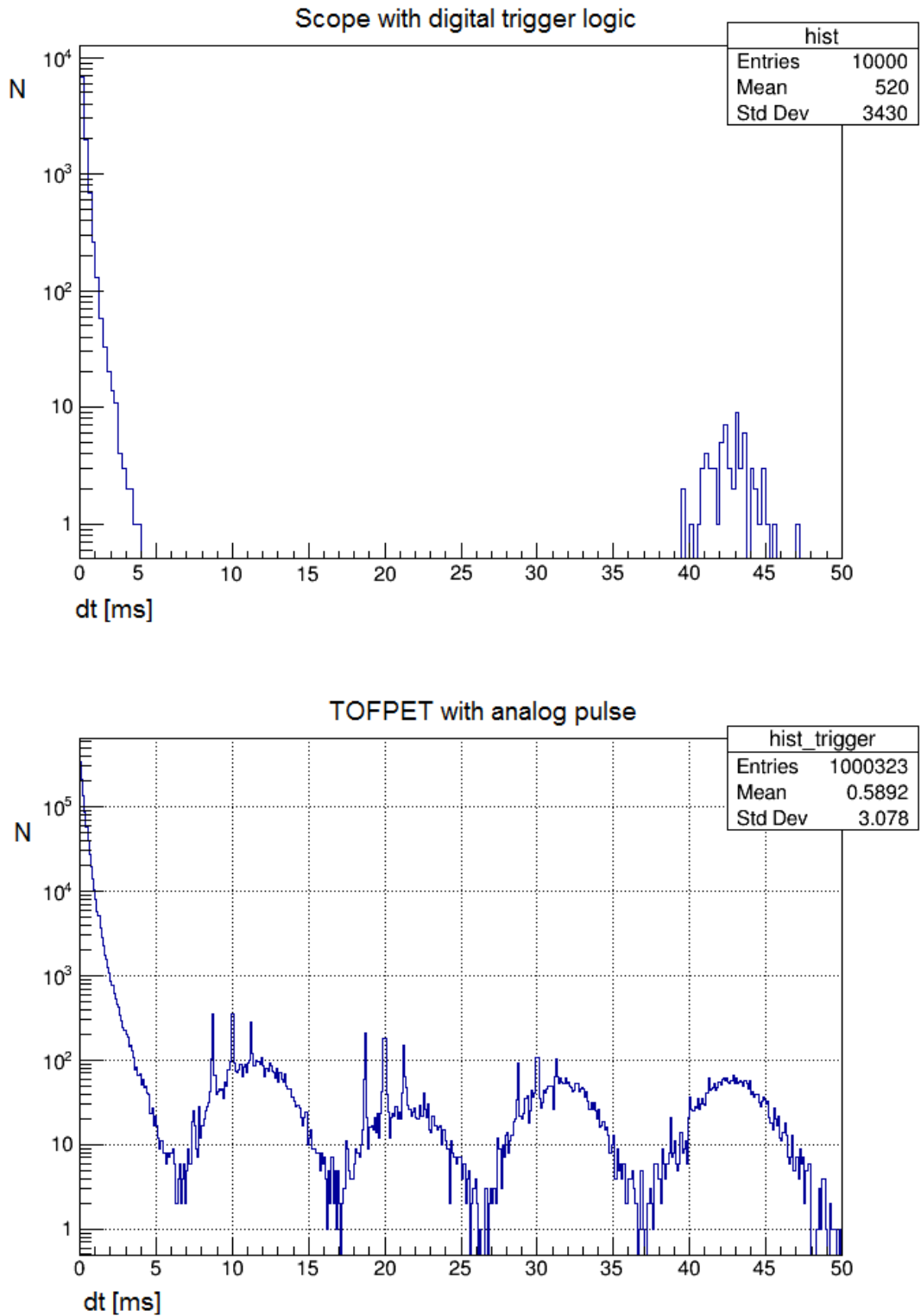
Figure 6.7: Time delay between consecutive trigger pulses: The upper plot shows a measurement with a fast oscilloscope connected to the digital output of the AND logic. 10000 events were recorded. The lower plot shows the same quantity as evaluated by the TOFPET. It can be seen that no more than 5 ms elapse between two consecutive electrons in the vast majority of events. There is also an interesting structure between 5 and 50 ms that was also partially visible in the scope measurement. It is probably related to machine specific properties of the testbeam facility.
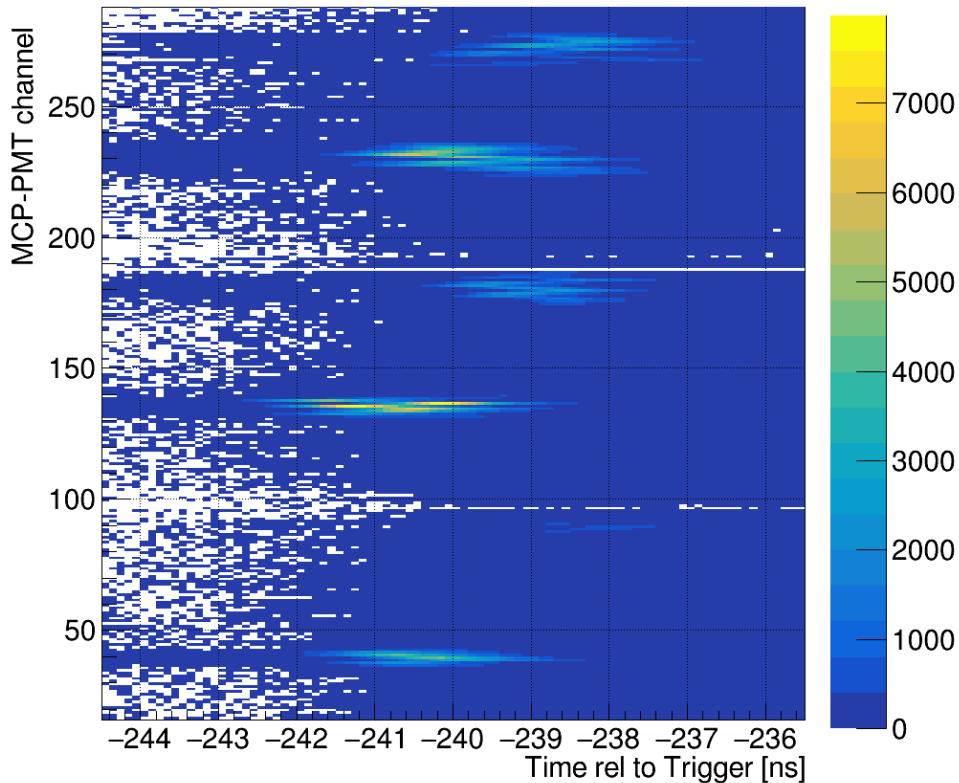
Figure 6.8: Position dependent time of arrival of Cherenkov photons. The relative displacements of individual channel times is caused by the TDC calibration which was performed with the help of an internal test pulse generator of the TOFPET. Consequently individual channel delays are not included in the calibration and the means of the distributions vary in the order of a nanosecond. In principle this figure can be used as a calibration for the channel timestamps.

The figure shows that the Cherenkov photons arrive about 240 ns prior to the trigger pulse, which corresponds to the latency of the trigger detectors and the logic units. As the time calibration for the individual TOFPET channels has been done with the internal test pulse generator, the time signatures of neighboring channels are not perfectly smooth and variations on the order of one nanosecond can be seen. However, the Monte Carlo study revealed that the time-of-arrival of the Cherenkov photons is also smeared out by about 0.5 ns due to the angular acceptance of the prisms (see section 6.4). It should be mentioned that the relative time shift of the individual channels is not an indicator for poor performance but can simply be calibrated with the help of figure 6.8.

After studying figure 6.8 an appropriate time window for photon gating can be set. Due to the excellent signal to noise ratio, one global window with a length of 10 ns was set, corresponding approximately to the time region that is shown in figure 6.8. The time window allows to discard almost all dark counts and show accumulated hit patterns. Fig-

ure 6.9 shows how the Cherenkov photons would hit the MCP-PMT if one were to look at the front of the sensor. The figure shows only the hits that are within the time gate
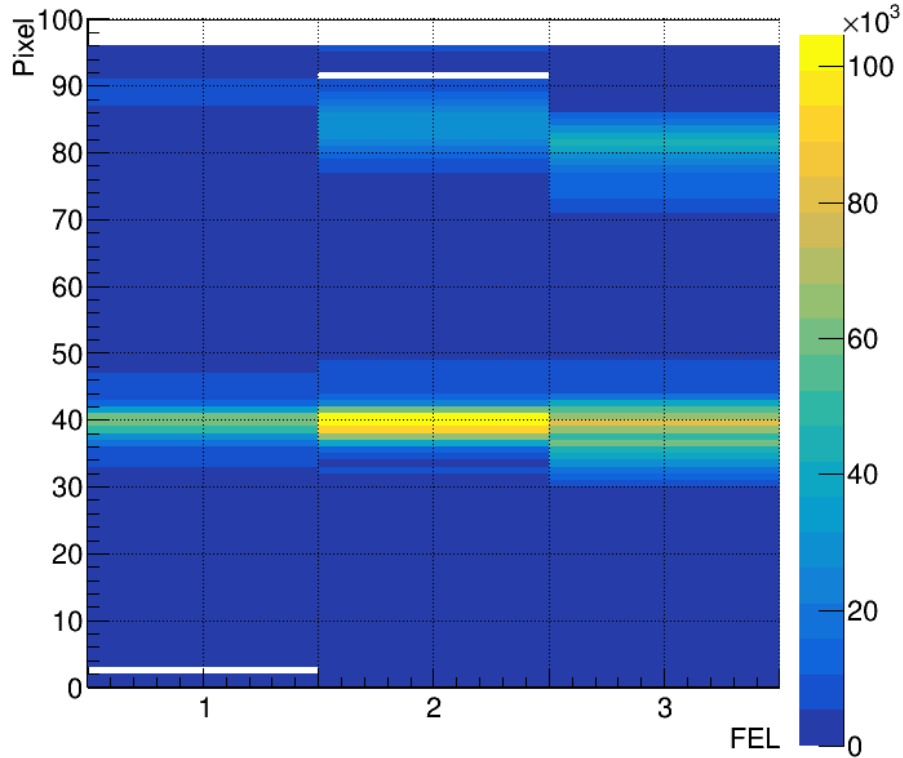
Figure 6.9: The hitpattern of the Cherenkov photon after applying timecuts.

window. A very clear Cherenkov peak can be seen in all three columns. It is also observable that each column shows a somewhat smaller peak several channels away from the direct Cherenkov peak. These structures are caused by photons that are reflected on the lower edge of the radiator plate and enter the FEL afterwards. These photons have the same Cherenkov angle, but their projected direction of travel has a steeper angle versus the normal vector of the FEL. In the language of section 2.3.4, the angle α_{FEL} is different what leads to a different position of impact for these photons. The two peak structure of each MCP-PMT column can be seen more clearly in the projections shown in figure 6.10.

From figures 6.9 and 6.10 it can also be seen that the central column of the MCP-PMT has the strongest photon signal, i.e. the most counts in the Cherenkov peak. This is due to the optical coupling of the FEL to the prism which was done differently for all three FELs. The optical contact bonding has a better optical quality due to the lack of micro bubbles and other impurities.

One can also see that in addition to the Cherenkov peaks for direct and indirect photons,

139
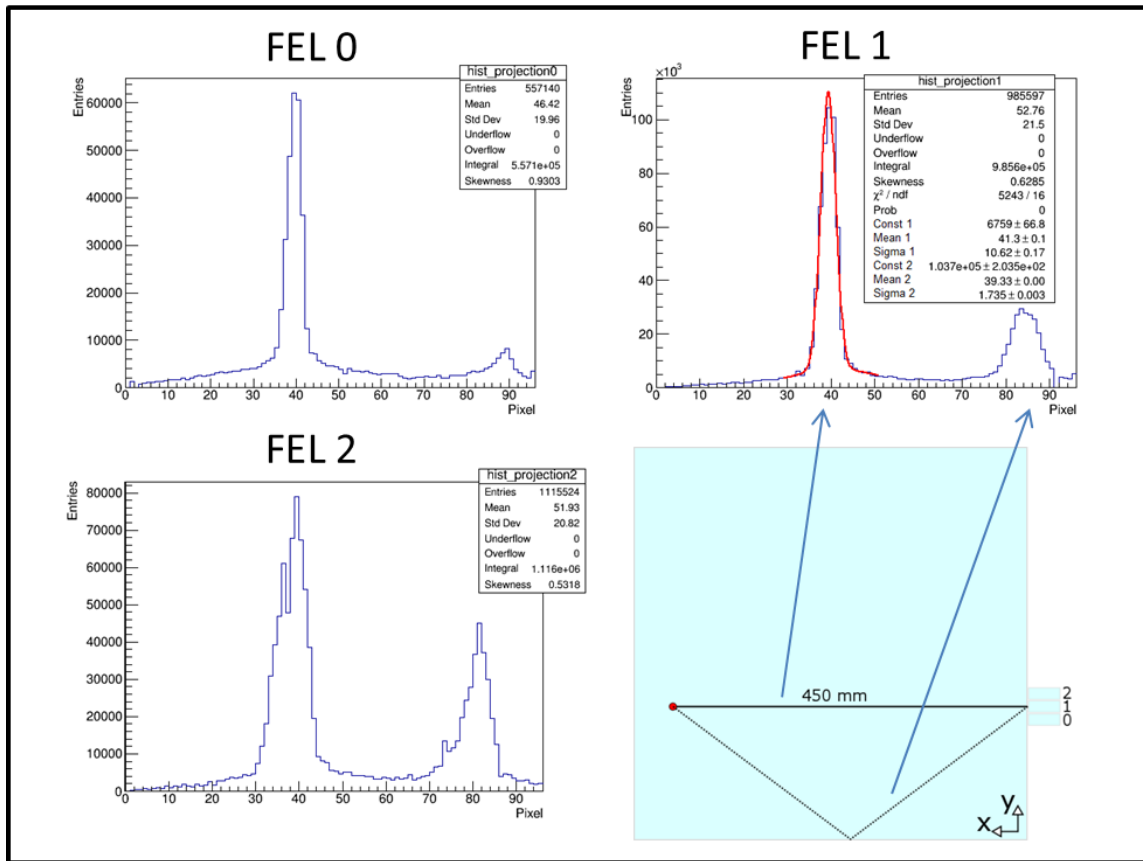
Figure 6.10: Cherenkov peaks in all columns of the MCP-PMT: The three plots represent one MCP-PMT column each. The amount of detected photons throughout the run can be read off the vertical axis while the pixel position along the column is represented by the horizontal axis. All columns registered direct and reflected photons. The width of the Cherenkov peak of the central column was fitted with the sum of two GAUSSIAN functions and a width of about 1.7 pixels is retrieved.

there is also some background underneath the signal. The background originates from optical stray light, from crosstalk (recoil) of the MCP-PMT and probably also from electron showers and deflections as a result of interactions between beam particles and air molecules.

Another interesting cross check is to examine the number of hits that are registered between two trigger timestamps. Like in the laboratory measurements the number of photons should be governed by POISSON statistics again. Figure 6.11 shows this distribution for this particular run. Figure 6.11 includes also a fit with a POISSON distribution which reveals a mean number of detected photons of about 3 (one per FLG), which corresponds nicely to Monte Carlo predictions as shown in section 6.4.

Another interesting feature is the time resolution that the combination of the MCP-PMT and the TOFPET readout can achieve. The time resolution can be derived by studying
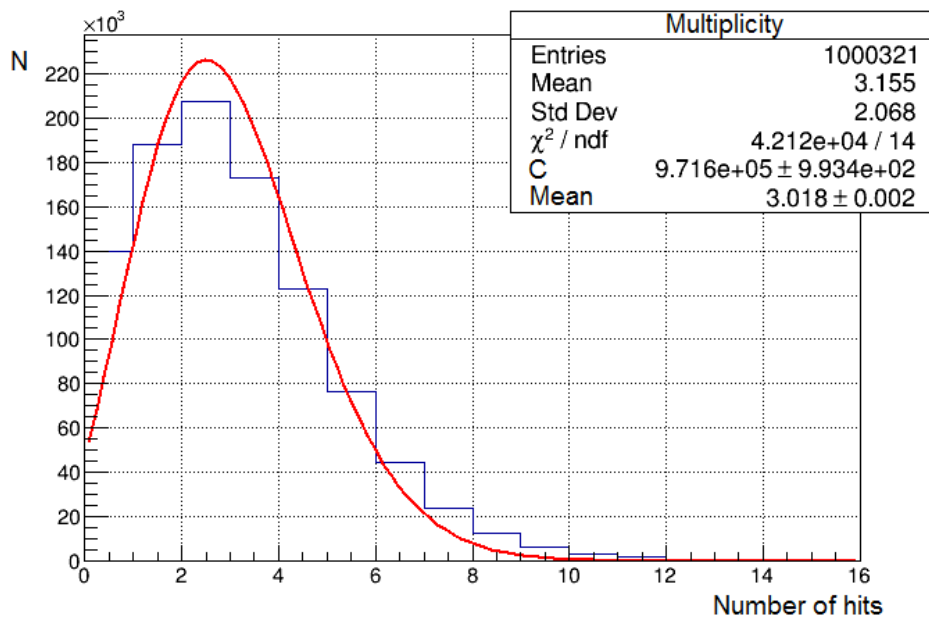
Figure 6.11: Hit statistics of the prototype: The number of registered hits between two trigger pulses has been fitted with a POISSON distribution and a mean of about 3 photons per event was retrieved.

the time difference between hits in one event. All uncertainties from the trigger system are avoided by this technique. Ideally the difference is taken between pixels that have some (spatial) distance to each other in order to avoid charge sharing or increased cross talk. The test beam provides an ideal environment to study this effect under very realistic conditions. The figures 6.12 and 6.13 show distributions of event based time differences between two pixels of the MCP-PMT. In figure 6.12 the difference was taken between one pixel of the FEL 0 that lies in the middle of the direct Cherenkov peak and a corresponding one of the FEL 2. This means that an entire column is between both pixels and charge sharing cannot cause both pixels to fire simultaneously. Consequently, the time differences correspond to events in which both pixels have been struck by Cherenkov photons individually. The resulting distribution has been fitted with the sum of two GAUSSIAN functions. While one function models the signal itself, the second one describes the background that mainly originates from charge sharing of neighboring anodes and from cross talk. A standard deviation of about 450 ps can be obtained from this measurement. This value has to be divided by $\sqrt{2}$ to account for the fact that both hits will be registered with individual uncertainties, leading to an individual time resolution of about 320 ps. The MCP-PMT alone should have a time resolution well below 100 ps and the TOFPET ASIC has a binning of 50 ps. Some additional uncertainty arises from the smearing of the time-of-arrival of the photons due to variations in path lengths. In the Monte Carlo

141
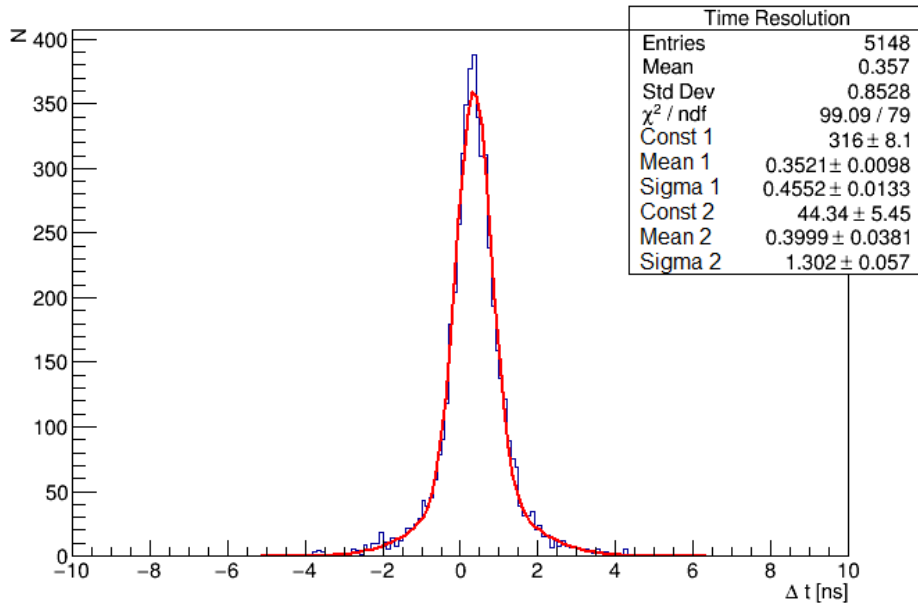
Figure 6.12: Time resolution obtained from time differences between two directly illuminated pixels. More information is given in the text.

simulation, the time smearing in the center of the Cherenkov peak exceeds 90 ps. Finally, the timing is not walk-corrected and the pulse height distribution of the output pulses will add more uncertainties.

It should be noted that at least some of the error contributions can still be lowered. The time smearing due to charge sharing of neighboring anodes will drop significantly if a magnetic field is applied. Since the time-over-threshold of the hits is available (see figure 6.14), a walk-correction could be implemented. A dedicated calibration procedure would be advantageous to exploit the full potential of this measure. Ideally, all pixels would be individually illuminated with single photons from a laser while a fast trigger is available. Then the time walk of each channel could be determined individually and the variations in the channel specific height of the baseline and local gain inhomogeneities of the MCP could be calibrated. With all that being said, the time resolution of 320 ps, achieved in these comparably adverse conditions, is already much better than the required design goal of one nanosecond. Another cross check of the time resolution can be done via taking the difference between the direct Cherenkov photons and the ones that were reflected on the lower edge of the radiator (see figure 6.10). In figure 6.13 the timestamps of the most active pixel in the peak for indirect photons are subtracted from the timestamps of the most active pixel in the direct Cherenkov peak. Like in figure 6.12 the resulting distribution was fitted with the sum of two GAUSSIAN functions. The time resolution is

worse by about 10 ps. By comparing the mean of the curves in the figures 6.12 and 6.13 it can be seen that the additional path length that the reflected photons have to travel is reflected in a mean difference of 2 ns in travel time. The two pixels that are struck by direct photons are only a few hundreds of picoseconds apart. All these findings are backed up by the Monte Carlo simulation.
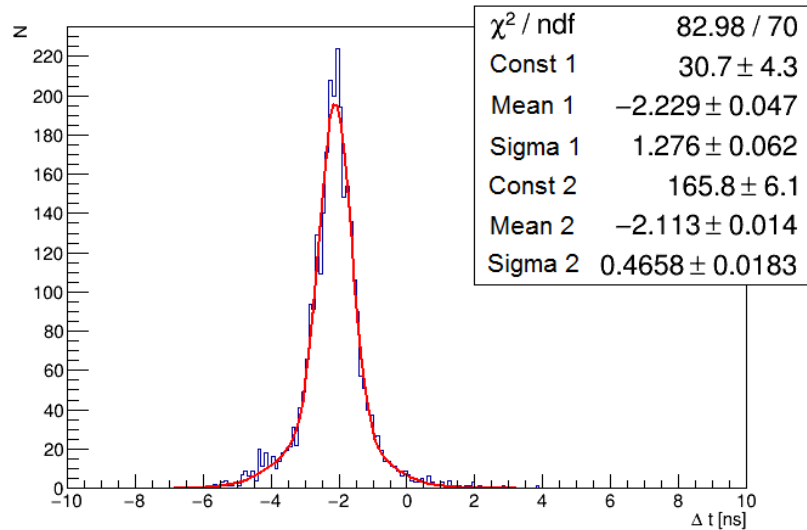
Figure 6.13: Time differences between a directly and an indirectly illuminated pixel. A fit with two GAUSSIAN functions reveals a combined width of about 465 ps.
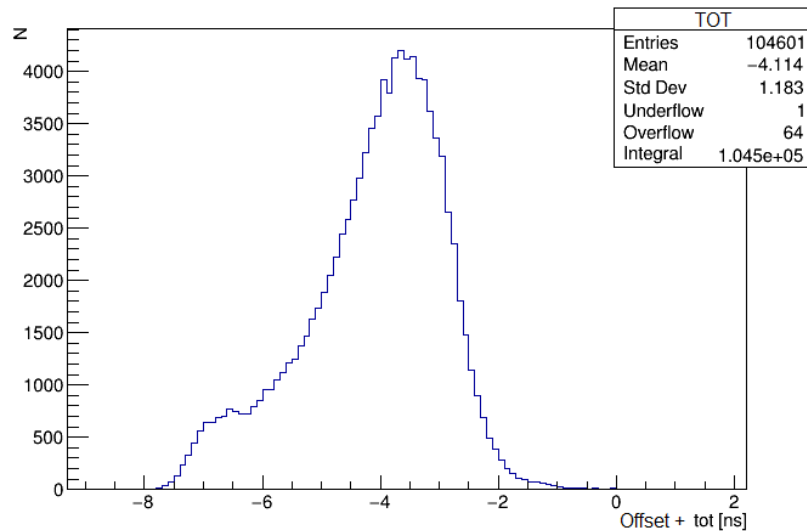
Figure 6.14: The time-over-threshold (TOT) distribution of all hits belonging to the most active pixel of the central FEL (pixel 39 of FEL 1 in figure 6.10).

6.4 Monte Carlo simulation

As previously stated, a dedicated Monte Carlo simulation of the run that was studied so far has been done by M. SCHMIDT [61]. The whole geometry of the prototype has been included in a full standalone GEANT 4 simulation. The properties of the optical components, the quantum efficiency and the collection efficiency of the MCP-PMT have been taken into account as well. A toy model for the charge sharing of the MCP-PMT (but not for cross talk) was also implemented. In the simulation 1000 electrons were fired at the prototype at the same parameters as in the real measurement (x = 453.9 mm y = 170.5 mm and $\varphi = 14°$). The smearing of the particle tracks according to the beam specifications at DESY has been accounted for as well. However, one unknown property is the reflectivity of the mirror coating of the FEL for low wavelength light. Figure 6.15 shows a measurement that was done by the manufacturer of the FELs. Unfortunately,
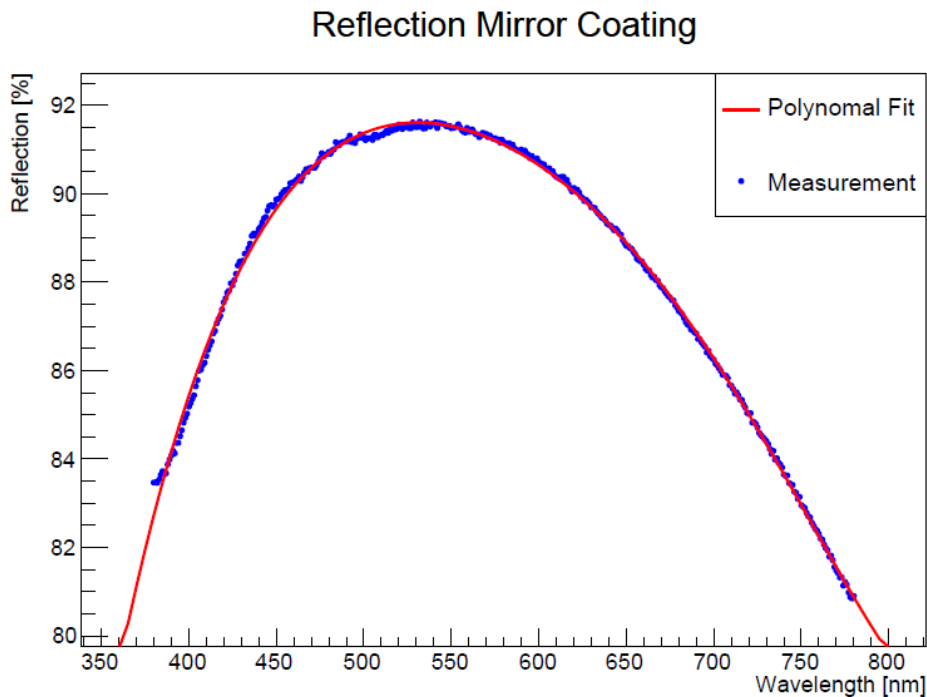
Figure 6.15: The reflectivity of the FEL mirror is only measured between about 375 to 775 nm. An extended measurement is necessary to properly predict Cherenkov patterns.

the measurement was only done with wavelengths down to about 375 nm. The measurements with smaller wavelengths were underway at the time of writing of this work. The available data were fitted with a polynomial and the extrapolation was used to predict the behavior of the coating in the region where no data had been taken. Unfortunately, this uncertainty has a rather strong impact on the expected width of the Cherenkov peak

due to growing dispersion effects.
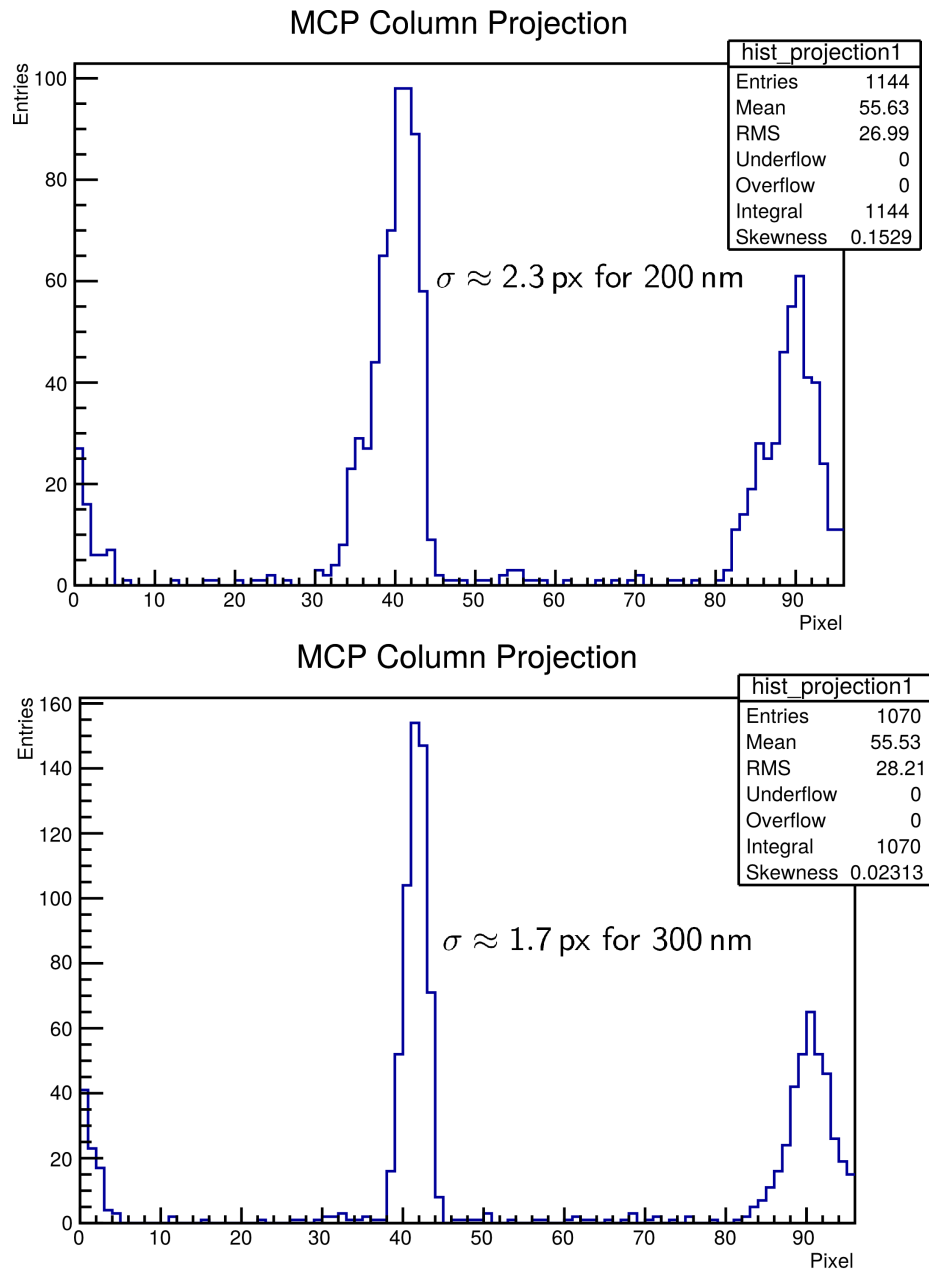
Figure 6.16: Width of Cherenkov peaks for different reflectivities of the FEL mirror as predicted by MC studies [61]. The width depends on the cut-off wavelength of the mirror reflectivity. If a wavelength of 300 nm is chosen, a width of 1.7 pixels is obtained.

Figure 6.16 illustrates that the width of the Cherenkov peak shrinks from 2.3 pixels to 1.7 pixels if the cut-off wavelength is shifted from 200 nm to 300 nm. This means that the theoretical width of the Cherenkov peak cannot be determined without additional knowledge about the reflectivity of the mirror. According to figure 6.10 a cut-off wavelength

145

of 300 nm would lead to the best agreement with the measurement where a result of 1.7 pixels was obtained. The number of photons per trigger (about 1 photon per trigger per FEL) is also in nice agreement with the actual measurement.
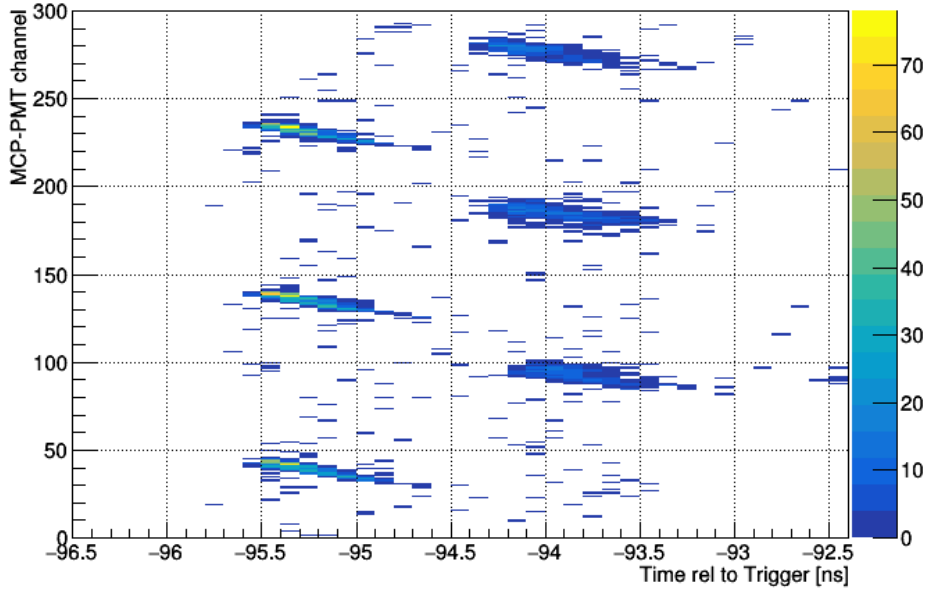
Figure 6.17: Position dependent time of arrival of Cherenkov photons in the MC study.

Figure 6.17 shows the simulated version of figure 6.8. The lack of background compared to the actual measurement comes mainly from the absence of cross talk (recoil electrons) and interactions between beam particles and air molecules. Apart from that the relative positions of the structures that correspond to direct and reflected photons are very similar and an overall confirmation of the measurement.

6.5 Parameter Scans

In this section the influence of the track parameters on the impact position of the Cherenkov photons will be analyzed. Parameter scans have been done during the beam time to allow systematic studies. All runs of these scans have been analyzed similarly to the example run discussed in the preceding section. Table 6.2 gives an overview of the parameter scans that will be shown.

Scan	x [mm]	y [mm]	φ in degree	# runs	Figure	Comment
Angle scan	450	170	from 0 to 22 in steps of 2	12	6.19	Beam spot on same height as the central FEL
High resolution y scan	347	from 2.6 to 495.6 in steps of 17	10	30	6.20	Step size corresponds to the width of one FEL
X,Y Scan part 1	250	from 19.6 to 478.6 in steps of 51	15	10	6.21	Step size corresponds to the width of one ROM
X,Y Scan part 2	350	from 19.6 to 478.6 in steps of 51	15	10	6.22	Step size corresponds to the width of one ROM
X,Y Scan part 3	450	from 19.6 to 478.6 in steps of 51	15	10	6.22	Step size corresponds to the width of one ROM

Table 6.2: Overview of the analyzed parameter scans.

As stated in section 2.3, the angle of the incoming charged particle with respect to the radiator plane has a direct influence on the angle of travel of the Cherenkov photon. During the angle scan the beam hit the radiator far away from the ROM (x = 450 mm). The distance of the beam spot reduces the angular smearing due to the angular acceptance of the prism. Additionally, the beam struck at the height of the central FEL (y coordinate), resulting in α_{FEL} being (close to) 90°. Both facts (i.e. small angular smearing and $\alpha_{\text{FEL}} \approx 90°$) combined allow the assumption that a rotation of the prototype by an angle φ will also increase/decrease the angle of travel of all Cherenkov photons that enter (the central) FEL by φ, as illustrated in figure 6.18. The imaging function of the FEL responds to linearly changing angles of travel with a linear shift in the position of photon impact in its focal plane. Consequently, the result of the rotation of the prototype should lead to a linear displacement of the
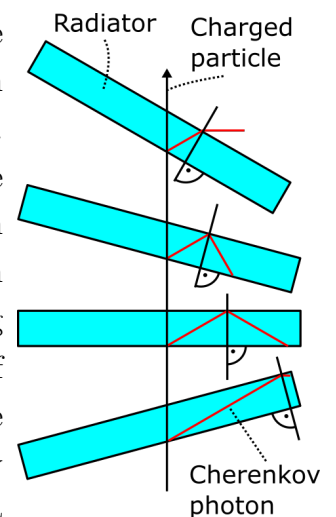
Figure 6.18

Cherenkov peak. A look at figure 6.19 reveals that this prediction is confirmed by the data. As expected, scanning an angular range of 22° suffices to scan across the entire
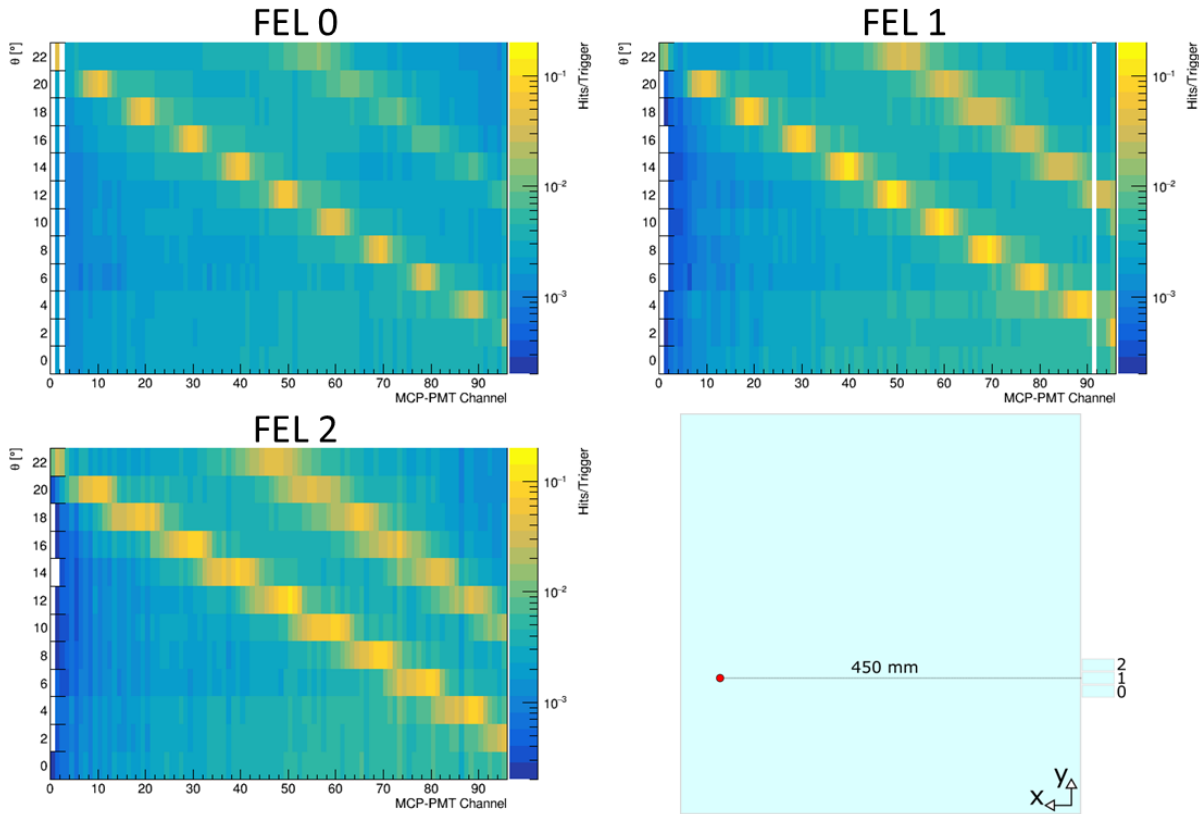
Figure 6.19: The angle scan. A rotation of the prototype translates into a linear displacement of the Cherenkov peak.

angular acceptance of the ROM. It can also be seen that the peaks that correspond to the reflections are also shifted during rotation. Some more generic observations can also be drawn from the figure. Firstly, the FEL 0 shows strongly reduced light yield. This was to be expected since big air bubbles were caught between the prism and the FEL during their gluing. According to laser measurements [54], a reduction in light yield of about 40% can be expected in comparison to the almost flawlessly coupled FEL 1. This number is confirmed by the comparison of both FELs in figures 6.10 and 6.19. For example, figure 6.10 shows a reduction in light yield of 557140 versus 985597 photons corresponding to about 43% loss.

Secondly, FEL 2 shows a somewhat broadened imaging function, leading to increased widths of the Cherenkov peak in a systematic fashion. A possible reason for this might be an optical imperfection because the phenomenon is visible over the whole column.

The next parameter scan from table 6.2 is the *high resolution y scan*. It was done at a fixed

angle and the x coordinate of the beam spot was also left constant throughout the scan. The main goal is to simulate a fully equipped radiator edge, i.e. the hypothetical situation that one entire radiator edge is connected to FELs without any gaps between them. Instead of actually building such a prototype with 30 FELs and doing one measurement, 30 measurements were done with the available prototype. This *trick* works if the beam spot is moved at a step size that corresponds to the width of one FEL. Only the photons that are reflected off the lower edge of the radiator are not fully comparable in both scenarios.
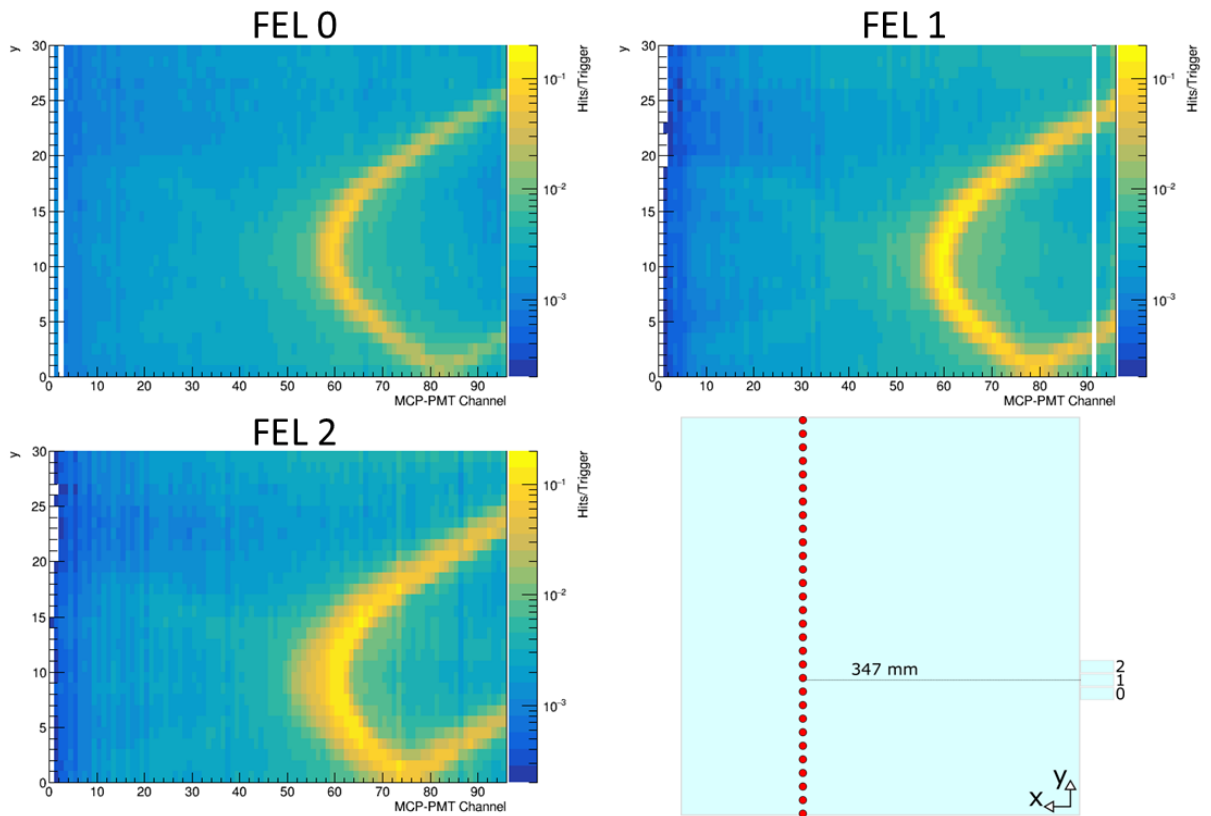
Figure 6.20: The high resolution y scan simulates a fully equipped radiator. The resulting structure is often called *Cherenkov Smile*.

Figure 6.20 shows a summary of this scan. Approximately 90 Gigabytes of raw data were recorded in more than 5 hours of beam time for this illustration. The distinct shape of the resulting structure (sometimes called *Cherenkov smile*) shows the importance of a precise knowledge of the track parameters for the working principle of this detector. All photons have the same Cherenkov angle but due to the track angle and different angles α_{FEL} each FEL projects the entering photons on a different pixel of the MCP-PMT. The careful observer will notice a second smile that looks like a mirror image (mirrored with

respect to a vertical line at about channel 50) of the primary one, but much weaker in intensity. This structure has been also predicted by Monte Carlo simulations and is caused by additional reflections in the FEL [21].

In the limit that the distance of the beam spot and the instrumented radiator edge is infinite, figure 6.20 would show a vertical line. The shorter this distance becomes, the more *smile-like* will the response of the focusing optics become. In other words: A decrease of the distance between beam spot and radiator edge will increase the curvature of the Cherenkov smile. This prediction was also systematically explored with a series of y-scans taken at different distances from the instrumented radiator edge. As shown in table 6.2, three y-scans were done at distances of 250 mm, 350 mm, and 450 mm, respectively. This time the step size was increased threefold to 51 mm which corresponds to the width of one ROM instead of one FEL like in figure 6.20. Additionally, the radiator was rotated to 15° in order to capture a bigger part of the smile, i.e. to move it towards lower MCP-PMT channel numbers. The analysis of these 3 scans can be seen in the figures 6.21 and 6.22.
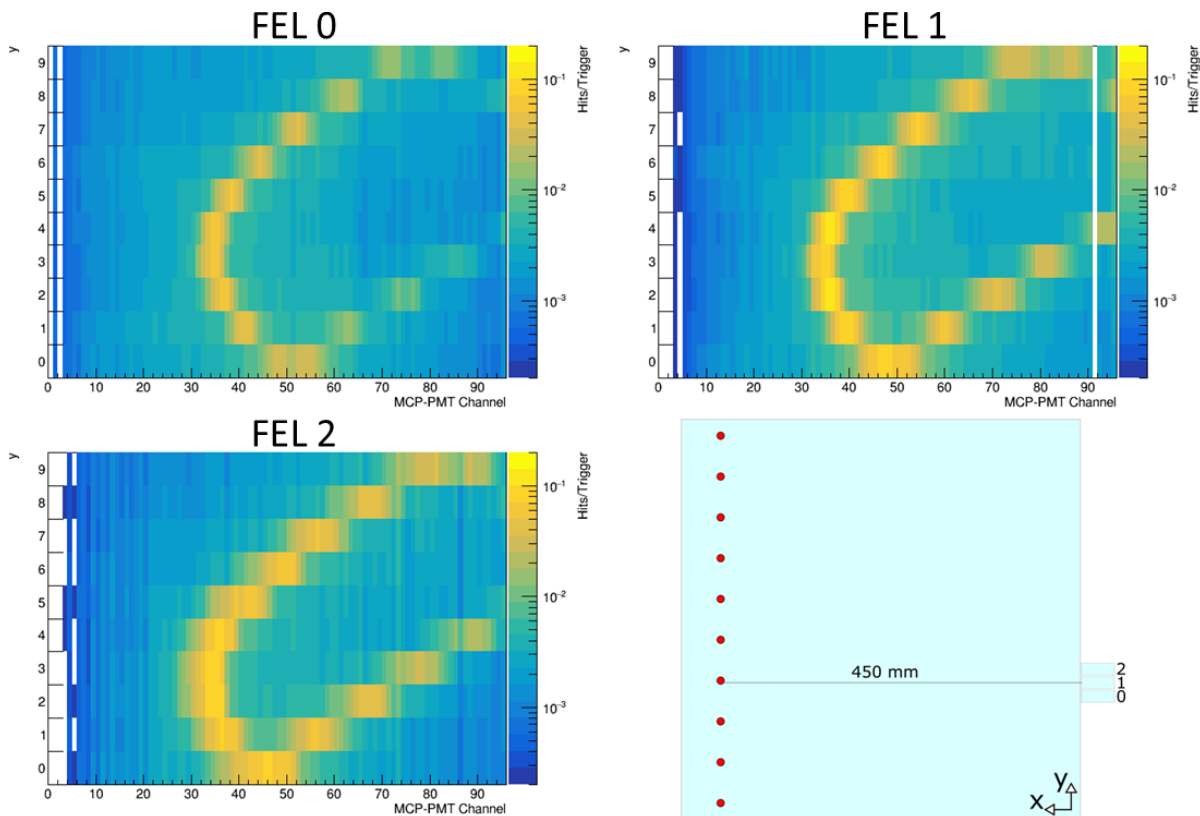
Figure 6.21: Part 1 of the XY Scan shows the smallest curvature.
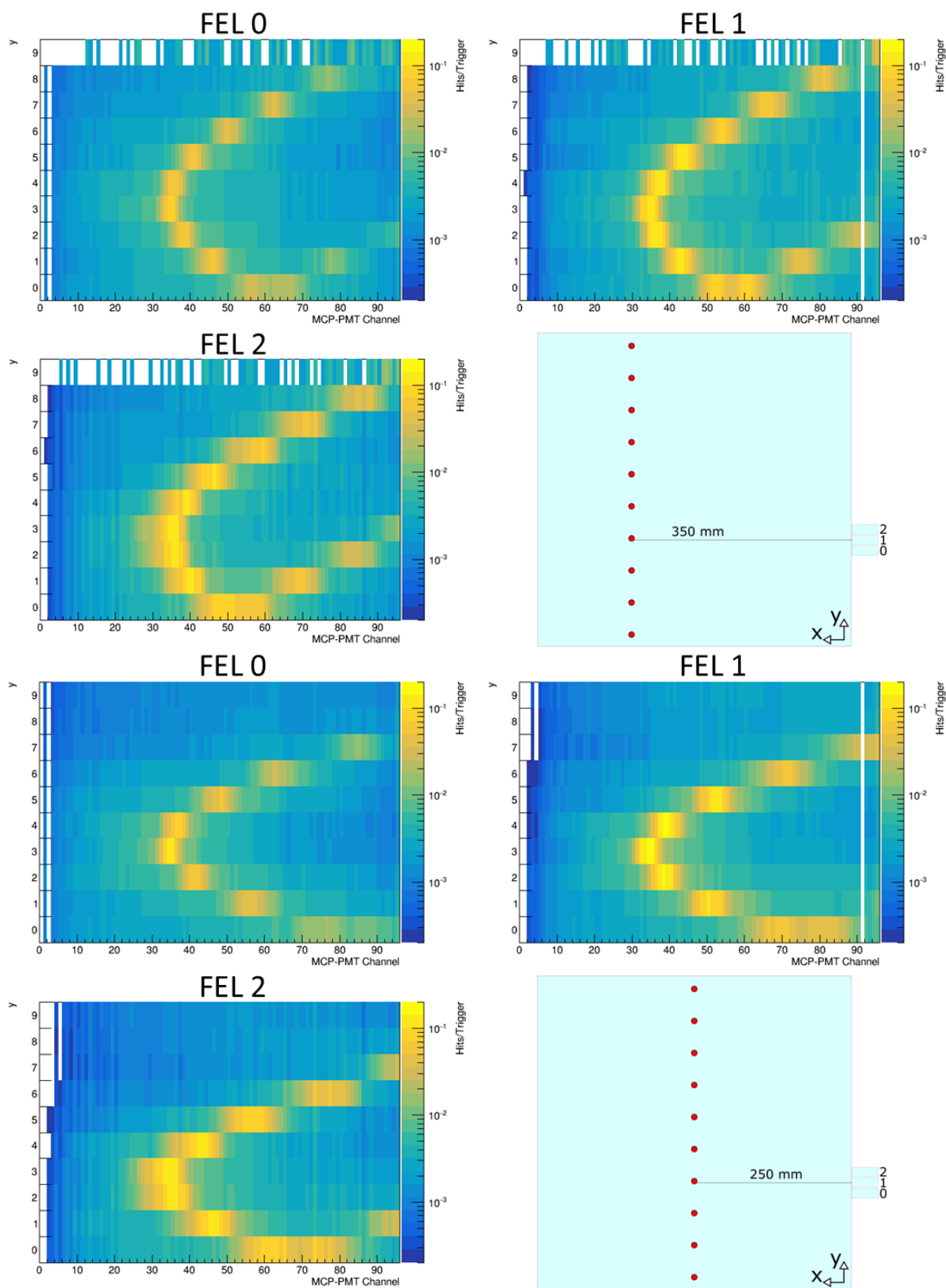
Figure 6.22: A decrease in the distance between the beam spot and the instrumented radiator edge translates into an increase in the curvature of the Cherenkov smile.

151

The figures show that the curvature does in fact increase with less distance between the beam and the readout. It can also be seen that the Cherenkov peaks are broader at closer distances which is a direct consequence of the (azimuthal) angular acceptance of the FELs.

In summary, this testbeam was a very successful demonstration of the capabilities of the Photonis MCP-PMT and the TOFPET ASIC readout. The single photon resolution and the number of detected photons agree with Monte Carlo predictions and the time resolution is already within the design constraints with more room for improvement.

Additional analysis of the recorded data as well as comparison with more elaborate and detailed Monte Carlo simulations will also be published in [61].

7 Summary and Outlook

In this thesis it has been shown that the TOFPET ASIC is a very suitable device for the electronic readout of MCP-PMTs with finely segmented anode geometries. This has been confirmed by measurements in the laboratory as well as during the testbeam campaign at DESY. The demands on the temporal and spatial resolution of the photon detection system have been reached with this combination and single (Cherenkov) photons have been registered with high efficiency and performance.

The MCP-PMTs that have been used with the TOFPET ASIC have been evaluated with different test setups. The changes of the performance parameters in magnetic fields have been studied with permanent magnets and with a strong electric dipole magnet. The sensors have been read out with the TOFPET ASIC and with fast oscilloscopes and the test setups are ready to be used for future quality assurance of new devices. It has been found that the magnetic fields at PANDA will improve the position resolution of the MCP-PMT based photon readout. The compression of the charge cloud by the magnetic field is strong enough to minimize charge sharing up to a point where only one anode can capture the entire electron avalanche what also leads to reduced data rates. At the same time, cross talk - caused by recoil electrons - is heavily reduced by the magnetic fields. However, even magnetic fields strengths of about $800\,\mathrm{mT}$ did not cause strong undersampling in the transition region between two anodes, which would lead to a loss of detection efficiency.

A very successful testbeam campaign with $3\,\mathrm{GeV/c}$ electrons has been undertaken at DESY with the 2016 EDD prototype. This was the first testbeam where only close-to-final components have been used as far as the optics and the photon readout are concerned. The results that have been obtained are in good agreement with a dedicated Geant 4 simulation. Especially the width of the measured Cherenkov peaks (i.e. the single photon resolution) and the number of detected Cherenkov photons meet the expectations. The testbeam has also been used to infer the time resolution of the photon detection system which has been measured to be about $320\,\mathrm{ps}$ without further corrections (e.g. for time walk) applied. From the author's point of view, future steps towards the design and
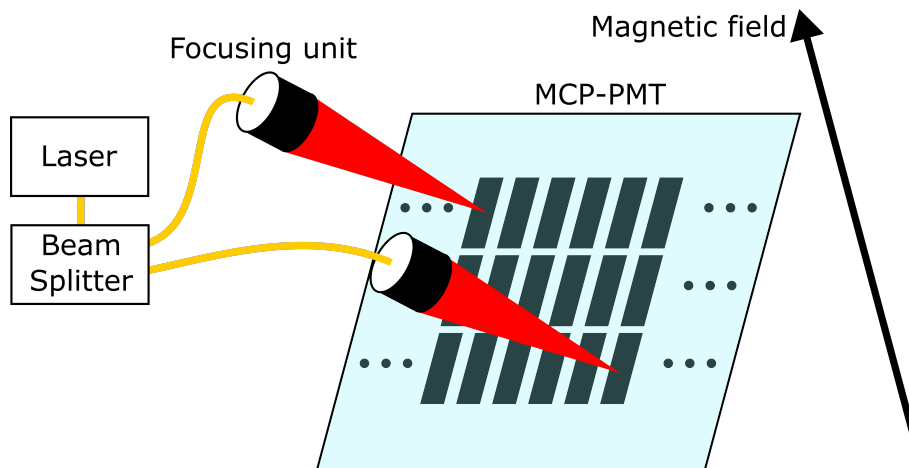
Figure 7.1: Possible setup for further studies of the single photon time resolution.

production of a final photon detection system for the EDD should include the actions described hereafter.

The time resolution of the system can be studied in more depth with a setup like the one illustrated in figure 7.1 which could be built like the setups presented earlier but with a second focus optic included. This would allow to simultaneously illuminate anodes with enough distance between them to exclude charge sharing or cross talk with single photons. The time difference between hits in both anodes can be taken what helps by avoiding jitter from trigger circuits. In comparison to the testbeam setup, the main advantages are an improved focusing of the incoming light and the possibility to apply magnetic fields.

A deeper study of the rate capability of the final photon detection system could be done similarly to the study that has been presented in chapter 3 (see figure 3.15). The only additional hardware that would be needed is an optic which homogeneously illuminates the entire active area of the sensor. This study should also be done in the presence of a magnetic field. With this setup, one could test the rate capability of the entire photon detection system. It should be noted here, that the maximum rate per channel of the TOFPET ASIC of 160 kHz - as assured by the manufacturer - is absolutely sufficient and exceeds the rate capability of the MCP-PMT. Still, a confirmation in a real experiment would resolve any doubts.

The 2016 EDD prototype consisted of only one ROM. Tests with multiple ROMs, all read out by one TOFPET DAQ system, e.g. with the help of the Giessen muon cosmics teststand would be exciting and useful.

PETSYS Electronics - the manufacturer of the TOFPET ASIC - is currently developing the next iteration of the ASIC: The TOFPET ASICv2. This iteration includes some

major improvements like improved rate stability, dynamic range and more efficient data handling. It would be interesting to test this next version and study the usefulness of the improvements for the EDD project.

Danksagung

Bibliography

[1] *FAIR, Facility for Antiproton and Ion Research, Green Paper - The Modularized Start Version*, http://www.fair-center.eu/fileadmin/fair/publications_FAIR/FAIR_GreenPaper_2009.pdf

[2] *FAIR, Baseline Technical Report, Executive Summary*, ISBN 3-9811298-0-6

[3] https://panda.gsi.de/article/panda-detector-overview, Accessed in January 2017

[4] A. Khoukaz et al. on behalf of the PANDA Collaboration, *Technical Design Report for the PANDA Internal Targets*, March 2012, available via http://www.fair-center.eu/

[5] K. Brinkmann et al. on behalf of the PANDA Collaboration, *Technical Design Report for the PANDA Micro Vertex Detector*, November 2011, arXiv:1207.6581

[6] P. Gianotti et al. on behalf of the PANDA Collaboration, *Technical Design Report for the PANDA Straw Tube Tracker*, Eur. Phys. J. A (2013) 49: 25, DOI: 10.1140/epja/i2013-13025-8

[7] L. Schmitt, *PANDA Detector Overview* (Talk), PANDA Russia Workshop, 25-27 May 2015, Moscow, Russia

[8] F. Sauli, *The gas electron multiplier (GEM): Operating principles and applications*, Nucl. Instr. and Meth. 805 (2016) 2–24, http://dx.doi.org/10.1016/j.nima.2015.07.060

[9] I. Lehmann et al. on behalf of the PANDA Collaboration, *Technical Design Report for the PANDA Solenoid and Dipole Spectrometer Magnets*, February 2009, available via https://panda.gsi.de/oldwww/archive/public/P_magn_TDR.pdf

[10] G. Alexeev et al. on behalf of the PANDA Collaboration, *Technical Design Report for the PANDA Muon System*, September 2012, available via http://www.fair-center.eu/fileadmin/fair/publications_exp/Muon_TDR.pdf

[11] F. Heinsius et al. on behalf of the PANDA Collaboration, *Technical Design Report for the PANDA Electromagnetic Calorimeter*, October 2008, arXiv:0810.1216v1

[12] M. Albrecht et al., *The Forward Endcap of the Electromagnetic Calorimeter for the PANDA Detector at FAIR*, Journal of Physics: Conference Series, Volume 587 (2015), doi:10.1088/1742-6596/587/1/012050

[13] S. Brunner et al., *Time resolution below 100 ps for the SciTil detector of PANDA employing SiPMs*, January 2014, arXiv:1312.4153v2

[14] C. Mead, *Quantum Theory of the Refractive Index*, Phys. Rev. 110, 359 (1958)

[15] J. Vavra, *Optical properties of RICH detectors*, Nucl. Instr. and Meth. A 766 (2014) 189–198

[16] C. Schwarz et al., *The PANDA Barrel DIRC*, JINST 11 (2016) C05013

[17] J. Schwiening et al., *The PANDA Barrel DIRC* (Talk), 9th International Workshop on Ring Imaging Cherenkov Detectors (RICH 2016), 5-9 September 2016, Bled, Slovenia

[18] M. Traxler et al., *TRB development* (Talk), International Workshop on Fast Cherenkov Detectors - Photon detection, DIRC design and DAQ, November 11–13, 2015, Giessen, Germany.

[19] M. Düren al., *The PANDA time-of-propagation disc DIRC*, JINST 4 (2009) C12013

[20] M. Düren al., *The PANDA 3D Disc DIRC*, JINST 7 (2012) C01059

[21] O. Merle, *Development, design and optimization of a novel Endcap DIRC for PANDA*, Dissertation JLU Giessen, (2014)

[22] D. Bettoni et al. on behalf of the PANDA Collaboration, *Physics Performance Report for PANDA: Strong Interaction Studies with Antiprotons*, arxiv:0903.3905.

[23] O. Merle, *Development of Reconstruction Methods and Algorithms for the PANDA Disc DIRC*, Diploma Thesis, JLU Gießen (2009)

[24] M. Rolo et al., *TOFPET ASIC for PET applications*, JINST 8 (2013) C02050

[25] M. Patsyuk, *Simulation, Reconstruction, and Design Optimization for the PANDA Barrel DIRC*, Dissertation, Johann Wolfgang Goethe-Universität Frankfurt am Main (2014).

[26] D. Lange, *The EvtGen particle decay simulation package*, Nucl. Instr. and Meth. A 462 (2001) 152-155

[27] F. Tokanai et al., *Newly developed gaseous photomultiplier*, Nucl. Instr. and Meth. A 766 (2014) 176-179

[28] T. Sumiyoshi et al., *Development of a gaseous PMT with micro-pattern gas detectors*, Nucl. Instr. and Meth. A 639 (2011) 121–125

[29] C. Natarajan et al., *Superconducting nanowire single-photon detectors: physics and applications*, http://dx.doi.org/10.1088/0953-2048/25/6/063001

[30] L. Redaelli et al. *Design of broadband high-efficiency superconducting-nanowire single photon detectors*, arXiv:1602.06846

[31] J. Rieke et al., *Resolution changes of MCP-PMTs in magnetic fields*, 2016 JINST 11 C05002

[32] H. Ibach, H. Lueth, *Festkörperphysik*, 7. Auflage, p. 436, Springer Verlag

[33] F. Thusel, *Physik der Halbleiterbauelemente*, Chapter 3, Springer Verlag

[34] T. Frach, *Optimization of the digital Silicon Photomultiplier for Cherenkov light detection*, 2012 JINST 7 C01112

[35] Y. Qiang et al., *Radiation hardness tests of SiPMs for the JLab Hall D Barrel calorimeter*, Nucl. Instr. and Meth. A 698 (2013) 234–241

[36] R. Heilmann, *Geschichte der Lichtsensorik*, Fachhochschule München, http://dodo.fb06.fh-muenchen.de/heilmann/PDFs/Geschichte_Lichtsensorik.pdf, June 2016

[37] S. Jokela et al., *Secondary electron yield of emissive materials for large-area micro-channel plate detectors: surface composition and film thickness dependencies* doi:10.1016/j.phpro.2012.03.718

[38] W. Demtröder, *Experimentalphysik 3*, Atome, Moleküle und Festkörper, 3. Auflage, ISBN 3-540-21473-9

[39] J.A. Bittencourt, *Fundamentals of Plasma Physics*, ISBN: 978-0-387-20975-3

[40] P. T. Farnsworth, Electron Multiplier, US Patent Office, 1930, US 1969399 A

[41] J.L. Wiza, *Microchannel Plate Detectors*, Nucl. Instr. and Meth. Vol. 162, (1979) 587–601

[42] Serge Duarto Pinto, PHOTONIS TECHNOLOGIES, private communication, 2015

[43] A. Lehmann et al., *Studies of MCP properties*, 2009 JINST 4 P11024

[44] A. Lehmann et al., *CERN MCP-TOF Results*, TOF-Meeting, Vienna, 01.12.2015

[45] A. Lehmann et al., *Lifetime of MCP-PMTs*, Talk at the DIRC 2015, Rauisch-holzhausen, 11.11.2015

[46] A. Lehmann et al., *Recent Developments with Microchannel-Plate PMTs*, Talk at the RICH 2016, Bled, 06.09.2016

[47] F. Uhlig et al., *Performance studies of microchannel plate PMTs*, Nucl. Instr. and Meth. A 695 (2012) 68-70

[48] F. Uhlig , *Charakterisierung und Anwendung von schnellen Photosensoren im Hinblick auf ihren Einsatz im PANDA-Experiment*, Dissertation Friedrich-Alexander-Universität Erlangen-Nürnberg, (2015)

[49] A. Britting, *Analyse und signifikante Verbesserung der Lebensdauer von Microchannel-Plate Photomultipliern hinsichtlich ihrer Applikation für das PANDA-Experiment*, Friedrich-Alexander-Universität Erlangen-Nürnberg, (2013)

[50] M. Barnyakov and A. Mironov, *Photocathode aging in MCP PMTs*, 2011 JINST 6 C12026

[51] A. Brandt, *MCP-based detectors for ultra-fast timing applications*, Workshop on micro-channel plate based detectors, 04.12.2014

[52] A. Lehmann et al., *Lifetime of MCP-PMTs*, 2016 JINST 11 C05009

[53] http://www.petsyselectronics.com/web/, Accessed in January 2017

[54] E. Etzelmüller, *Developments towards the Technical Design and Prototype Evaluation of the PANDA Endcap Disc DIRC*, Dissertation JLU Giessen, (2017)

[55] J. Rieke et al., *A Disc-DIRC Cherenkov Detector with High Resolution Micro Channel Plate Photomultiplier Tubes*, 2014 IEEE NSS/MIC, DOI: 10.1109/NSS-MIC.2014.7431161

[56] http://www.alsgmbh.com/pilas.html, Accessed in January 2017

[57] S. Korpar et al., *Photonis MCP-PMT as a light sensor for the BelleII RICH*, Nucl. Instr. and Meth. A639 (2011) 162–164

[58] J. Va'vra et al., *A 30 ps timing resolution for single photons with multi-pixel Burle MCP-PMT*, Nucl. Instr. and Meth. A572 (2007) 459–462

[59] S. Korpar et all, *Timing and cross-talk properties of BURLE multi-channel MCP PMTs*, Nucl. Instr. and Meth. A595 (2008) 169–172

[60] R. Diener, *PCMAG Solenoid Upgrade at DESY Testbeam Area T24/1*, AIDA 3rd Annual Meeting, Vienna, 2014

[61] M. Schmidt, *Particle Identification with Endcap Disc DIRC at PANDA*, Dissertation, JLU Gießen, in preparation

[62] Angelo Rivetti, private communication, 2014

List of Figures

List of Tables